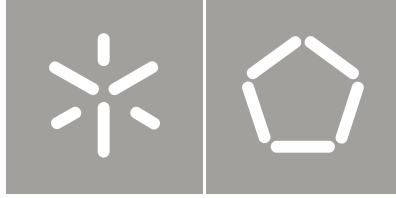




Universidade do Minho
Escola de Engenharia

Mauro César Rabuski Garcia

SHRINKAGE AND EJECTION FORCES IN
THERMOPLASTICS REINFORCED WITH
GLASS FIBRES AND NANOCCLAYS



Universidade do Minho
Escola de Engenharia

Mauro César Rabuski Garcia

SHRINKAGE AND EJECTION FORCES IN
THERMOPLASTICS REINFORCED WITH
GLASS FIBRES AND NANOCCLAYS

Tese de Doutoramento
Ciência e Engenharia de Polímeros e Compósitos

Trabalho efectuado sob a orientação do
Professor Doutor António José Vilela Pontes
Professor Doutor Aurélio da Costa Sabino Netto

Abstract

The process of injection moulding is a complex theme of study, and the manufacture of the moulds requires knowledge about materials, processing and design methods. The larger challenge for designers and engineers is to obtain one product within established tolerances. The prediction of shrinkage enables the engineers to know the final size and shape of the parts. There are commercial codes to simulate the injection moulding process and, thus, help to design runner system, cooling system, weld lines, air traps, and shrinkage. However, there is no software known that could determine the ejection force and, therefore, help to design the ejection system.

In this work, a study of shrinkage and ejection force was carried out using deep tubular parts of several materials. This work develops a model to predict the shrinkage and ejection force of mouldings in polypropylene composites reinforced with glass fibre or nanoclays.

The experimental part of this work consists in producing the parts with an instrumented mould with monitorisation of the temperature, pressure and ejection force. The final dimensions were also measured after 48 hours to calculate as-moulded shrinkage. Several other tests were done to characterize the material namely DSC, DMA, TMA and rheometry. The tensors of orientation of fibres were determined due to its influence on the shrinkage. The content of fibre, the length and diameter of the glass fibres were evaluated. The coefficient of friction between the steel and polymer was determined to calculate the ejection force. The simulations using the Moldflow software provided the temperature profile across the thickness of the part.

The mathematical model that was developed is based on the thermomechanical model to calculate the residual stresses and shrinkage in composites, developed by Kaspar Jansen, and a thermomechanical model to calculate the ejection force in tubular mouldings produced in unreinforced materials, developed by António Pontes. The proposed model is an attempt to predict the shrinkage and ejection force combining those previous models. The results of the model were compared with the experimental results and were found to be in a good agreement.

Resumo

O processo de moldação por injeção é complexo e o fabrico de ferramentas para produzir uma peça requer conhecimento sobre materiais, processamento e metodologias de projeto. O maior desafio para os projetistas e engenheiros é obter uma peça moldada dentro das tolerâncias estabelecidas. A previsão da contração permite aos projetistas prever a dimensão final e a forma das peças produzidas. Há softwares comerciais para simular o processo de injeção e prever, desta maneira, o sistema de alimentação, arrefecimento, linhas de soldadura, retenções de ar, e a contração, mas, não existe software conhecido, para prever a força de extração e, portanto, o sistema de extração.

Neste trabalho, um estudo da contração e força de extração foi realizado em moldações tubulares profundas para diversos materiais. O objetivo deste trabalho é desenvolver um modelo para prever a contração e força de extração moldadas em compósitos de polipropileno com fibra de vidro e nanoargila.

A parte experimental deste trabalho consiste em produzir peças num molde instrumentado com sensores de temperatura, pressão e força de extração e após 48 horas procedeu-se a medição das moldações para efetuar o cálculo da contração pós moldação. Diversos outros testes foram realizados para caracterizar o material como DSC, DMA e TMA e reometria. Os tensores de orientação das fibras foram determinados, pois influenciam a contração. A quantidade de fibra, o comprimento e diâmetro da fibra de vidro foram também medidos. Os coeficientes de atrito entre o aço e o polímero foram medidos, pois são necessários para calcular a força de extração. Os campos de temperatura ao longo da espessura da peça foram obtidos através das simulações com o software Moldflow.

O modelo matemático foi baseado no modelo termomecânico para prever as tensões residuais e contração em materiais reforçados com Fibras de Vidro Curtas desenvolvido por Kaspar Jansen e no modelo termomecânico para prever as forças de extração e contração em peças tubulares com materiais não reforçados desenvolvido por António Pontes. O modelo proposto é uma tentativa de prever a contração e a força de extração combinando os modelos anteriores de Kaspar Jansen e António Pontes. Os resultados de previsão do modelo desenvolvido foram comparados com os resultados experimentais e apresentaram uma boa concordância.

Acknowledgements

This research work is the result of the effort of several people, institutions and resources. Therefore, I would like to mention the principal supports that I receive during all the period of this thesis, mainly that sort of help without I could do this work.

First of all, I thank to Professor António José Vilela Pontes, researcher and scientific supervisor of this thesis for all help and support, his time and encouragement. I have certain that if I had not his help in difficult periods I could not finish this work.

I want also to thank to the Professor Aurélio da Costa Sabino Netto, co-supervisor, for the help in critical periods, suggestions of improvement the work and his friendship.

Professor António Sergio Duarte Pouzada by the encouragement to come to the University of Minho to make my Phd in Science and Polymer Engineering.

I have also to mention the Instituto Federal Sul-Rio-grandense, mainly, the Campus of Sapucaia do Sul-RS, Brazil by the permission to remain in Portugal during the preparation of this thesis and the financial support during this period.

It would be impossible to develop this work without the equipments of IPC – Institute of Polymer and Composites – Polymer Department of University of Minho and the assistance of technicians of the laboratories as Maurício José Aires Malheiro, Serafim José Pinto Sampaio, Manuel Fernando Martins Escourido and Francisco Mateus Ribeiro.

I would like to thank the ladies of the secretary of the Polymer Engineering Department Ana Paula Brites, Lucia Soares and Patrícia Cavaco for all help during this time in Guimarães, their good education and professional competences.

I have a special acknowledgment to Fernando Mendes and Simão Pereira for their support in information technology.

The friendship of portuguese Msc. Manuel Carvalho Ferreira by the time that worked together in some experimental parts of this thesis, without his support the start of this work would have more difficult.

I have thank to my family in Brazil, mainly my parents, my Brazilian friends in Portugal and in Brazil to help me a lot emotionally.

I thank to the Cesar Pedrini Neto, Brazilian personal friend and colleague at IFSUL, for the help and friendship and all discussions about polymer further the virtual coffee philosophical.

I need also to remember my colleagues from Redondel, the office that I remained during my Phd in Guimarães, by the healthy living, especially to Sacha Trevelyan Mould and Fantina Esteves for useful tips.

For Dr. Mladen Feodorov Motovilin, Delft University of Technology, personal friend, helped me in the thermomechanical analysis.

Prof^a. and colleague at IFSUL Bênia Costa Rilho for her help in mathematics.

For Brazilian friends Etienne Amorin and Nívea Taís and Iranian friend Shafagh Dinparast Tohidi, personal great friends in Guimarães.

And finally, I have to thank this friendly country, Portugal, for their welcoming people, natural beauty and lovely living.

Table of contents

1	Introduction	1
2	State of the art	4
2.1	<i>Injection moulding</i>	4
2.1.1	The process	4
2.1.2	Behaviour of polymer during the injection moulding process	6
2.1.3	Modelling of the injection moulding process	9
2.1.3.1	Filling phase	10
2.1.3.2	Packing phase	12
2.1.3.3	Unified model.....	13
2.1.3.4	Optimization of injection moulding	15
2.2	<i>Shrinkage</i>	16
2.2.1	Variables affecting shrinkage	18
2.2.1.1	Processing conditions	18
2.2.1.2	Project of the mould/part.....	21
2.2.1.3	Characteristics of Material	22
2.2.2	Shrinkage anisotropy	24
2.2.3	Influence of fibre orientation in shrinkage	26
2.2.4	Prediction of the shrinkage	27
2.2.4.1	Statistical modelling approach	29
2.2.4.2	Thermodynamic modelling approach.....	30
2.2.4.3	Thermomechanical modelling approach	33
2.2.4.4	Reinforced short fibre modelling approach.....	35
2.2.4.4.1	Short-fibre composites	35
2.2.4.4.2	Orientation tensors	37
2.2.4.4.3	Glass fibre	38
2.2.4.5	Reinforced nanoclay modeling approach.....	44
2.3	<i>Ejection forces in injection moulding</i>	47
2.3.1	Ejection system.....	47
2.3.2	Variables affecting the ejection force	48
2.3.3	Prediction of the ejection force.....	49
2.4	<i>Objectives of the work</i>	54
3	Models to predict shrinkage and ejection force	56
3.1	<i>Thermo-mechanical model for injection moulded plates</i>	56
3.1.1	Strain in thickness direction: effect of mould deformation	59
3.1.2	In-plane shrinkage	60
3.2	<i>Thermo-mechanical model for cylindrical tubes</i>	60
3.2.1	Assumptions of the model	61
3.2.2	Ejection force.....	64

3.3	<i>Thermo-mechanical model for reinforced moulded plate</i>	66
3.4	<i>Thermo-mechanical model for reinforced injection moulded products in cylindrical tubes</i>	72
4	Experimental methods and simulation techniques	78
4.1	<i>Materials and characterisation</i>	78
4.1.1	Polypropylene	78
4.1.2	Nanoclays	79
4.1.3	Material identification codes	79
4.1.4	Melting temperature, crystallization temperature and degree of crystallinity	79
4.1.5	Storage modulus	82
4.1.6	Coefficient of linear thermal expansion	85
4.1.7	Rheology characterization	87
4.1.8	Coefficient of Friction measurement	91
4.1.9	Measurement of the glass fibre percentage	94
4.1.10	Glass fibre measurement (length and diameter)	95
4.2	<i>Injection moulding</i>	98
4.2.1	Moulding conditions	99
4.2.2	Data acquisition	99
4.2.3	Fibre Orientation Measurement	102
4.2.4	Measurement of shrinkage	104
4.3	<i>Simulation of temperature field</i>	106
4.3.1	Mesh	106
4.3.2	Rheology description	107
4.3.3	PVT description	108
4.3.4	The SciLAB software	109
5	Results and Discussion	110
5.1	<i>Injection moulding</i>	110
5.1.1	Moulding pressure	110
5.1.2	Temperature evolution	114
5.2	<i>Shrinkage</i>	115
5.2.1	Variation along the flow path	115
5.2.2	Thickness shrinkage	118
5.2.3	Effect of the mould temperature	121
5.2.4	Effect of the content of glass fibre	123
5.2.5	Effect of content of nanoclays	124
5.3	<i>Ejection force</i>	126
5.4	<i>Fibre Orientation Measurement data</i>	127
5.5	<i>Model implementation</i>	130

5.6	<i>Assessment of the model accuracy</i>	132
5.6.1	Shrinkage.....	132
5.6.2	Ejection force.....	136
6	Conclusions	140
	<i>Shrinkage</i>	<i>140</i>
	<i>Ejection force</i>	<i>141</i>
7	Further work	143
8	References	144
9	Appendix	160

List of figures

Figure 2.1 - Injection moulding cycle	5
Figure 2.2 - Velocity profile of the melt in the mould, adapted from [7], [8], [10].	6
Figure 2.3 - Velocity, temperature and shear rate profiles in the filling of the impression, adapted of [7], [8], [10].	7
Figure 2.4 - Stages of injection process.....	8
Figure 2.5 - Influence of several factor on shrinkage [14]	19
Figure 2.6 - PVT curve evaluating shrinkage [113]	31
Figure 2.7 - The orientation of a single axisymmetric particle is described by the angles, θ and ϕ , or by a unit vector p directed along the particle axis [122]	36
Figure 3.1 - Schematic view of the mould during polymer solidification.....	56
Figure 3.2 - Scheme of cross-section of tubular part [3],[174]	61
Figure 3.3 - Schematic representation of forces before ejection	65
Figure 3.4 - Orthotropic material and transversally isotropic in 2-3 plane (adapted [179])	74
Figure 4.1 - Crystallization curve for polypropylene without reinforcement.....	82
Figure 4.2 – Three point bending mode [189].....	83
Figure 4.3 - DMA output for PP without reinforcement	84
Figure 4.4 – Schematic diagrams of TMA apparatus [190]	86
Figure 4.5 - Experimental curve obtained of TMA for PP without reinforcement	87
Figure 4.6 – Pistons of Advanced Capillary Rheometer RH 10.....	88
Figure 4.7 - Polypropylene without reinforcement at 220°C	89
Figure 4.8 - PP 10% glass fibre at 220°C	90
Figure 4.9 - PP 30% glass fibre at 226.7°C	90
Figure 4.10 - Concept of Mouldfriction [192].....	91
Figure 4.11 - View of the mouldfriction installed in a universal testing machine	92

Figure 4.12 - Friction test for PP with 10% of glass fibre.....	93
Figure 4.13 - Photograph of sample with 30% of glass fibre.....	96
Figure 4.14- Histogram of sample with 10% glass fibre.....	98
Figure 4.15 – Tubular part.....	98
Figure 4.16 - Moulding part with the positions of pressure and temperature sensors..	100
Figure 4.17 - Location of temperature and pressure sensors [173]	100
Figure 4.18 - Location of cell load sensors [173].....	101
Figure 4.19 - Ejection force evolution for PP30% glass fibre and mould temperature of 75°C.....	102
Figure 4.20 – Location of the samples for fibre orientantion.....	103
Figure 4.21 - Sample after polish operation	103
Figure 4.22 - Equipment used to acquire the pictures of samples.....	104
Figure 4.23 - Tesa 3D CMM Equipment to measure the moulding dimensions.....	105
Figure 4.24 - 3D mesh from Moldflow	106
Figure 4.25 - Part and cooling system	107
Figure 5.1 - Pressure evolution during an injection cycle of neat PP with mould temperature of 30°C	111
Figure 5.2 - Influence of the mould temperature in the pressure evolution for PP – Domolen 1100L.....	112
Figure 5.3 - Influence of glass fibre content in the cavity pressure evolution at mould temperature of 75°C	112
Figure 5.4 - Influence of nanoclay content in the pressure evolution at mould temperature of 50°C	113
Figure 5.5 - Influence of nanoclay on the pressure evolution of reinforcement PP of mould temperature of 75°C	114
Figure 5.6 - Evolution of temperature along of the injection cycle for PP with 2% of nanoclay different mould temperatures	115

Figure 5.7 - As-moulded diametrical shrinkage at different position along the flow path for PP tubes with mould temperature of 30°C.....	116
Figure 5.8 - As-moulded diametrical shrinkage at different position along the flow path for PP tubes with mould temperature of 75°C.....	117
Figure 5.9 - As-moulded diametrical shrinkage for different position along the flow path for PP tubes with different contents of nanoclay.....	117
Figure 5.10 – As-moulded diametrical shrinkage along the flow path for PP tubes with 10% and 30% of glass fibres	118
Figure 5.11 - Thickness shrinkage for PP without reinforcement.....	119
Figure 5.12 - Thickness shrinkage for PP with 6% of nanoclay	119
Figure 5.13 -Thickness shrinkage for PP with 10% of glass fibre	120
Figure 5.14 - Thickness shrinkage for PP with 30% of glass fibre	120
Figure 5.15 - Shrinkage of the external diameter of different mould temperatures	121
Figure 5.16 - Shrinkage of the internal diameter with various mould temperatures	122
Figure 5.17 - Shrinkage dependence of the mould temperature for PP without reinforcement in several positions along the flow path.....	122
Figure 5.18 – Shrinkage of external diameter at the position T2 for different glass fibre content and different mould temperatures	123
Figure 5.19 – Shrinkage of internal diameter at position T2 for different glass fibre content for different mould temperatures	124
Figure 5.20 – Internal diameter at position T2 for different content of nanoclays at different mould temperatures	125
Figure 5.21 – External shrinkage diameter of position T2 for different content of nanoclays at different mould temperatures.....	125
Figure 5.22 - Ejection forces in relation to content of nanoclays for mould temperatures of 30°C, 50°C and 75°C	126
Figure 5.23 - Ejection forces in relation to content of glass fibre for mould temperatures of 30°C, 50°C and 75°C	127

Figure 5.24 - Tensors for PP with 10% of glass fibre for mould temperature of 50°C near from the gate	128
Figure 5.25 - Tensors for PP with 10% of glass fibre for mould temperature of 50°C far from the gate.....	128
Figure 5.26 - Tensors for PP with 30% of glass fibre for mould temperature of 50°C near from the gate	129
Figure 5.27 - Tensors for PP with 30% of glass fibre for mould temperature of 50°C far from the gate.....	129
Figure 5.28 - Comparison between the model and experimental shrinkage in the flow direction at different mould temperature for PP0.....	132
Figure 5.29 - Comparison between the model and experimental average diametrical shrinkage in relation to the mould temperature for PP0.....	133
Figure 5.30 - Comparison between the model and experimental average diametrical shrinkage for different content of nanoclay near to the gate and far from the gate at the mould temperature of 75°C	134
Figure 5.31 - Comparison between the model and experimental diametrical shrinkage in relation to the content of glass fibre near from the gate and far from the gate for the mould temperature of 75°C	134
Figure 5.32 - Comparison between the model and experimental diametrical shrinkage in relation to the content of glass fibre 10% and nanoclay 2% added simultaneously near from the gate and far from the gate for the mould temperature of 50°C.....	135
Figure 5.33 - Comparison between the model and experimental diametrical shrinkage in relation to the content of glass fibre 30% and nanoclay 2% added simultaneously near from the gate and far from the gate for the mould temperature of 30°C.....	136
Figure 5.34 - Comparison between the model and experimental ejection force in relation to the mould temperature for PP0.....	137
Figure 5.35 - Comparison between the model and experimental ejection force in relation to the mould temperature for PP6N	137
Figure 5.36 - Comparison between model and experimental results for ejection force in relation to the content of glass fibre in different mould temperatures.....	138

Figure 5.37 - Comparison between model and experimental results for ejection force for material with glass fibre and glass fibre with addition of nanoclay	139
Figure A4. 1 - Crystallization curve for PP2N	179
Figure A4. 2 - Crystallization curve for PP6N	179
Figure A4. 3 - Crystallization curve for PP10N	180
Figure A4. 4 - Crystallization curve for PP10GF	180
Figure A4. 5 - Crystallization curve for PP30GF	181
Figure A4. 6 - Crystallization curve for PP10GF2N	181
Figure A4. 7 - Crystallization curve for PP30GF2N	182
Figure A5. 1 - Storage modulus for several materials relation to the temperature.....	183
Figure A5. 2 - DMA curves for PP with 2% of nanoclay	183
Figure A5. 3 - DMA curves for PP with 6% of nanoclay	184
Figure A5. 4 - DMA curves for PP with 10% of nanoclay	184
Figure A5. 5 - DMA curves for PP with 10% of glass fibre	185
Figure A5. 6 - DMA curves for PP with 30% of glass fibre	185
Figure A5. 7 - DMA curves for PP with 10% of glass fibre and 2% of nanoclay	186
Figure A5. 8 - DMA curves for PP with 30% of glass fibre and 2% of nanoclay	186
Figure A6. 1 - Curve for thermal expansion coefficient for PP2N.....	187
Figure A6. 2 - Curve for thermal expansion coefficient for PP6N.....	187
Figure A6. 3 - Curve for thermal expansion coefficient for PP10N.....	188
Figure A6. 4 - Curve for thermal expansion coefficient for PP10GF	188
Figure A6. 5 - Curve for thermal expansion coefficient for PP30GF	189
Figure A6. 6 - Curve for thermal expansion coefficient for PP10GF2N	189
Figure A6. 7 - Curve for thermal expansion coefficient for PP30GF2N	190
Figure A8. 1 - DSC curves for materials with different reinforcements	195
Figure A9. 1- Polypropylene without reinforcement in the temperature of 240°C.....	196

Figure A9. 2- Polypropylene without reinforcement in the temperature of 260°C.....	196
Figure A9. 3 - PP 10% glass fibre in the temperature of 200°C	197
Figure A9. 4 - PP 10% glass fibre in the temperature of 240°C	197
Figure A9. 5 - PP 30% glass fibre in the temperature of 200°C	198
Figure A9. 6 - PP 30% glass fibre in the temperature of 253,3°	198

List of tables

Table 4.1- General properties of polypropylene grades	78
Table 4.2 - Materials and identification code	79
Table 4.3 - The test data of DSC	80
Table 4.4 - Crystallization temperature for the materials	81
Table 4.5 - Storage modulus for all materials studied	84
Table 4.6 - Coefficient of linear thermal expansion for several materials	86
Table 4.7 - Correspondence among experimental materials and Moldflow materials ...	88
Table 4.8 - Test temperatures used in the rheological experiments	89
Table 4.9 - Coefficient of friction in relation to material and roughness of the mould..	94
Table 4.10 - Measurement of percent of glass fibre (10%)	94
Table 4.11 - Measurement of percent of glass fibre (30%)	95
Table 4.12 - Length measurement of 10% glass fibre and 30% glass fibre	97
Table 4.13 - Diameter measurement of 10% glass fibre and 30% glass fibre.....	97
Table 4.14 - Moulding conditions	99
Table 4.15 - Shrinkage for PP - mould temperature 30°C	105
Table 4.16 - Parameters for the Cross-WLF model (Moldflow 6.1).....	108
Table 4.17 - Parameters of the modified Tait equation	109
Table 5.1 - Parameters of the models used for unreinforced PP	130
Table 5.2 - Glass fibre parameters	131
Table 5.3 - Comparison among the results of the model and experimental data of ejection force for materials in relation of the mould temperature	139
Table A1. 1 - Property typical value for Domolen 1100L [181].....	160
Table A1. 2 - Property typical value for Domolen P1-013-V10-N [183]	161
Table A1. 3 - Property typical value for Domolen P1-102-V30-N [184]	162

Table A2. 1 - Shrinkage for PP - mould temperature 30°C.....	163
Table A2. 2 - Shrinkage for PP - mould temperature 50°C.....	163
Table A2. 3 - Shrinkage for PP - mould temperature 75°C.....	163
Table A2. 4 - Shrinkage for PP10GF - mould temperature 30°C	164
Table A2. 5 - Shrinkage for PP10GF - mould temperature 50°C	164
Table A2. 6 - Shrinkage for PP10GF - mould temperature 75°C	164
Table A2. 7 - Shrinkage for PP30GF - mould temperature 30°C	165
Table A2. 8 - Shrinkage for PP30GF - mould temperature 50°C	165
Table A2. 9 - Shrinkage for PP30GF - mould temperature 75°C	165
Table A2. 10 - Shrinkage for PP2N - mould temperature 30°C.....	166
Table A2. 11 - Shrinkage for PP2N - mould temperature 50°C.....	166
Table A2. 12 - Shrinkage for PP2N - mould temperature 75°C.....	166
Table A2. 13 - Shrinkage for PP6N - mould temperature 30°C.....	167
Table A2. 14 - Shrinkage for PP6N - mould temperature 50°C.....	167
Table A2. 15 - - Shrinkage for PP6N - mould temperature 75°C	167
Table A2. 16 - Shrinkage for PP10N - mould temperature 30°C.....	168
Table A2. 17 - Shrinkage for PP10N - mould temperature 50°C.....	168
Table A2. 18 - Shrinkage for PP10N - mould temperature 75°C.....	168
Table A2. 19 - Shrinkage for PP10GF2N - mould temperature 30°C.....	169
Table A2. 20 - Shrinkage for PP10GF2N - mould temperature 50°C.....	169
Table A2. 21 - Shrinkage for PP10GF2N - mould temperature 75°C.....	169
Table A2. 22 - Shrinkage for PP30GF2N - mould temperature 30°C.....	170
Table A2. 23 - Shrinkage for PP30GF2N - mould temperature 50°C.....	170
Table A2. 24- Shrinkage for PP30GF2N - mould temperature 75°C.....	170
Table A3. 1 - Ejection force for PP0	171
Table A3. 2 - Ejection force for PP10GF	172

Table A3. 3 - Ejection force for PP30GF	173
Table A3. 4 - Ejection force for PP2N	174
Table A3. 5 - Ejection force for PP6N	175
Table A3. 6 - Ejection force for PP10N	176
Table A3. 7 - Ejection force for PP10GF2N	177
Table A3. 8 - Ejection force for PP30GF2N	178
Table A7. 1- Parameters used for polypropylene with 2% of nanoclay in the model..	191
Table A7. 2 - Parameters used for polypropylene with 6% of nanoclay in the model.	191
Table A7. 3 - Parameters used for polypropylene with 10% of nanoclay in the model	192
Table A7. 4 - Parameters used for polypropylene with 10% of glass fibre in the model	192
Table A7. 5 - Parameters used for polypropylene with 30% of glass fibre in the model	193
Table A7. 6 - Parameters used for polypropylene with 10% of glass fibre and 2 % of nanoclay in the model.....	193
Table A7. 7 - Parameters used for polypropylene with 30% of glass fibre and 2 % of nanoclay in the model.....	194

List of symbols

A – Contact area

\tilde{a}_{ij} – Component of matrix inverse of the thickness averaged stiffness A_{ij}

B - Half thickness of the rectangular impression

B - Factor in Tait equation whose meaning is a function of temperature alone with two material constants (eq. 2.6)

b1m - Constant in Tait equation (eq. 2.7)

b1s - Constant in Tait equation (eq. 2.8)

b2m - Constant in Tait equation (eq. 2.7)

b2s - Constant in Tait equation (eq. 2.8)

b3m - Constant in Tait equation (eq. 2.10)

b3s - Constant in Tait equation (eq. 2.11)

b4m - Constant in Tait equation (eq. 2.10)

b4s - Constant in Tait equation (eq. 2.11)

b5 - Constant in Tait equation (eq. 2.12)

b6 - Constant in Tait equation (eq. 2.12)

b7 - Constant in Tait equation (eq. 2.14)

b8 - Constant in Tait equation (eq. 2.14)

b9 - Constant in Tait equation (eq. 2.14)

C - Universal constant for Tait equation, value of 0.0894 (eq. 2.6)

CM - Mould compliance

d – Diameter of glass fibre

d_k - Inner diameter of the part (eq. 2.20)

E - Elastic modulus

F_C - Other interaction forces with the mould

F_e - Ejection force

F_{fi} - Friction force

F_R - Release force

F_S - Stretching force due to the pressure

G - Shear modulus

H - Thickness of the tubular impression

L - Height of core (eq. 2.19)

l - Length of glass fibre

l_0 - Initial length

l_r - Length at room temperature under atmospheric pressure

P - Unit vector directed along the particle axis (glass fibre)

P - Contact pressure

p - Pressure

p - Cartesian components of P (orientation of glass fibre)

p - Pressure Tait equation (eq. 2.6)

P_a - Atmospheric pressure (eq. 2.19)

P_{atm} - Atmospheric pressure

p_c - Contact pressure acting on the core surface

p_{gf} - Pressure distribution inside the impression at the instant of the gate solidification

p_u - Negative pressure (eq. 2.20)

xx

Q_{ij} - Stiffness matrix coefficient

R0 - Internal radius

R1 - External radius

Rm - Average radius

S_{ii} - Stress component in the i direction

s₁% - Percentage of shrinkage

S^h - Thickness shrinkage

S_D - Base thickness (eq. 2.20)

S_F - Thickness of the part (eq. 2.20)

Sh_{Dm} - Diametrical shrinkage

Sh_r - Thickness shrinkage

S_l - Linear shrinkage

S_v - Volumetric shrinkage

S^{||} - Linear shrinkage in the flow direction

S[⊥] - The linear in-plane shrinkage perpendicular to the flow direction

T - Temperature Tait equation (eq. 2.6)

t - Part wall thickness (eq. 2.19)

t - Time

T - Temperature

T_e - Ejection temperature

T_g - Glass transition temperature

T_{room} - Room temperature

T_s - Solidification temperature

$t_{x,shr}$ – Moment of begin of shrinkage

t_z^* - Onset of the thickness shrinkage

t_r^* - Shrinkage onset in the i direction

t_{s0} - Start of solidification

t_{sz} - Solidification onset of a layer z .

V - Volume

v - Specific volume

v_0 – Initial specific volume

\bar{v}_0 - Gap-wise averaged initial specific volume

v_r - Specific volume at room temperature under atmospheric pressure

v_t - Term to account for the volume decrease due to crystallization in the Tait P-V-T equation

W_1 - Width of long side of core (eq. 2.19)

W_2 - Width of short side of core (eq. 2.19)

z_s - Position of the solid-melt interface or solidified layer thickness

α - Coefficient of thermal expansion

α - Angle

β - Linear compressibility

Γ - Poisson's ratio (eq. 2.19)

ε_{ii} - Observable strain in the i direction

ε^p - Hydrostatic strain

ε_{ii}^T - Thermal strain in the i direction

η – Relation between elastic modulus of glass fibre and matrix to the Halpin-Tsai equations

θ - Orientation angle of fibre

θ - Angle

μ - Coefficient of friction

ν - Poisson's ratio

σ - Stress

ϕ - Orientation angle of fibre

ψ - Probability density function for orientation of fibres

1 Introduction

The quality and efficiency have been the requirement of all companies in the industrial market, more intensified by the globalization. Both features must be linked to obtain best results along competitive market in all producing areas. This situation is required by the industries because the consumers desire more in less time and at lower cost.

There is no exception for the polymer industries, mainly thermoplastics processing industries, they must improve their results in this competitive market. This aim only will be achieved if all stages of production of an article have a quality system implemented. This quality system ranges from the conception of the product to the achievement the product ready to use. This objective was better achieved when the CAD, CAM and CAE were implemented in the companies. Today the manufacturers have to reduce the time to production. Generally the design of the product and the manufacturing tools are made simultaneously. The computational simulation avoids many bad performances when the product will be in service.

The injection moulding is the main process for manufacturing plastics products. The first step to obtain a product with a good quality is to carry on various CAE analyses to obtain the best processing conditions. This information is used in the design stages of the part and the mould. During the project of the part the designer has to develop several systems for the perfect working of the mould when in operation. Besides the concept of the injection moulded product, others systems of the mould must be designed such as feeding and gating, cooling, guiding system, venting and ejection.

The aim of this research focus on the ejection system. From knowing the form of the plastics part and the ejection forces it is possible to obtain a suitable ejection system, this including the type of ejection system to be used: hydraulic, pneumatic or mechanical. If the forces are underestimated the projected system cannot extract the part from the mould and in some cases the part can be damaged. In the literature there are not enough studies about ejection forces.

One of the more meaningful variables influencing the ejection force is the shrinkage of the part, but this parameter is not easy to predict, because the shrinkage depends on the

geometry of the part and the mould, the type of material and the processing conditions. This complexity is due to the transformation of the polymer since of beginning of the process until the extraction of the part from the mould. The polymer goes from solid state to plasticized state and becomes solid again. During this process the material is subjected to an environment with high pressure and temperature. There is an expansion of the molecules and the material is moulded in the form of the impression. During the permanence of the material inside the mould, during the cooling time the moulding decreases its dimensions owing to shrinkage. The dimension of the part is less than the impression and the designer must consider this factor to obtain the correct dimensions in the mouldings surfaces.

This research work studies shrinkage and ejection forces in a set of composite polypropylenes with glass fibres and nanoclays. A tubular geometry was used and a mathematical model was developed to predict the shrinkage and the ejection forces for reinforced materials.

An instrumented mould was used to monitor the pressure, temperature and ejection forces in the tubular parts. These data were employed to validate the model developed in this work. Computation simulations were also carried out to get the temperature field inside the part during the entire process.

This thesis is organized as follows. Firstly, a brief introduction about the work is presented to contextualize of the subject in the area of study, and some general comments are done about injection moulding.

In chapter 2 it is presented the state of the art on the topics related with this research. It starts with the injection moulding process where an overview of the process is delineated and the historical about modelling of the injection moulding process, including the various stages of the process such as filling, packing, unified models, and some considerations about the process optimization. The shrinkage phenomena and their prediction is described with reference to the variables that affect it such as processing conditions, design of mould and part and characteristics of the materials. The anisotropy of shrinkage is also reviewed because one of the materials in study is a fibrous composite. Existing models to describe shrinkage are reviewed. This chapter ends with the detailed objectives of this work.

In the chapter 3 the review of the models to predict shrinkage are described including the model of Kaspar Jansen to predict the shrinkage in rectangular plates moulded with reinforced material. It includes the development of the model to predict the shrinkage and ejection forces for tubular parts moulded with reinforced material is presented.

The chapter 4 described the experimental methods and simulation techniques used in this work. The materials used are characterized using various experimental tests as DSC, DMA, rheological test, and TMA. The features of the tubular part, the processing conditions, equipments used in the production of the tubular parts are presented. The characterization tests of the mouldings, as measurement of glass fibre percentage, measurement of diameter and length of glass fibre, are also described. Moreover, the measurement of the coefficient of friction using a prototype equipment is presented. On the other hand, the simulation techniques are described, demonstrating the features of the software and conditions for the simulations.

The chapter 5 presents the results and their discussion. The experimental and predicted results are shown and some details are discussed. The pressure, temperature and ejection forces evolution are presented. The shrinkage and ejection forces are shown and the explanation of their variation is done.

Finally the conclusions are presented and commented.

The suggestions for further work are mentioned in the last chapter 7. A research work will never finish, but it is only a step and incentive to seek more knowledge.

2 State of the art

2.1 Injection moulding

2.1.1 The process

Thermoplastic injection moulding had its origin in metal casting. The first injection machine for plastics was developed during the U. S. civil war due to ivory shortage. In 1869, John Wesley Hyatt used celluloid instead of ivory. The first injection machine, Hyatt's machine, was patented in 1872 [1]. In 1921, another injection moulding machine was built by H. Buchholz. This machine was a plunger-type that was widely used in the past [2]. The injection moulding machine known nowadays was designed in 1956 with the introduction of the reciprocating screw for plasticizing and transfer the melt for the mould. This kind of machine keeps its features until today.

Injection moulding is among the processes of plastics moulding with the best cost-benefit relation. The complete unit for injection moulding consists of the injection moulding machine, a temperature control and ancillaries such as: material drier, material handling systems and robots to help ejection of the parts [2],[3].

The injection moulding process produces identical parts from an impression. The plasticized material is forced into the mould where it is maintained under pressure until the solid state is obtained. However, once the mould is filled and the part begins to solidify, additional amount of material must be introduced to compensate the polymer shrinkage during the solidification phase. Without this additional amount of melt, the dimensions of part will not be reached [4],[5].

The injection cycle was described by several authors in the specialized literature [2]–[8].

The injection moulding cycle begins when the mould is closed; the melt is injected in the mould, Figure 2.1. The material, in the form of pellets, enters in the barrel by the hopper. The pellets are melted inside the barrel, the heating is provided by electric resistance around the barrel and by friction between the barrel walls and the material. The reciprocating screw is used to carry and to press the material. During the plasticization

the screw moves backwards and the injection unit provides a back pressure. The screw stops when the next amount of material is accumulated.

In the injection phase, the reciprocating screw moves forward and presses the melt to the machine nozzle, runner system and gates, and finally, the impressions in the mould.

After the filling of impressions, the holding pressure is maintained to compensate the material shrinkage. At the end of holding phase, the screw returns and the next plasticization occur. The melt material is accumulated in front of the screw and the next shot is ready.

In the moment that the material enters in the mould, the material starts to cool. This cooling phase is more evident during the holding phase. When the part is cooled and solidified, it is ejected from the mould.

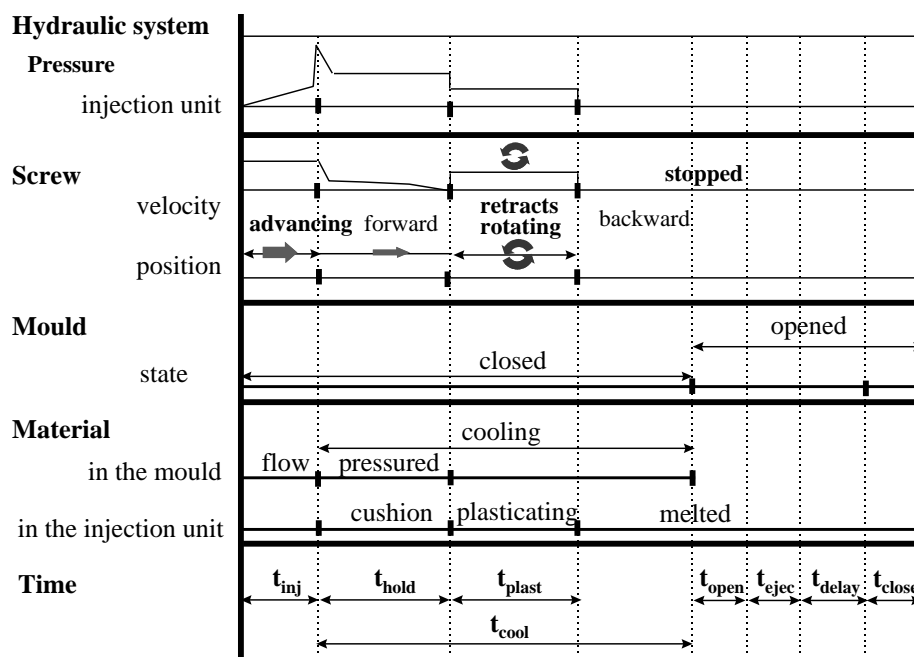


Figure 2.1 - Injection moulding cycle

Injection moulding cycle (t_{inj} - injection time, t_{hold} - holding time, t_{plast} - plasticizing time, t_{cool} - cooling time, $t_{open/close}$ - mould opening/closing time, t_{ejec} - ejection time, t_{delay} - delay time)

2.1.2 Behaviour of polymer during the injection moulding process

The environment of the flow of polymer into the impression is a typical situation of unsteady, non-isothermal and three-dimensional flow, of a compressible and viscoelastic fluid.

The injection phase starts with the filling of the impression until the moment of switch-over to the holding phase. During the flow, the polymer is submitted to the associated effects to the flow (shearing and heating) and the cooling due to heat loss to the moulding walls. In the Figure 2.2, it is shown the velocity profile of flowing molten polymer, [7], [8], [10]–[12]. In this figure it is visible the fountain flow and the formation of the solidified layer when the melt polymer meets the cool moulding wall. In this layer, after solidification of material, there is no additional flow and between the two solidified layers can be found the melt core of the material, this core remains fluid.

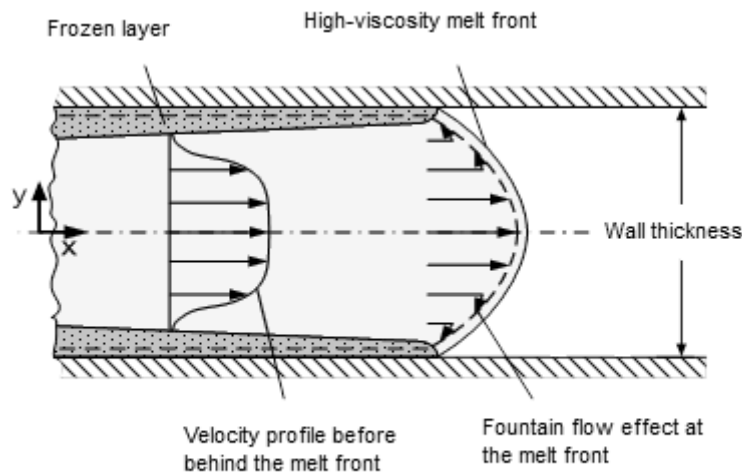


Figure 2.2 - Velocity profile of the melt in the mould, adapted from [7], [8], [10].

The highest velocity gradient found in the flow zone occurs at the vicinity of solidified layer. Nevertheless, because of the high viscosities found in this region, this maximum velocity is not exactly adjacent of the solidified layer. Moreover, in this higher velocity gradient region, the melt is submitted to pronounced shearing flow; due to this reason the polymer has its molecules orientated in the main direction of the flow. Because that the maximum orientation is just located below of moulding surface.

The thickness reduction of section due to the polymer solidified at the moulding walls, the maximum velocity found in this area is quite higher than velocity of flow front. Consequently, the melt particles, when reach the flow front, decrease their velocity occurring a perpendicular flow in relation to the mould wall in this area; this phenomenon is called fountain flow effect. This effect causes a stretching of the molecules of the flow front that are cooled owing to the contact with air inside the cavity and pressed against the cavity wall. The contact of polymer with the cooler wall causes the solidification instantaneously. This is the reason why the polymer is so oriented at the skin of the injection moulded parts. If the filling happens with uniform velocity, the orientation will be better and the superficial quality of the part too.

Although, the dominant flow in the filling phase is the shear flow, the highest velocity components are in the flow direction. The Figure 2.3 shows the velocity profile, shear rate, and temperature during the filling of the impression. It is possible to note that the temperature has two peaks near the cavity wall; it happens due to viscous dissipation. The maximum temperature occurs in the region of the maximum shear rate. The velocity is higher at the centre of the cavity because the no slip condition.

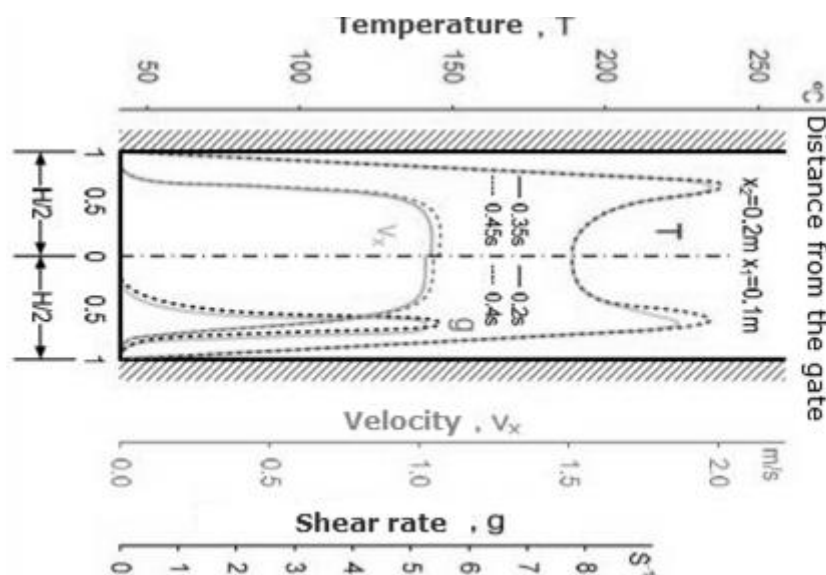


Figure 2.3 - Velocity, temperature and shear rate profiles in the filling of the impression, adapted of [7], [8], [10].

Other important factor in the injection moulding is the cavity pressure, Figure 2.4. It is possible to identify three stages: injection, compression and holding pressure. These three stages are related with some effects and also the part quality. The injection stage affect the appearance of injected part and the compression stage and the holding stage is responsible by the part dimensions. Briefly, there are several parameters that influence the pressure curves such as: oil temperature, melt temperature, mould temperature and injection velocity.

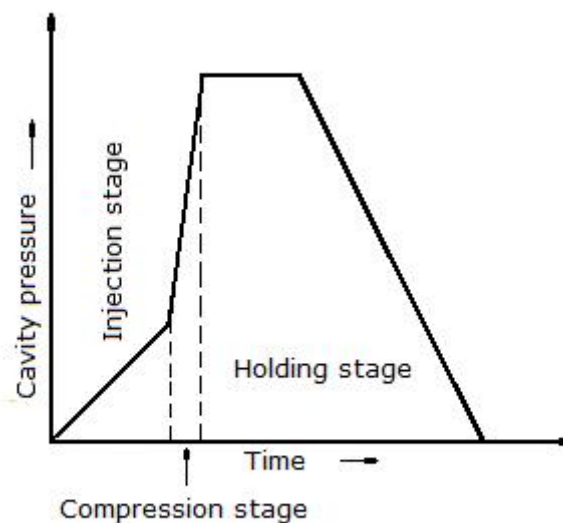


Figure 2.4 - Stages of injection process

The holding/packing phase starts at the moment of switch-over until the solidification of the gate. The most important aspect of the holding phase is the addition of more material to compensate the volumetric shrinkage of the part during its cooling. The holding/packing stage is extremely important in the determination of the final quality of the product. Underpacking results in dimensional variation and sink marks. Overpacking causes premature mould opening, flashing, difficulties at the ejection and excess of residual stresses that results in warpage [13].

The cooling phase begins immediately after of the entrance of material in the impression, including the injection and holding phases. However, the cooling time must be extended until the end of holding phase, because the melting has not been cooled yet. It is not recommended to eject the part yet.

After part ejection from the mould, the part is exposed to a new set of mechanical and thermal conditions. Although, if the part remains in the cavity, its shrinkage and possible warpage are avoided mechanically, due to the restraint imposed by cavity walls. Instead of the part deformation, will arise internal residual stresses during the cooling of the part. After the demoulding of the part, a bit of the stress will be relieved through the appearance of deformations and the shrinkage process happens without external constrain.

2.1.3 Modelling of the injection moulding process

Computational simulations helps designers and engineers to study many options in processing and design in injection moulding without loss of time and resources. The simulations provide new ways to consider projects and to experiment others concepts before manufacturing the tools and obtaining the injection moulded products. Through computational programmes it is possible to determine the dependence of variables and the most important factors in the injection moulding process [6].

The computational simulation is based on several assumptions and simplifications, as any process in development, for the injection moulding process being complex and the limitations of hardware and knowledge about the physics of the problem. These simplifications consider the geometry, mathematical model, involved parameters, phase of process. Currently the CAE systems are broadly used because the design cycle of the product must be faster and the production costs diminished [6].

Commonly the modelling of the process involves the conservation equations: mass, momentum and energy, which govern the physical phenomena. Furthermore, the constitutive equations related with the material are also used, namely, the relationship between the viscous stress tensor and the rate of strain tensor are constitutive equations. The mentioned equations need restrictions, boundary conditions, represented by geometries and physical parameters. These set of equations and their boundary conditions make the system complex to find an analytical solution, making it is necessary to call upon numerical solutions [13].

The simulation of the injection moulding process has been used in several degrees of complexity according to the objectives of the simulation. This complexity is due to the

mathematical formulation of conservation equations, constitutive laws and assumptions about material and techniques to solve the problem [15], the fields of temperature, pressure and velocity enable to know the microstructure distribution and, hence, the characteristics of final product. [15],[16].

The equations mentioned above must be solved simultaneously, namely, in the coupled form. During the process, the temperature, pressure fields must be obtained together with the advance of melt front flow. Depending on the solution required, the fluid is considered non-Newtonian and parameters as, temperature and crystallinity that depend on the time [15].

Injection moulding is developed in three stages: filling, holding or packing and cooling or solidification [12],[16].

2.1.3.1 Filling phase

The computational simulation of injection moulding began in the seventies with models developed for the filling phase. In 1970, Harry and Parrot [18], proposed a model to predict the fill length and fill time of the thin constant transversal section cavities. Besides the resolution of conservation equations this model considered heat conduction and viscous heat generation. It enabled good results in predicting a short shot for thin and also complete fill in thicker cavities. Berger and Gogos [19], in 1973, developed a numerical solution for the mould filling of rigid PVC melt in a circular impression. One year later, Tadmor and Broyer [20] described a method to describe the flow in narrow gaps of variable thickness and any desired shape. Other model presented in 1975 by Lord and William [21] increased the complexity of the relationship including viscosity, shear rate and temperature and solved real problems in injection moulding. The same authors, in the same year, [22] developed a finite difference analysis which predicted temperature, pressure and velocity distributions in straight and tapered, hot and cold walled circular flow channels.

In the eighties years Hieber and Shen [23] detailed a formulation of the model based on the generalized Hele-Shaw flow for an inelastic, non-Newtonian fluid with non-isothermal conditions applicable to thin cavities of planar geometry. In 1980, Isayev and

Hieber [24], applied the Leonov viscoelastic constitutive equation in the filling and cooling stages. The theory was developed with the following assumptions: one-dimensional, unsteady, non-isothermal flow of polymer between two parallel plates and further provided non-isothermal relaxation after cessation of the flow. They concluded that the most important factors that affect residual stresses and birefringence are melt temperature and flow rate. Sanou et al. [25] (1985) realized a study in a rectangular impression with three different thickness in unfilled and glass fibre-filled polypropylene and polystyrene. Their study focused on the shapes of flow fronts by short-shots and deduced that the thickness of cavity is the most important factor in these shapes. In 1986, Kamal et al. [26] used Marker-and-Cell computational scheme (Lafleur and Kamal [16] presented a good review of this technique), to obtain the filling time and flow front position and the velocity, temperature, pressure and shear stress distribution inside the cavity. In the same year, Mavridis et al. [27] developed a simulation in Newtonian and Shear-thinning fluids in two dimensional channels and tubes using the finite element technique. The consideration of fluid with a free surface advancing at a constant velocity was used. Gogos et al. [28] also used the Marker-and-Cell numerical technique solving the transient problem. The flow was considered isothermal and the fluid incompressible, following the power law model. Chen and Liu, (1989), [29] considered the effect of transient melt solidification in two-phase model for polypropylene and polyethylene. The authors used the Hele-Shaw for non-Newtonian fluids and a modified Cross model to describe viscosity under non-isothermal conditions. The energy equation was used to predict the solidified layer thickness and temperature profile.

During the nineties, Papathanasiou and Kamal [30] in 1993, presented a two-dimensional non-isothermal melt flow model, for viscoelastic materials whose properties vary with temperature, shear rate and pressure. The model works with converging and diverging flow patterns induced by complex boundary shape. Due to the possibility of changing the cavity thickness, this is considered a process parameter. In the same year, Kamal and Papathanasiou [31] developed an experimental program with reciprocating screw injection moulding machine. Also in 1993, Friedrichs and Güçeri [32] used a hybrid two-dimensional 2D/3D technique. The 2D Hele-Shaw formulation was used behind the flow front where this formulation is enough to describe the flow phenomena. On the other hand, at the fountain flow region, where all velocity components are significant, the 3D formulation was used with the pressure Poisson formulation. In 1998, Pichelin and

Coupez [33] worked with 3D filling for incompressible and viscous flow and the solver uses stable of first order tetrahedral elements of MINI-elements family for pressure and velocity. The motion equation was solved by explicit discontinuous Taylor-Galerkin; and Hétu et al. (1998), [34] also studied a 3D finite element model which used the generalized Stoke equation for velocity and pressure and Carreau law and Arrhenius constitutive models.

Kumar, Ghoshdastidar and Muje, [35] (2002), used a low density polyethylene (LDPE) injection mould-filling at constant flow rate during the production of a cylindrical part under isothermal and non-isothermal conditions, using the power law viscosity model for the non-zero shear rate zone. One year later, Galantucci and Spina [36] proposed an integrated approach to evaluate the gating system configurations to optimize the filling conditions of thermoplastic injection moulded parts. The finite element analysis and design of experiments were also used to optimize injection moulding process. Kim and Turng (2006) [37] presented a 3D numerical simulation that was compared with two numerical models used to solve the Stokes equations with three different tetrahedral elements (Taylor-Hood, MINI and equal-order).

2.1.3.2 Packing phase

The understanding of packing behaviour is important because the packing phase determines the mechanical properties and quality of the finished product. Moreover, the distribution of pressure influences the part shrinkage [38].

In 1981, Chung and Ryan [38] presented a method to evaluate the pressure distribution in the holding phase. This attempt is based on a general non-linear differential equation to describe packing stage. The considered geometry was a simple rectangular cavity, the fluid was Newtonian and several assumptions were disregard like inertial forces, body forces and viscoelastic effects. The same author [39] studied the motion of an isothermal Newtonian fluid whose compressibility obey the Spencer-Gilmore equation of state during the packing stage. He found that the most important factors were melt viscosity and boundary of cavity in the pressure build up.

Greener in 1986 [40] developed an expression to establish a general optimization criteria for the packing phase and to assess the effects of various process and material parameters on the packing response of the system. This expression uses the empirical Tait equation combined with the transient heat-conduction equation. Huilier [41] (1988) proposed a model that permits calculating the evolution of pressure and temperature fields and mass variations in simple geometries during the packing phase. The meaningful results of the simulation are local shrinkage and a good approximation of the weight of finished products. In 1993 Nguyen and Kama [42] obtained a set of equations governing the two-dimensional packing stage of a viscoelastic fluid assuming that the process is isothermal. The polymer was considered as a Maxwell fluid and the density followed to Spencer-Gilmore relation. The pressure equation was solved by the Galerkin finite element method. This work concluded that viscoelasticity rises in plane stresses and causes distortion in the final part. Chen (1994) [43] presented a two-phase model for simulating the post-filling stage for amorphous and semi-crystalline materials. Good results were obtained between this simulation and experimental pressure and from previous investigations in the literature.

In 2005 [44] Zhou and Li developed a mathematical model to predict the warpage of plastics products. The model was based on the principle of viscoelastic mechanics and the linear isothermal-viscoelastic constitutive equation. The warpage was determined from the stress model.

2.1.3.3 Unified model

Kamal and Kenig (1972) [45], presented a mathematical model that considers all stages of the injection moulding: filling, packing and cooling. They solved the spreading radial flow in a semi-circular impression. After, the authors proved their model with a reciprocating-screw injection moulding machine to check the validity of a proposed theoretical model for injection moulding. Three years later, Kamal et al. [46] showed two models for simulating the injection moulding of thermoplastics in thin, rectangular cavities. One is the model presented in 1972 and the other is a two-dimensional analysis which assumes that viscosity and temperature change strongly across the narrow gap but

vary weakly in the directions of flow. Both models consider the non-Newtonian viscosity with temperature variation.

Kamal and Lafleur (1982), [47] developed a model that in the filling stage considers the simplified flow in the channels and the accurate flow in the cavity. In the cavity the fluid is considered as viscoelastic and compressible and the flow is transient and non-isothermal. In the packing stage, due to the compressibility of the polymer melt, one equation of state must be used, like the Spencer-Gilmore. In the cooling, the problem is treated as transient heat transfer by conduction of a polymer melt between two plates. Lafleur and Kamal (1986) [48] developed an inelastic model like the previous models, but the complete stress field must be calculated to predict microstructure and orientation distributions. In the packing phase the Nakamura's crystallization equation is used to calculate the crystallinity. In the cooling stage the White-Metzner equation is simplified to a simple Maxwellian relaxation mode. The stresses are described using the Matsui-Bogue theory of non-isothermal large deformation viscoelastic fluid behaviour. This model predicts the thermo-mechanical history during the injection moulding process.

In 1991, Chiang (1991) [49][50], based on the implementation and verification of a hybrid finite-element/finite-difference, and presented a model for the Hele-Shaw flow of a compressible viscous fluid under non-isothermal conditions. The shear viscosity of the polymeric material is represented by a Cross model for the shear rate dependence and a WLF type functional form for the temperature and pressure dependence, while the specific volume is modelled in terms of a double-domain Tait equation. Han and Im (1997) [51] presented a similar model with volume control approach. Hieber, 2002, [52] used the differential Nakamura equation for the crystallization kinetics.

In 1995, Douven [53] proposed a decoupled method to calculate flow-induced stresses. The kinematics of the flow field was determined, employing a viscous, generalized Newtonian constitutive law for the Cauchy stress tensor in combination with the balance laws. The Leonov model and the Wagner model were used as compressive constitutive equations.

2.1.3.4 Optimization of injection moulding

After the simulation of the injection moulding process being well-developed many commercial codes were implemented and used by the industry, like Moldflow or Moldex 3D and by the researchers dedicated themselves to the optimization of the process.

Bikas, Pantelidis and Kanarachos (2002) [54] presented the NASPLAN code, for complex and multi-cavity moulds. The NASPLAN code has optimization methods whose leads to flow balancing and improved part quality avoiding defects such as warpage, non-uniform shrinkage, sink marks, etc. Turng and Peic (2002), [55] implemented an integrated CAE system to determine the optimal design and process variables for injection moulding; moreover they compared several optimization algorithms in relation to the computational efficiency and effectiveness.

Lam et al. (2003) [56] developed a simulation system where it is possible to specify the quality measuring criteria such as minimum cavity pressure and shear stress, a uniform distribution of cooling time, end-of-fill temperature and volumetric shrinkage or several criteria in the same time.

Kim and Turng (2004) [57] made a state-of-the-art and developed three-dimensional computer-aided engineering (CAE) simulation for injection moulding. They saw the emerging three-dimensional CAE being applied in design and manufacture of complex injection moulded parts.

Ozcelik and Erzurumlu (2006) [58] used design of experiments (DOE), Taguchi orthogonal array and Moldflow to study the effects of several parameters of injection moulding aiming the best gate location, filling and flow, and the minimum warpage of product. ANOVA, artificial neural network and Genetic algorithm (ANN/GA) were also used in this research. Changyu et al. (2007) [59], beyond the tools employed by Ozcelik developed a method used in the process optimization to improve the volumetric shrinkage in a part. The results showed that the combining ANN/GA method is an effective tool for the process optimization of injection moulding.

Tang et al. (2007) [60] developed a mould that produced a thin plate to study the warpage applying the experimental design of Taguchi method. The results suggested that the most effective factor on the warpage was the melt temperature and that the filling time had little influence on the warpage.

Zhou and Turng (2007) [61] studied a form to determine the optimal process conditions without user intervention. The authors applied a method based on the Gaussian process

capable of giving simultaneously both a prediction and an estimate of the confidence (variance) for the prediction. The method helps the professional to determine the optimal process conditions. Zhou et al. (2009) [62] created a desktop, low-cost and independent virtual injection moulding system, which was implemented based on the techniques such as virtual reality, finite element analysis, motion simulation and scientific visualization. With this integration several influences can be evaluated from product design to manufacturing, capable of improving the mouldability and the quality of moulded products.

Chen et al. [56] 2009 [63] used the Moldflow code and DOE applied to thin-shell plastic component to reduce warpage dependent of process parameter in injection moulding. The melt temperature and the packing pressure were found to be the most significant factors in the process.

Ferreira et al. (2010) [64] applied the Multidisciplinary Design Optimization (MDO) methodology to obtain improvements in the injection moulding process considering the system in a global way: structural, thermal, rheological and mechanical. The assessment of analysis showed a large impact of the sprue diameter enhancing the importance of the feeding system on the quality.

Fernandes et al. (2010) [65] implemented a Multiobjective Optimization Genetic Algorithm, denoted as Reduced Pareto Set Genetic Algorithm with Elitism (RPSGAe), to the optimization of the polymer injection moulding process. The aim is to implement an automatic optimization scheme capable of defining the values of important process operating conditions yielding the best performance in terms of prescribed criteria.

2.2 Shrinkage

The part presents different dimensions of the mould after the injection moulding process. This reduction of the dimensions is called mould shrinkage or as-moulded shrinkage, or simply shrinkage [66]. These differences depend not only on material characteristics, but also on processing conditions, which determine the distributions of pressure and temperature histories, [67] and on the design of part and mould.

Fisher [68] presents more accurate terms in-mould shrinkage or moulded-part shrinkage, although the shrinkage being a volume phenomenon, usually, it is referred to as the

difference between the linear dimension in the part and the linear dimension of the mould at room temperature. According to the ASTM D955-0 standard [69] the shrinkage must be measured 24-48 h after ejection. The term post-mould shrinkage refers to any additional shrinkage that occurs after the initial 48-h period [68].

If the dimensional change in volume was considered, this change is called as volumetric shrinkage. The volumetric shrinkage can be defined as

$$S_v = \frac{\bar{v}_0(t) - v_r(T_{room}, P_{atm})}{\bar{v}_0(t)}, \quad (2.1)$$

where $v_r(T_{room}, P_{atm})$ is the specific volume at room temperature under atmospheric pressure, and $\bar{v}_0(t)$ is the gap-wise averaged initial specific volume. The specific volume depends on the pressure and temperature history and thus the volumetric shrinkage can be calculated using PVT diagrams.

The volumetric shrinkage involves the change of dimension in three spatial directions. These changes can be different for each direction. Therefore it is important to consider the dimensional change in length, i.e., the linear shrinkage, defined by [70]

$$S_l = \frac{l_0 - l_r}{l_0}, \quad (2.2)$$

where l_0 is the initial length, and l_r is the corresponding length at room temperature under atmospheric pressure. If the shrinkage is isotropic, then the linear shrinkage is related to the volumetric shrinkage by

$$S_l = 1 - (1 - S_v)^{\frac{1}{3}} \approx \frac{1}{3} S_v \quad (2.3)$$

For anisotropic shrinkage, it is customary to classify the linear shrinkage into parallel shrinkage S^{\parallel} (the linear shrinkage in the flow direction), perpendicular shrinkage S^{\perp} (the linear in-plane shrinkage perpendicular to the flow direction) and the thickness shrinkage S^h . When $S_v \ll 1$,

$$S_v \approx S^{\parallel} + S^{\perp} + S^h \quad (2.4)$$

No simple relationship between the linear shrinkage components is available. Their values depend on the type of material and processing.

2.2.1 Variables affecting shrinkage

A set of factors affect the shrinkage of the injection moulding part. At first, the processing conditions have a high contribution on the shrinkage, followed by the mould/part design and material characteristics, because all affect the dimensional tolerances that moulders can reasonably expect to achieve during the processing [67].

2.2.1.1 Processing conditions

The shrinkage in parts moulded by injection moulding is controlled by the temperature and pressure in the cavity and the compressibility of resin during the packing phase. Thus, the control of the process conditions is primordial to obtain the parts within acceptable tolerances.

All studies conclude that the parameters of the holding (packing) stage are the most significant in shrinkage. A higher holding pressure reduces part shrinkage along all directions. Increasing the holding time also reduces shrinkage. The amount of holding pressure affects the shrinkage of the part, this phase of the process being deeply linked with the design of the gate and runner system.

Mamat et al. 1995 [71] evaluated some processing conditions on the shrinkage for PP and reinforced PP with 40% calcium carbonate. The results showed that holding pressure and packing time are the most significant parameters, cooling runners, however, could significantly influence local shrinkage values. Jansen et al., 1998, [72] studied the same parameters for polystyrene and noted that, by increasing holding pressure the in-plane shrinkages varied from 0.6-1.3% while the product thickness increased from about 1% to 10%. Later, Jansen, Van Dijk and Husselman (1998) [73] expanded their studies for seven common thermoplastics. They found that the holding pressure always is the key parameter. The melt temperature is slightly less important and the injection velocity and mould temperature do not presented a general trend for all polymers.

Other important processing parameters that affect the shrinkage are the melt temperature of polymer and mould temperature that influence the cooling rate. The literature indicates that the melt temperature and mould temperature have the same influence on shrinkage.

Warmer moulds increase the shrinkage but reduce post-mould shrinkage and cold moulds have the opposite effect. Cold moulds reduce shrinkage, especially when the material is a semi-crystalline. When the cooling is faster the molecules have less time to arrange themselves, decreasing the shrinkage, this effect being more intense if the material is semi-crystalline. The time to cool is also important because if there is more time, the crystalline structures will be larger and more numerous, and consequently the material will shrink more.

Chang and Faison, 2000, [72,73] applied the Taguchi method to investigate the effects of the processing conditions on the shrinkage for HDPE, a PS and ABS. The authors concluded that an amorphous material shrinks less than semi-crystalline. The mould and melt temperatures, and time and pressure packing are the most important factors that influence the shrinkage.

The Figure 2.5 represents the behaviour of shrinkage according various processing parameters and design part.

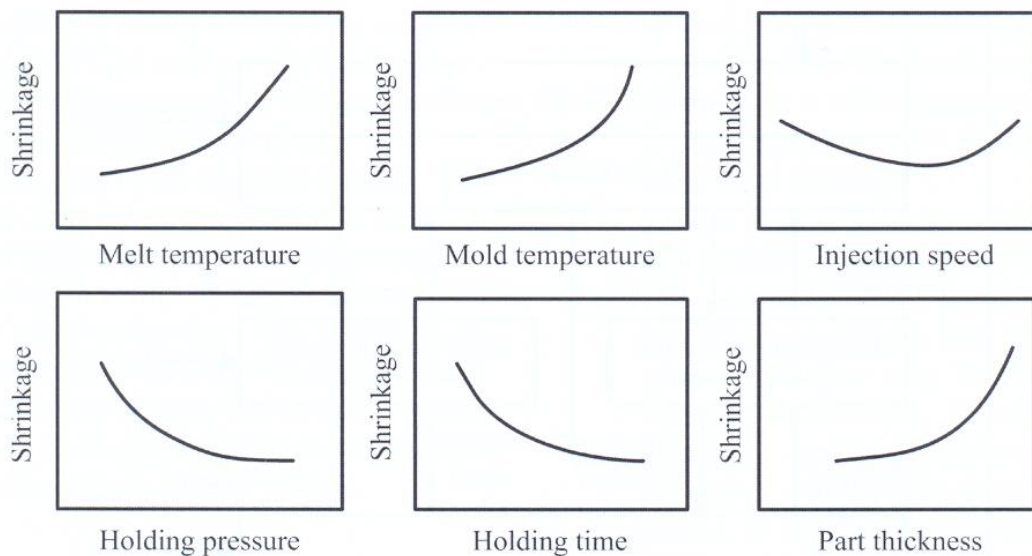


Figure 2.5 - Influence of several factor on shrinkage [14]

Wang and Yoon (1999) [76] used two tools, CAE software and DOE, to assessment the influence of processing conditions on the shrinkage and warpage. Like for other authors the packing pressure is the most important factor affecting the shrinkage and warpage. It

happens due to the higher packing that can deliver more material into the impression and, therefore, reduce the shrinkage and warpage.

Postawa and Koszkul 2005 [77] studied the influence of parameters of processing on shrinkage (longitudinal and perpendicular) injection moulding parts made from semi-crystalline POM and amorphous PS. The change in mass and processing shrinkage of POM depends much on the clamp pressure and less on the injection temperature. However, for PS, it depends, mainly on the temperature of the injected plastic and the mould, and slightly less on the clamp pressure.

Kramschuster 2006, [78] investigated the effects of processing conditions on the shrinkage and warpage behaviour of a box-shaped PP part using conventional and microcellular injection moulding. The results showed that the supercritical fluid content and the injection speed affect the shrinkage and warpage of microcellular injection moulded parts most significantly, whereas hold pressure and hold time have the most significant effect on the shrinkage and warpage of conventional injection moulded parts.

Kurt et al. 2010 [79] studied the effects of moulding parameters and concluded that packing pressure and melt temperature are dominant factors which determine the quality of parts.

Hakimian et al. (2012) [80] evaluated the influence of processing parameters in injection moulding of microgears in a four cavity mould, and using three thermoplastic materials, PC/ABS, PPE/PS and POM filled with glass fibres. Moulding parameters such as packing time, cooling temperature, moulding and melting temperatures, packing and injection pressures, and fibreglass percentages are the most important factors affecting warpage and shrinkage. The best improvement in the shrinkage and warpage analyses were obtained from PPE/PS and PC/ABS, respectively. PPE/PS was the best polymer composite in the shrinkage analysis because of its molecular structure and minimum temperature at the flow front range, while the PC/ ABS behaved better in the warpage analysis.

2.2.1.2 Project of the mould/part

The project of the mould and the part design are features that influence the shrinkage of the moulded product in injection moulding. There are many variables to consider in relation to the design like the size and shape of the part, the size and length of the runners, gates, the wall thickness of the part, the operation of the mould and the effectiveness of the cooling channels in the mould and the flow patterns within the mould. These factors may affect shrinkage in several ways. First, geometry determines pressure distribution inside the impression and its evolution with time. Second, geometrical constraints affect the shrinkage boundary conditions. Third, geometry may affect flow and hence cause orientation resulting in shrinkage anisotropy.

Gordillo et al. (1999) [81] compared the experimental and simulated shrinkage for isotactic PP. These researchers studied the influence of geometrical factors and processing conditions on the shrinkage. The wall thickness is one of the most important factors. If the wall thickness of the part is increased, more time is required for cooling and larger crystalline structures will develop, if the material is semi-crystalline, which increases shrinkage.

Later, studies on the effect of wall thickness allowed more understanding about shrinkage on thin-wall mouldings. Liao et al. (2004) [82] investigated the optimal process conditions of thin-wall of a cell phone cover and Liao and Hsieh [83] applied back-propagation artificial neural networks in predicting the shrinkage and warpage of injection-moulded thin-wall parts.

Jafarian and Shakeri, 2005, [84] investigated the effects of critical relaxation time, initial melt temperature, mould temperature, pack pressure, gate freezing on shrinkage of plastics parts, and developed a simple flat model and a simulation code. They obtained good results confirming the model.

Cheng-Hsien Wu and Yu-Jen Huang, 2007, [85] evaluated the cavity deformation which arises during the injection moulding process. A structural analysis program was developed to predict the cavity deformation and experiments were carried out with PMMA parts. The numerical simulation results were improved in predicting the shape and size of a final product by taking the cavity deformation into account.

S. Fathi and A.H. Behravesh (2007) [86] presented an experimental investigation on the visualization of (material/mould) separation development during the in-mould shrinkage of injection moulded parts. The purpose is to correlate the separation times with the shrinkage. The results indicate that although there is a meaningful correlation between shrinkage and separation time in the non-constrained mould, this correlation is highly disturbed in the presence of a constraint.

2.2.1.3 Characteristics of Material

Plastics materials have positive coefficients of thermal expansion and are compressible in the molten state. As a result, the volume occupied by the material changes with both, temperature and pressure [68]. Various phenomena occur when the polymer changes physical state, for instance, the solidification of material inside the mould influences the shrinkage of the product directly, more precisely, the cooling rate.

Semi-crystalline thermoplastics are particularly influenced by the cooling rate. The polymer chains in the melt are in a disorganized state, and upon solidification they form a dense structure. With increasing crystallinity, the density and the shrinkage of the structure increase. Resler, 1999, [87] considered the effect of cooling rate, also called super-cooling, in injection moulding process. This super-cooling affects directly the crystallization temperature of semi-crystalline materials, thereby causing variations in volumetric shrinkage. As cooling rate is increased, the amount of crystallite formation is decreased. This results in a less dense material as well as a lower volumetric shrinkage.

The behaviour of materials, amorphous or semi-crystalline, is totally different in relation of shrinkage, even, if the resin has fillers or reinforcements. Powders, flakes and fibres are generally incorporated into plastics to selectively modify mechanical properties of the virgin material. The use of fibre reinforcements also produces differential shrinkage between the flow and cross-flow moulding axes of the part, resulting in warpage. Most fillers and reinforcements are inorganic and have relatively low coefficients of thermal expansion (CTE). When an injection moulded composite is cooled during processing, the fillers and reinforcements tend to shrink significantly less than the polymeric matrix to which they are added. Particulate and flake fillers both tend to reduce the overall shrinkage when added to amorphous or semi-crystalline polymers. The reduction in

shrinkage is approximately proportional to their concentration. Powders, beads, and flakes are geometrically more uniform than fibres fillers.

The use of pigments tends to increase the cross-flow shrinkage in semi-crystalline materials. For example, PP typically shrinks about 10% more in the in-flow direction than in the cross-flow direction [68].

Velarde and Yeagley (1999) [88] observed that the direction and magnitude of shrinkage depends upon processing conditions, wall thickness, flow type, material characteristics and part location. Disregarding the contributions of processing conditions, already mentioned by other authors, the semi-crystalline polymers shrink more than amorphous polymers due to the crystallinity, and the fillers decrease shrinkage. Considering the gate position, the polymer will shrink more away from the gate, since less packing pressure is applied at that region. Pomerleau and Sanschagrin (2006) [89] used a profilograph to obtain dimensional measurements, along the flow direction and across the flow direction. The effects of holding pressure and injection velocity on shrinkages was evaluated using DOE at three locations on the plates. The effects of holding pressure on shrinkage are significant: higher holding pressure leads to lower shrinkage. A positive effect of injection velocity is observed on parallel to flow shrinkage but no significant effect is observed on across flow shrinkage.

Shelesh-Nezhad and Taghizadeh in 2007 [90] investigated the influence of adding 10 μm talc particles on the shrinkage and the mechanical properties of injection moulded PP-talc composites. The data indicated that the maximum flexural strength, maximum impact strength, and isotropic shrinkage were achieved by adding 10, 20, and 30% by weight of talc respectively. The flake-shape structure of talc filler played an important role in determining the moulded part shrinkage and mechanical properties.

De Santis et al. 2008, [91] studied the complete evolution of shrinkage from the instant of first solidification inside the mould to some minutes after demoulding for a typical multiphase industrial polymer with a small percentage of talc in a rectangular moulding. Simulation and experimental works were carried out and the results confirm that the shrinkage decreases when the holding pressure and the holding time are increased, the constraints inside the mould reduce the as-moulded shrinkage at low holding pressure and time. The use of strain gauges to directly measure the shrinkage inside the mould showed that the shrinkage onset is delayed by increasing the holding pressure. Their thermo-

mechanical model gives a satisfactory description of the shrinkage and also of its onset inside the mould, and shows the relevance of using the degree of crystallinity as a criterion of solidification.

Gershon et al. [92] 2008 used the full-field deformation technique of Digital Image Correlation (DIC) to characterize the non-uniform shrinkage in thermoplastics commonly used in traditional and emerging moulding processes. From their experiments, it has been shown that there is a large increase in shrinkage strain associated with the transition of the polymer from the molten to the solid state, and as it is cooled below the Vicat softening point.

2.2.2 Shrinkage anisotropy

The common causes of non-uniform shrinkage are differential orientation, differential crystallinity, differential cooling, materials characteristics, differential thermal strain, moulding conditions and mould constrains [68].

In general, oriented material with molecules or fibres aligned with the flow or parallel to it shrinks in a more anisotropic manner than non-oriented material. The degree of orientation imparted by the melt flow during the mould filling process has a large influence on the shrinkage exhibited by the moulding. During mould filling, the polymer molecules undergo stretching that many result in molecular orientation and anisotropic shrinkage. Natural, unfilled plastic materials tend to shrink more along the direction of flow (in-flow shrinkage) compared with the direction perpendicular to flow (cross-flow shrinkage), while the shrinkage of reinforced materials is restricted along the direction of fibre orientation. In general, mould shrinkage tends to be more isotropic when the degree of orientation imparted during mould filling is minimized, and when favourable conditions for molecular relaxation exist.

For semicrystalline materials, if some part of the mould cools at a slower rate, that area will be more crystalline and, hence, shrink more. This is the case for parts with different thicknesses, and for hot spots such as where material is in contact with outside corners of a core or with core pins.

Differential cooling can occur when the moulding surfaces are at different temperatures, as they frequently are around core pins, inside and outside mould corners, near gates, and where there are thickness variations. Hot spots cause problems in two ways: with added crystallinity and with a longer/late cooling time [68].

Differential thermal strain may be due to geometric effects, i.e. where there are section thickness changes, sharp inside corners, or other geometric conditions that cause variable cooling or unusual orientation. The more abrupt the change, or the greater the differential cooling rate, the more severe is the thermal strain [68].

Moulding conditions can lead to excessive stresses caused by unusually high or low melt temperature or pressure, or unusually long injection time or short cycles. Moulding conditions can vary greatly, based on part size and part thickness [68].

Mould constraints can contribute to non-uniform shrinkage. Usually the part is free to shrink in thickness. It is usually less free to shrink in length and width due to the geometry of the part. There may be cores, ribs, or edges that are firmly anchored so that the part cannot move until it is out of the mould [68].

Jansen (1998) [93] measured the coefficients of thermal expansion, elastic modulus, Poisson constants and linear compressibility to assess the anisotropy of these properties in injection moulded PP plates. A simple composite model was proposed which could predict all thermal and mechanical properties mentioned above from data of the amorphous and crystalline phases. It turned out that individual values were slightly over or underpredicted correctly. The only prediction which disagreed with the measurements was that of the coefficient of thermal expansion, which was found to be larger in the flow direction than in the width direction. In the same year, Jansen, Van Dijk and Freriksen [94] carried out a systematic study of the effect of fibre concentration and moulding conditions on fibre orientation and shrinkage in injection moulded composites. Shrinkage predictions were seen to agree well with experimentally measured shrinkages.

Kwon et al., 2005 [89],[94],[95], developed a way to predict anisotropic shrinkage of semi-crystalline polymers in injection mouldings using the flow-induced crystallization, frozen-in molecular orientation, elastic recovery and PVT equation of state. The elastic recovery and frozen-in stresses and birefringence were obtained by a non-linear viscoelastic model. The flow-induced crystallization was described via the elevated

melting temperature affected by entropy production with modified kinetics of the crystallization. PP parts were produced by varying packing time, flow rate, melt temperature and mould temperature, and anisotropic shrinkage of mouldings were measured. The experimental results were compared with the simulated data.

Postawa and Gnatowski (2007) [97] applied a Dynamic Mechanical Thermal Analysis method giving possibility in the very precise solution. Samples taken at the beginning of the flow path had better mechanical properties but poor suppressing properties. However, samples taken parallel to the flow direction in the mould (at temperatures over 40 deg) displayed better suppressing properties.

2.2.3 Influence of fibre orientation in shrinkage

The thermal and mechanical properties of the material strongly depend on the fibre orientation field. The composite is stronger along the major orientation direction and weaker in the transverse direction. Because of this anisotropy, the moulded product may develop high internal stresses and warp at unexpected places and consequently the shrinkage will be affected. Xia et al. [98] (1995) developed an analytical method for the prediction of stiffness of fibre reinforced injection mouldings including the effects of fibre orientation and fibre length distributions using two probability density functions on the basis of a generalized laminated-plate theory.

Mlekusch, 1999, [99] compared several micromechanical models for determining the stiffness and thermal expansion coefficients of short-fibre-reinforced thermoplastics. The orientation averaging procedure is extended with the help of orientation tensors to non-symmetric, transversely isotropic tensors. Furthermore, simplifications concerning the material symmetry are given, allowing the use of the classical thin-laminate theory to describe the composite. Finally, the values calculated with the various theories are compared with measurements on specimens from a specially designed tests component.

Neves et al. [100] 2001, carried out an assessment of Moldflow simulations and experimentally determined fibre orientation distributions at three points along the flow path and 12 layers across the thickness of a circular centre gated moulding. The material used is a 10% weight short glass fibre reinforced PC. At the centreline of the disc and

close to the wall, the predictions of fibre orientation in most of the moulding conditions are close to the experimental data. At the intermediate points, the fibre orientation in the flow direction is consistently overestimated.

Hine et al. 2002 [101] developed a new numerical procedure for predicting the elastic and thermoelastic properties of short fibre reinforced composites. The numerical predictions were compared with those from three commonly used micromechanical models, namely those of Halpin/Tsai, Tandon/Weng and Cox (shear lag). The effect of volume fraction and aspect ratio were investigated and the numerical approach was used to investigate which effect a distribution of fibre lengths would have on the prediction of mechanical properties.

Thomason 2002 [102] developed an improved method for obtaining the micromechanical parameters, interfacial shear strength, fibre orientation factor, and fibre stress at composite failure using input data from macromechanical tests. They measured the mechanical properties and residual fibre length distributions of glass fibre reinforced PP containing different levels of glass fibre. The data were used as input for the model. The trends observed for the resultant micromechanical parameters obtained by this method were in good agreement with data obtained by other methods.

2.2.4 Prediction of the shrinkage

Due to the importance of the shrinkage to obtain precise dimensions of injection moulded parts, the study of predicting this phenomenon is indispensable. Some authors carried out research to measure and predict the shrinkage through of experimental methods and mathematical formulation over time, respectively.

Han and Wang (1997) [103] developed a method to obtain material properties which include the effect of crystallinity. Injection-moulding experiments have been conducted to measure the shrinkage of a part using a slowly-crystallizing polymer, in this case PET. Shrinkage has been measured and a simulation program was developed to describe the injection-moulding process. The predicted shrinkage and measured shrinkage are found to agree reasonably well.

Choi and Im, 1999, [104] carried out an analysis of shrinkage and warpage of injection moulded parts considering the residual stresses in amorphous polymers. For residual stress analysis, a thermo-rheologically simple viscoelastic material model was introduced to consider the stress relaxation effect and to describe the mechanical behaviour according to the temperature evolution. The deformation of injection moulded parts after ejection induced by the residual stress and temperature change was analysed using a linear elastic three-dimensional finite element approach. The results were compared with experimental data available in the literature.

Lotti et al. (2002) [105] developed a neural network architecture to predict the shrinkage of an iPP injection moulded plaque after changing four processing conditions: melt and mould temperatures, holding pressure and flow rate. This work used DOE and Moldflow. The shrinkage predictions were compared with experimental, neural network and statistical results. It was observed that the neural network architecture had the best performance in the shrinkage prediction.

Yang and Kwon, 2007, [106] created a numerical system to predict birefringence, residual stress and final shrinkage in the injection moulding process using hybrid finite element-difference method for a general three dimensional thin part geometry. This model considers density relaxation phenomena. Deformations at and after ejection have been considered using thin shell viscoelastic finite element method. The model achieves good correspondences between numerical results and experimental data.

Speranza et al. [107] (2007) studied the as-moulded shrinkage of poly(vinylidene fluoride) injection moulded samples in a simple rectangular cavity under different holding pressures. The shrinkage decreased on increasing holding pressure and the shrinkage increased on increasing the distance from the injection point. The shrinkage along the flow direction was higher than the transverse on-plane direction due to the anisotropy of the elastic modulus and of the coefficient of linear thermal expansion. The numerical simulation was carried out, and when the anisotropy in material properties was considered the results were satisfactory.

Yang and Kwon 2008 [108] presented a work divided in two parts, part I, with the physical modelling and numerical formulation for a new lateral motion modelling and part II with the validation of the model comparing the calculated residual stress profile with the literature data. The predicted results of the birefringence, residual stress

distribution, and shrinkage showed better agreement with corresponding experimental data.

Altan (2010) [109] studied optimal injection moulding conditions for minimum shrinkage using the Taguchi experimental design and the analysis of variance (ANOVA) methods. PP and PS were injected in rectangular-shaped specimens under various processing parameters. The researcher concluded that the most significant parameters were the packing pressure and melt temperature for the PP and PS mouldings, respectively. Injection pressure had the least effect on the shrinkage of either material.

Isayev et al., 2010, [110] presented an upwinding scheme to improve the efficiency of the viscoelastic simulation in moulding of optical products using a numerical techniques. The approach was applied to simulate the flow-induced birefringence and anisotropic shrinkage in disk mouldings using a nonlinear viscoelastic constitutive equation, orientation functions and equation of state. Good agreement was found in the results.

Lucyshyn et al. (2012) [111] determined the transition temperatures of several polymers using DSC with different cooling rates. These data were used to calculate the shrinkage and warpage of box-shaped test parts by Moldflow. The results showed a strong influence of the transition temperatures on the simulation results of a 3D model and a very low influence when a 2.5D model was used.

The methods that were developed for prediction the shrinkage can be classified in three groups: Statistical modelling approach, Thermodynamic modelling approach and Thermo-mechanical modelling approach.

2.2.4.1 Statistical modelling approach

One approach largely adopted in the literature is based on the statistical modelling of shrinkage as a function of the moulding parameters and design factors [67] .

Walsh 1993 [112] declared that the warpage of injection moulded components is caused by variations in shrinkage. Walsh implemented a routine for shrinkage calculation in software for the simulation of injection moulding. Shrinkages, along the directions

parallel and perpendicular to that of material orientation, are calculated by means of a linear combination of variables, F_i :

$$S = a_0 + a_1F_1 + a_2F_2 + a_3F_3 + a_4F_4 + \dots \quad (2.5)$$

where the coefficients a_i are the constants, determined by a regression analysis on data obtained in a series of experimental tests, and F_i are intended to represent all different material properties, process variables and characteristics of the mouldings as obtained from flow analysis, which affect shrinkage.

The statistical approach allows the isolation of the effect of a single variable on shrinkage, thus obtaining typical dependencies. The main shortcomings of such an approach are the lack of generality in the results obtained, which are linked to a given set of processing conditions and to a given geometry.

2.2.4.2 Thermodynamic modelling approach

This method considers the responses of polymer solids and melt during melt processing, represented by a PVT diagram, Figure 2.6, obtained from the material supplier or a standard data source [68]. The shrinkage and warpage will depend on the material properties (PVT, thermal properties, etc.), the part geometry (wall thickness, gate location, mould constraints, etc.), and the moulding conditions (temperature, pressures, flow rates, etc.).

An appropriate model to describe the behaviour of polymers is the double domain Tait equation, used to model polymer behaviour during melt processing. From the Tait equation and a set of constants, any specific volume of a polymer can be determined by knowing only the temperature and pressure of the system.

This form of the Tait equation is simply a prediction of the specific volume, $v(T,p)$, as a function of temperature and pressure. The three conditional terms, $v(T)$, $B(T)$, and $v(T,p)$,

change forms based on whether the selected temperature is above or below the freeze line. That is why this equation is called “Double Domain Equation”.

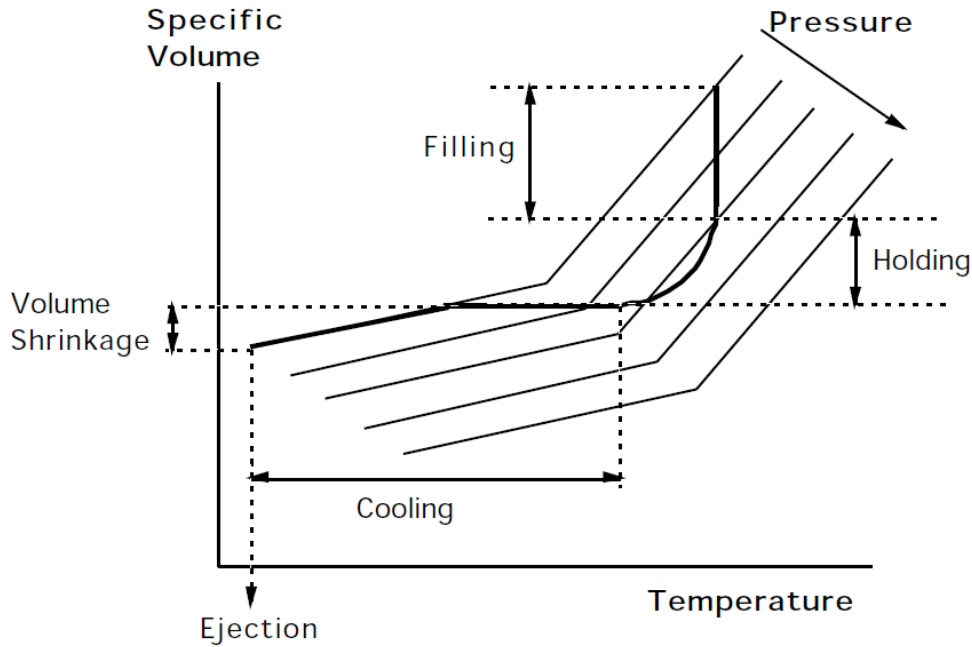


Figure 2.6 - PVT curve evaluating shrinkage [113]

It is not necessary to know this equation exactly. It is important only to know that it is coded into all mould-filling software. Plastics suppliers have generated the necessary databases of PVT constants to describe most of their many materials.

$$v(T, p) = v_0(T) \left[1 - C \ln \left(1 + \frac{p}{B(T)} \right) \right] + v_t(T, p) \quad (2.6)$$

$$v_0(T) = b_{1m} + b_{2m}T \quad \text{if } T > T_t \quad (2.7)$$

$$v_0(T) = b_{1s} + b_{2s}T \quad \text{if } T < T_t \quad (2.8)$$

$$\bar{T} = T - b_5 \quad (2.9)$$

$$B(T) = b_{3m} \exp(-b_{4m}\bar{T}) \quad \text{if } T > T_t \quad (2.10)$$

$$B(T) = b_{3s} \exp(-b_{4s}\bar{T}) \quad \text{if } T < T_t \quad (2.11)$$

$$T_t(p) = b_5 + b_6p \quad (2.12)$$

$$v(T, p) = 0 \quad \text{if } T > T_t \quad (2.13)$$

$$v(T, p) = b_7 \exp(b_8 \bar{T} - b_9 p) \quad \text{if } T < T_t \quad (2.14)$$

These constants have a physical meaning: b_{1m} to b_{4m} describe the pressure and temperature dependence of the melt; b_{1s} to b_{4s} are constants describing the pressure and temperature dependence of the solid; b_5 is T_g ; b_6 is the pressure dependence of T_g ; b_7 to b_9 are particular to semi-crystalline polymers and describe the shape of the melting transition as a function of pressure and temperature. These constants are unique to each plastic formulation. C is a universal constant; generally, a value of 0.0894 leads to good results. The subscript m refers to the material when in the molten state and the subscript s to the solid material.

The local-mould shrinkage in an injection-moulded part is the result of many factors. Local pressure variations are a primary source of different shrinkage in different locations of a moulded part. For isotropic amorphous polymers moulded in simple parts, a good estimate of shrinkage is possible using the PVT predictions. When filler systems are incorporated into the plastics moulding compound, the shrinkage will be a function of the amount, the shape, and the orientation of the filler at each location in the part. Estimating the shrinkage of semi-crystalline polymers requires the additional use of data relating to the kinetics of crystallization.

Many attempts have been made to model shrinkage using PVT (pressure-volume-temperature) diagrams. Following the volume dependency on pressure and temperature, an isotropic value for density change after gate sealing can be obtained. These models do not consider details in shrinkage developments and are obviously limited to predictions of average shrinkage, neglecting any directional effect. Actually, large differences in shrinkage are usually observed along different directions. The plane shrinkage of these products is affected by details of the evolution of the solidification pressure, while thickness shrinkage is affected only by solidification pressure of the last solidified layer and by Poisson effects due to in-plane deformation. Linear shrinkage is not easily calculated from volumetric data, and a thermo-mechanical analysis is required [67].

Although the equations of state cannot predict any densification effect, PVT diagrams can, however, be used to calculate density distribution in products solidified under continuously changing pressure. If no volume relaxation is present below T_g , the equation of state can still be used to derive all relevant thermodynamic parameters (thermal expansion, volume compressibility) also in the solid state. The pressure induced

densification phenomenon is mainly due to the dependence of the glass transition temperature upon solidification conditions.

Hassan et al., 2010, [114] evaluated the effect of the cooling system on the shrinkage rate of a PS product during injection moulding. They used the PVT approach and a Cross-type rheological model for the polymer material. Different cooling layouts were assumed and the effect of their positions on the cooling process was studied. The results indicated a good agreement between the numerical solution and those in the literature.

2.2.4.3 Thermomechanical modelling approach

Thermomechanical approaches take in account the evolution of shrinkage from the moment of first solidification and a balance between restraining and constraining forces. Consider a molten slab cooling inside a mould divided in a series of layers in mechanical equilibrium in the direction of thickness: these layers solidify at different times. Each layer shrinks according to its density increase related to its temperature, pressure and crystallization history [67].

The layers are subjected a balance of forces while inside the mould and after ejection, and the stresses develop in the layers according to the material behaviour.

In the in-mould shrinkage the dimensions are regulated by the mechanical equilibrium between internal stresses and external forces acting on the solid layers. If the moulding is constrained inside the mould, the product in-plane dimensions are fixed.

Thickness shrinkage is regulated by the release of pressure at ejection, Poisson effect in relation to in-plane shrinkage, thermal and contraction until room temperature.

Thermomechanical approaches allow more realistic directional shrinkage predictions and, by linking dimensional accuracy to the stress distribution inside the impression, also provide a description residual stresses.

Bushko and Stokes (1995) [115] used the solidification of a molten layer of a thermoplastic between cooled parallel plates to model the mechanics of part shrinkage and the build-up of residual stresses in the injection-moulding process. The packing

pressure is shown to have a significant effect on part shrinkage, but a smaller effect on residual stresses. Mould and melt temperatures were shown to have a much smaller effect. The processing parameters appear to affect the through-thickness shrinkage more than the in-plane shrinkage. One year later, they [116] continued this work that allows material to be added to fill the space created by the pressure applied during solidification; thus their model can be used to assess packing-pressure effects in injection moulding. For several sets of boundary conditions, parametric results are presented on the effects of the packing pressure in plaques geometry. Plaques that can shrink in the in-plane direction while in the mould are shown to shrink more and to have higher residual stresses than plaques that are fully constrained while in the mould.

Jansen and Titomanlio, 1996, [117] presented a simple elastic model for residual stresses and shrinkage of a thin solidifying product. It accounts for shrinkage anisotropy between in-plane and thickness directions, caused by different constraints in deformation. The model uses local values for temperature, pressure, crystallization, and (if present) extent of reaction, which belong to the standard output of most simulation codes. It is therefore assumed to be valid also for complex shaped products. This work shows the link between simple theories predicting shrinkage, density distributions in polymer products. They [118] also developed a simple elastic model to study the effect of in-mould shrinkage on final product dimensions and residual stress distributions. The friction between the polymer and the mould wall surface as well as the deformation of the mould impression was considered. The as-moulded dimensions were calculated from the stress change during ejection. This means that boundary condition effects (geometrical constraints, friction effects) can also be included. The effect of molecular orientation, however, can only be included indirectly (via differences in expansion and crystallization coefficients).

Kabanemi (1998) [119] developed a numerical simulation model for predicting residual stresses and residual deformations which arise during the injection moulding of thermoplastic polymers during the post-packing stage. The volume relaxation was used for the calculation of residual stresses. The finite element method employed is based on the theory of shells as an assembly of flat elements. The approach allows the prediction of residual deformations and residual stresses layer-by-layer like a truly three-dimensional calculation. Numerical results are in qualitative agreement with experimental observations. The influence of the mould temperature on residual stresses and warpage was also analyzed.

Azdest and Behraves (2008) [120] presented an analytical approach to predict the in-mould constrained shrinkage of injection moulded semi-crystalline plastics parts. The existence of mould constraints exerts a noticeable effect on the final dimensions of moulded parts due to the viscoelastic characteristics of polymeric materials. Variation of in-mould cooling time introduces variations in final part dimensions that depend on the constraints.

De Santis et al. (2010) [121] explored the influence of holding pressure and time, and geometric constraints, on the shrinkage of a semi-crystalline polymer. Adopting a technique using strain gauges, the time at which shrinkage started inside the mould was measured as a function of the holding pressure. Experimental results were compared with predictions for shrinkage obtained by a code developed at the University of Salerno, which takes into account crystallization kinetics and the effect of crystallinity on material properties. In particular, a solidification criterion based on the degree of crystallinity was identified.

2.2.4.4 Reinforced short fibre modelling approach

2.2.4.4.1 Short-fibre composites

There is a kind of reinforcement applied in composites, short-fibres, whose main attribute is the elongated shape where the length is smaller than the overall dimensions of the part. Short-fibres are used in injection moulding, as well as in sheet moulding and short-fibre GMT's (glass-mat reinforced thermoplastics) [122].

The most common fibre used in polymer composites is the glass fibre. The reason of that are advantages like high strength, low cost, high chemical resistance, and good insulating properties. The disadvantages are low elastic modulus, poor adhesion to polymers, high specific gravity, sensitivity to abrasion (reduces tensile strength), and low fatigue strength [123].

The manufacturing method influences the properties of short-fibre polymer composites due to the orientation of the fibres inside the part. Hence, the design of short-fibre composite part must be thoroughly planned.

A description of short-fibre orientation is important to predict the properties of the composite. Commonly, a single fibre is regarded as an axisymmetric particle, like represented in the Figure 2.7. The orientation of the unique fibre is described by two angles, θ and ϕ , or by a unit p directed along the particle axis. The representation is shown below

$$p_1 = \sin\theta\cos\phi \quad p_2 = \sin\theta\sin\phi \quad p_3 = \cos\theta \quad (2.15)$$

where (p_1, p_2, p_3) are the Cartesian components of p .

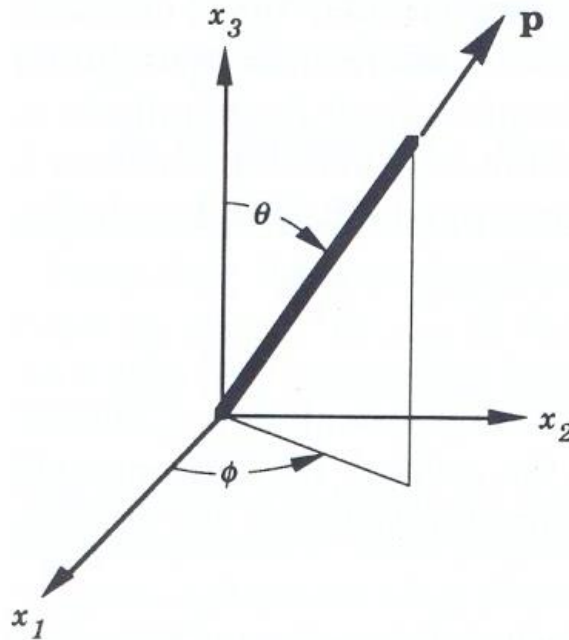


Figure 2.7 - The orientation of a single axisymmetric particle is described by the angles, θ and ϕ , or by a unit vector p directed along the particle axis [122]

A composite has many fibres and at this case a distribution function is necessary. The number of fibres can be considered as very large population, then a probability density function for orientation is $\psi(\theta, \phi)$ or $\psi(p)$. This function represents the probability of any fibre to be in the range between θ_1 and $\theta_1 + d\theta$, and between ϕ_1 and $\phi_1 + d\phi$, is

$$P(\theta_1 \leq \theta \leq \theta_1 + d\theta, \phi_1 \leq \phi \leq \phi_1 + d\phi) = \psi(\theta_1, \phi_1) \sin\theta_1 d\theta d\phi \quad (2.16)$$

Wherefore every fibre with the same angle can be considered, the integral over all angles must be equal unity:

$$\int_{\phi=0}^{2\pi} \int_{\theta=0}^{\pi} \psi(\theta, \phi) \sin \theta d\theta d\phi = \int \psi(p) dp = 1 \quad (2.17)$$

Here $\int dp$ denotes the integral over all possible values of p .

In practical cases ψ varies with the position and time and for a large number of fibres the function is not practical to calculate. So, a more efficient description of orientation to use in process models is required. A possible solution would be to use tensors to describe the fibre orientation. Instead of using a statistical function and can work with the average orientation.

The tensors are represented by the quantities a_{ij} and a_{ijkl} that follow the transformation rules for tensors, where

$$a_{ij} = \langle p_i p_j \rangle$$

$$a_{ijkl} = \langle p_i p_j p_k p_l \rangle$$

with i, j, k and l taking the values 1, 2 and 3 in all possible combinations.

The nine components of a_{ij} are the components of a second-rank tensor, like stress or strain. Similarly, a_{ijkl} is a fourth-rank tensor like stiffness or compliance. These quantities are commonly called orientation tensors, conformation tensors or moment tensors.

2.2.4.4.2 Orientation tensors

The use of tensors to represent the glass fibre orientation had its beginning with the work of Jeffery in 1922, [124] who had studied the rotation of two circular cylinders in a viscous fluid which is developed for a single ellipsoid immersed in a viscous fluid. Since this model does not account for fibre-fibre interaction, and does not consider the effect of

fibres on the velocity field, it is only useful for dilute suspensions. Thereafter, Advani and Tucker [125], 1985, described the orientation of fibres by orientation tensors and its influence in the properties of the material. In 1987, Advani and Tucker [126] used a set tensors to describe the probability distribution function of fibre orientation in suspensions and composites containing short rigid fibres. These tensors are related to the coefficients of a Fourier series expansion of the probability distribution function. They obtained the equations of change for orientation the second- and fourth-order tensors; these can be used to predict the orientation of fibres by flow during processing. Tensors offer considerable advantage for numerical computation because they are a compact description of the fibre orientation field.

2.2.4.4.3 Glass fibre

In the previous section it was described the geometrical characteristics of glass fibres in polymer matrix. Due to these characteristics several researchers developed a lot of works with this material.

Xavier (1982) [127] studied the correlation of processing conditions with morphology and mechanical properties in PP reinforced with glass fibre moulded by injection moulding. The aim of this study was the optimization of processing conditions to obtain composites with desired properties. The author concluded that the knowledge of the morphological state of the polymer composite assures that the mechanical properties are meaningful, and permit fabrication of injection-moulded articles with tailor-made mechanical properties.

Pipes et al., 1982, [128] presented a work for polymers reinforced with discontinuous fibres showing their influence in the orientation state using elastic constants, thermal coefficients of expansion and tensile strength.

Vincent and Agassant, in 1986, [129] used a polyamide with short glass fibres centre gated moulded disc using optical microscopy techniques to study the influence the orientation in the properties of parts obtained by injection moulding. The orientations at the core and the surface were different. The numerical scheme and computation method were implemented and presented good agreement with experimental data.

Altan et al. (1990) [130] developed a numerical technique to determine the three-dimensional fibre orientation in complex flows. The fibre orientation field was specified in terms of orientation tensors, which are used in several constitutive models. This method is applied to *quasi*-steady state Hele-Shaw flows to predict the flow induced fibre orientation. The numerical solutions are obtained for channel and converging flows.

Matsuoka, in 1990, [131] presented a numerical scheme to predict fibre orientation in three-dimensional thin-walled injection moulded parts in short-fibre thermoplastic composite. The Folgar and Tucker's orientation equation was used. The equation was solved about a distribution function of fibre orientation by using a finite difference method with input of velocity data from a mould filling analysis. The mould filling was assumed to be a non-isothermal Hele-Shaw flow of a non-Newtonian fluid and analyzed by finite element method. Computed orientation parameters were compared with measured thermal expansion coefficients of moulded square plates of glass-fibre-reinforced PP. A good correlation was found.

Akay and Barkley (1991) [132] evaluated the mouldings for fibre orientation distribution, in tensile and dynamic mechanical tests and fracture analyses in short-glass fibre-reinforced PP and polyamide. They concluded that the melt and mould temperatures, and the injection ram speed influence the fibre orientation field. The prediction was worse in the material systems containing significant production- induced voids.

Randy and Tucker III, in 1992, [133] developed the theory and numerical methods to simulate filling and fibre orientation in simple linear injection mouldings. This simulation was applied for the flow of a generalized Newtonian fluid where the velocities can be solved independently of fibre orientation. A finite difference solution calculates the temperature and velocity fields along the flow direction and through the thickness of the part. The fibre orientation is then integrated numerically along the path lines. The simulation predicts that the orientation will vary through the thickness, causing the moulding to appear layered. The outer "skin" layer is predicted only if the effects of the fountain flow and heat transfer are included in the simulation.

Bay and Tucker III, in 1992, [134] measured the fibre orientation of two parts injection moulded from polyamide 6.6 reinforced with 43 wt% of glass fibres. The orientation was measured in polished cross sections and reported as a function of position, both across the thickness and in the flow direction. The experiments were compared with predictions

of the simulation. The simulation prediction showed the presence, nature, and location of the layers very well. However, it overpredicted the small out-of-plane fibre orientation and places the core-shell transition too close to the mid-plane. Injection time is an important parameter, but injection temperature and mould temperature have little effect on the fibre orientation. The experiments and predictions confirmed the basic understanding of fibre orientation in injection moulded composites.

Bay and Tucker III, [135] also in 1992, presented a method for measuring three-dimensional fibre orientation in fibre-reinforced polymers. The orientation of individual fibres was determined from the elliptical intersections between the cylindrical fibres and the polished section. This can be done using either manual digitization or automated image analysis. Equations were developed for non-uniform fibre lengths, using both number-average and weight-average measures of orientation. Sources of systematic, measurement, and sampling error were discussed, and equations for sampling error and the propagation of the error of measurement were derived.

Reifschneider and Akay, in 1994 [136] showed an application of a finite element simulation of mould filling and prediction of fibre orientation in fibre filled compression moulded parts for three dimensional thin-walled geometries. Following a simulation of the filling process, a set of transport equations are solved to predict the locally planar orientation of short fibre composites. The final orientation field throughout the part provide the necessary information to obtain a locally orthotropic mechanical model of the composite. Derivations of the orthotropic mechanical properties obtained from the fibre orientation results are outlined.

Cintra and Tucker III, 1995, [137] presented a new family of closure approximations, called orthotropic closures, what were developed for modelling the flow-induced fibre orientation. These closures approximate the fourth-order moment tensor for fibre orientation in terms of the second-order moment tensor.

Davidson et al. (1997) [138] developed an image analysis system based on a small network of parallel processors hosted in a personal computer to measure the orientation of glass and carbon fibres in a polymer matrix from a polished section using optical microscopy. This technique allows the fibre orientation to be measured accurately over large sample areas.

Neves et al. (1998) [139] determined experimentally the through-thickness fibre orientation distribution of injection moulded polycarbonate plates by light reflection microscopy and manual digitization of polished cross sections. Fibre length distribution was determined by pyrolysis tests followed by image analysis. A statistical analysis was done to determine the confidence limits of the fibre orientation results. The fibre orientation distribution was described by using second-order orientation tensors. The through thickness stiffness variations were determined by the orientation averaging approach. This layer stiffness distribution was used to simulate the behaviour of beams subjected to three points bending with a finite element (FEM) ANSYS model. The results were compared with experimentally determined flexural stiffness both in the flow direction and in the transverse flow direction.

Zhang et al. (1998) [140] investigated the transverse creep behaviour of unidirectionally reinforced glass fibre composites with an unsaturated polyester matrix. The matrix model included effects of physical ageing of the resin and, in its general 3D-formulation, was able to describe time-dependent lateral contraction. The 3D-model was implemented into a FEM package. The excellent agreement obtained between the FEM calculations and experimentally obtained strains for various model (uniaxial and multiaxial) loading situations lends confidence to the ability of the model to describe the time-dependent behaviour of the unsaturated polyester under general 3D loading situations.

Lee and Jang, 1999, [141] fabricated glass fibre mat reinforced PP composites with the variation of glass fibre content. Tensile, flexural and high rate impact tests were conducted to investigate the effect of glass fibre content on the mechanical properties of the glass-fibre-mat/PP composite. Deformation and fracture behaviour of the glass-fibre-mat/PP composites was investigated to study the relationship with the mechanical property data. The tensile and flexural modulus increased with the increment of glass fibre content. However, the tensile and flexural strengths exhibited maximum values and showed a decrease at the higher glass fibre content. The impact absorption energy also exhibited a similar result with the tensile and flexural property data.

Zheng et al., 1999, [142] described a numerical method for the prediction of residual stresses, shrinkage and warpage in injection moulded fibre-reinforced thermoplastics. Effects of pressure and thermal history, fibre orientation state and stress relaxation were taken into account through the simulation of the filling, packing and cooling stages of the

injection moulding process. The final dimension and shape of the part after ejection were calculated by a FEM structural analysis. An anisotropic linear thermo-viscoelastic material model was employed to describe the constitutive behaviour of the material.

Fu et al. (2000) [143] studied composites of PP reinforced with short glass fibres and short carbon fibres. The tensile properties of these composites were investigated. It was noted that an increase in fibre volume fraction led to a decrease in mean fibre length as observed previously. The relationship between mean fibre length and fibre volume fraction was described by an exponential function with an offset. The results showed that mean glass and carbon fibre lengths decrease with increasing fibre volume fractions and the combined effect of fibre volume fraction and fibre length determines the final tensile properties of the composites.

Eberhardt and Clarke, 2001, [144] described the confocal technique for fibre-orientation distribution measurement and the associated errors. Novel image processing and management routines have been implemented to fully to automate the data acquisition, and consequently significant sample areas could be analysed within hours.

Pontes et al. (2003) [145] considered the effectiveness of the interaction parameter C on controlling the predicted patterns of the fibre orientation. C is important on the qualitative prediction of the fibre orientation. It affects significantly the patterns of fibre orientation predicted in the flow simulations. Larger values of C , tend to make the fibre orientation close to a random in-plane distribution whereas lower values predict a clear alignment in the flow direction.

Vincent et al., 2005, [146] carried out the observation and quantification of fibre orientation in a rectangular plaque with adjustable thickness and moulded with 30 and 50 wt% short fibre reinforced polyarylamide. An automated 2D optical technique was used to determine fibre orientation. It was shown that the gate design and various levels of fibre interactions, due to different fibre concentrations, were responsible for these observations. Secondly, computer simulations of flow and fibre orientation were shown. The agreement with the actual data was good, except in the case of the core for thin plaques. The limitations that have to be resolved come not only from the standard fibre orientation equations, but also from the flow kinematics computation.

Toledo et al. (2008) [147] studied the behaviour of composites formed by laminae reinforced with unidirectional fibres to calibrate the general model. Three-dimensional finite element models were used to study the distribution of stresses and strains inside the composite. This study presented comparisons between elastic properties of laminae obtained with the FEM model, the Mori–Tanaka method, the model for composite studied, and experimental data. The results showed that the calibrated model describes the behaviour up to failure of the composite laminates. The failure mode of the composite produced by the failure of one or more of its components could be identified.

Phelps and Tucker, 2009, [148] developed a fibre orientation model that incorporates anisotropic rotary diffusion (ARD). From the kinetic theory was derived the evolution equation for the second-order orientation tensor, correcting some errors in earlier treatments. Model parameters were selected by matching the experimental steady-state orientation in simple shear flow, and by requiring stable steady states and physically realizable solutions. Also, concentrated fibre suspensions align more slowly with respect to strain than models based on Jeffery's equation. The final model was suitable for use in mould filling and other flow simulations, and it improved predictions of fibre orientation for injection moulded long-fibre composites. Adding ARD to a Jeffery-type fibre orientation model offers greatly improved ability to match experimental data, compared to the isotropic Folgar–Tucker model.

Miled et al., 2012, [149] proposed a first integrated approach of the injection moulding of fibre reinforced thermoplastics starting from rheology of the material, orientation equation, interaction parameter and closure approximation. The resulting local fibre orientation distribution is then used in two ways, in order to predict the mechanical properties of the part: first, using classical analytical homogenization theories, but based on the computed orientation tensor and not on an experimental one, and then, using numerical homogenization which consists in generating a Representative Elementary Volume (REV), determining its unidirectional mechanical properties of the part.

2.2.4.5 Reinforced nanoclay modeling approach

Polymer nanocomposites consist of a polymeric material (e.g., thermoplastics, thermosets, or elastomers) and a reinforcing nanoscale material (nanoparticle). The nanoparticle has at least one dimension in nanometer scale. Polymer nanocomposites show major improvements in mechanical properties, gas barrier properties, thermal stability and fire retardancy. The most commonly used nanoparticles referred to the literature are [150], [151], [152] :

- Montmorillonite organoclays (MMT)
- Carbon nanofibres (CNF)
- Polyhedral oligomeric silsesquioxane (POSS)
- Carbon nanotubes [multiwall (MWNT), small-diameter (SDNT), and single-wall (SWNT)]
- Nanosilica (N-silica)
- Nanoaluminum oxide (Al_2O_3)
- Nanotitanium oxide (TiO_2)

The montmorillonite nanoclays are the most widely investigated nanoparticles in a variety of polymer matrices for a spectrum of applications.

In most cases, polymer nanostructured materials exhibit multifunctionality. Several of the functions of these materials are listed below:

- Thermal: increased thermal resistance, higher glass transition temperature (T_g) or heat deflection temperature (HDT) are reduced coefficient of thermal expansion (CTE).
- Mechanical: increased modulus, strength, toughness and elongation (in some cases).

Thostenson (2005) [153] provided an overview of recent advances in nanocomposites research. The state of knowledge in processing, characterization, and analysis/modelling

of nanocomposites were presented with a particular emphasis on identifying fundamental structure/property relationships. The author stated that multi-scale hybrid composites have also been produced using nanoclay as reinforcement for the matrix material. The motivation of adding nanoclay to a resin matrix is for enhancing the resin stiffness. The benefits of such improvement was demonstrated in the compressive strength of fibre composites, which is influenced by the matrix shear modulus.

Lei et al., 2006, [154] studied the effect of the clay chemistry and source on the processing and properties of the nanocomposites. Various analyses techniques were used to characterize the dispersion and the properties of the nanocomposites, using scanning electron microscopy (SEM), differential scanning calorimetry (DSC) and dynamical mechanical analysis (DMA). All the types of clay have demonstrated the apparent nucleating effect because the crystallization took place at higher temperature upon cooling. The crystallization temperatures are also affected by the intercalant characteristics.

Díaz, 2007, [155] realized a comparative study in PP-clay nanocomposites and PP containing conventional inorganic fillers such as calcium carbonate (CaCO_3) and glass fibre focusing on dimensional stability, structure, mechanical and thermal properties. The relative influence of the filler was observed from dimensional stability measurements and structural analysis by WAXD, TEM, and thermal and mechanical properties. PP/clay nanocomposites exhibited an improvement in dimensional stability and were the only composites capable of reduced shrinkage in both in-flow and cross-flow directions. The flexural modulus of PP increased nearly 20% by compounding with 4% organoclay, as compared to a similar performance obtained by compounding with 10 wt% of CaCO_3 or approximately 6 wt% of glass fibre.

De Paiva et al. [156], 2008, developed a research to give an overview of properties, synthesis and applications, and to describe the research performed until the present moment. The study of organoclays was a large field and showed an immense potential to be explored. It was summarized in 69 important papers of the recent literature, indicated a strong tendency of the use of bentonites or sodium montmorillonites, quaternary alkylammonium salts and the cation exchange technique to prepare organoclays. Approximately 80% of the papers described the use of the cation exchange reactions, generally in aqueous solution, to modify the clay minerals.

Kanny et al., 2008, [157] presented a study in wear rates and quasistatic mechanical properties of PP infused with layered organo-modified montmorillonite nanoclays. Test results showed that PP infused with 2 wt% of organomodified montmorillonite gives improved mechanical strength, higher fracture toughness, and lower wear rates. The general improvement in properties, which includes but not limited to the thermal barrier properties, may be attributed to the change in structure.

Carrión, et al., 2008, [158] prepared a new polycarbonate nanocomposite containing a 3 wt% proportion of the organically modified montmorillonite bentone 2010 and determined its tribological properties under a pin-on-disc configuration against stainless steel. The good tribological performance of the new nanocomposite was attributed to this uniform microstructure and to the increase in the nanoclay stacking distance.

Litchfield and Baird, 2008, [159] studied the effect of nanoclay concentration on the molecular orientation and drawability of poly(ethylene terephthalate) PET. The drawability at 83°C in hot air increased by the addition of nanoclay, but the maximum draw ratio was independent of nanoclay concentration. The average molecular orientation of the PET chain was found to mimic the trend in mechanical property improvements, namely Young's modulus and tenacity.

Paul and Robeson (2008) [160] reviewed the technology involved with exfoliated clay-based nanocomposites on the important areas including barrier properties, flammability resistance, biomedical applications, electrical/electronic/optoelectronic applications and fuel cells. The important question of the “nano-effect” of nanoparticle or fibre inclusion relative to their larger scale counterparts was addressed relative to crystallization and glass transition behaviour.

Santos et al. [161] (2009) showed that the properties of PP nanocomposites are dependent on the quaternary ammonium salt in the montmorillonite (MMT). Depending on the preparation the nanocomposite can exhibit an increase in its impact properties, while other preparation shows an increase in the flexural modulus.

2.3 Ejection forces in injection moulding

The knowledge of magnitude of ejection force is determinant to the design the ejection system. The magnitude of the release force may also suggest the need for changing the position of the part in the mould and, therefore, the whole ejection system. Besides this, knowing the release forces and the parameters which affect them, it provides the possibility of reducing this force by making minor changes in the part configuration. Basically, two sort of forces can be expected [70]:

- Opening forces: they are generated if the mould is jammed by too little shrinkage or too much deformation.
- Release forces which are subdivided into: loosening forces and pushing forces. The loosening force are present for all parts with cores and are generated by the shrinking of the moulding onto the core. They can also be noticed with thin slender ribs with little taper. Here they may cause a fracture of the lamellae which form the ribs. The pushing forces: they can arise from too little taper of a core and the resulting friction between part and core.

2.3.1 Ejection system

The ejection system of an injection mould must be designed carefully specially if the ejection forces involved are high. Important considerations include location of parting line of the mould relative to the part during mould opening, tapering vertical surfaces that must be draw from a core or cavity, and undercuts that will prevent the part from being ejected.

The ejector system has various requirements [7]: to eject the part without destroying it, to leave no visible marks on the part, to load the parts equally during ejection, to have a set position of the ejector pins and to coordinate the ejector system with the cooling system.

There are many means of applying the ejection force required to eject this part from the core. The simplest, least expensive, and easiest means would be the use of ejector pins.

Others ways are ejector sleeves, stripper plates, stripper rings, blade ejection and air ejection. When there are undercuts in the part it is necessary consider other way to realize the ejection of the part, like: stripping, collapsible cores, lifters, unscrewing moulds and side core or split cavities [6,159].

The ejectors pins are driven forward by the ejector plate. Return pins are included to drive the plate back by the cavity plate when the mould closes. Return pins are included as either a primary means of returning the ejector pins or as a back-up if a hydraulically driven system fails to return the ejector plate and pins [6]. Use of pins sometimes results in excessive stress because of their small contact area with the part and part deformation or damage might occur due to the unbalance ejection force. Wang (1996) [163], describes an efficient algorithm for optimising the arrangement and the selection of ejectors.

2.3.2 Variables affecting the ejection force

Yu et al., 1992, [164] studied a combination of experimental, analytical, and statistical means to establish equations for calculating ejection temperature according to the material properties, part thickness, and moulding conditions such as injection and mould temperatures.

There are various parameters that influence the ejection force, grouped in four groups: mould, moulding, moulding material and processing [70].

In relation to the mould and mould material the rigidity will not permit the deformation of the part during the ejection; the cooling, depending on the material of the mould, will be faster or slower and this will affect the shrinkage determining the facility or difficulty to release the part. The treatment of the mould surface will influence the friction, because if the roughness is high, it will increase the ejection force.

Other important characteristic are linked with the project of the product: thickness, cross sections, projected area and presence or absence of undercuts. The designers must design the most simple system to realise the part and this system must be the cheapest as possible.

The processing parameters influence the quality of the part and mainly the shrinkage, and hence the ejection force. These included the pressure build-up and temperature of

moulding. The temperature of moulding results from the melt temperature, mould temperature and time of demoulding.

Other attributes of the moulding material as friction, modulus of elasticity, thermal characteristics (coefficient of expansion thermal and coefficient of compressibility linear) and thermodynamic behaviour also influence the shrinkage. When the shrinkage increases the ejection force tends to increase too.

2.3.3 Prediction of the ejection force

Menges, Michaeli and Mohren [70] presented various methods for computing the release forces, mostly based on coefficients of static friction for determining demoulding and opening forces for sleeves or box-shaped parts. These include expressions to calculate the ejection forces for open cylindrical sleeve, closed cylindrical sleeves, open rectangular sleeve, closed rectangular sleeve and threaded sleeve.

Burke and Malloy (1991) [165] presented an estimate for mathematical calculation to determine the ejection force, if the exact material characteristics are known for the processing range.

For deep draw mouldings produced using cavities and cores, such as sleeves or box shaped parts, the release force is given by the relationship between the plastic-steel coefficient of friction, μ , the contact pressure P , and the area of contact A :

$$F_R = \mu PA \quad (2.18)$$

The equation above can be expanded to include the special case of a box shaped molding with a sealed end:

$$F_E = \mu E(T) \alpha (T_s - T_E) \frac{8tL}{1\gamma} + (W_1 W_2 P_a) \quad (2.19)$$

where $E(T)$ is the elastic modulus at the temperature of ejection (Pa), α , the coefficient of thermal expansion (m/m/°C), T_s , the temperature of plastic when shrinkage begins (°C), T_e , the part temperature at time of ejection (°C), t , the part wall thickness (m), L , the height

of core (m), W_1 , the width of long side of core (m), W_2 , the width of short side of core (m), P_a , the atmospheric pressure (Pa) and μ , the Poisson's ratio.

Shen et al., 1999, [166] tested different configurations of mould cavities and cores, open (or closed), hollow, thin walled cones in various thicknesses, diameters, lengths, and cone angles. The ejection force was measured using a tensile test machine and a specially designed tool. The dependence of the ejection force on the size, wall thickness, cone angle, elastic modulus, Poisson's ratio of the moulded parts, and the friction coefficient between steel and plastics are considered and a new method for calculating the ejection force in an acceptably accurate way was presented. The calculation formula of the ejection force indicates that: the ejection force is directly proportional to the thickness and length of the part and has little relationship with the radius of the part; the thermal contraction strain and Young's modulus of the plastics impose considerable influence on the ejection force; a high friction coefficient, f , leads to a high ejection force.

Pantani in his thesis (1999) [113] investigated the effect of in-mould shrinkage on the final dimensions of a rectangular plate, the effect geometrical constraints were observed by adding inserts to the mould cavity. Furthermore, a new technique, by which shrinkage can be followed from the moment it starts inside the mould to soon after ejection, was applied. Equations for shrinkage prediction based on a thermomechanical model were implemented in a computer. In this way, also important features of injection moulding modelling (in particular the effect of mould deformation) normally neglected by commercial codes, were underlined. Predicted results were successfully compared with experimental data, mainly of pressure and shrinkage evolution.

Sasaki et al. [167] concluded that the ejection forces decrease when the surface roughness of mould decreases. Several types of PVD films were coated on to the mould cores to prevent the increasing of ejection forces. Some of these PVD films effectively prevent the increasing of ejection forces.

Delaunay et al., 2000, [168] studied the nature of the thermal contact between the polymer and the mould during the holding and cooling phases. The results of this study showed that the thermal contact resistance between the polymer and the mould is not negligible and not constant with time. The polymer temperature at the surface can be 20°C higher than the mould surface temperature. Moreover, asymmetric air gaps have been observed when cavity pressure becomes equal to atmospheric pressure, therefore asymmetric

temperature profile in the thickness are generated. In injection moulding simulation softwares, many assumptions are often made to simplify the solutions of equations. Among them, contact is taken as perfect between the polymer and the mould.

Delaunay et al. 2000 [94],[169] presented a simple method to locally determine mould rigidities: over-packed slabs are injected and local deflections are determined from measurements of the local residual pressure, the local in-plane shrinkages and the plate thickness. They also showed the influence of the mould deflection on dimensional properties. If the cavity thickness is small as in their 1-mm-thick plate mould, considering an infinitely rigid mould could not lead to realistic predictions of polymer pressure history, volumetric shrinkages and part mass. If the cavity pressure is high and if the cavity thickness is small, taking into account the mould rigidity is necessary to get realistic predictions of cavity pressure, volumetric shrinkage or part mass. But, as mould rigidities are very dependent on the mould location and design, an elastic calculation should be coupled with the cooling simulation.

Hopkinson and Dickens, 2000, [170] developed equations to predict ejection forces that were used to estimate the ejection forces required to push the moulding from a stereolithography (SL) core. During the practical experiments the ejection forces were measured. The combination of predicted tool strength and ejection forces were intended to be used a basis for determining whether a SL tool would fail under tension during ejection. This would help designers and manufacturers to decide whether SL tooling is suitable for a specific application.

Wang et al. (2000) [171] developed numerical and experimental studies on the ejection stage of plastics injection moulding process. A numerical approach was proposed to predict the ejection force in the mould-part constraining, and the friction forces as the product cools in the mould cavity up to the moment of ejection. A FEM thermo-viscoelastic solidification analysis has taken into account the stress and volume relaxation behaviour of polymers under the cavity-constrained condition. Various cases of the ejector pin layout are evaluated to examine the effect of the number, location and dimension of ejector pins, so as to identify the balanced layout causing minimum stress and deformation of the product. Numerical and experimental results have shown that the ejection force to remove an injection moulded product is governed by the mould-part constraining and friction forces during the demoulding process. The proposed approach

is based on this mechanism so that it can reasonably predict the ejection force and its distribution over the ejector pins, as validated by the measurements on PC boxes.

In SL moulds fracture were observed mainly during the ejection stage, as a result of excessive ejection forces. Pham et al. 2002, [172] carried out an ejection force model combining the effects of thermal shrinkage and mechanical interlocking due to stair-steps on the surface of SL tools. Finite element analyses were performed to validate and complement the ejection force equation. Measured forces and temperatures from injection moulding experiments indicated that the ejection force model is valid for SL moulds of both circular and non-circular shape. The average differences between measured and predicted ejection forces were approximately 10%.

Pontes et al., 2002, [173] recorded the data during processing namely pressure, temperature and ejection force. Their data showed that the holding conditions influence the ejection force and are related to the diametrical shrinkage. It was verified that the ejection force measurements using this relatively complex mechanical system were recorded with an average error of 3,5% which is meaningless for this kind of equipment. The ejection force changes inversely with respect to the holding pressure due to the decreasing diametrical shrinkage. The holding time did not affect the ejection force due to the fast solidification of the material that makes difficult the injection of more material into the impression and consequently minimize the effect of holding time on ejection force.

Pontes and Pouzada (2004) [97,172] studied the effect of processing on the ejection force required for deep tubular mouldings moulded in three common thermoplastics. These authors found that the temperature at the surface of the core influences the ejection force and that there is an injection temperature that minimizes the ejection force. The behaviour of the ejection force in relation to the injection temperature seems to be the combined result of shrinkage and frictional resistance. The shrinkage decreases because of the increasing pressure transmission during the holding phase. The frictional resistance associated to the coefficient of friction increases as a result of the better filling of the grooves and undulations. The ejection force varies inversely with the mould temperature. For a constant ejection time, this is the result of the moulding surface temperature varying according to the mould temperature. In general, the ejection force changes inversely with the holding pressure. The reduction of the diametrical shrinkage associated to the holding

pressure rise, which implies a smaller force to eject the moulding, is responsible for this behaviour. At low holding pressures a reduction of the ejection force is observed. This arises from the larger through thickness shrinkage that causes the detachment of the material from the moulding cavity surface and consequently a higher temperature of the moulding.

Pontes et al., 2005, [175] worked out a simulation algorithm based on a thermomechanical model and their predictions were compared with experimental data obtained from a fully-instrumented mould (pressure, temperature, and force). Three common thermoplastics were used for the tubular mouldings: PP, PS and PC. The model data for the ejection force closely agree with the experimental data for these three materials. The injection moulding tests were simulated using the software C-Mold (for PC and PS) and UNISA code (for PP). The predictions of the temperature profiles and the experimental pressure data were adopted as input to a thermomechanical model for the predictions of ejection forces. For an isotactic PP, the prediction of the ejection force as a function of the surface temperature of the core using the thermomechanical model is in close agreement with the experimental data. A maximum deviation of 5% between the predicted and experimental data is observed. For all materials, the thermomechanical model agrees well with the experimental data when the holding pressure is varied. Some divergence was observed in the case of the amorphous materials (PC and PS), at low holding pressures. This is probably due to the simulated temperatures being calculated by a program that does not consider the detachment of the material from the moulding cavity surface. This phenomenon causes the temperature to remain higher due to the poorer heat conduction transfer.

Bhagavatula et al. (2004) [176] estimated ejection forces for moulded parts that have been used by the industry, and compared these models to simulation and experimental results for a simple cylindrical sleeve. With the shrinkage measurements taken at the time of ejection, it is possible to apply these data to the ejection force estimation using an equation to compare the analytical model to actual ejection force data as well as the simulation. Comparing the simulated ejection force to the analytical result, it was observed that the simulation is slightly higher. This may be due to non-isothermal conditions being assumed in the simulation whereas the analytical result is isothermal. For a closed cylindrical sleeve, the contribution of the vacuum force must be accounted for, as described in equation

$$F_R = \mu E(T_E) \left[\frac{s_1\%}{100} \right] \left[2\pi S_F l + \frac{d_k \pi S_D}{1-\nu} \right] + \frac{d_k^2 \pi}{4} p_u \quad (2.20)$$

where F_R is the release or ejection force, μ the coefficient, $E(T_E)$ the elastic modulus at the average ejection temperature, s_1 the percentage shrinkage, ν the Poisson's ratio of the polymer, S_F the thickness of the part, S_D the base thickness, d_k the inner diameter of the part and p_u is the negative pressure ($p_u(\text{max})=100\text{kPa}$). The final term in the above equation accounts for the vacuum force created between the core of the mould and the part when it is ejected.

Charneau et al. (2008) [177] studied the impact of coatings on ejection stage in terms of unsticking the part from the mould surface and generation of scratches. The injection tests were made a cube-shaped insert in an instrumented mould (with force sensors) on three polymers which differ in nature: an amorphous polymer PC, a semi-crystalline one PBT and a blend of copolymers (styrene acrylonitrile/ acrylonitrile butadiene styrene). Those data were correlated to shrinkage of the polymer part, adhesion between polymer and mould surface and friction coefficient between those surfaces during the demoulding stage. Surface energies of the polymers as well as those of the coatings were measured, and their evolutions with temperature were used to take adhesion into account. The study of the demoulding forces showed a role of the coatings depending on the polymer and its nature, and roughness of the coating. They noted that ejection consisted of two stages: unsticking of the part and dynamic friction. Amorphous polymers are mainly affected by the first step, related to the adhesion at polymer/mould interface, whereas PBT, due to a higher shrinkage, is very sensitive to dynamic friction.

2.4 Objectives of the work

The ejection system must be designed precisely in order the part can be ejected without deformation. The knowledge of ejection forces allows to design the ideal system. This objective will be reached if the parameters that influence the ejection force are determined rigorously, such as the shrinkage of the part, coefficient of friction between the part and mould, and material characteristics.

The objectives of this work are:

- To produce tubular mouldings in controlled processing conditions in terms of temperature, pressure and ejection force using an instrumented mould;
- Measurement of the shrinkage of the tubular parts produced in PP with different reinforcements (nanoclay and glass fibres);
- To study the hybridisation effect of using nanoclays with glass fibres;
- To develop a thermomechanical model to predict the shrinkage and ejection force of the tubular parts;
- To validate the model predictions of shrinkage and ejection with the experimental data;

3 Models to predict shrinkage and ejection force

3.1 Thermo-mechanical model for injection moulded plates

The aim of this section is to present the thermo-elastic model of Titomanlio and Jansen [67],[72],[91],[107],[117],[118],[121]. The model permits to predict shrinkage and calculate residual stresses. This model was developed considering a thin slab.

Let z denote the thickness coordinate, let x and y represent the other two perpendicular directions, Figure 3.1. This represents an impression moulded by injection moulding. The thickness varies from zero, at the surface, to B at the mid-plane. At the region inside the part, the polymer is molten and in the contour of the part it can be seen as a solid layer. It is considered that the impression is totally filled when the holding phase begins. In the core there is pressure acting and varying with time $p(t)$. The thickness of the part is $2B$ and the position of the solid-melt interface is $z_s(t)$.

The solid layers are considered perfectly elastic and shrink uniformly. The polymer cools instantaneously when it contacts with the mould walls and the relaxation process is neglected.

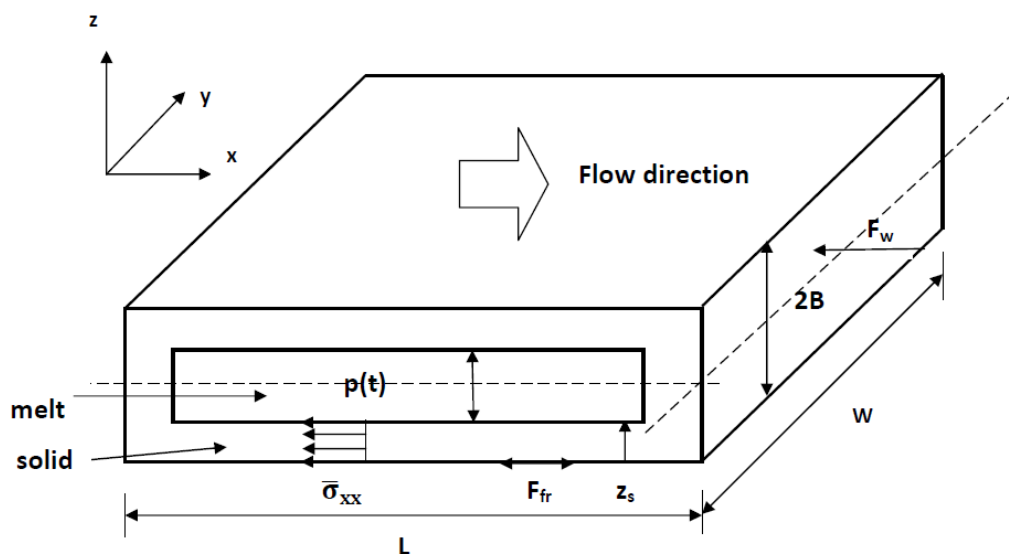


Figure 3.1 - Schematic view of the mould during polymer solidification

Considering that the shear stress components are neglected in the solidified layer the stress $\sigma_{xy} = \sigma_{yz} = \sigma_{xz} = 0$ and $\varepsilon_{xy} = \varepsilon_{yz} = \varepsilon_{xz} = 0$.

The Hooke's law for this physical situation is described below (equation 3.1). Considering σ_{ii} the total mechanical stress in the i direction, this is defined as

$$\sigma_{ii} = S_{ii} - p \quad (3.1)$$

where $S_{ii}(x, z, t)$ is the stress component in the direction of i and p is melt pressure.

In the direction z (stress in thickness does not depend on z), then

$$\begin{aligned} \sigma_{xx} &= S_{xx} - p \\ \sigma_{yy} &= S_{yy} - p \\ \sigma_{zz} &= -p \end{aligned} \quad (3.2)$$

where the stress components are

$$\begin{aligned} S_{xx} &= \frac{E}{1-\nu^2} [\varepsilon_{xx} + \nu\varepsilon_{yy}] \text{ solid part} \\ S_{yy} &= \frac{E}{1-\nu^2} [\varepsilon_{yy} + \nu\varepsilon_{xx}] \text{ solid part} \\ S_{zz} &= 0 \end{aligned} \quad (3.3)$$

In the fluid all stresses are equal, $-p$, and thus

$$S_{xx} = S_{yy} = S_{zz} = 0$$

The strain is composed by

$$\varepsilon_{ii} = \varepsilon_{ii}^{obs} - \varepsilon_{ii}^T - \varepsilon^p \quad (3.4)$$

All the components of the strain are dependent on the co-ordinate x and on time t .

The thermal strain is given by

$$\varepsilon_{ii}^T(x, r, t) = \int_{T_s}^T \alpha \cdot dT \cong \alpha(T - T_s) \quad (3.5)$$

The linear thermal expansion is

$$\alpha = \frac{1}{3.V(x,z,t)} \left(\frac{\partial V}{\partial T} \right) \quad (3.6)$$

The specific volume is a function of pressure, temperature and crystallisation.

Finally the hydrostatic strain that is dependent on pressure and is given by

$$\varepsilon^p(x, t) = - \int_0^p \beta. dp \cong \beta. p \quad (3.7)$$

where the linear compressibility of the material is

$$\beta = \frac{1}{3.V(x,z,t)} \left(\frac{\partial V}{\partial p} \right) \cong \frac{1-2\nu}{E} \quad (3.8)$$

Thus

$$\sigma_{xx} = \frac{E}{1-\nu^2} [\varepsilon_{xx}^{obs} - \varepsilon_{xx}^T - \varepsilon^p + \nu(\varepsilon_{yy}^{obs} - \varepsilon_{yy}^T - \varepsilon^p)] - p \quad (3.9)$$

and

$$S_{xx} = \frac{E}{1-\nu^2} [\varepsilon_{xx}^{obs} - \varepsilon_{xx}^T - \varepsilon^p + \nu(\varepsilon_{yy}^{obs} - \varepsilon_{yy}^T - \varepsilon^p)] \quad (3.10)$$

The balance in the equation below must be satisfied for each solidified layer as soon as shrinkage starts in the x -direction.

$$\sigma_{xx}(x, t). z_s(x, t) = [S_{xx}(x, t) - p(x, t)]. z_s(x, t) = F_S + F_{f_i} + F_C \quad (3.11)$$

where F_S is the stretching force due to the pressure, F_{f_i} is the friction force in the x direction, and F_C is any other interaction with the mould.

Or, in integral form

$$\int_0^B \sigma_{xx} dz = \int_0^{z_s} S_{xx} dz - Bp(t) = F_S + F_{f_i} + F_C = F_x(t) \quad (3.12)$$

The Leibnitz's theorem is used to differentiate the equation

$$\frac{d}{dt} \int_0^{z_s} S_{xx} dz = \int_0^{z_s} \dot{S}_{xx} dz + S_{xx} \dot{z}_s = \dot{F}_x(t) \quad (3.13)$$

After the necessary mathematic treatment and remembering that the force balance must be satisfied after each time interval dt , the stress at the solid-melt interface is zero, and there is a uniform deformation of solidified layer, it is possible to obtain

$$\overline{\dot{S}_{xx}} = \frac{\bar{E}}{1-\nu^2} [\dot{\varepsilon}_{xx} + \nu \dot{\varepsilon}_{yy}] - \frac{1}{1-\nu} \overline{E \frac{1}{3V} \dot{V}} = \frac{\dot{F}_x}{z_s} \quad (3.14)$$

$$\overline{\dot{S}_{yy}} = \frac{\bar{E}}{1-\nu^2} [\dot{\varepsilon}_{yy} + \nu \dot{\varepsilon}_{xx}] - \frac{1}{1-\nu} \overline{E \frac{1}{3V} \dot{V}} = \frac{\dot{F}_y}{z_s} \quad (3.15)$$

The evaluation of shrinkage and thermal stresses requires temperature and pressure histories, PVT behaviour, mechanical constants of the solid polymer and friction factor between polymer and mould.

The shrinkage equations after $t_{x,shr}$ (moment of begin of shrinkage) for in-plane strain are

$$\varepsilon_{xx}(x, t) = \int_{t_{x,shr}}^t \frac{1}{\bar{E}} \left(\frac{E}{3V(x,z,t)} \dot{V} \right) dt + \int_{t_{x,shr}}^t \frac{\dot{F}_x - \nu \dot{F}_y}{z_s(t) \bar{E}} dt \quad (3.16)$$

$$\varepsilon_{yy}(x, t) = \int_{t_{x,shr}}^t \frac{1}{\bar{E}} \left(\frac{E}{3V(x,z,t)} \dot{V} \right) dt + \int_{t_{x,shr}}^t \frac{\dot{F}_y - \nu \dot{F}_x}{z_s(t) \bar{E}} dt + \varepsilon_{yy}^*(x, t_{x,shr}) \quad (3.17)$$

And the stresses can be derived from the general equations:

$$S_{xx}(x, z, t) = \int_{t_{sz}(x)}^t -\frac{E}{1-\nu} \cdot \frac{1}{3} \frac{1}{V(x,z,t)} \dot{V} + \frac{E}{1-\nu^2} \left(\varepsilon_{xx}(x, t) - \nu \varepsilon_{yy}(x, t) \right) dt \quad (3.18)$$

$$S_{yy}(x, z, t) = \int_{t_{sz}(x)}^t -\frac{E}{1-\nu} \cdot \frac{1}{3V(x,z,t)} \dot{V} + \frac{E}{1-\nu^2} \left(\varepsilon_{yy}(x, t) - \nu \varepsilon_{xx}(x, t) \right) dt \quad (3.19)$$

3.1.1 Strain in thickness direction: effect of mould deformation

The onset of the thickness shrinkage in t_z^* is defined by the condition

$$p(t_z^*) = 0$$

It means that the pressure is zero when the part starts to shrink in the thickness.

After the beginning of the thickness shrinkage, the strain in this direction is derived from Hooke's law, whereas for the molten part is given by volume shrinkage:

$$\varepsilon_{zz}^{obs} = \frac{1+\nu}{1-\nu} \int_{t_z^*}^t \frac{1}{3V} \dot{V} dt - \frac{\nu}{1-\nu} \left(\dot{\varepsilon}_{xx}^{obs} + \dot{\varepsilon}_{yy}^{obs} \right) \Big|_{t_z^*}^t \text{ for solid part} \quad (3.20)$$

$$\varepsilon_{zz}^{obs} = \int_{t_z^*}^t \frac{1}{3V} \dot{V} dt \text{ for molten part} \quad (3.21)$$

$$\varepsilon_{zz}(x, t) = \frac{1}{B} \left(\int_0^{z_s} \varepsilon_{zz, solid}^{obs} dz + \int_{z_s}^B D_{z, melt}^{obs} dz \right) + C_M P_{gf} \quad (3.22)$$

The term $C_M P_{gf}$, has been included due to the mould deformation. C_M has dimensions of a compliance that is related to the rigidity of the mould. P_{gf} is the pressure distribution inside the impression at the moment of the gate freezes off.

In this particular case it has been considered that the part is constrained to shrink inside the mould during the solidification due to the friction between polymer and moulding or geometrical effects. In short there is no shrinkage inside the mould. This meaning that

$$\varepsilon_{xx}^{obs} = \varepsilon_{yy}^{obs} = \varepsilon_{zz}^{obs} = 0$$

3.1.2 In-plane shrinkage

The in-plane shrinkage after ejection ($t > t_e$) is given by

$$\varepsilon_{xx}^{obs}(x, t) = \frac{1}{3} \ln \left(\frac{V(x, z, t)}{V_s(x, z)} \right) \quad (3.23)$$

where V_s is the specific volume at moment of solidification.

And thickness shrinkage

$$Sh_z(x, t) = \frac{1+\nu}{1-\nu} \ln \left(\frac{V(x, z, t)}{V(x, z, t_z^*)} \right) - \frac{2\nu}{1-\nu} \frac{1}{3} \ln \left(\frac{V(x, z, t)}{V_s(x, z)} \right) + C_M P_{gf} \quad (3.24)$$

3.2 Thermo-mechanical model for cylindrical tubes

This section describes the Pontes model [3],[173]–[175] using the same reasoning by Titomanlio and Jansen but applied to a tubular geometry.

Consider a thin tube of thickness, H , whose cooling occurs inside and outside. Let r be the radial co-ordinate ranging from R_0 (internal surface) to R_l (external surface), θ the angular co-ordinate and x the longitudinal co-ordinate of the tube Figure 3.2.

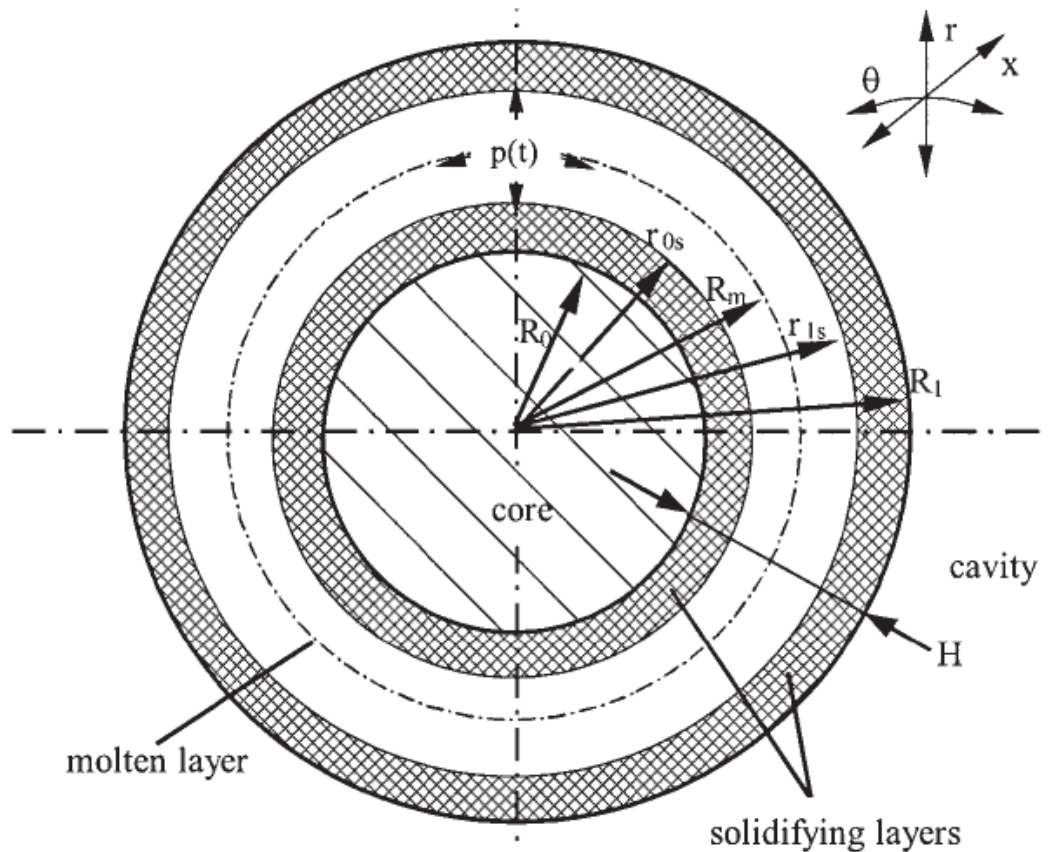


Figure 3.2 - Scheme of cross-section of tubular part [3],[174]

This scheme above represents the tube with solid layers that has contact with the mould wall in the cavity and the core. Inside these two solid layers there is molten polymer in process of solidification. It is considered that there is symmetry in relation to the average radius, R_m and constant temperature profile in the tangential direction. The interface solid-melt changes with the time and is represented by $r_{0s}(r,t)$, in relation to the core and $r_{1s}(r,t)$ in relation to the cavity.

3.2.1 Assumptions of the model

The following assumptions are considered in relation to the thin walled tube and solidification symmetry with respect to the average radius, R_m [175].

1. Continuity of stress and strain at the solid-melt interface;

2. The tangential stress, $\sigma_{\theta\theta}$, at any radial position is constant as resulting from the symmetry;
3. The radial stress, σ_{rr} , is independent from the radial co-ordinate, r ;
4. The shear components can be neglected in the solidified layer ;
5. The deformation of the solidified layer is uniform (the deformation in the θ and x directions do not depend on r)
6. No out of plane deformation occurs during solidification;
7. The solid polymer is elastic, whereas the melt is considered unable to withstand relevant tensile stresses;
8. The frozen-in-flow-induced stresses can be neglected (flow-induced stresses are typically one order of magnitude lower than the thermal-pressure induced stresses);
9. Temperature, pressure, positions of solid-melt interface and crystallisation status are known at each instant.

The stresses σ_{ii} and strains ε_{ii} in cylindrical co-ordinates are x , θ and r , respectively.

The stress components for solid layer can be written as

$$\begin{aligned}\sigma_{xx} &= \frac{E}{1-\nu^2} [\varepsilon_{xx} + \nu\varepsilon_{\theta\theta}] - \frac{\nu}{1-\nu} p(x, t) \\ \sigma_{\theta\theta} &= \frac{E}{1-\nu^2} [\varepsilon_{\theta\theta} + \nu\varepsilon_{xx}] - \frac{\nu}{1-\nu} p(x, t) \\ \sigma_{rr} &= -p(x, t)\end{aligned}\tag{3.25}$$

or

$$\begin{aligned}\sigma_{xx} &= S_{xx}(x, r, t) - p(x, t) \\ \sigma_{\theta\theta} &= S_{\theta\theta}(x, r, t) - p(x, t) \\ \sigma_{rr} &= -p(x, t)\end{aligned}\tag{3.26}$$

where

$$\begin{aligned}
 S_{xx} &= \frac{E}{1-\nu^2} (\varepsilon_{xx}^{obs} + \nu \varepsilon_{\theta\theta}^{obs}) - \frac{E}{1-\nu} (\varepsilon_{xx}^T + \varepsilon^p) \\
 S_{\theta\theta} &= \frac{E}{1-\nu^2} (\varepsilon_{\theta\theta}^{obs} + \nu \varepsilon_{xx}^{obs}) - \frac{E}{1-\nu} (\varepsilon_{\theta\theta}^T + \varepsilon^p) \\
 S_{rr} &= 0
 \end{aligned} \tag{3.27}$$

The stress distribution is evaluated after each time interval, dt , as

$$\dot{S}_{\theta\theta} = \frac{E}{1-\nu^2} (\dot{\varepsilon}_{\theta\theta}^{obs} + \nu \dot{\varepsilon}_{xx}^{obs}) - \frac{E}{1-\nu} \left(\frac{1}{3V} \dot{V} \right) \tag{3.28}$$

The dot denotes derivation in relation to time, and

$$\dot{\varepsilon}_{xx}^T + \dot{\varepsilon}^p = \dot{\varepsilon}_{\theta\theta}^T + \dot{\varepsilon}^p = \alpha \dot{T} - \beta \dot{p} = \frac{1}{3V} \dot{V} \tag{3.29}$$

When the part is inside the mould it is considered it can shrink just in the thickness direction and is not allowed to shrink in other directions.

The strain in the thickness direction considering

$$\sigma_{rr} = -p(x, t)$$

is given by

$$\varepsilon_{rr}^{obs} = \frac{1+\nu}{1-\nu} \left(\frac{\partial V}{3V} \right) - \frac{\nu}{1-\nu} (\varepsilon_{\theta\theta}^{obs} + \varepsilon_{xx}^{obs}) \tag{3.30}$$

The thickness shrinkage must be evaluated as from its onset at $t = t_r^*$.

t_r^* is determined from the condition:

$$p(t_r^*) = 0$$

The thickness shrinkage until ejection is determined by considering the strains in both solid and molten layers

$$\varepsilon_{rr, \text{solid}}^{obs} = \frac{1+\nu}{1-\nu} \int_{t_r^*}^{t_e} \frac{1}{3V} \dot{V} dt - \frac{\nu}{1-\nu} (\varepsilon_{\theta\theta}^{obs} + \varepsilon_{xx}^{obs}) \Big|_{t_r^*}^{t_e} \tag{3.31}$$

$$\varepsilon_{rr, \text{molten}}^{obs} = \int_{t_r^*}^{t_e} \frac{1}{3V} \dot{V} dt \tag{3.32}$$

At the start of thickness shrinkage, t_r^* , the reference dimensions coincide with the mould dimensions. Considering symmetry in relation to the average radius (R_m) the thickness shrinkage $Sh_r(x,t)$ is obtained by integrating $\varepsilon_{rr}^{obs}(x, r, t)$ from the internal surface, R_0 , of the tube to its average radius, R_m :

$$Sh_r(x, t)|_{t_r^*}^{t_e} = -\frac{1}{R_m - R_0} \left[\int_{R_0}^{r_{os}} \varepsilon_{rr}^{obs} dr + \int_{r_{os}}^{R_m} \varepsilon_{rr}^{obs} dr \right] \Big|_{t_r^*}^{t_e} \quad (3.33)$$

The shrinkage in the thickness direction causes strain changes in the tangential direction. The beginning shrinkage t_r^* , until ejection, is

$$\varepsilon_{\theta\theta}|_{t_r^*}^{t_e} = -Sh_r|_{t_r^*}^{t_e} \frac{H}{2R_m} \quad (3.34)$$

Considering that until ejection, $\dot{\varepsilon}_{\theta\theta}^{obs}=0$, by integrating equation over time from the moment of the solidification of the first layer, it results for the stress distribution before ejection:

$$S_{\theta\theta}(x, r, t) = -\int_{t_{s,0}}^t \frac{E}{1-\nu} \frac{1}{3V} \dot{V} dt + \int_{t_r^*}^t \frac{E}{1-\nu^2} \varepsilon_{\theta\theta}^{obs} dt \quad (3.35)$$

It must be noted that $\dot{\varepsilon}_{\theta\theta}^{obs}=0$ as from the moment of solidification of the first layer, $t_{s,0}$, until the start of thickness shrinkage, t_r^* .

An equation similar to previous equation can be written for the x direction by interchanging the subscripts θ and x, and multiplying the observable strain $\varepsilon_{\theta\theta}^{obs}$ by Poisson's ratio.

$$S_{xx}(x, r, t) = -\int_{t_{s,0}}^t \frac{E}{1-\nu} \frac{1}{3V} \dot{V} dt + \int_{t_r^*}^t \frac{\nu E}{1-\nu^2} \varepsilon_{\theta\theta}^{obs} dt \quad (3.36)$$

3.2.2 Ejection force

Consider the geometry in the Figure 3.3

$$\frac{p_c(x)}{\cos(\alpha)} d\theta r(x) dx - 2\bar{\sigma}_\theta(x, t_e) H_{part} dx \sin\left(\frac{d\theta}{2}\right) = 0 \quad (3.37)$$

$$\sin\left(\frac{d\theta}{2}\right) \approx \frac{d\theta}{2} \quad (3.38)$$

$$p_c(x) = \frac{2\bar{\sigma}_\theta(x, t_e) H_{part} \cos(\alpha)}{r(x)} \quad (3.39)$$

$$F_e = \mu \int p_c dA \quad (3.40)$$

$$dA = \frac{2\pi(x)dx}{\cos(\alpha)} \quad (3.41)$$

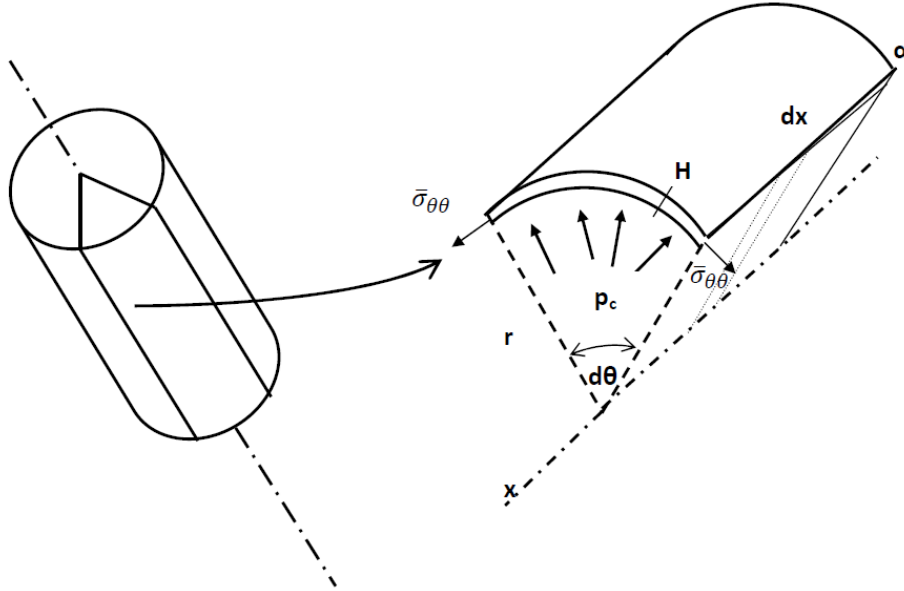


Figure 3.3 - Schematic representation of forces before ejection

$$F_e = 2\pi\mu H_{part} \int_0^L \overline{\sigma_{\theta\theta}}(x, t_e) dx \quad (3.42)$$

The average tangential stress before ejection, $\overline{\sigma_{\theta\theta}}(x, t_e)$, is obtained substituting in equation 3.32, the equation 3.31 and averaging it over the thickness. In this analysis it is considered that the modulus of the polymer is constant and equal to the modulus at the average ejection temperature, $E(\overline{T_e})$, and the melt pressure at ejection, $p(x, t_e)$, is zero. Thus

$$\overline{\sigma_{\theta\theta}}(x, t) = -\frac{E(\overline{T_e})}{1-\nu} \int_{t_{s0}}^{t_e} \frac{1}{3V} \dot{V} dt - \frac{E(\overline{T_e})}{1-\nu^2} \frac{H}{2R_m} Sh_r(t) \Big|_{t_r^*}^{t_e} \quad (3.43)$$

After integration

$$\overline{\sigma_{\theta\theta}}(x, t) = -\frac{E(\overline{T_e})}{1-\nu} \frac{1}{3} \ln \left(\frac{V(x, r, t_e)}{V_s(x, r)} \right) - \frac{E(\overline{T_e})}{1-\nu^2} \frac{H}{2R_m} Sh_r(t) \Big|_{t_r^*}^{t_e} \quad (3.44)$$

The function $V_s(x, r)$ is the specific volume at the moment of solidification.

Substituting in equation 3.44 the equation 3.43 it follows that

$$F_e = \mu \frac{2\pi H_{part}}{1-\nu} E(\bar{T}_e) \int_0^L \left(-\frac{1}{3} \ln \left(\frac{V(x,r,t_e)}{V_s(x,r)} \right) - \frac{H}{(1+\nu)2R_m} Sh_r(t) \Big|_{t_r^*}^{t_e} \right) dx \quad (3.45)$$

The expression above indicates that the ejection force is directly dependent on the elastic modulus at ejection temperature, the coefficient of friction (considered here as a constant), the thickness of the part and the variation of the (average) volume shrinkage between solidification and the ejection time.

The last term inside the integral is included if the tube shrinks in the thickness direction. This may happen for lower holding pressure or times leading to the reduction of the force required to eject the part.

To calculate the diametrical shrinkage and thickness shrinkage can be used

$$Sh_{Dm}(x, t) \Big|_0^t = -\frac{1}{3} \overline{\ln \left(\frac{V(x,t)}{V_s(x)} \right)} \quad (3.46)$$

$$Sh_r(x, t) \Big|_0^t = \frac{1+\nu}{1-\nu} \frac{1}{3} \overline{\ln \left(\frac{V(x,t)}{V(x,t_e)} \right)} + \frac{2\nu}{1-\nu} \frac{1}{3} \overline{\ln \left(\frac{V(x,t)}{V_s(x)} \right)} - \left(\frac{R_m - r_{0s}(t)}{R_m - R_0} \right) \frac{1}{3} \ln \left(\frac{V(x,t)}{V(x,t_r^*)} \right) \Big|_{t_r^*}^{t_e} - C_M p_{gf} \quad (3.47)$$

The term $C_M p_{gf}$ has been included here (as it was done in the case of the plate case) to account for the relative thickness variation of the as-mould product due to the mould deformation. The term p_{gf} is the pressure distribution inside the impression at the instant the gate solidifies. The mould compliance C_M can be obtained by a simplified analysis of the core and cavity deformations.

3.3 Thermo-mechanical model for reinforced moulded plate

The model proposed by Jansen et al. [91],[94] uses the fibre orientation state, temperature and pressure fields as input and predicts shrinkage. The properties of the unidirectional ply are calculated from the properties of matrix and fibre. The moulded product is considered as a laminate with finite number of plies. The fibre orientation is known for

each ply and for all laminate. The ply properties and the pressure and temperature history are used to calculate the shrinkage and residual stress distribution.

The glass fibre shear modulus is evaluated by [123],[178]–[180]

$$G_f = \frac{E_f}{2(1+\nu_f)} \quad (3.48)$$

Matrix volume fraction (V_m)

$$V_m = 1 - V_f \quad (3.49)$$

Let 1, 2 and 3 denote the flow, transverse and thickness direction, respectively. The ply properties are calculated with the Halpin-Tsai equations. The elastic modulus is

$$E_1 = E_m \frac{1+2\left(\frac{l}{d}\right)\eta_L V_f}{1-\eta_L V_f}, \quad \eta_L = \frac{\frac{E_f}{E_m}-1}{\frac{E_f}{E_m}+2\frac{l}{d}} \quad (3.50)$$

$$E_2 = E_m \frac{1+2\eta_T V_f}{1-\eta_T V_f}, \quad \eta_T = \frac{\frac{E_f}{E_m}-1}{\frac{E_f}{E_m}+2} \quad (3.51)$$

The Poisson's coefficients are

$$\nu_{12} = V_f \nu_f + V_m \nu_m, \quad (3.52)$$

$$\nu_{21} = \frac{\nu_{12} E_2}{E_1} \quad (3.53)$$

The shear modulus is

$$G_{12} = G_m \frac{1+\eta_G V_f}{1-\eta_G V_f}, \quad \eta_G = \frac{\frac{G_f}{G_m}-1}{\frac{G_f}{G_m}+1} \quad (3.54)$$

The Stiffness matrix of a uniaxial ply is

$$Q_{11} = \frac{E_1}{1-\nu_{12}\nu_{21}}, \quad Q_{12} = \frac{\nu_{21}E_1}{1-\nu_{12}\nu_{21}}, \quad Q_{21} = Q_{12}, \quad Q_{22} = \frac{E_2}{1-\nu_{12}\nu_{21}}, \quad Q_{66} = G_{12} \quad (3.55)$$

In the matrix form

$$Q \begin{bmatrix} Q_{11} & Q_{12} & Q_{13} \\ Q_{21} & Q_{22} & Q_{23} \\ Q_{61} & Q_{62} & Q_{66} \end{bmatrix} \quad (3.56)$$

The expansion thermal coefficients are given by the Schapery equations:

$$\alpha_1 = \frac{E_f \alpha_f V_f + E_m \alpha_m V_m}{E_f V_f + E_m V_m} \quad (3.57)$$

$$\alpha_2 = (1 + \nu_f)\alpha_f V_f + (1 + \nu_m)\alpha_m V_m - \alpha_1(\nu_f V_f + \nu_m V_m) \quad (3.58)$$

Consider that a planar orientation distribution function $\psi(\theta)$ is known, with $\psi(\theta)d\theta$ being the probability of finding a fibre between θ and $\theta + d\theta$. Then the orientation averaged stiffness of a ply is obtained by integrating over all angles between 0 e 2π with

$$\langle f(\theta) \rangle = \int_0^{2\pi} f(\theta)\psi(\theta)d\theta \quad (3.59)$$

The orientation fibre tensor was obtained experimentally.

where

$$a_{11} = \langle \cos^2 \theta_1 \rangle \quad (3.60)$$

$$a_{22} = \langle \sin^2 \theta_2 \rangle \quad (3.61)$$

θ_1 and θ_2 are given by:

$$\theta_1 = \cos^{-1} \sqrt{a_{11}} \quad (3.62)$$

and

$$\theta_2 = \sin^{-1} \sqrt{a_{22}} \quad (3.63)$$

where the coefficients of the 4th order tensor are

$$a_{1111} = \langle \cos^4 \theta_1 \rangle \quad (3.64)$$

$$a_{2222} = \langle \sin^4 \theta_2 \rangle \quad (3.65)$$

$$a_{1122} = \langle \cos^2 \theta_1 \sin^2 \theta_2 \rangle \quad (3.66)$$

The average stiffness matrix is then corrected as:

$$\langle Q_{11} \rangle = a_{1111}Q_{11} + a_{2222}Q_{22} + 2a_{1122}(Q_{12} + 2Q_{66}) \quad (3.67)$$

$$\langle Q_{22} \rangle = a_{2222}Q_{11} + a_{1111}Q_{22} + 2a_{1122}(Q_{12} + 2Q_{66}) \quad (3.68)$$

$$\langle Q_{12} \rangle = a_{1122}(Q_{11} + Q_{22} - 4Q_{66}) + (a_{1111} + a_{2222})Q_{12} \quad (3.69)$$

$$\langle Q_{66} \rangle = a_{1122}(Q_{11} + Q_{22} - 2Q_{12}) + (a_{1111} - 2a_{1122} + a_{2222})Q_{66} \quad (3.70)$$

The coefficients of thermal expansion average in longitudinal and transverse direction are

$$\langle \alpha_1 \rangle = a_{11} \alpha_1 + a_{22} \alpha_2 \quad (3.71)$$

$$\langle \alpha_2 \rangle = a_{22} \alpha_1 + a_{11} \alpha_2 \quad (3.72)$$

The composite stiffness is averaged over the thickness. If the total thickness is h , the composite stiffness, A_{ij} , is

$$A_{ij} = \overline{\langle Q_{ij} \rangle g(z)} \quad (3.73)$$

where

$$\overline{g(z)} = \frac{1}{h} \int_{-\frac{h}{2}}^{\frac{h}{2}} g(z) dz \quad (3.74)$$

The expansion thermal coefficients for the composite are

$$\overline{\alpha_1} = \tilde{\alpha}_{1j} \overline{Q_{jk}(z) \alpha_k(z)} \quad (3.75)$$

$$\overline{\alpha_2} = \tilde{\alpha}_{2j} \overline{Q_{jk}(z) \alpha_k(z)} \quad (3.76)$$

The average linear compressibility for the composite are

$$\overline{\beta_1} = \tilde{\alpha}_{1j} \overline{Q_{jk}(z) \beta_k(z)} \quad (3.77)$$

$$\overline{\beta_2} = \tilde{\alpha}_{2j} \overline{Q_{jk}(z) \beta_k(z)} \quad (3.78)$$

This model uses the Modified Classical Laminate Theory. To understand how pressures get “frozen in” it is necessary to consider the stress history of a layer that cools through the solidification temperature, T_s . At reference time $t = -\infty$, the pressure is assumed to equal to zero. The stress history then consists of a fluid part and a solid part:

$$\sigma_i = -P|_{-\infty}^{t_{sz}} + \int_{t_{sz}}^t \dot{\sigma}_i dt \quad (3.79)$$

where t_{sz} stands for the instant of solidification of layer z , and σ_i is the elastic stress of the solid part. The general orthotropic stress equations are given by:

$$\sigma_i = Q_{ij} \varepsilon_j^* \quad (3.80)$$

$$\varepsilon_j^* = \varepsilon_j - \alpha_j \Delta T = S_{ij} \sigma_j \quad (3.81)$$

For the cylindrical geometry it is assumed that $x \rightarrow 1, \theta \rightarrow 2$ and $r \rightarrow 3$

The Hooke Law for each dimension are

$$\sigma_1 = Q_{11}\varepsilon_1^* + Q_{12}\varepsilon_2^* + Q_{13}\varepsilon_3^* \quad (3.82)$$

$$\sigma_2 = Q_{21}\varepsilon_1^* + Q_{22}\varepsilon_2^* + Q_{23}\varepsilon_3^* \quad (3.83)$$

$$\sigma_3 = Q_{31}\varepsilon_1^* + Q_{32}\varepsilon_2^* + Q_{33}\varepsilon_3^* = -P \quad (3.84)$$

Separating ε_3^* em σ_3 :

$$\varepsilon_3^* = -\frac{Q_{31}\varepsilon_1^*}{Q_{33}} - \frac{Q_{32}\varepsilon_2^*}{Q_{33}} - \frac{P}{Q_{33}} \quad (3.85)$$

and replacing in

$$\sigma_1 = Q_{11}\varepsilon_1^* + Q_{12}\varepsilon_2^* + Q_{13}\left(-\frac{Q_{31}\varepsilon_1^*}{Q_{33}} - \frac{Q_{32}\varepsilon_2^*}{Q_{33}} - \frac{P}{Q_{33}}\right) \quad (3.86)$$

Rewriting

$$\sigma_i = \sum_{j=1}^2 Q_{ij}^{PS} \varepsilon_j^* - \sum_{i=1}^3 Q_{i3}^P P \quad i = 1, 2 \quad (3.87)$$

From literature [179]:

$$Q_{13}^P = \frac{Q_{13}}{Q_{33}} = \frac{\nu_{13}\nu_{12}\nu_{23}}{1-\nu_{12}\nu_{21}} \quad (3.88)$$

$$Q_{23}^P = \frac{Q_{23}}{Q_{33}} = \frac{\nu_{23}+\nu_{21}\nu_{13}}{1-\nu_{12}\nu_{21}} \quad (3.89)$$

$$Q_{11}^{PS} = \frac{E_1}{1-\nu_{12}\nu_{21}} \quad (3.90)$$

$$Q_{12}^{PS} = Q_{21}^{PS} = \frac{\nu_{12}E_1}{1-\nu_{12}\nu_{21}} \quad (3.91)$$

$$Q_{22}^{PS} = \frac{E_2}{1-\nu_{12}\nu_{21}} \quad (3.92)$$

Consider the layer that solidifies at T_s temperature. It has a fluid part and a solid part

$$\sigma_i = -P|_{-\infty}^{t_{sz}} + \int_{t_{sz}}^t \dot{\sigma}_i dt \quad (3.93)$$

$$\sigma_i = -P|_{-\infty}^{t_{sz}} + \int_{t_{sz}}^t [Q_{ij}^{PS} \varepsilon_j^* - Q_{i3}^P P] dt \quad (3.94)$$

$$\sigma_i = -P|_{-\infty}^{t_{sz}} + Q_{ij}^{PS} \varepsilon_j^* \int_{t_{sz}}^t [-Q_{i3}^P P] dt \quad (3.95)$$

$$\sigma_i = -[P_{t_{sz}} - P_{-\infty}] + Q_{ij}^{PS} \varepsilon_j^* - Q_{i3}^P \int_{t_{sz}}^t [P] dt \quad (3.96)$$

$$\sigma_i = -P_{t_{sz}} + P_{-\infty} + Q_{ij}^{PS} \varepsilon_j^* - Q_{i3}^P [P_t - P_{t_{sz}}] \quad P_t = P \quad (3.97)$$

$$\sigma_i = -P_{t_{sz}} + Q_{ij}^{PS} \varepsilon_j^* + Q_{i3}^P P_{t_{sz}} - Q_{i3}^P P \quad (3.98)$$

$$\sigma_i = Q_{ij}^{PS} \varepsilon_j^* - Q_{i3}^P P - P_{t_{sz}} + Q_{i3}^P P_{t_{sz}} \quad (3.99)$$

$$\sigma_i = Q_{ij}^{PS} \varepsilon_j^* - Q_{i3}^P P - (1 - Q_{i3}^P) P_{t_{sz}} \quad P_{t_{sz}} = P_s \quad (3.100)$$

$$\sigma_i = Q_{ij}^{PS} \varepsilon_j^* - Q_{i3}^P P - (1 - Q_{i3}^P) P_s \quad (3.101)$$

It is know that

$$S_{11} Q_{11}^{PS} + S_{12} Q_{21}^{PS} = 1 \quad (3.102)$$

$$S_{11} Q_{12}^{PS} + S_{12} Q_{22}^{PS} = 0 \quad (3.103)$$

$$1 - Q_{13}^P = Q_{11}^{PS} \beta_1 + Q_{12}^{PS} \beta_2 \quad (3.104)$$

$$\beta_1 Q_{31} + \beta_2 Q_{32} + \beta_3 Q_{33} = 1 \quad (3.105)$$

Thus

$$\sigma_i = Q_{ij}^{PS} \varepsilon_j^* - Q_{i3}^P P - (1 - Q_{i3}^P) P_s \quad (3.106)$$

$$\sigma_i = Q_{ij}^{PS} (\varepsilon_j - \alpha_j (T - T_s)) + (Q_{ij}^{PS} \beta_j - 1) P - (Q_{ij}^{PS} \beta_j P_s) \quad (3.107)$$

$$\sigma_i = Q_{ij}^{PS} (\varepsilon_j - \alpha_j (T - T_s)) + Q_{ij}^{PS} \beta_j P - P - Q_{ij}^{PS} \beta_j P_s \quad (3.108)$$

$$\sigma_i = -P + Q_{ij}^{PS} [\varepsilon_j - \alpha_j (T - T_s) + \beta_j (P - P_s)] \quad (3.109)$$

It is assumed the product to be fully constrained before mould opening (no slip boundary condition). At ejection the product will then shrink uniformly to reach stress equilibrium. Since just after ejection the pressure terms vanish, the strains are given by

$$\sigma_i = -P + Q_{ij}^{PS} [\varepsilon_j - \alpha_j (T - T_s) + \beta_j (P - P_s)], P=0 \quad (3.110)$$

$$\varepsilon_j^* = \frac{\sigma_i}{Q_{ij}^{PS}} = \varepsilon_j - \alpha_j (T - T_s) + \beta_j (P - P_s) \quad (3.111)$$

Integrating over the thickness and time

$$\varepsilon_i = \bar{\alpha}_j (\bar{T} - T_s) - \bar{\beta}_j (\bar{P} - P_s) \quad (3.112)$$

Remembering that

$$\bar{\alpha}_1 = \tilde{a}_{1j} \overline{Q_{jk}(z) \alpha_k(z)} \quad (3.113)$$

$$\bar{\alpha}_2 = \tilde{a}_{2j} \overline{Q_{jk}(z) \alpha_k(z)} \quad (3.114)$$

$$\bar{\beta}_1 = \tilde{a}_{1j} \overline{Q_{jk}(z) \beta_k(z)} \quad (3.115)$$

$$\bar{\beta}_2 = \tilde{a}_{2j} \overline{Q_{jk}(z) \beta_k(z)} \quad (3.116)$$

$$\varepsilon(t_e') = \tilde{a}_{ij} \left[\overline{Q_{jk}^{ps} \alpha_k (T - T_s)} - \overline{Q_{jk}^{ps} \beta_k (P - P_s)} \right] \quad (3.117)$$

It can be obtained the ambient temperature shrinkage considering \tilde{a}_{ij} stands for A_{ij}^{-1} , being the matrix inverse of the thickness averaged stiffness A_{ij} . During further cooling the frozen-in pressure contribution remains constant and the shrinkage is caused only by thermal effects. The final strains then become

$$\varepsilon_i(t_\infty) = \tilde{a}_{ij} \left[\overline{Q_{jk}^{ps} \alpha_k (T - T_\infty)} + \overline{Q_{jk}^{ps} \beta_k P_s} \right] \quad (3.118)$$

3.4 Thermo-mechanical model for reinforced injection moulded products in cylindrical tubes

At this moment, there is no model to predict shrinkage and ejection forces for reinforced injection moulded products in cylindrical tubes. This is the model developed by this work and use some fundamentals of previous models referred at item 3.1 to 3.3.

This model uses the Modified classical Laminate Theory [179] and consider what happen with the stress when the layer cools at solidification temperature. The stress is compound by a fluid part and solid part during its freezing. In the start of solidification σ_i is the elastic stress of the solid part. Considering the cylindrical geometry it is assumed that $x \rightarrow 1, \theta \rightarrow 2$ and $r \rightarrow 3$, respectively.

The orthotropic stress equations for these directions are given by

$$\sigma_1 = Q_{11} \varepsilon_1^* + Q_{12} \varepsilon_2^* + Q_{13} \varepsilon_3^* \quad (3.119)$$

$$\sigma_2 = Q_{21} \varepsilon_1^* + Q_{22} \varepsilon_2^* + Q_{23} \varepsilon_3^* \quad (3.120)$$

$$\sigma_3 = Q_{31} \varepsilon_1^* + Q_{32} \varepsilon_2^* + Q_{33} \varepsilon_3^* = -P \quad (3.121)$$

separating ε_3^* em σ_3 in the equation 3.121

$$\varepsilon_3^* = -\frac{Q_{31} \varepsilon_1^*}{Q_{33}} - \frac{Q_{32} \varepsilon_2^*}{Q_{33}} - \frac{P}{Q_{33}} \quad (3.122)$$

considering that $Q_{13}^P = \frac{Q_{31}}{Q_{33}}$ and $Q_{23}^P = \frac{Q_{32}}{Q_{33}}$ and replacing in the equation 3.122

$$\varepsilon_3^* = -Q_{13}^P \varepsilon_1^* - Q_{23}^P \varepsilon_2^* - \frac{P}{Q_{33}} \quad (3.122)$$

According Kasper Jansen [91],[94]

$$\beta_1 Q_{31} + \beta_2 Q_{32} + \beta_3 Q_{33} = 1 \quad (3.123)$$

Isolating Q_{33} in the equation 3.124

$$\beta_3 Q_{33} = 1 - \beta_1 Q_{31} + \beta_2 Q_{32} \quad (3.124)$$

$$Q_{33} = \frac{1}{\beta_3} - \frac{\beta_1 Q_{31}}{\beta_3} - \frac{\beta_2 Q_{32}}{\beta_3} \quad (3.125)$$

Returning the equation 3.123 and considering that pressure varies with the time until the full solidification of the layer

$$\varepsilon_3^* = -Q_{13}^P \varepsilon_1^* - Q_{23}^P \varepsilon_2^* - \int_{t_{sz}}^t \frac{P(t)}{Q_{33}} dt \quad (3.126)$$

$$\varepsilon_3^* = -Q_{13}^P \varepsilon_1^* - Q_{23}^P \varepsilon_2^* - \frac{(P-P_s)}{\frac{1}{\beta_3} - \beta_1 \frac{Q_{31}^{PS}}{\beta_3} - \beta_2 \frac{Q_{32}^{PS}}{\beta_3}} \quad (3.127)$$

$$\varepsilon_3^* = -Q_{13}^P \varepsilon_1^* - Q_{23}^P \varepsilon_2^* - \beta_3 \frac{(P-P_s)}{1 - \sum_{j=1}^2 Q_{3j} \beta_j} \quad (3.128)$$

$$\varepsilon_3 - \alpha_3(T - T_s) = -Q_{13}^P (\varepsilon_1 - \alpha_1(T - T_s)) - Q_{23}^P (\varepsilon_2 - \alpha_2(T - T_s)) - \beta_3 \frac{(P-P_s)}{1 - \sum_{j=1}^2 Q_{3j} \beta_j} \quad (3.129)$$

$$\varepsilon_3 = -Q_{13}^P (\varepsilon_1 - \alpha_1(T - T_s)) - Q_{23}^P (\varepsilon_2 - \alpha_2(T - T_s)) - \beta_3 \frac{(P-P_s)}{1 - \sum_{j=1}^2 Q_{3j} \beta_j} + \alpha_3(T - T_s) \quad (3.130)$$

$$\varepsilon_3 = -\sum_{i=1}^2 Q_{i3}^P [\varepsilon_i - \alpha_i(T - T_s)] + \alpha_3(T - T_s) - \beta_3 \frac{(P-P_s)}{1 - \sum_{j=1}^2 Q_{3j} \beta_j} \quad (3.131)$$

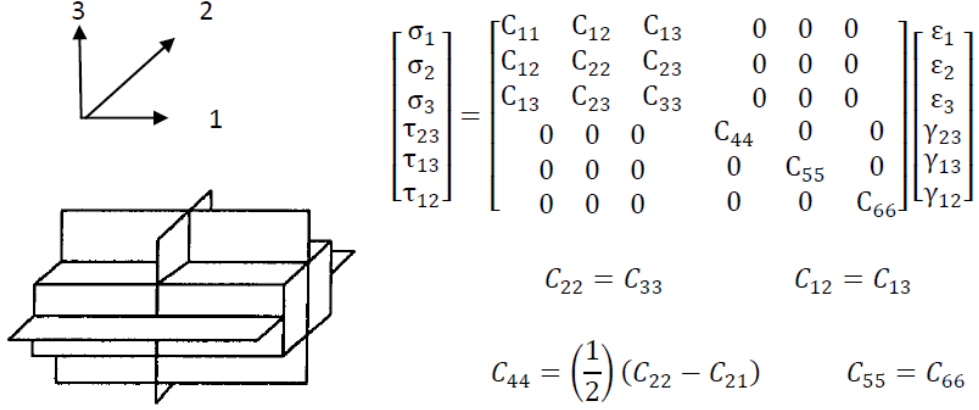
Then, for the solid part

$$\varepsilon_3 = -\sum_{i=1}^2 Q_{i3}^P [\varepsilon_i - \alpha_i(T - T_s)] + \alpha_3(T - T_s) - \beta_3 \frac{(P-P_s)}{1 - \sum_{j=1}^2 Q_{3j} \beta_j} \quad (3.132)$$

And for the fluid part

$$\varepsilon_3 = \alpha_3(T - T_s) - \beta_3 \frac{(P-P_s)}{1 - \sum_{j=1}^2 Q_{3j} \beta_j} \quad (3.133)$$

Considering orthotropic material and transversally isotropic in 2-3 plane Figure 3.4 [179]:



$$\begin{bmatrix} \sigma_1 \\ \sigma_2 \\ \sigma_3 \\ \tau_{23} \\ \tau_{13} \\ \tau_{12} \end{bmatrix} = \begin{bmatrix} C_{11} & C_{12} & C_{13} & 0 & 0 & 0 \\ C_{12} & C_{22} & C_{23} & 0 & 0 & 0 \\ C_{13} & C_{23} & C_{33} & 0 & 0 & 0 \\ 0 & 0 & 0 & C_{44} & 0 & 0 \\ 0 & 0 & 0 & 0 & C_{55} & 0 \\ 0 & 0 & 0 & 0 & 0 & C_{66} \end{bmatrix} \begin{bmatrix} \epsilon_1 \\ \epsilon_2 \\ \epsilon_3 \\ \gamma_{23} \\ \gamma_{13} \\ \gamma_{12} \end{bmatrix}$$

$$C_{22} = C_{33} \quad C_{12} = C_{13}$$

$$C_{44} = \left(\frac{1}{2}\right)(C_{22} - C_{21}) \quad C_{55} = C_{66}$$

Figure 3.4 - Orthotropic material and transversally isotropic in 2-3 plane (adapted [179])

The properties were considered the same values of the matrix in the third dimension, in the cylindrical coordinate $r \rightarrow 3$, namely thickness of the part.

$$v_{13} = v_m \quad (3.134)$$

$$\alpha_3 = \alpha_m \quad (3.135)$$

$$\beta_3 = \beta_m \quad (3.136)$$

And the G_{23} and v_{23} were obtained by [179]

$$G_{23} = \frac{1}{2}(Q_{22}^{PS} - Q_{21}^{PS}) \quad (3.137)$$

$$v_{23} = \frac{E_2}{2G_{23}} - 1 \quad (3.138)$$

According Kasper Jansen [91],[94], Q_{13}^P and Q_{23}^P , can be evaluated

$$Q_{13}^P = \frac{v_{13} + v_{12}v_{23}}{1 - v_{12}v_{21}} \quad (3.139)$$

$$Q_{23}^P = \frac{v_{23} + v_{21}v_{13}}{1 - v_{12}v_{21}} \quad (3.140)$$

In the beginning of shrinkage, t_r^* , the part dimensions are the same as the mould dimensions:

$$Sh_3|_{t_r^*}^{t_e} = -\frac{1}{R_m - R_0} \left(\int_{R_0}^{r_{0s}} \epsilon_3^{obs} solid d_3 + \int_{r_{0s}}^{R_m} \epsilon_3^{obs} melt d_3 \right) |_{t_r^*}^{t_e} \quad (3.141)$$

The stress equation in coordinate $\theta \rightarrow 2$

$$\sigma_2 = \underbrace{\sum_{j=1}^2 Q_{2j}^{PS} [\epsilon_j - \alpha_j(T - T_s) + \beta_j(P - P_s)]}_{S_2} - P \quad (3.142)$$

S_2

where S_2 is

$$S_2 = \sum_{j=1}^2 Q_{2j}^{PS} [\varepsilon_j - \alpha_j(T - T_s) + \beta_j(P - P_s)] \quad (3.143)$$

$$S_2 = Q_{21}^{PS} [\varepsilon_1 - \alpha_1(T - T_s) + \beta_1(P - P_s)] + Q_{22}^{PS} [\varepsilon_2 - \alpha_2(T - T_s) + \beta_2(P - P_s)] \quad (3.144)$$

The differential of equation in relation to time is

$$\dot{S}_2 = Q_{21}^{PS} [\dot{\varepsilon}_1 - \alpha_1(\dot{T} - T_s) + \beta_1(\dot{P} - P_s)] dt + Q_{22}^{PS} [\dot{\varepsilon}_2 - \alpha_2(\dot{T} - T_s) + \beta_2(\dot{P} - P_s)] dt \quad (3.145)$$

Until the ejection $\dot{\varepsilon}_1 = 0$ and with the integral of the above equation over the time, since the solidification moment of the first layer, this results in stress distribution before the ejection:

$$S_2 = Q_{21}^{PS} \left[\int_{t_{s,0}}^t -\alpha_1(\dot{T} - T_s) + \beta_1(\dot{P} - P_s) \right] dt + Q_{22}^{PS} \left[\int_{t_r^*}^t \dot{\varepsilon}_2 - \alpha_2(\dot{T} - T_s) + \beta_2(\dot{P} - P_s) \right] dt \quad (3.146)$$

where $t_{s,0}$ is the moment of solidification for the first layer.

In the case of S_1 :

$$\sigma_1 = \underbrace{\sum_{j=1}^2 Q_{1j}^{PS} [\varepsilon_j - \alpha_j(T - T_s) + \beta_j(P - P_s)]}_{S_1} - P \quad (3.147)$$

$$S_1 = \sum_{j=1}^2 Q_{1j}^{PS} [\varepsilon_j - \alpha_j(T - T_s) + \beta_j(P - P_s)] \quad (3.148)$$

$$S_1 = Q_{11}^{PS} [\varepsilon_1 - \alpha_1(T - T_s) + \beta_1(P - P_s)] + Q_{12}^{PS} [\varepsilon_2 - \alpha_2(T - T_s) + \beta_2(P - P_s)] \quad (3.149)$$

In the form differential equation

$$\dot{S}_1 = Q_{11}^{PS} [\dot{\varepsilon}_1 - \alpha_1(\dot{T} - T_s) + \beta_1(\dot{P} - P_s)] dt + Q_{12}^{PS} [\dot{\varepsilon}_2 - \alpha_2(\dot{T} - T_s) + \beta_2(\dot{P} - P_s)] dt \quad (3.150)$$

with $\dot{\varepsilon}_2 = 0$

$$S_1 = -Q_{11}^{PS} \left[\int_{t_{s,0}}^t \alpha_1(\dot{T} - T_s) + \beta_1(\dot{P} - P_s) \right] dt + Q_{12}^{PS} \left[\int_{t_r^*}^t \dot{\varepsilon}_2 - \alpha_2(\dot{T} - T_s) + \beta_2(\dot{P} - P_s) \right] dt \quad (3.151)$$

$$\begin{aligned}\bar{\sigma}_2 = \bar{\sigma}_\theta = & -Q_{21}^{PS} \left[\int_{t_{s,0}}^t \alpha_1(\dot{T} - T_s) + \beta_1(\dot{P} - P_s) \right] dt \\ & + Q_{22}^{PS} \left[\int_{t_r^*}^t \dot{\epsilon}_2 - \alpha_2(\dot{T} - T_s) + \beta_2(\dot{P} - P_s) \right] dt\end{aligned}\quad (3.152)$$

Knowing that

$$\dot{\epsilon}_2 = -Sh_3(x, t) \Big|_{t_r^*}^{t_e} \frac{H}{2R_m} \quad (3.153)$$

$$\begin{aligned}\bar{\sigma}_2 = \bar{\sigma}_\theta = & -Q_{21}^{PS} \left[\int_{t_{s,0}}^t \overline{\alpha_1(\dot{T} - T_s) + \beta_1(\dot{P} - P_s)} \right] dt + Q_{22}^{PS} \left[\int_{t_r^*}^t \left(-Sh_3(x, t) \Big|_{t_r^*}^{t_e} \frac{H}{2R_m} \right) - \right. \\ & \left. \overline{\alpha_2(\dot{T} - T_s) + \beta_2(\dot{P} - P_s)} \right] dt\end{aligned}\quad (3.154)$$

$$\bar{\sigma}_2 = \bar{\sigma}_\theta = -Q_{21}^{PS} \left[\overline{\alpha_1(T - T_s) + \beta_1(P - P_s)} \right] + Q_{22}^{PS} \left[\frac{H}{2R_m} Sh_3(t) - \overline{\alpha_2(T - T_s) + \beta_2(P - P_s)} \right] \quad (3.155)$$

Remembering that the ejection force is obtained by

$$F_e = 2\pi\mu H_{part} \int_0^L \bar{\sigma}_\theta(x, t_e) dx \quad (3.156)$$

Replacing the equation 3.156 in the equation 3.157 was achieved the expression for ejection force for reinforced material in cylindrical geometry

$$\begin{aligned}F_e = 2\pi\mu H_{part} \int_0^L Q_{21}^{PS} \left[\overline{[-\alpha_1(T - T_s) + \beta_1(P - P_s)]} \right] + Q_{22}^{PS} \left[-\frac{H}{2R_m} Sh_3(t) - \right. \\ \left. \overline{\alpha_2(T - T_s) + \beta_2(P - P_s)} \right] dx\end{aligned}\quad (3.157)$$

In this moment it's necessary to consider that

$$\bar{\alpha}_1 = \tilde{a}_{1j} \overline{Q_{jk}(z) \alpha_k(z)} \quad (3.158)$$

$$\bar{\alpha}_2 = \tilde{a}_{2j} \overline{Q_{jk}(z) \alpha_k(z)} \quad (3.159)$$

And

$$\bar{\beta}_1 = \tilde{a}_{1j} \overline{Q_{jk}(z) \beta_k(z)} \quad (3.160)$$

$$\overline{\beta_2} = \tilde{a}_{2j} \overline{Q_{jk}(z)\beta_k(z)} \quad (3.161)$$

Replacing $\overline{\alpha_1}$, $\overline{\alpha_2}$, $\overline{\beta_1}$ and $\overline{\beta_2}$ for the expressions above in equation 3.158

$$F_e = 2\pi\mu H_{part} \left\{ Q_{21}^{PS} \left[\int_0^L - \sum_{j=1}^2 \tilde{a}_{1j} \sum_{k=1}^2 \overline{Q_{jk}\alpha_k(T - T_s)} + \sum_{j=1}^2 \tilde{a}_{1j} \sum_{k=1}^2 \overline{Q_{jk}\beta_k(P - P_s)} \right] dx + Q_{22}^{PS} \left[\int_0^L - \frac{H}{2R_m} Sh_3(t) \Big|_{t_r^*}^{t_e} - \sum_{j=1}^2 \tilde{a}_{2j} \sum_{k=1}^2 \overline{Q_{jk}\alpha_k(T - T_s)} + \sum_{j=1}^2 \tilde{a}_{2j} \sum_{k=1}^2 \overline{Q_{jk}\beta_k(P - P_s)} \right] dx \right\} \quad (3.163)$$

Remembering that

$$Sh_3 = - \sum_{i=1}^2 Q_{i3}^P [\varepsilon_i - \alpha_i(T - T_s)] + \alpha_3(T - T_s) - \frac{\beta_3(P - P_s)}{1 - \sum_{j=1}^2 Q_{3j}\beta_j} \Big|_{t_r^*}^{t_e} \quad (3.164)$$

The equation 3.163 indicates that the ejection force is dependent of the coefficient of friction between the mould and composite; the matrix of rigidity of the composite (elastic modulus at moment of the ejection); shrinkage of the composite (depends of the characteristics of the material, geometry and processing conditions).

4 Experimental methods and simulation techniques

4.1 Materials and characterisation

In this work three grades of PP (Domo Chemicals) were used. PP is a semicrystalline material with a wide range of applications due to its good mechanical properties [181].

When an enhancement of properties is required PP can be reinforced with glass fibres or nanofillers. The compounding with glass fibres leads to greater mechanical resistance, lower thermal dilatation coefficient, good impact strength, higher tensile strength resistance and large flexibility conformation [182]. In this work a nanoclay (nanoMax[®] polyolefin masterbatch) was also used as reinforcement as it is expected to influence in the shrinkage and ejection forces. In the literature, these effects have not been searched yet, as well as if the nanoclays can facilitate the part ejection.

4.1.1 Polypropylene

Domolen 1100L is a homopolymer PP with a conventional molecular weight distribution used mainly in injection moulding applications [181]. The data sheet of the material is in the appendix A1, Table A1. 1. The grade Domolen P1-013-V10-N has 10% of glass fibre, its properties are listed in the Table A1. 2 [183] and Domolen P1-102-V30-N has 30% of glass fibre, its properties being also listed in the Table A1. 3 [184].

The main properties of PP grades are summarised in the Table 4.1.

Table 4.1- General properties of polypropylene grades

Properties	Domolen 1100L	Domolen P1-013- V10-N	Domolen P1-102- V30-N
Melt flow rate (g/10min)	6	8	7.5
Modulus of elasticity (MPa)	1500	3500	6700
Melting point (°C)	163	166	167
Density (mg/cm ³)	0.91	0.93	1.12

4.1.2 Nanoclays

The masterbatch NanoMax[®] is one of the polyolefin based masterbatches produced by Nanocor in the pellet form [185]. The P-802 grade contain 50% wt% Nanomer[®] nanoclay. Normally, the nanoclays, are added in the range 8-12 wt% for mechanical improvement and 2-8 wt% to improve the flame retardation.

4.1.3 Material identification codes

The mouldings in this work were moulded in various materials namely virgin PP, PP with 10% glass fibre (P1-013-V10-N), PP with 30% glass fibre (P1-102-V30-N) and PP with several contents of nanoclays (P-802), that is, 2%, 6% and 10% of nanoclay. Furthermore, parts with glass fibre and nanoclay were also moulded: 2% of nanoclay with 10% of glass fibre and 2% of nanoclay with 30% of glass fibre. The Table 4.2 shows the reference code to be used with these materials in this thesis.

Table 4.2 - Materials and identification code

Material	Identification code
PP without reinforcement	PP0
PP with 10% of glass fibre	PP10GF
PP with 30% of glass fibre	PP30GF
PP with 2% nanoclay	PP2N
PP with 6% nanoclay	PP6N
PP with 10% nanoclay	PP10N
PP with 10% glass fibre and 2% nanoclay	PP10GF2N
PP with 30% glass fibre and 2% nanoclay	PP30GF2N

4.1.4 Melting temperature, crystallization temperature and degree of crystallinity

The DSC (Differential scanning calorimetry) was used to determine the melting temperature, degree of crystallinity and crystallization temperature [186],[187]. The assessed range temperature is between -180°C and 600°C [7],[187]. The sample is small (<20 mg) [7],[186]. Polymer samples are encapsulated in small aluminium pans, thermocouples are put in contact with the outside pans. The tested polymer sample is put

in one of pan, while the substance of comparison is put in the other pan,.The temperature is programmed to increase linearly during the experiment. The difference of temperature between the two pans is measured [7], [188].

If the material is semi-crystalline, the degree of crystallinity can be obtained as

$$\chi = \frac{\Delta H_{SC}}{\Delta H_C} \quad (4.1)$$

where χ is the degree of crystallinity, ΔH_{SC} is the heat fusion of the polymer sample, and ΔH_C is the enthalpy of fusion of a 100% crystalline sample [187].

DSC was performed with all the 8 materials previously mentioned.

The DSC test (ASTM D 3417-83) was carried out in a Perkin Elmer Pyris 1 device, at a heating rate of 10°C/min between -30°C and 200°C. The test data are shown in the Table 4.3, including the sample mass, the melting temperature and the degree of crystallinities.

As can be see with a higher percentage of nanoclay the melt temperature decreases. The glass fibre content seems does not change the melt temperature and the degree of crystallization.

The graphic outputs of the tests are shown in the appendix A8.

Table 4.3 - The test data of DSC

Material	Mass (mg)	<i>T_m</i> (°C)	χ_c
PP0	11,2	167.7	42.5
PP10GF	9,0	170.7	41.1
PP30GF	12,7	166.5	39.5
PP2N	11,7	165.5	34.4
PP6N	18,0	167.7	41.8
PP10N	13,7	167.6	40.0
PP10GF2N	14,0	167.7	41.7
PP30GF2N	13,8	167.2	44.1

The DSC test also enabled to obtain the crystallization temperature of the 8 materials. The results for crystallization temperature of the materials used in this work is shown in the Table 4.4. The Figure 4.1 represents the crystallization curve of PP without

reinforcement, it can be observed that the peak crystallization temperature is around 116 °C. The other curves are in the appendix A.4.

Table 4.4 - Crystallization temperature for the materials

Material	Onset average temperature (°C)	Peak crystallization temperature (°C)	Average enthalpy (cooling) (J/g)
PP0	121,28	116,49	-91,12
PP2N	131,96	126,55	-90,75
PP6N	131,95	126,87	-94,74
PP10N	133,49	127,94	-88,68
PP10GF	134,35	130,67	-91,94
PP30GF	132,94	127,44	-68,13
PP10GF2N	136,65	132,35	-79,49
PP30GF2N	132,30	127,32	-69,08

The Table 4.4 shows the onset average temperature obtained by the intersection between the extension of base line and the extension of the peak line. It is possible to note that PP has the lower crystallization temperature and that the materials with nanoclay have the higher crystallization temperature, this suggesting the nanoclay acts as a nucleating agent. If the glass fibre is considered it has the opposite effect: the material with less glass fibre starts to crystallize later. However when nanoclays are introduced the trend to crystallization is anticipated if the amount of nanoclays is around 10%.

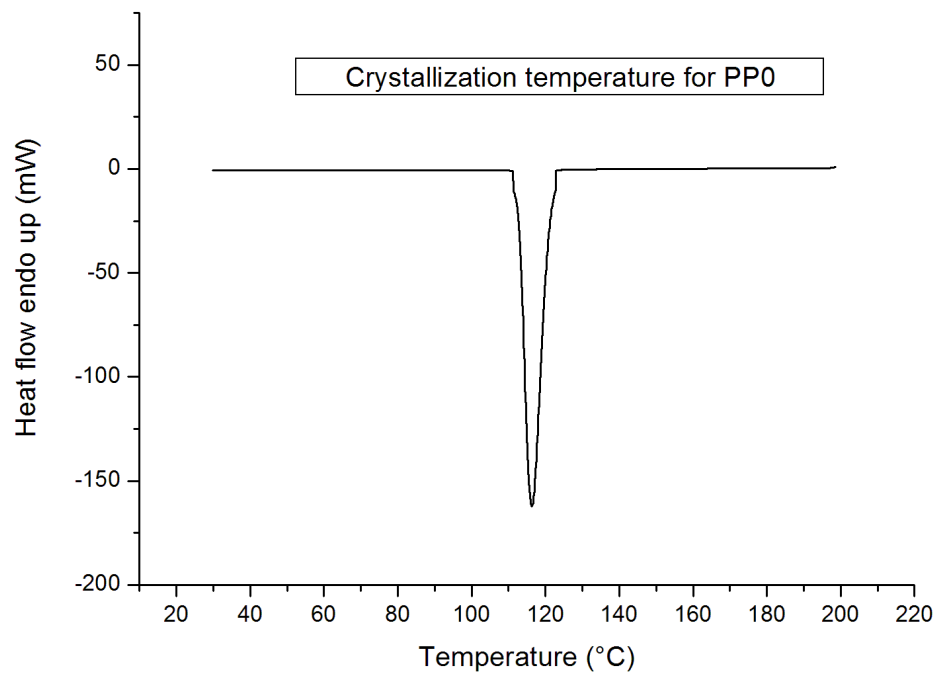


Figure 4.1 - Crystallization curve for polypropylene without reinforcement

4.1.5 Storage modulus

Dynamic Mechanical Analysis is a technique where a cyclic deformation is applied to a sample. This allows the material response to stress, temperature, frequency and other variables to be studied [189].

DMA works by applying a sinusoidal deformation to a sample of known geometry. The sample can be subjected to a controlled stress or a controlled strain. For a known stress, the sample will then deform a certain amount. In DMA this is done sinusoidally. The deformation is related to its stiffness [189].

DMA tests were realized to obtain the storage modulus in relation to the temperature. In these tests a sinusoidal stress is applied and the strain in the material is measured, allowing the determination of the complex modulus. The temperature of the sample or the frequency of the stress are often varied, leading to variations in the complex modulus.

The dynamic mechanical properties were measured with the dynamic mechanical analyser PerkinElmer DMA 7. Specimens with 1.5 mm thick, 3 mm wide, and 20 mm long were tested in a three-point-bending configuration, Figure 4.2. The storage modulus (E_0), loss modulus (E_{00}), and loss factor ($\tan \delta$) as a function of the temperature were obtained at a heating rate of $10^\circ\text{C}/\text{min}$ from -25 to 190°C and at a fixed frequency of 1 Hz. The ASTM D-5023-01 standard was used for the tests.

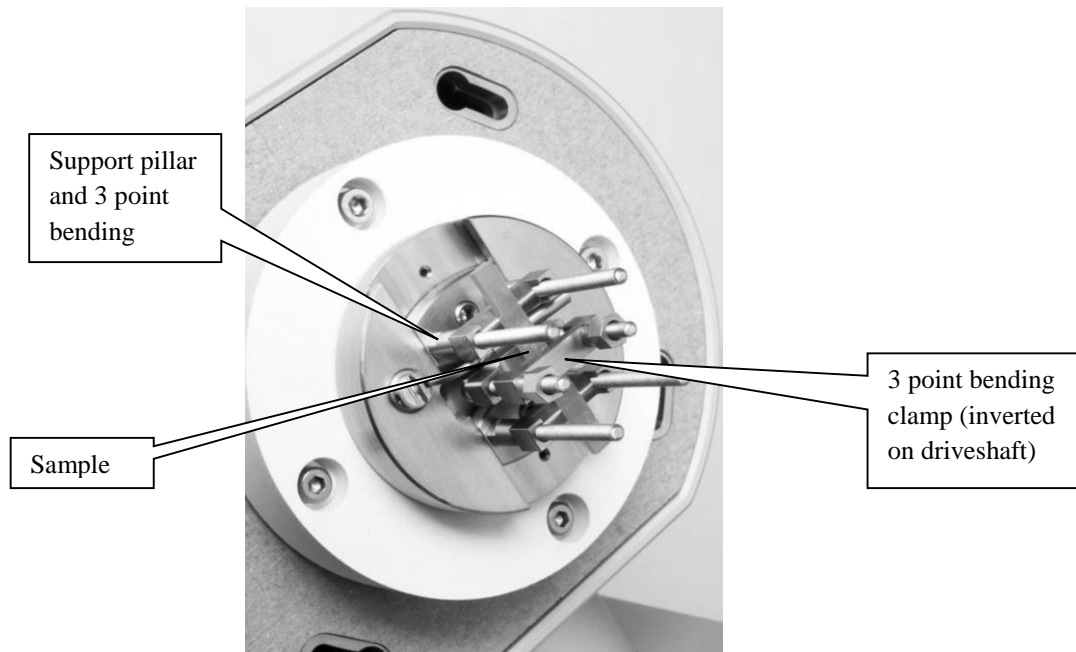


Figure 4.2 – Three point bending mode [189]

The testing parameters were:

- Static load: 800 kN
- Dynamic load: 770 kN
- Frequency: 1Hz
- Heating speed: $10^\circ\text{C}/\text{min}$

The tests were carried out with the same materials tested in DSC. The results of DMA for the materials used are listed in the Table 4.5 and in the graphic form in the appendix A5 together with the DMA curves for reinforced materials. At the table can be observed that the storage modulus decreases with the temperature.

Table 4.5 - Storage modulus for all materials studied

Material	Nominal temperature (°C)		
	30	50	75
	Storage modulus (GPa)		
PP0%	1.5	1.1	0.8
PP2%N	0.9	0.7	0.5
PP6%N	1.4	1.0	0.6
PP10%N	1.9	1.4	0.9
PP10%GF	1.9	1.6	1.3
PP30%GF	2.4	2.0	1.4
PP10%GF2%N	1.3	1.1	0.9
PP30%GF2N	2.2	1.9	1.5

The DMA output for PP without reinforcement is shown in the Figure 4.3, for the remaining materials the curves are in the appendix A.5.

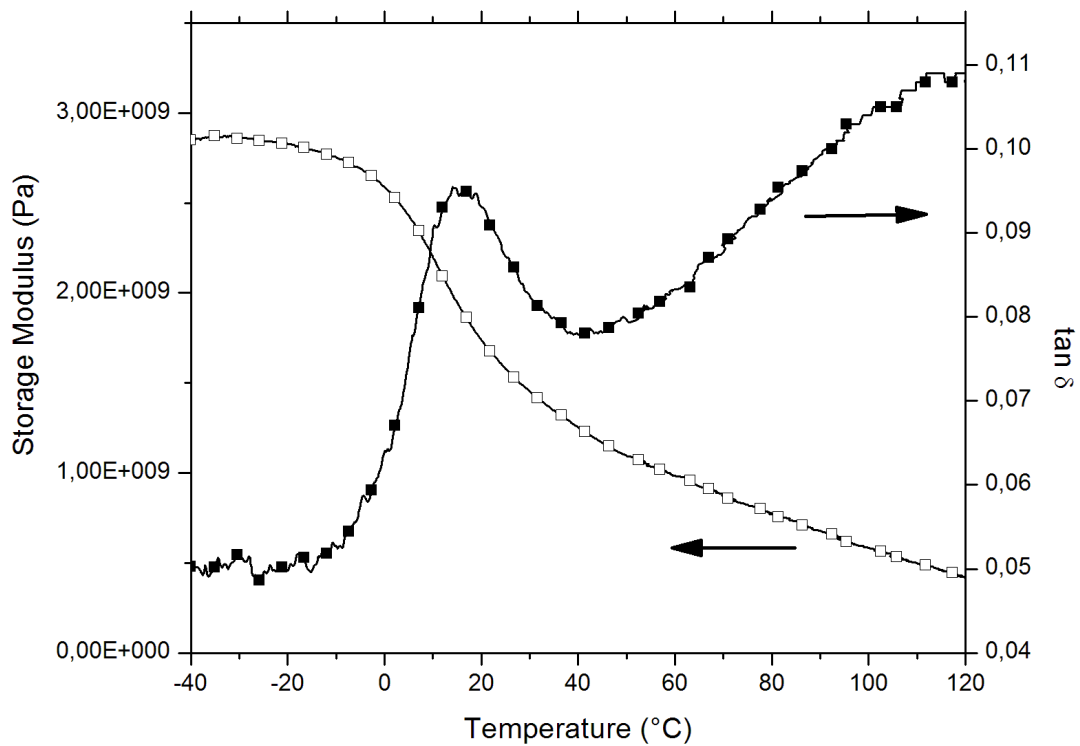


Figure 4.3 - DMA output for PP without reinforcement

4.1.6 Coefficient of linear thermal expansion

The thermomechanical analysis was done to measure the linear coefficient of thermal expansion of the materials used in this work. The thermomechanical analysis uses a dilatometer to determine the linear thermal expansion of a solid as a function of temperature. The measured expansion of the specimen can be used to determine the coefficient of linear thermal expansion α [190],[191].

The coefficient of linear thermal expansion may be evaluated as the mean $\bar{\alpha}$, in accordance with DIN 53 752 or ISO 113591 Part 1 and 2.

The mean coefficient of linear thermal expansion $\bar{\alpha}$ is obtained with the following equation

$$\bar{\alpha} = \frac{1}{l_0} \cdot \frac{l_2 - l_1}{T_2 - T_1} = \frac{1}{l_0} \cdot \frac{\Delta l}{\Delta T} \quad (4.2)$$

where l is related to the length and T in relation to the temperature.

The equipment used in this experiment was a Perkin Elmer Diamond TMA. The force of 50 mN was applied to the sample and was held for 34 min. The equipment was programmed for heating from 25°C to 170°C at 10°C/min, holding for 5 min at 170°C and cooling from 170°C to 25°C at the same rate of the heating.

The method is based on a glass rod, holding the sample with specific force on a crystal plate. The samples are 3-4 mm in diameter disks obtained from injection moulded plates. The glass rod holds the sample and allows measuring its thickness accurately during the entire test. The whole system, glass rod, crystal plate/base and the sample are inserted in the small furnace, where the temperature is controlled and increased at a rate, Figure 4.4. The temperature is increased to the melting temperature of the sample material, and then maintained for 5 min. After this time, the samples were cooled-down.

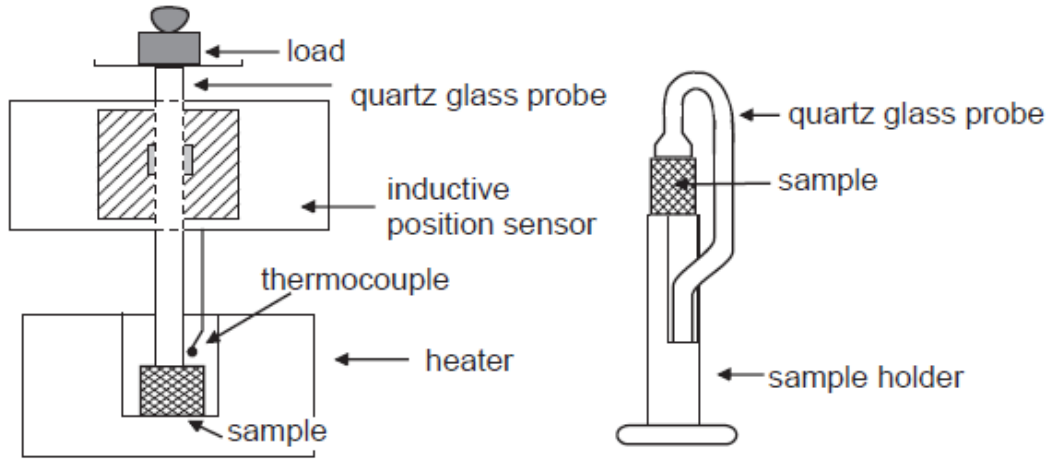


Figure 4.4 – Schematic diagrams of TMA apparatus [190]

The results of the coefficients of linear thermal expansion are showed in the Table 4.6. An example of curve obtained from the test of thermomechanical analysis for PP without reinforcement is shown in Figure 4.5, and for others materials are in the appendix A6.

Table 4.6 - Coefficient of linear thermal expansion for several materials

Material	Coefficient of linear thermal expansion ($10^{-4} \text{ }^{\circ}\text{C}^{-1}$)
PP0	2,28
PP2N	1,96
PP6N	2,00
PP10N	1,84
PP10GF	1,60
PP30GF	1,63
PP10GF2N	2,95
PP30GF2N	2,99

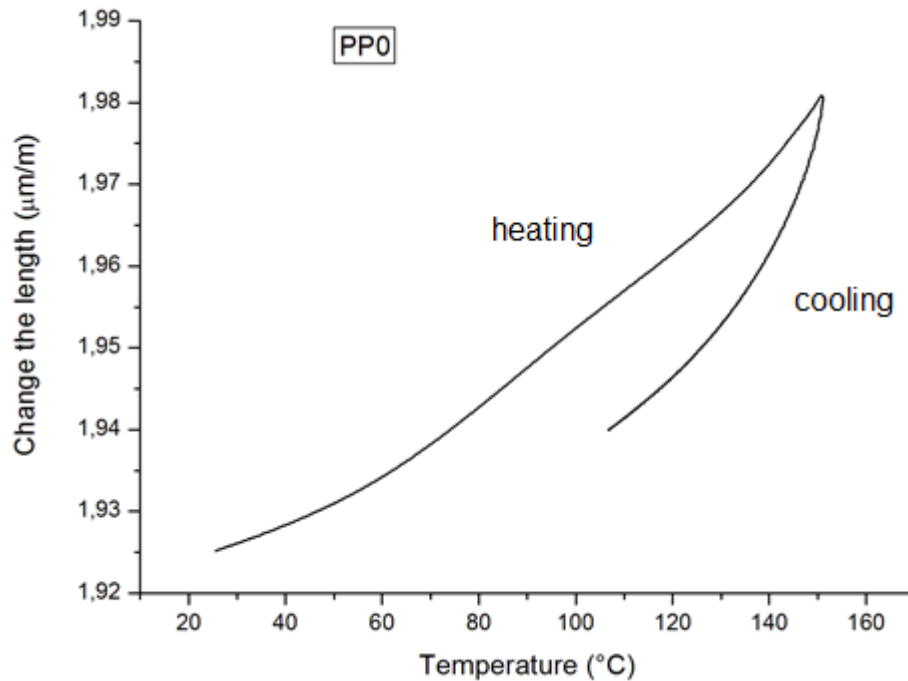


Figure 4.5 - Experimental curve obtained of TMA for PP without reinforcement

4.1.7 Rheology characterization

The rheology characterization was carried out to compare the material data used in the experimental work and those in the simulation.

The capillary rheometer used was a Rosand RH10. This equipment is able to evaluate the viscosity of materials as a function of speed (shear rate) and temperature. This is measured by heating the material within the bore of a temperature-controlled barrel, and then forcing the material at a defined speed through an accurately-dimensioned capillary die. The pressure above the capillary is measured. The viscosity is a function of this pressure-drop, the piston speed and the test geometry. The Figure 4.6 shows a close up of the pistons.

This process is repeated at several speeds to produce a profile of viscosity as a function of speed (shear rate). The temperature may be defined as that at which processing is usually carried out, or the test may be repeated at several temperatures [192].



Figure 4.6 – Pistons of Advanced Capillary Rheometer RH 10

The Rosand RH 10 works in conjunction with the Flowmaster[®] software. It allows to perform experiments and to analyse the data produced in the experiments.

The Table 4.7 shows the correspondence among the materials used in this work and the Moldflow materials available in the database.

Table 4.7 - Correspondence among experimental materials and Moldflow materials

Material	Experimental materials	Moldflow
PP without reinforcement	Domolen 1000L	MOPLN HP501L
PP 10% Glass fibre	Domolen P1-013-V10-N	PX0056
PP 30% Glass fibre	Domolen P1-102-V30-N	GC30P100-01

The die diameter used was of 2 mm and the shear rate range 1-10000 s⁻¹. The temperatures used for each material are shown in the Table 4.8 and were chosen for comparison with the viscosity curves of the Moldflow database.

Table 4.8 - Test temperatures used in the rheological experiments

Material	Test temperature (°C)
MOPLEN HP501L	220, 240 and 260
PX0056	200, 220 and 240
GC30P100-01	200, 226,7 and 253,3

The results from the rheology characterization are shown in the Figure 4.7 for neat PP, Figure 4.8 for PP with 10% glass fibre and Figure 4.9 for PP with 30% glass fibre. As it can be seen, there is a good agreement between the material data used in this work and the material data in the simulation software database.

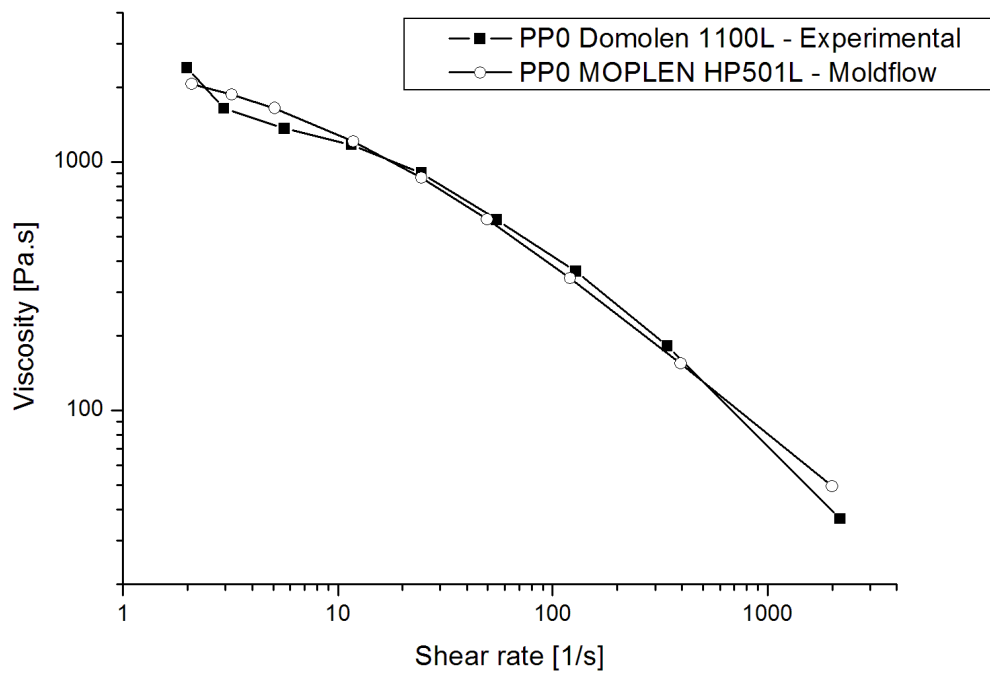


Figure 4.7 - Polypropylene without reinforcement at 220°C

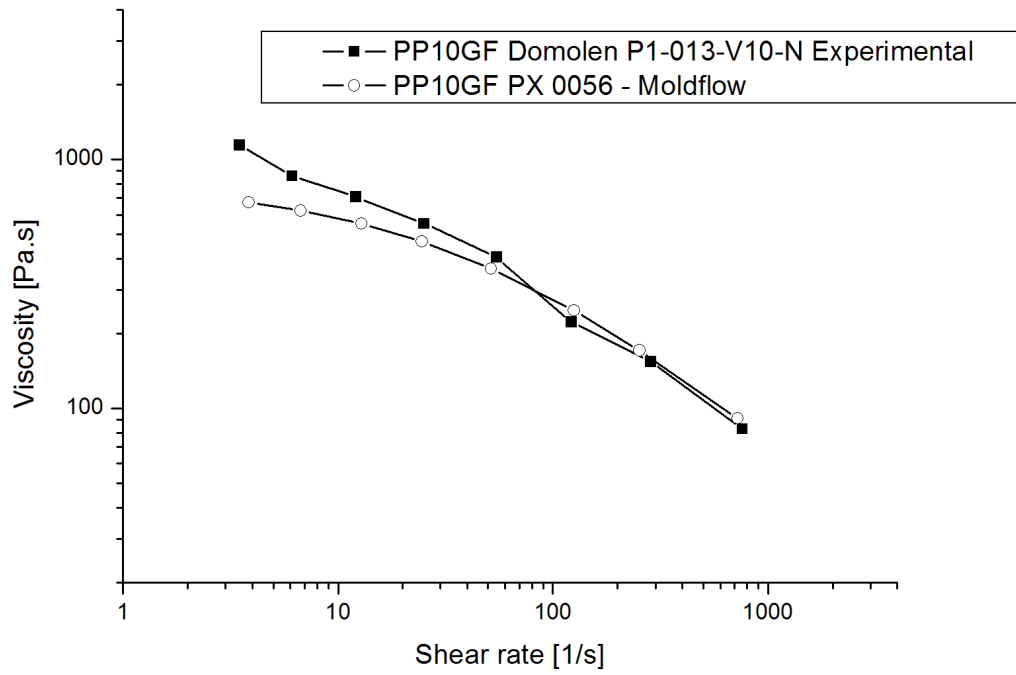


Figure 4.8 - PP 10% glass fibre at 220°C

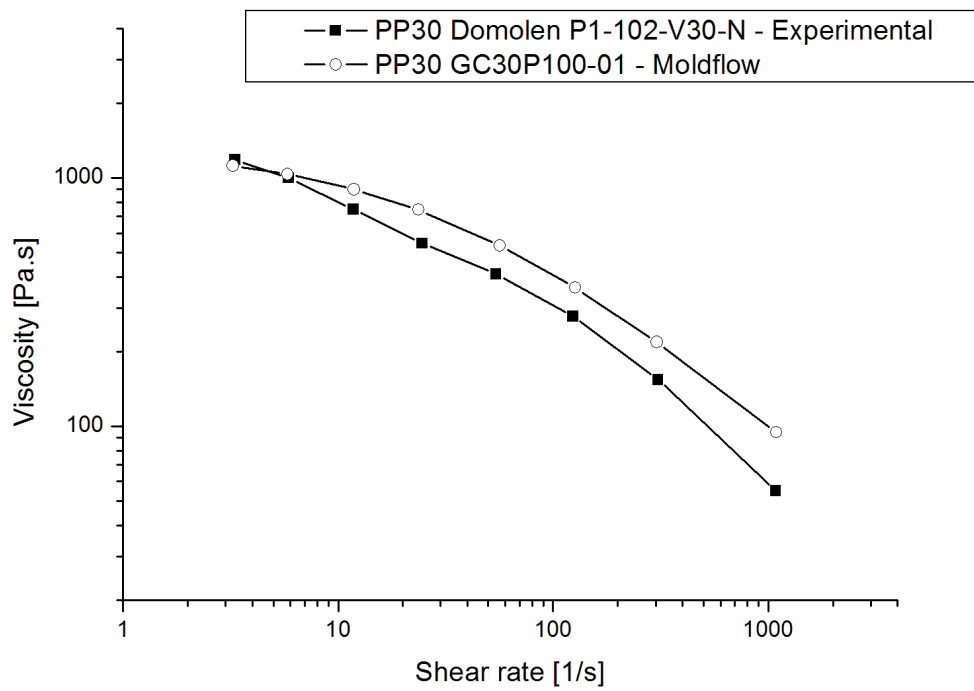


Figure 4.9 - PP 30% glass fibre at 226.7°C

4.1.8 Coefficient of Friction measurement

For this work it was necessary to inject samples of the materials. The samples are rectangular plates, with dimensions of 62mm x 31 mm x 2 mm, in the same equipment where the other mouldings were produced.

The tests were carried on the prototype equipment that enables the study of the effect of different parameters on the coefficient of friction relevant for the injection of plastic parts from mould in as-moulding conditions[193]. The concept of this equipment (known as *Mouldfriction*) is shown in the Figure 4.10 [194]

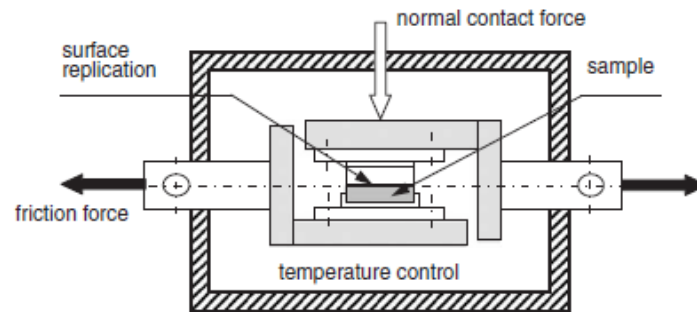


Figure 4.10 - Concept of Mouldfriction [192]

The Mouldfriction equipment has various functional systems, such as temperature control, control of contact pressure for replication of the surface and for testing, and movement guiding. A brief description of these functional systems follows next [194]–[196].

Temperature control: this feature is important for a good replication of the surface at temperatures close to melting temperature of semicrystalline materials, or above the glass transition temperature in case of amorphous materials. It is also important to maintain the temperature during the friction test.

The heating is achieved by cartridge heaters allowing the temperature to rise from room temperature up to the replication temperature within a reasonable time (typically 5 min). Some 5 mm insulating plates are used to minimize heat losses.

Cooling down from replication temperature to the testing temperature is obtained by circulating water in the cooling circuit.

Control of contact pressure: a pneumatic cylinder is used to produce the contact pressure. The control of the pressure is obtained with a piezo-resistive pressure sensor.

Monitoring of friction force: the use of a tensile test machine is an easy and reliable way to control and acquire the friction force data during the test. The prototype apparatus was designed to be mounted and work with a universal tensile testing machine.

In Figure 4.11, it is shown the Mouldfriction installed on the universal testing machine.



Figure 4.11 - View of the mouldfriction installed in a universal testing machine

The testing routine includes the following steps:

1. Heating of the mouldings surface up to the replication temperature.
2. Stabilization of the temperature.
3. Application of contact pressure to get surface replication.
4. Cooling down to the testing temperature.

5. Friction test at selected cross-head speed.

The cycle time for the complete routine is typically 15-20 min.

The tests were carried out at a cross head rate of 10 mm/min, and the maximum temperature of operation was 160°C. The pressure of contact was 4.3 MPa, the pressure at the manometer was 5 bar and the normal contact force was obtained by Netto [197] in the calibration line

$$N = 1.85 \times P_{man} \times 100 + 14.43 \quad (4.3)$$

where N is the normal force, P_{man} is the pressure registered by manometer and 14.43 is a constant.

The roughness used were R_a 0.2 μm , 0.6 μm and 0.8 μm , remembering that the surface roughness in the mould is 0.5 μm .

A typical curve of the friction test for PP with 10% of glass fibre is shown in Figure 4.12

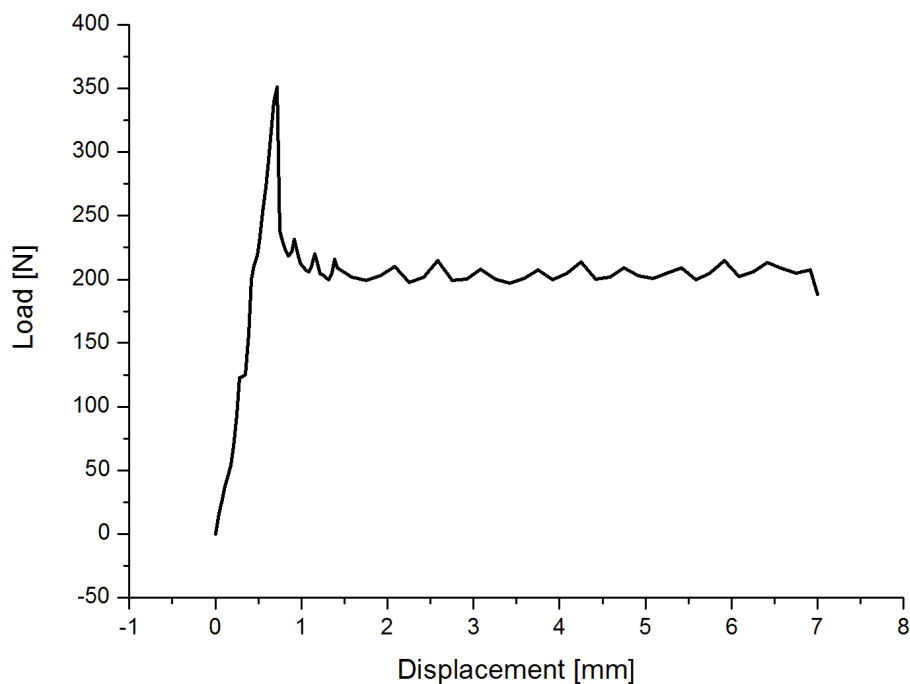


Figure 4.12 - Friction test for PP with 10% of glass fibre

The results of coefficient of friction are shown in the Table 4.9.

From the experimental data it can be concluded that when the mould surface is rougher the friction coefficient is greater. This happens because the grooves difficult the sliding

the part with the surface of the mould. Furthermore, it can be noted that with PP nanoclay composites, the coefficient of friction decreases. The nanoclays seem to behave as a lubricant. For PP with glass fibres the coefficient of friction increases with the content of glass fibre.

Table 4.9 - Coefficient of friction in relation to material and roughness of the mould

Roughness (μm)	Static coefficient of friction							
	PP0	PP2N	PP6N	PP10N	PP10GF	PP30GF	PP10GF2N	PP30GF2N
0,2	0,32	0,31	0,24	0,23	0,25	0,33	0,25	0,31
0,6	0,43	0,40	0,36	0,43	0,38	0,44	0,39	0,45
0,8	0,38	0,32	0,28	0,30	0,31	0,37	0,30	0,36

4.1.9 Measurement of the glass fibre percentage

The glass fibre percentage was calculated according to the DIN EN ISO 3451 standard. The samples had the size around 10mm x 10mm and weighed around 0.30 g. These samples were put in the furnace at 630°C during 30 minutes. After this time, only the glass fibre remained into the melting pot. To evaluate the glass fibre percentage, the equation below was used:

$$\text{Glass fibre \%} = \frac{\text{Rest}}{\text{sample}} \cdot 100 \quad (4.4)$$

where *Rest* is the residue mass after calcination and *Sample* is the sample mass.

The data of glass fibre percentage are shown in the Table 4.10 and Table 4.11 for 10% of glass fibre and 30% of glass fibre, respectively.

Table 4.10 - Measurement of percent of glass fibre (10%)

10% glass fibre			
	Sample mass (g)	Residue mass (g)	% glass fibre
Sample 1001	0.354	0.041	11.58
Sample 1002	0.265	0.032	12.08
Sample 1003	0.254	0.031	12.20

Table 4.11 - Measurement of percent of glass fibre (30%)

30% glass fibre			
	Sample mass (g)	Residue mass (g)	% glass fibre
Sample 3001	0.341	0.105	30.79
Sample 3002	0.334	0.101	30.24
Sample 3003	0.347	0.105	30.26

4.1.10 Glass fibre measurement (length and diameter)

Some samples were cut of tubular parts and these pieces were done inside the oven until the polymer was totally consumed. After, this powder was put on the microscope and observed in Bright Field Microscopy to take pictures for later measurement of glass fibre.

The Bright Field Microscopy uses a basic microscope, in transmission or reflexion mode without special accessories to generate contrast. This technique is adequate to observe polymeric systems whose constituents have refractive index enough different enough (differences over 0.05). This technique is used to analyse the dispersion and pigment particle distribution, reinforcement and other additives. The Bright Field Microscopy in reflexion is applied, mainly, to analyse materials with significant contents (> 5%) of reinforcements, such as glass fibres [198].

In short fibre reinforced thermoplastic, the fibre length can vary from less than one fibre diameter to hundreds of fibre diameters. During extrusion and injection moulding processes, the shear forces exerted by the screw or ram break the fibres and result in a length distribution that is different from the original length of chopped strand fibres [199],[200].

The measurement of length and diameter of glass fibre was done using a transmission microscope Olympus BH2. The instrument was calibrated and pictures were taken. Three samples of 10% of glass fibre and three samples of 30% of glass fibre. From each sample 3 pictures were taken (a total of 18 pictures). An example is shown in Figure 4.13 for PP with 30% of glass fibre.

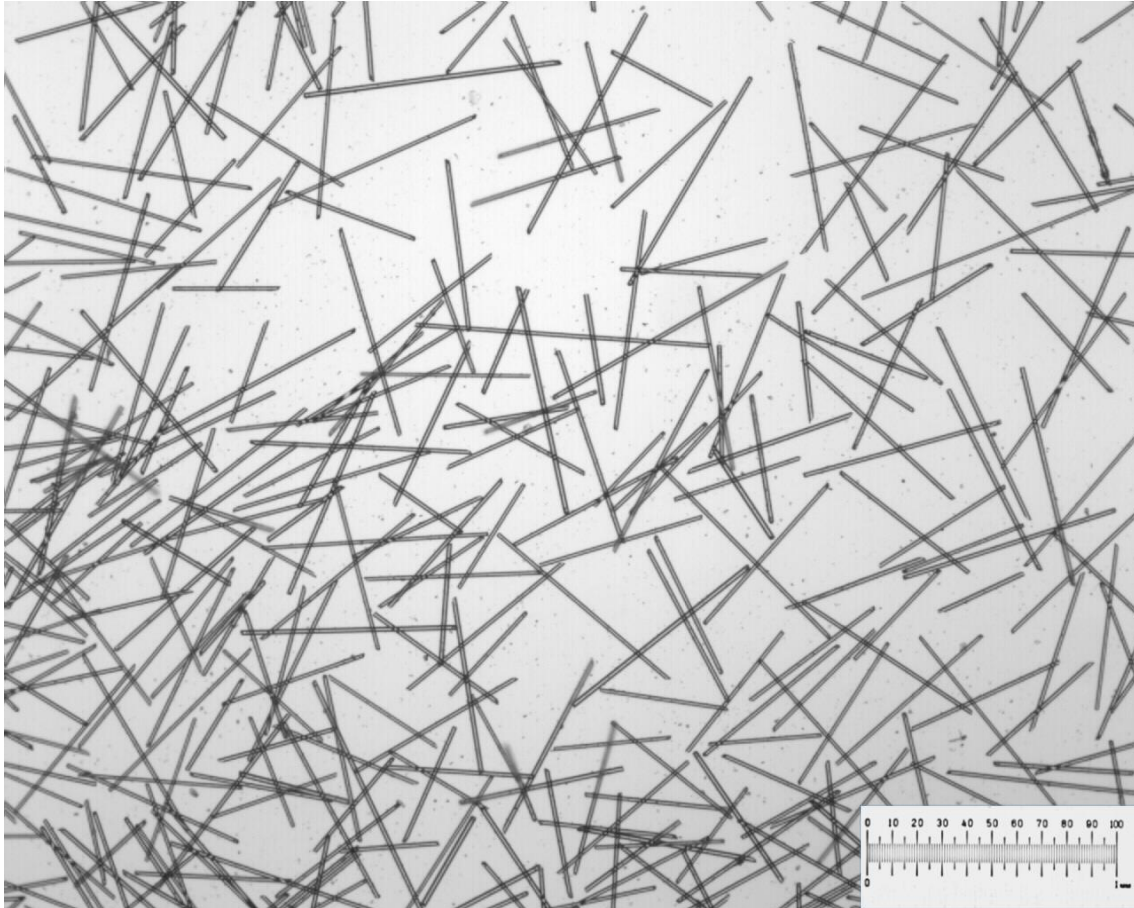


Figure 4.13 - Photograph of sample with 30% of glass fibre

The glass fibres length and diameter were measured in 100 fibres per photo. Fibre length histograms for 10% glass fibre and 30% glass fibre were generated, as well as fibre diameter histograms.

The results for the measurement of length and diameter of the fibres are shown in the Table 4.12 and Table 4.13, respectively.

The result can be shown in the form of histogram, for example, the histogram for sample 1 of 10% glass fibre is presented in the Figure 4.14.

Table 4.12 - Length measurement of 10% glass fibre and 30% glass fibre

10% Glass Fibre								
Sample 1			Sample 2			Sample 3		
Picture	\bar{x} (μm)	σ (μm)	Picture	\bar{x} (μm)	σ (μm)	Picture	\bar{x} (μm)	σ (μm)
1001	553,10	194,59	1001	633,80	168,87	1001	716,57	223,23
1002	530,63	201,02	1002	473,30	163,90	1002	533,57	174,99
1003	445,29	156,40	1003	466,77	164,50	1003	403,92	152,31
30% Glass Fibre								
Sample 1			Sample 2			Sample 3		
Picture	\bar{x} (μm)	σ (μm)	Picture	\bar{x} (μm)	σ (μm)	Picture	\bar{x} (μm)	σ (μm)
3001	372,03	106,93	3001	444,96	114,76	3001	374,31	98,89
3002	543,62	117,68	3002	514,72	112,87	3002	503,94	118,64
3003	400,80	144,63	3003	398,91	116,71	3003	384,58	99,90

Table 4.13 - Diameter measurement of 10% glass fibre and 30% glass fibre

			Sample 1 30% glass fibre			Sample 2 10% glass fibre		
Picture	\bar{x} (μm)	σ (μm)	Picture	\bar{x} (μm)	σ (μm)	Picture	\bar{x} (μm)	σ (μm)
1001	15,04	3,59	3001	16,63	4,27	1001	17,45	3,81
1002	14,95	3,37	3002	17,23	3,77	1002	16,37	3,77
1003	15,93	3,08	3003	17,49	4,13	1003	17,05	3,64

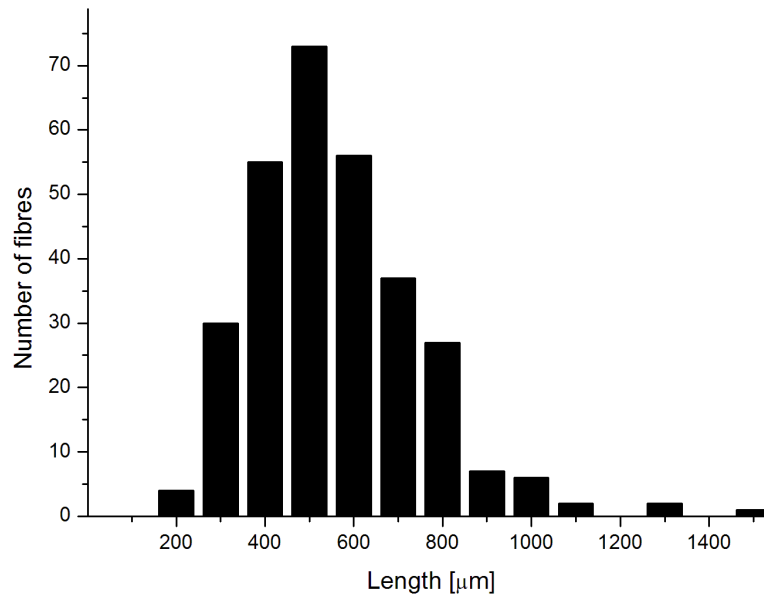


Figure 4.14- Histogram of sample with 10% glass fibre

4.2 Injection moulding

The materials were moulded in a deep tubular part (tube) with 2 mm of thickness wall. The mouldings with nominal dimensions of $D_{int}=60$ mm (internal diameter) and $L=146$ mm (length) were produced in an injection moulding machine Ferromatik Milacron FM 85 with a thermo regulator Piovan THN6P. The mouldings were produced with an instrumented mould [173]. In the Figure 4.15 it is shown the tubular part and its main dimensions.

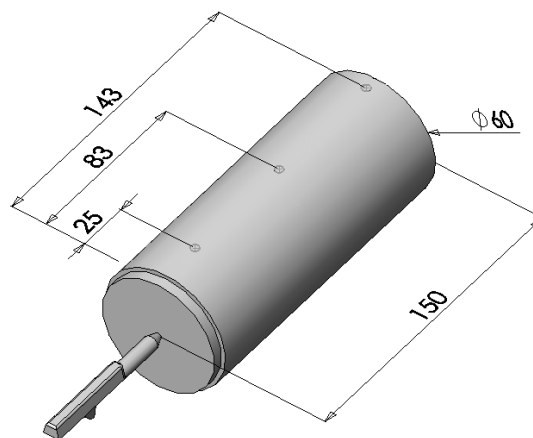


Figure 4.15 – Tubular part

4.2.1 Moulding conditions

The moulding conditions were chosen considering the recommended processing window for the materials used in this work.

The processing conditions for the various materials are listed in the Table 4.14.

Table 4.14 - Moulding conditions

Identification	PP0	PP10GF	PP30GF	PP2N	PP6N	PP10N	PP10GF2N	PP30GF2N
Cycle time (s)	50							
Cooling time (s)	12							
Injection velocity (mm/s)	70							
Injection pressure (set) (bar)	100							
Injection time (s)	0,93	0,87	0,83	0,93	0,87	0,83	0,87	0,83
Holding pressure (set) (bar)	25							
Holding time (s)	19							
Switchover (mm)	13,6	10	10	13,6	10	10	10	10
Temperature of the barrel zones (Hopper-Nozzle) (°C)	40-150-180-195-210-220							
Mould temperature (set) (°C)	30-50-75							

4.2.2 Data acquisition

The mould was equipped with three pressure sensors in the cavity and three pressure/temperature sensors in the core (along the flow path and facing each other at 25mm, 83 mm and 143 mm downstream of the gate). These positions in the cavity will be referred to as C1, C2 and C3, and in the core as B1, B2 and B3, and T1, T2 and T3, for the pressure and temperature sensors, Figure 4.16.

Priamus (Multi DAQ 8101 A and Mobile DAQ 8001 B) was used as data acquisition system with sensors that allow acquiring pressure, temperature and ejection force data.

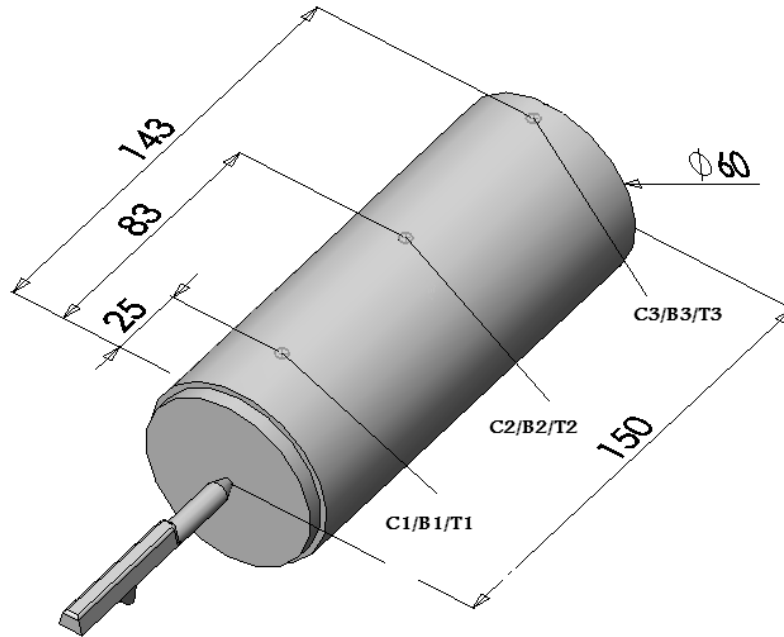


Figure 4.16 - Moulding part with the positions of pressure and temperature sensors

The location of temperature and pressure sensors is presented in Figure 4.17.

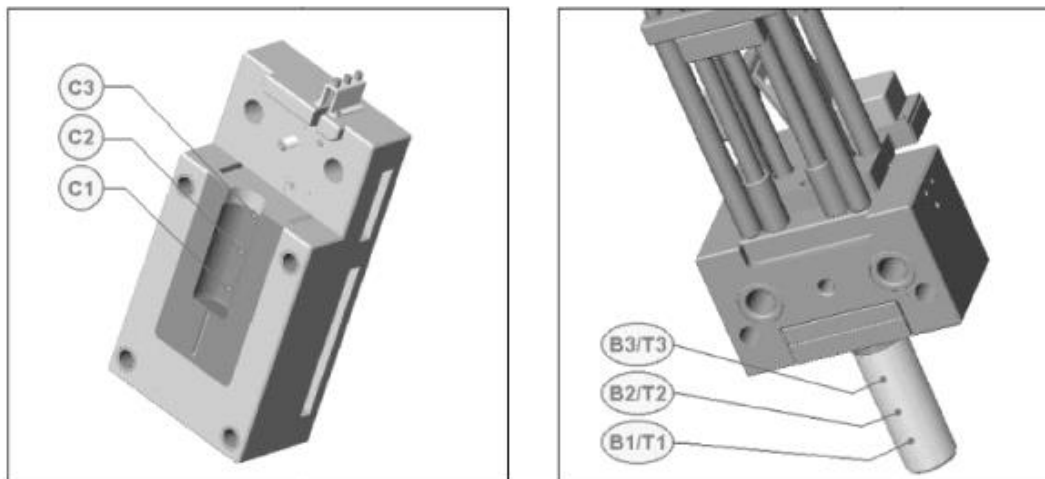


Figure 4.17 - Location of temperature and pressure sensors [173]

The data acquisition system consists of 3 sensors located in the cavity (Kistler 6157 BA 0.4) C1, C2 and C3 and 3 sensors for temperature and pressure located in the core (Kistler 6190 A 0.4) B1/T1, B2/T2 and B3/T3. The location of these sensors are at 25mm from the gate for the sensors # 1, 83 mm from the gate for the sensors # 2 and 143 mm from the gate for sensors # 3.

The ejection force evolution during the ejection was monitored with Kistler load cells (Kistler 9021 A) with range capacity of 0.01 N to 35 kN. The location of load cells in the ejector plate is indicated in the Figure 4.18 [173].

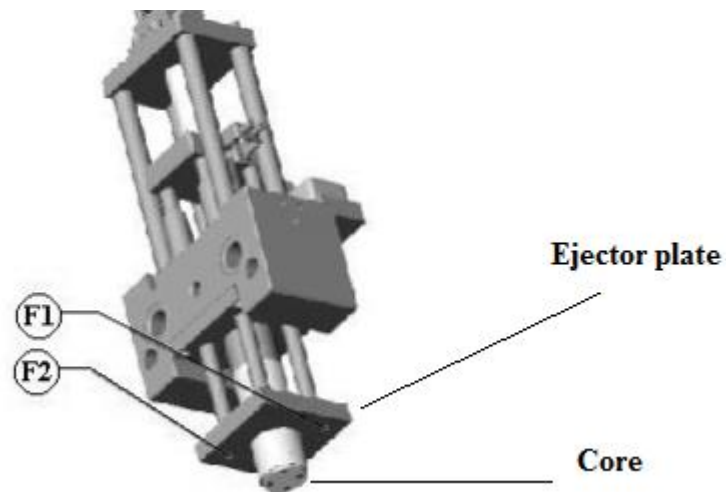


Figure 4.18 - Location of cell load sensors [173]

After acquisition, the data were worked with in spreadsheets to obtain the pressure, temperature and ejection force curves.

In the Figure 4.19, it is presented an ejection force curve to show how the ejection forces were obtained from the curve.

The total ejection force to extract the part from the mould was obtained adding F_1 and F_2 , as in the equation

$$F_e = F_1 + F_2$$

F_1 and F_2 being calculated from the acquired corresponding data.

The ejection forces data were calculated using the information from 10 injection moulding cycles by its average and respective standard deviation.

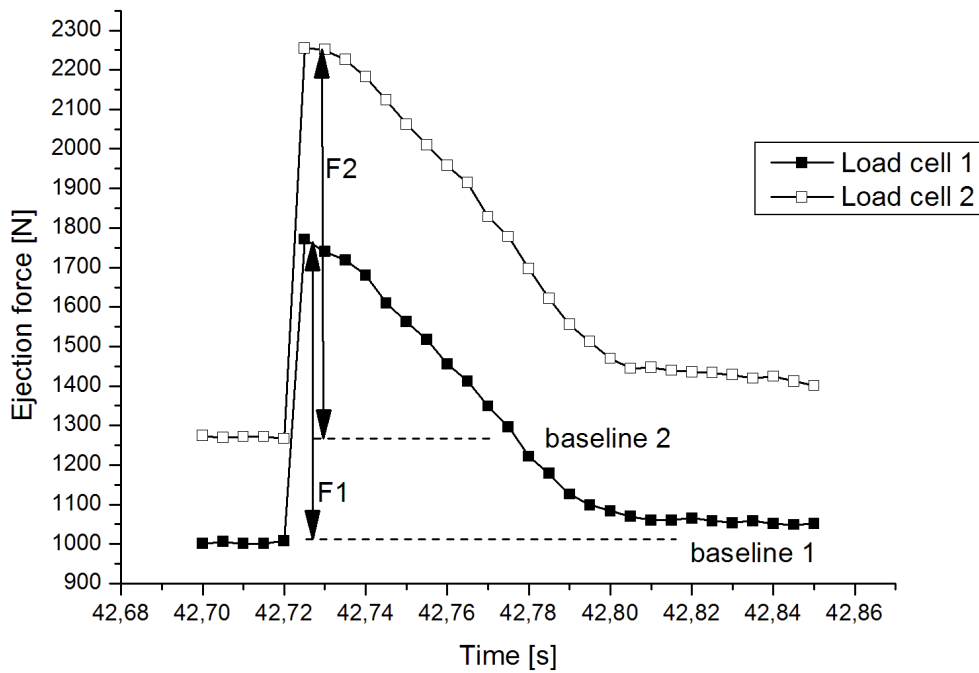


Figure 4.19 - Ejection force evolution for PP30% glass fibre and mould temperature of 75°C

4.2.3 Fibre Orientation Measurement

This process of fibre orientation measurement was described by Neves [139]. The objective of knowing the fibre orientation for assessing its influence on the shrinkage and the anisotropy of properties. The samples of the tubular parts measured 14mm x 7mm and were cut at 25 mm at 143 mm from the gate location, Figure 4.20. These locations were used as they correspond to where the pressure and temperature were measured. Two samples of each part were taken and in total 18 samples were prepared, 2 for each part and 3 for each moulding temperature. As mentioned, the material was injected using 3 different mould temperatures of 30°C, 50°C and 75°C.

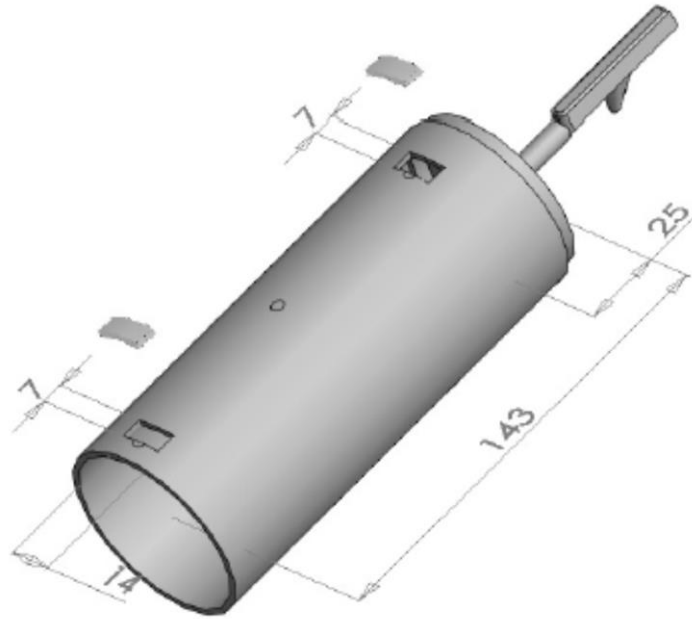


Figure 4.20 – Location of the samples for fibre orientation

The samples were cut using a saw, and mounted in a plastic mould and immersed in an epoxy resin. The cure took 8 hours to complete. Then the surface was polished in a polishing machine. This process uses various sandpaper, starting with the roughest sandpaper until the most refined sandpaper. Each sandpaper should be used until no trace is seen in the microscope. A ready sample is shown in the Figure 4.21.

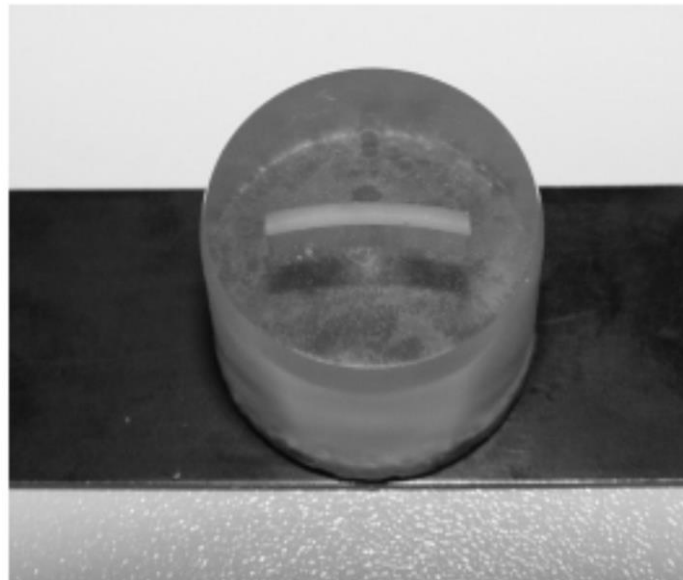


Figure 4.21 - Sample after polish operation

The surface was photographed in an Olympus Transmission Microscope with (objective resolution of 20x) and a Leica digital camera , the setup being shown in Figure 4.22.

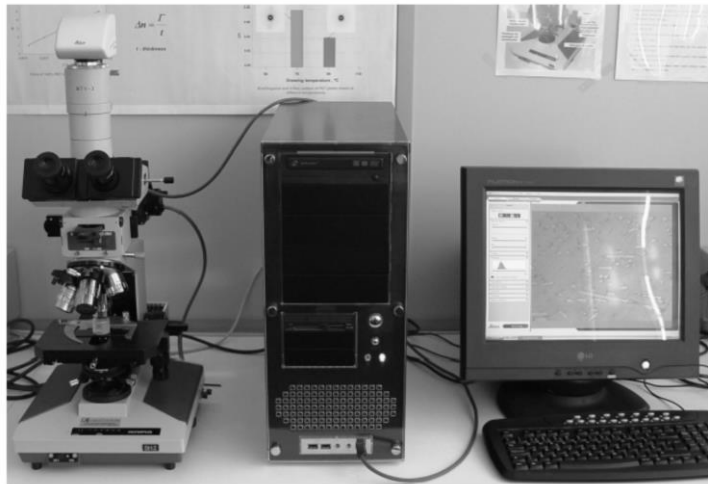


Figure 4.22 - Equipment used to acquire the pictures of samples

The Leica Qwin Pro Software was used to analyse the sample data. The pictures were taken in a dimension of 772 x 512 pixels and filed in bmp format. The number of photos taken was around 16 per sample.

All the pictures were analysed with the Ellipse Software for fibre measurement. This software gives the information about fibres, namely, dimensions, angle and relative position of fibre centre in the sample.

These data were worked on spreadsheets and the glass fibre orientation tensors were obtained and are shown in the chapter of results and discussion.

4.2.4 Measurement of shrinkage

The measurement of the dimensions allowing the calculation of the shrinkage was realized in the Tesa Micro-Hite 3D DCC CMM equipment, Figure 4.23. In this figure, the PP moulding were measured, it being possible to note the moment that the support and sensor set touch the moulding. This machine has an uncertainty of 3.5 μm according to the manufacturer. The equipment is controlled by joystick and a computational software PC-DMIS 4.2. This software enables to create and to execute programmes to measure various types of geometries.

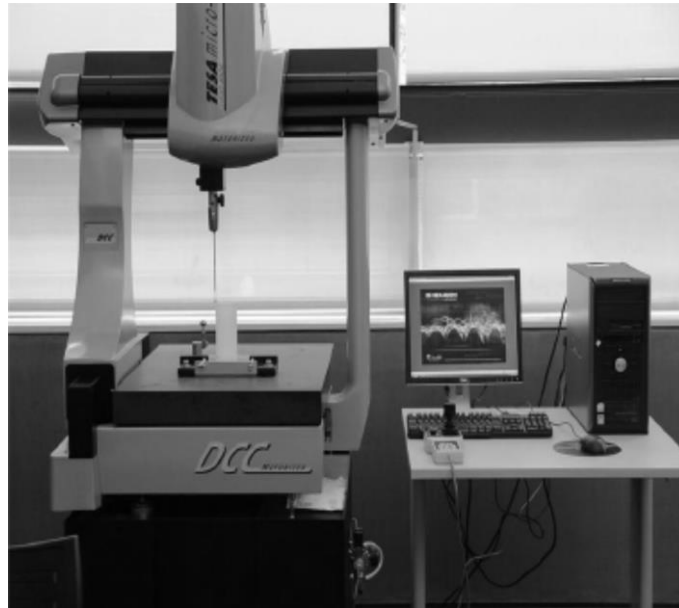


Figure 4.23 Tesa 3D CMM Equipment to measure the moulding dimensions

The software to measure the shrinkage was obtained by the creation of circle in the interior and in the exterior of the part in three different planes. These planes were in the position near from the gate, in the intermediate position in relation to the gate and far from the gate. The differences between the external and internal dimensions enable to evaluate the external diameter and internal diameter respectively. The length of the part was measured between two coordinates in the top of the part and the base of the tubular part. The shrinkage was calculated as the difference between the dimensions of the diameters of the mould and diameter measured by the machine. The results of the measurement for the neat PP are presented in the Table 4.15 and the other shrinkage data are in the appendix A2.

Table 4.15 - Shrinkage for PP - mould temperature 30°C

Measurement	Mould dimension [mm]	Sample 3		Sample 6		Sample 9		Average shrinkage among samples [%]
		Dimension [mm]	Shrinkage [%]	Dimension [mm]	Shrinkage [%]	Dimension [mm]	Shrinkage [%]	
Int. diameter (D3)	59,880	58,968	1,523	58,950	1,553	58,932	1,583	1,553
Int. diameter (D2)	58,830	57,898	1,584	57,894	1,591	57,884	1,608	1,594
Int. diameter (D1)	57,820	56,952	1,501	56,950	1,505	56,939	1,524	1,510
Ext. diameter (D3)	63,870	62,940	1,456	62,953	1,436	62,978	1,397	1,429
Ext. diameter (D2)	62,810	61,923	1,412	61,920	1,417	61,937	1,390	1,406
Ext. diameter (D1)	61,820	61,050	1,246	61,043	1,257	61,052	1,242	1,248
Height of part	146,000	144,503	1,025	144,480	1,041	144,481	1,040	1,036

4.3 Simulation of temperature field

The simulation software used in this work was Moldflow Plastics Insight 6.1. In the technical literature, there are many studies using Moldflow [64],[111],[202]–[204], showing the power of this computational tool. In this work, the aim of simulations was to compare its results with experimental data and also to help to explain possible reasons of disagreement among results and to obtain the temperature field during the injection moulding process.

4.3.1 Mesh

A 3D mesh of the tubular moulding is shown in Figure 4.24 and Figure 4.25. The 3D mesh of Moldflow uses full 3D Navier-Stokes equations, solves pressure, temperature and the three directional velocity components at each node. It also considers heat conduction in all directions and provides options to use inertia and gravity effects.

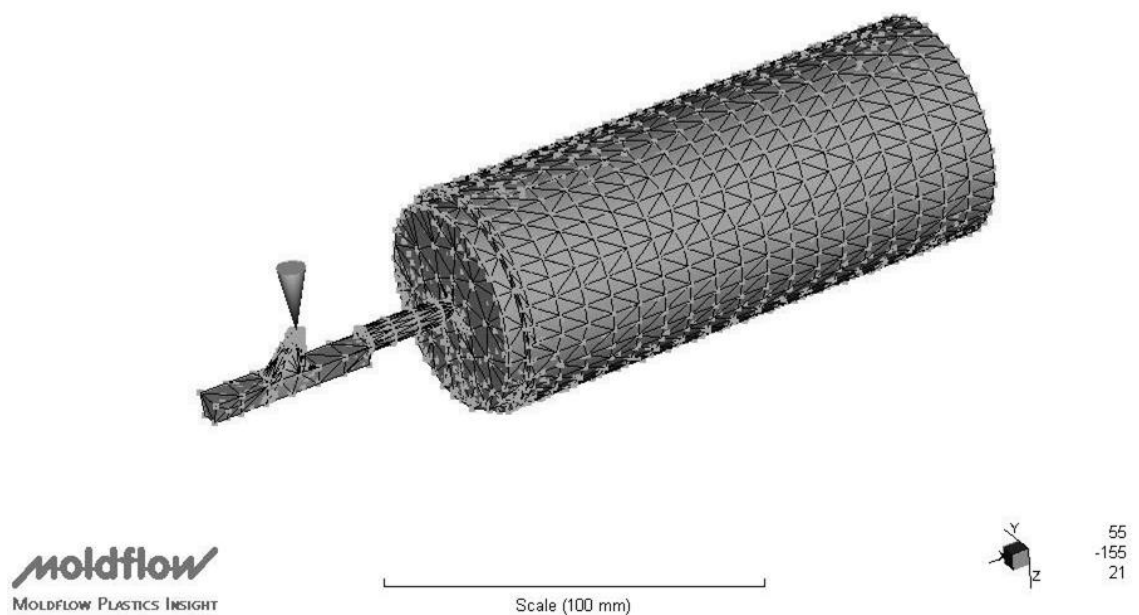


Figure 4.24 - 3D mesh from Moldflow

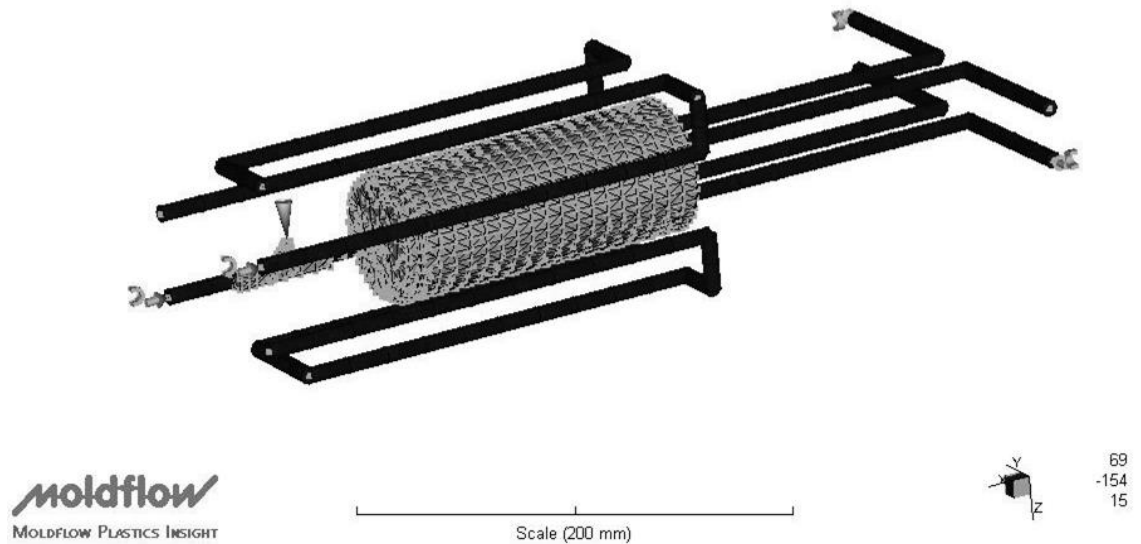


Figure 4.25 - Part and cooling system

The mesh has 10095 nodes, 186 beam elements and 54312 tetrahedral elements. The aspect ratio maximum is 97.7, average 28.25 and minimum 1.19.

4.3.2 Rheology description

The Cross Model was used to describe the viscosity of materials. The Cross can be represented by [205],[206]:

$$\eta = \frac{\eta_0}{1 + \left(\frac{\eta_0 \dot{\gamma}}{\tau^*}\right)^{1-n}} \quad (4.5)$$

where γ^* is the stress in which occurs the transition between the first Newtonian region and the Power Law region.

The Cross Model can still be changed to consider temperature effect, replacing η_0 for other function $\eta_0(T)$, according the equation below, where B and T_b are parameters obtained of the adjustment of this equation with the experimental measurements of η_0 in several temperatures:

$$\eta_0 = B \exp\left(\frac{T_b}{T}\right) \quad (4.6)$$

With this change, the modified Cross Model was obtained.

$$\eta = \frac{B \exp\left(\frac{T_b}{T}\right)}{1 + \left(\frac{\eta_0 \dot{\gamma}}{\tau^*}\right)^{1-n}} \quad (4.7)$$

In the Moldflow the Cross-WLF viscosity model uses the equation below for η_0

$$\eta_0 = D_1 \exp \left[\frac{-A_1(T-T^*)}{A_2+(T-T^*)} \right] \quad (4.8)$$

Where: η is the viscosity (Pa.s), $\dot{\gamma}$ is the shear rate (1/s), T is the temperature (K), $T^* = D_2 + D_3P$ where P is the pressure (Pa), $A_2 = A_2\sim + D_3P$ (K) and $n, \tau^*, D_1, D_2, D_3, A_1, A_2\sim$ are data-fitted coefficients.

The Cross-WLF model provides a good physical representation of the data. τ^* is related to the relaxation time of the material, D_2 is related to the glass transition temperature, T_g (Moldflow 6.1).

The materials used in the simulations of Moldflow were MOPLEN HP501L (Bassel Polyolefins Europe) for PP without reinforcement, PX0056: Borealis OPP SA for PP with 10% of glass fibre and GC30P100-01:Rhetec for 30% of glass fibre. The Table 4.16 shows the parameters for Cross-WLF model.

Table 4.16 - Parameters for the Cross-WLF model (Moldflow 6.1)

Parameter	MOPLEN HP501L	PX0056	GC30P100-01	Unit
N	0.2734	0.2903	0.2634	
τ	22027.2	32340	44578	Pa
D_1	2.60213×10^{15}	3.41877×10^{11}	1.22×10^{13}	Pa.s
D_2	263.15	263.15	263.15	K
D_3	0	0	0	K/Pa
A_1	33.714	24.334	27.952	
$A_2\sim$	51.6	51.6	51.6	K

4.3.3 PVT description

The Tait equation is generally used in CAE packages to model the polymer behaviour during melt processing [68],[206]. For the Tait equation and a set of constants, any volume of a polymer can be determined by knowing the temperature and pressure.

The parameters for Tait equation used in the Moldflow are shown in the Table 4.17.

Table 4.17 - Parameters of the modified Tait equation

Parameter	MOPLEN HP501L	PX0056	GC30P100-01	Unit
b5	452.15	446.15	449.15	K
b6	4.651×10^8	3.351×10^8	4×10^8	K/Pa
b1m	0.001318	0.001132	0.0009777	m^3/kg
b2m	9.481×10^7	8.001×10^7	4.499×10^7	m^3/kgK
b3m	7.112×10^7	8.347×10^7	1.55682×10^8	Pa
b4m	0.004308	0.004811	0.004428	1/K
b1s	0.001199	0.001049	0.0009473	m^3/kg
b2s	6.24×10^7	4.369×10^7	3.849×10^7	m^3/kgK
b3s	1.024×10^8	1.174×10^8	1.65415×10^8	Pa
b4s	0.008427	0.004983	0.006316	1/K
b7	0.0001184	8.325×10^{-5}	3.041×10^{-5}	m^3/kg
b8	0.1182	0.2257	0.118	1/K
b9	7.328×10^9	9.596×10^9	6.921×10^9	1/Pa

4.3.4 The SciLAB software

The SciLab – **Scientific Laboratory** – is a software to solve numerical calculus. It is a high performance tool used in complex situations by interaction or through programming. The SciLab belongs to a group of softwares that simulates environment of numerical computation, such as MatLab, Octave, Maple, Simulink, MuPAD, etc. Among these, the best known is the MatLab (Matrix Laboratory). The MatLab is a commercial software and SciLab is open source and free [207].

The SciLab is a product created and maintained by a consortium of companies formed in 2003 by INRIA (the french National Institute for Research in Computer Science and Control), The SciLab Consortium had joined the Digiteo Foundation in July 2008 [208]. It can be used in Windows or Linux and others environments, for several areas: engineering, petrochemical, meteorology, automotive industry, etc [209].

This work uses SciLab to implement the mathematical model to predict shrinkage and ejection forces in tubular parts in injection moulding. The model was already described in chapter 3.

5 Results and Discussion

5.1 Injection moulding

5.1.1 Moulding pressure

Through the pressure curves it is possible to explore data such as the extent of the filling, the holding and cooling development and also information about flow rate.

For each processing condition ten mouldings were analysed. After evaluation, it was checked the representative curve the entire experiment.

The Figure 5.1 shows the evolution of pressure in the impression for the tubular part. In this figure, the pressure curves in three locations along the part, near the gate (C1), in intermediate location (C2) and far from the gate (C3) are shown. The pressure curve is divided in regions I and II, the region I representing the injection phase and region II representing the holding phase.

The pressure evolution in the impression depends on many parameters. The most important parameters in its evolution are the injection velocity and the melt temperature [7].

The mould temperature has only a slight influence on the pressure evolution in the filling phase, because of the fast cooling rates, but there is a strong influence on the pressure evolution during the holding phase, because the wall temperature influences the cooling behaviour [210].

The most important aspect of the holding pressure phase is the addition of melt in the impression to compensate the effect of the thermal contraction of the melt during cooling. In the Figure 5.1 it is shown a peak in the pressure due to the late switchover.

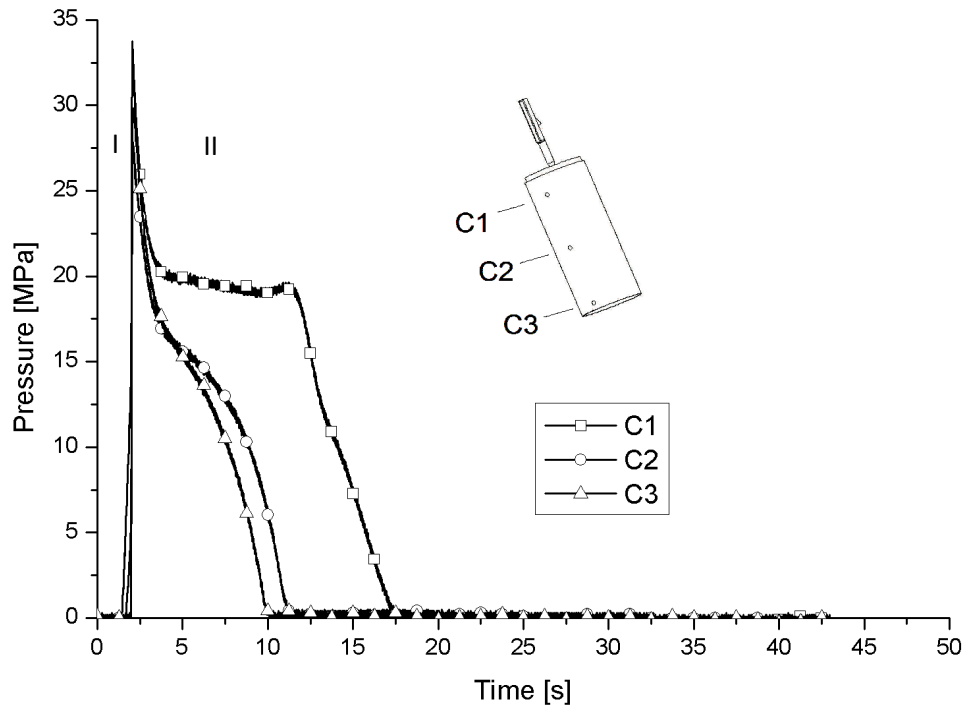


Figure 5.1 - Pressure evolution during an injection cycle of neat PP with mould temperature of 30°C

In the Figure 5.2, it is possible to observe the influence of mould temperature in the pressure evolution inside de cavity. Due to the higher mould temperature the melt polymer has more time to cool and consequently the holding phase is longer.

The maximum injection pressure was observed for the mould temperature of 75°C due to the lower pressure drop during the filling phase.

The results in Figure 5.3 show the influence of the glass fibre content in the pressure evolution for different amounts of reinforcement at mould temperature of 75°C. It is possible to note that for the higher glass fibre content the pressure drop is faster. This is due to the faster cooling rate and higher pressure drop of the PP with higher content of glass fibres.

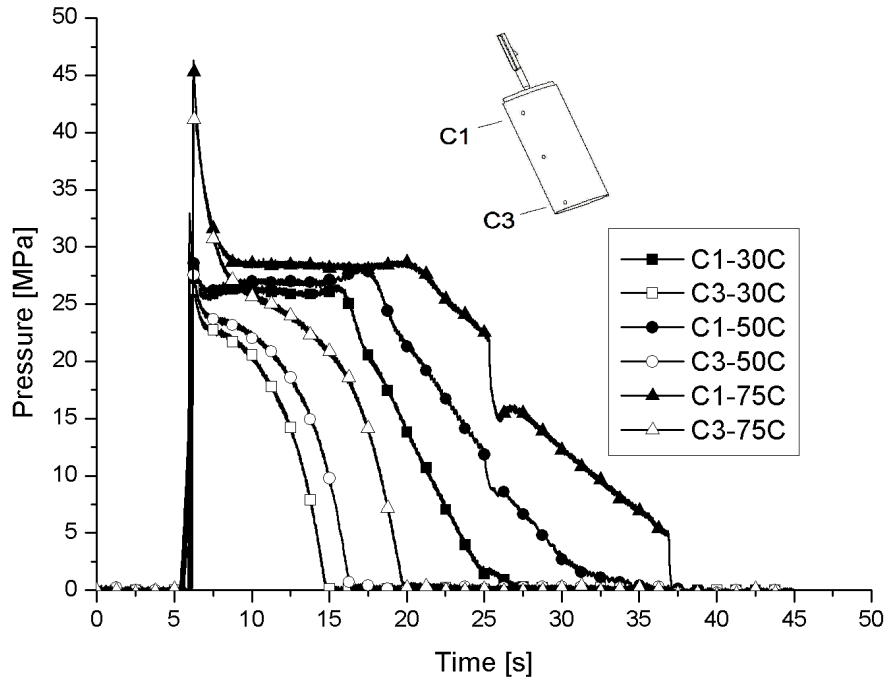


Figure 5.2 - Influence of the mould temperature in the pressure evolution for PP – Domolen 1100L

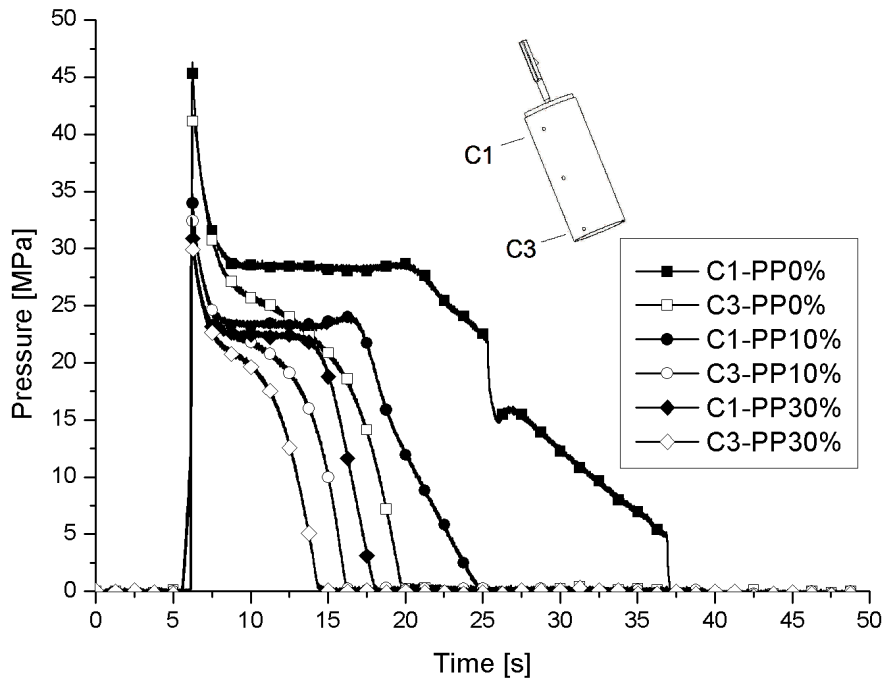


Figure 5.3 - Influence of glass fibre content in the cavity pressure evolution at mould temperature of 75°C

In the Figure 5.4 where the influence of nanoclay content is observed, the percentage of nanoclay used does not influence the pressure evolution.

It is also important to point out that the pressure evolution is similar to the pressure evolution observed with PP without reinforcements. This observation confirms that the nanoclay does not change the flow behaviour of the material when small percentage of nanoclay is added.

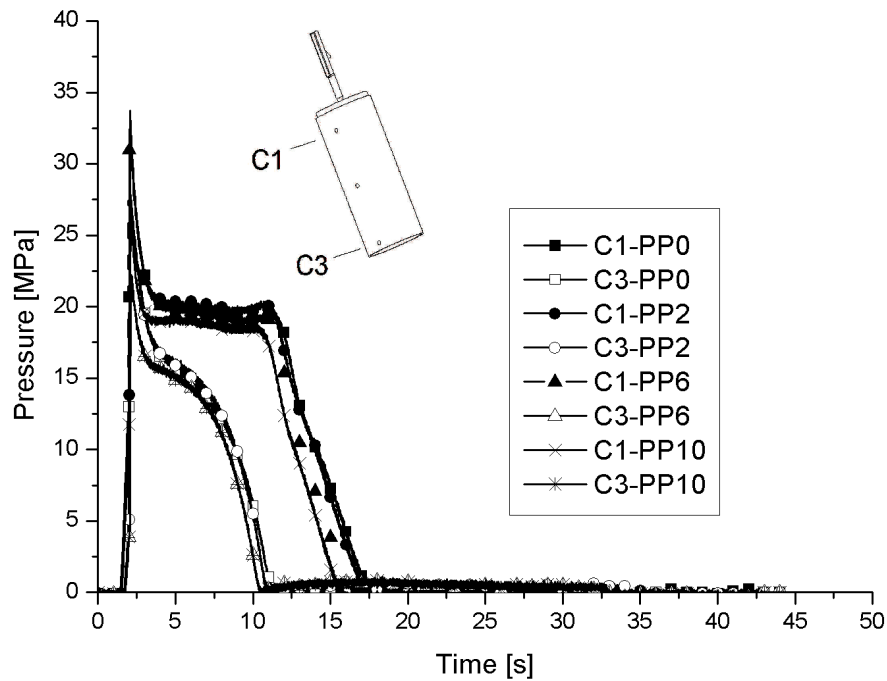


Figure 5.4 - Influence of nanoclay content in the pressure evolution at mould temperature of 50°C

In the Figure 5.5 is shown the effect of nanoclay on the pressure evolution of reinforced PP with 10% and 30% of glass fibre. It can be seen that the small incorporation of nanoclay (2%) does not affect the pressure evolution, and also flow behaviour of the reinforced PP.

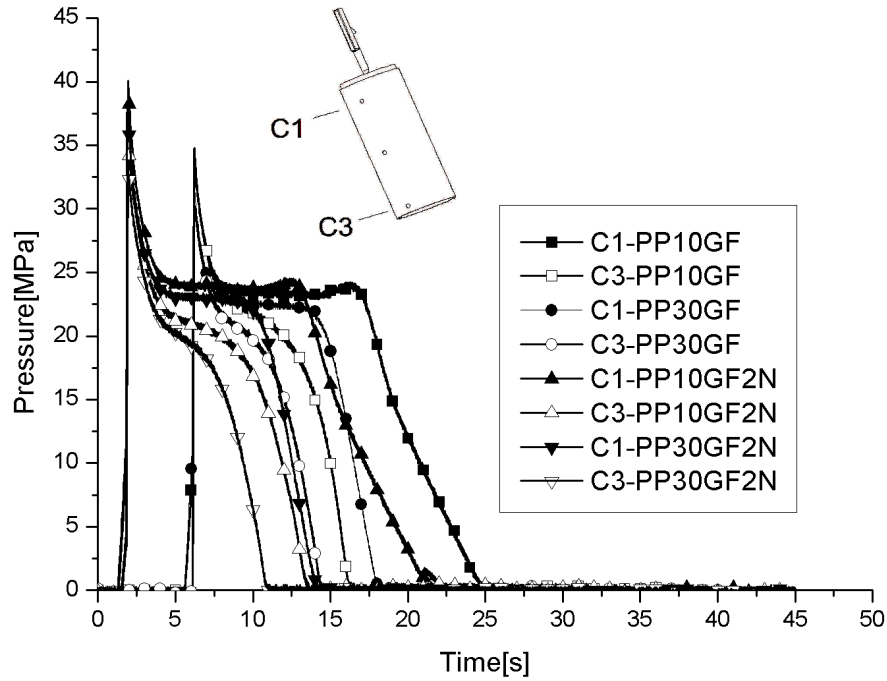


Figure 5.5 - Influence of nanoclay on the pressure evolution of reinforcement PP of mould temperature of 75°C

5.1.2 Temperature evolution

In the Figure 5.6 it is shown the evolution of temperature along the time for PP with 2% of nanoclay in the three used mould temperatures, 30°C, 50°C and 75°C. As it can be noted the evolution of temperatures are accordance with the mould temperature impose on the thermoregulator. This temperature evolution was used to validate the simulation temperature evolution using the Moldflow software. As mentioned previously the predicted temperature gradient was used in the predictions of shrinkage and ejection forces.

The small peak of the temperature observed in all curves around 35 s is due to the ejection of the part.

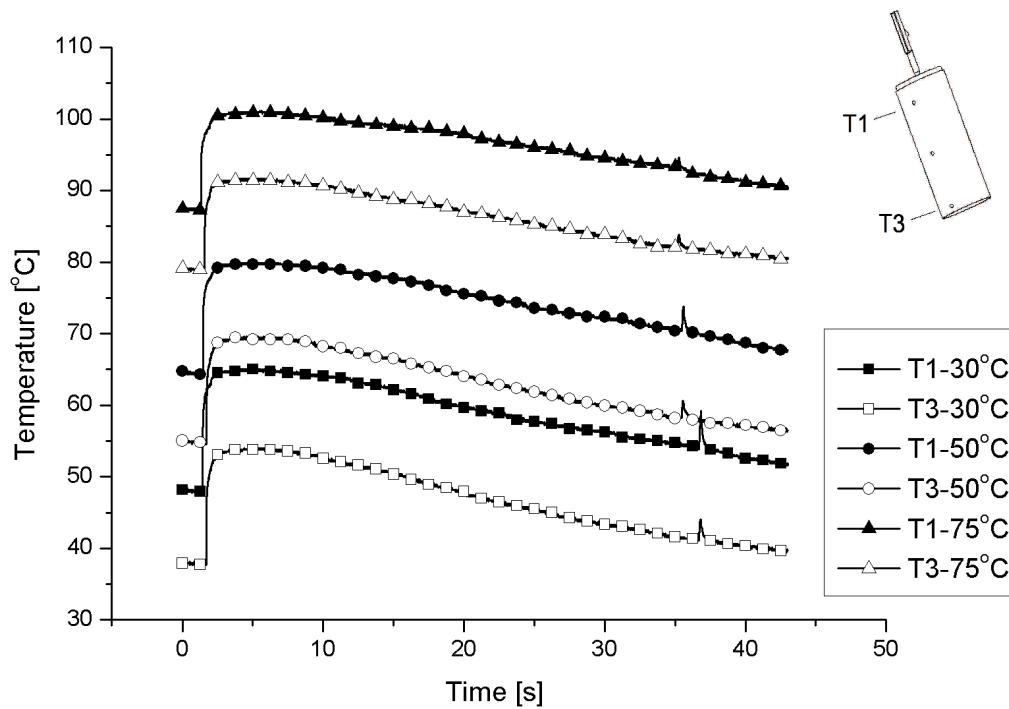


Figure 5.6 - Evolution of temperature along of the injection cycle for PP with 2% of nanoclay different mould temperatures

5.2 Shrinkage

In this section, it is made the discussion of the experimental results for the shrinkage along the flow path, in relation to the mould temperatures and level of reinforcement. These results are presented in relation to the diametrical shrinkage and thickness shrinkage. All the results of shrinkage calculations are shown in the appendix A2.

5.2.1 Variation along the flow path

In the Figure 5.7 and Figure 5.8, they are shown the results of the calculated diametrical shrinkage for PP without reinforcement for low and high mould temperatures. It can be seen a slight increase of diametrical shrinkage along the flow path, and the increase of internal diametrical shrinkage is more pronounced than the external diametrical shrinkage. This occurs due to the expansion on the thickness direction after ejection.

In these graphics, it can also be noted that there is a plateau after the intermediate region of the tubular parts.

Near the gate, the shrinkage is lower because the effect of holding pressure is more effective and consequently the compression of the part is higher far away from the gate, the values of the shrinkage, internal and external, tends to be closer.

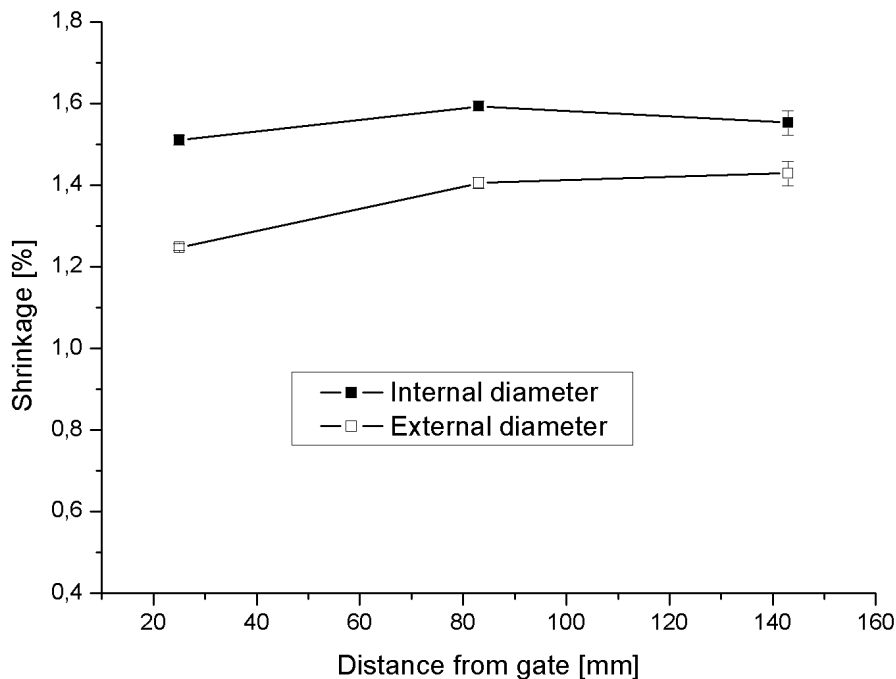


Figure 5.7 - As-moulded diametrical shrinkage at different position along the flow path for PP tubes with mould temperature of 30°C

The effect of mould temperature on the diametrical shrinkage is also shown in Figure 5.7 and 5.8. The increase of the mould temperature increases the diametrical shrinkage. This behaviour is due to higher temperature of the part at ejection when is used the higher temperature of the mould

In the Figure 5.9 it is represented the behaviour of shrinkage along the flow path with the mould temperature at 50°C for PP with different percentage of nanoclay.

As it can be seen the shrinkage of the internal diameter is also higher than external diameter as observed for unreinforced PP. This behaviour is due to the expansion after ejection, which decreases the internal diameter and increases the external diameter.

The higher shrinkage occurs far away from the gate in the external diametrical shrinkage. The material with nanoclays has almost the same results as pure PP.

Also can be seen that, when is added nanoclays as reinforcement, there is a reduction in the shrinkage as expected, due to the constraint effect of the reinforcements.

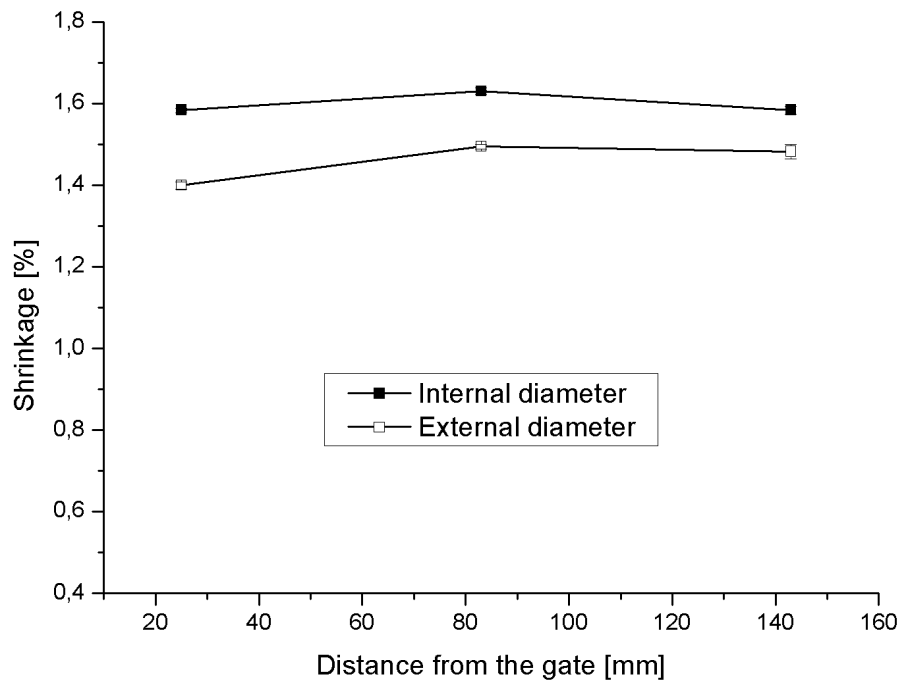


Figure 5.8 - As-moulded diametrical shrinkage at different position along the flow path for PP tubes with mould temperature of 75°C

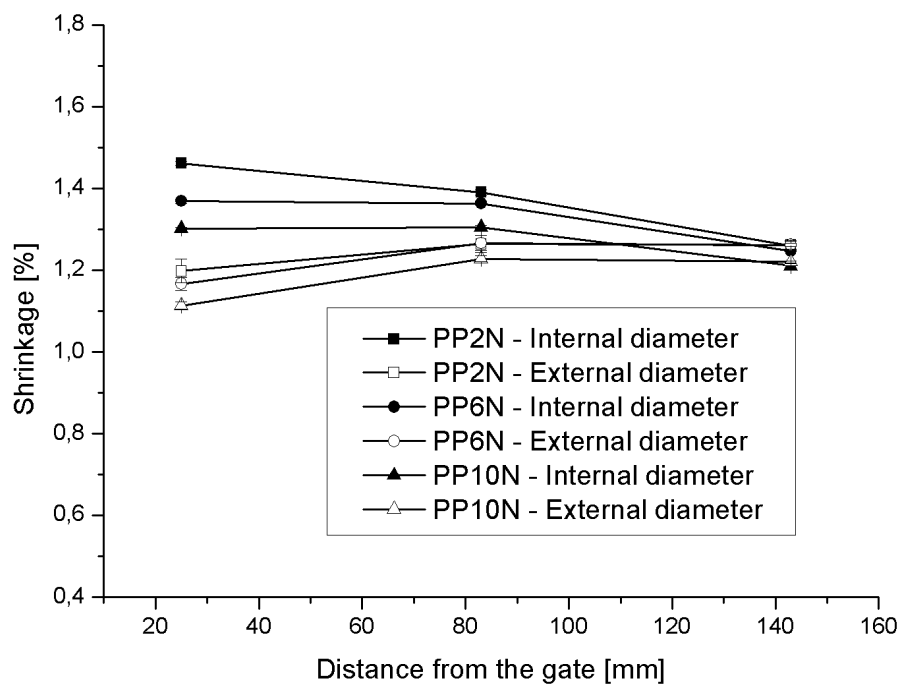


Figure 5.9 - As-moulded diametrical shrinkage for different position along the flow path for PP tubes with different contents of nanoclay

In the Figure 5.10 it is presented the effect of glass fibre on the as-moulded diametrical shrinkage along the flow path. As it can be seen the diametrical shrinkage decreases with the increase of glass fibre content. The shrinkage is higher near the gate and at intermediate region of the part. This apparent non sense is due to the fibre orientation pattern that changes with the flow path. It is possible to find that the a_{22} tensor is higher the region far away the gate, which constrains the diametrical shrinkage.

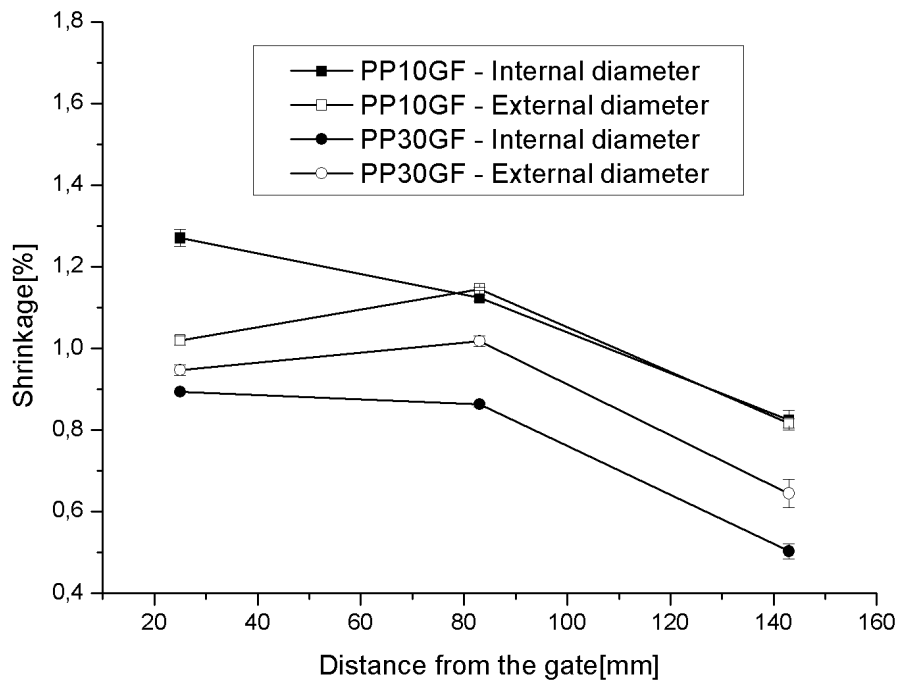


Figure 5.10 – As-moulded diametrical shrinkage along the flow path for PP tubes with 10% and 30% of glass fibres

5.2.2 Thickness shrinkage

The data summarized in Figure 5.11 and Figure 5.12 for the thickness shrinkage along the flow path correspond to PP without reinforcement and PP with 6% of nanoclay. The shrinkage is higher and positive far away from the gate it and near the gate is observed to have negative value (expansion). This behaviour is due to the fact that near the gate the material is over packed and when the mould opens the part expands. Afterwards, the part shrinks but not enough to compensate the previous expansion. The shrinkage is not significantly affected by the nanoclay addition.

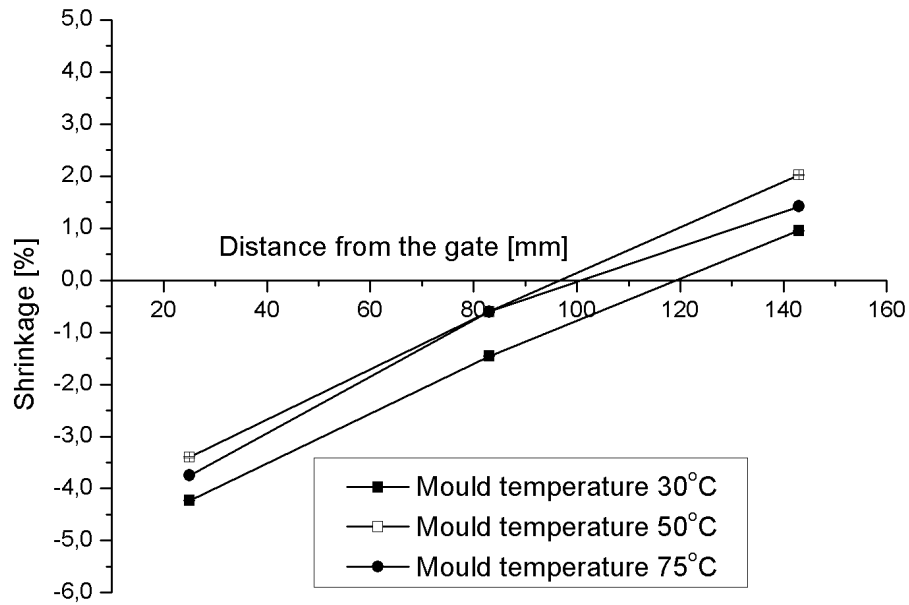


Figure 5.11 - Thickness shrinkage for PP without reinforcement

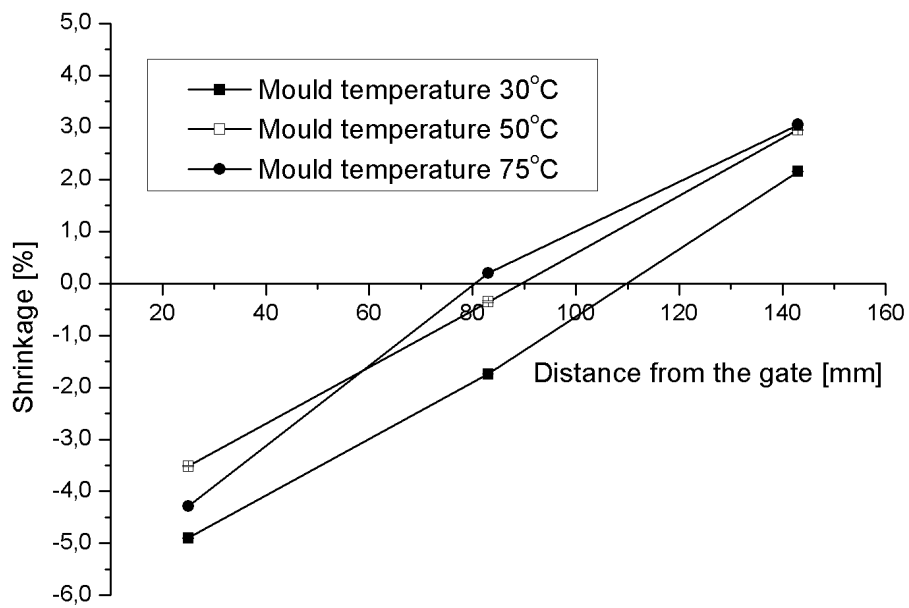


Figure 5.12 - Thickness shrinkage for PP with 6% of nanoclay

In Figure 5.13 and Figure 5.14 the results for glass fibre with 10% and 30%, respectively, are presented.

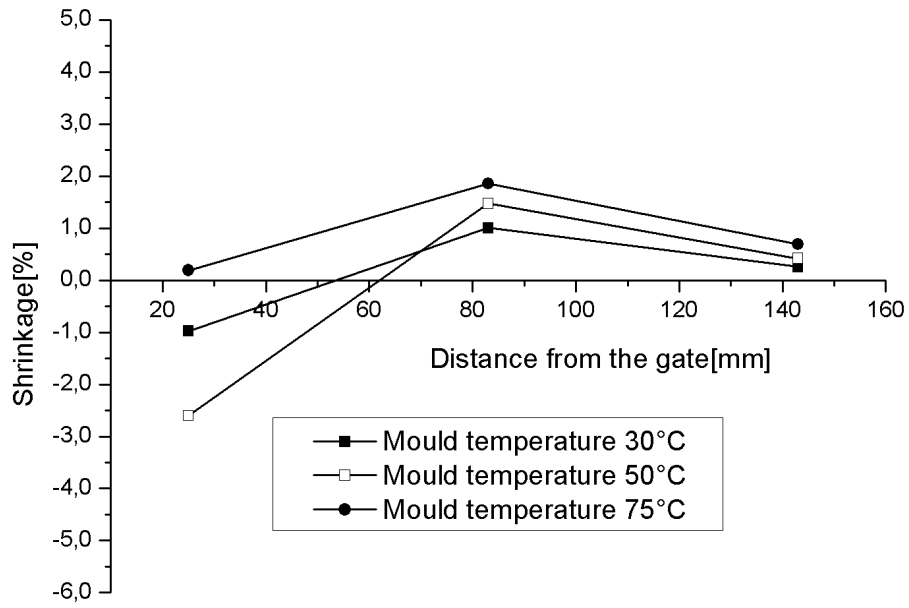


Figure 5.13 - Thickness shrinkage for PP with 10% of glass fibre

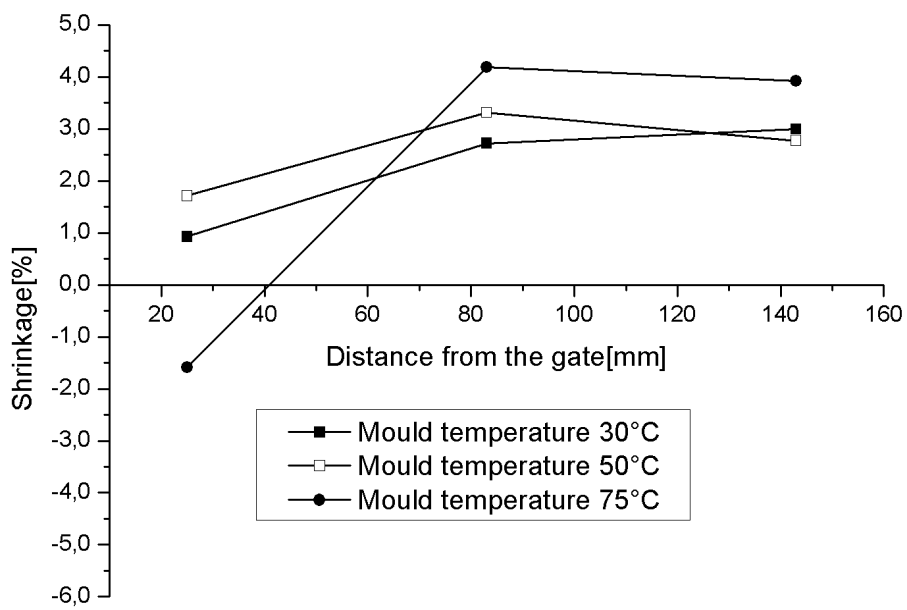


Figure 5.14 - Thickness shrinkage for PP with 30% of glass fibre

5.2.3 Effect of the mould temperature

In the Figure 5.15 and Figure 5.16 are presented the results of shrinkage in the position far from the gate in the flow path. As it can be seen when the mould temperature increases the shrinkage also increases. This behaviour is due to the fact that when the moulding is ejected at higher temperature the material has more time to shrink. It is also possible to note that the reinforced materials present shrink less than PP. In these figures the effect of the combination of nanoclays with glass fibre PP can also be observed. The presence of nanoclays decreases the shrinkage.

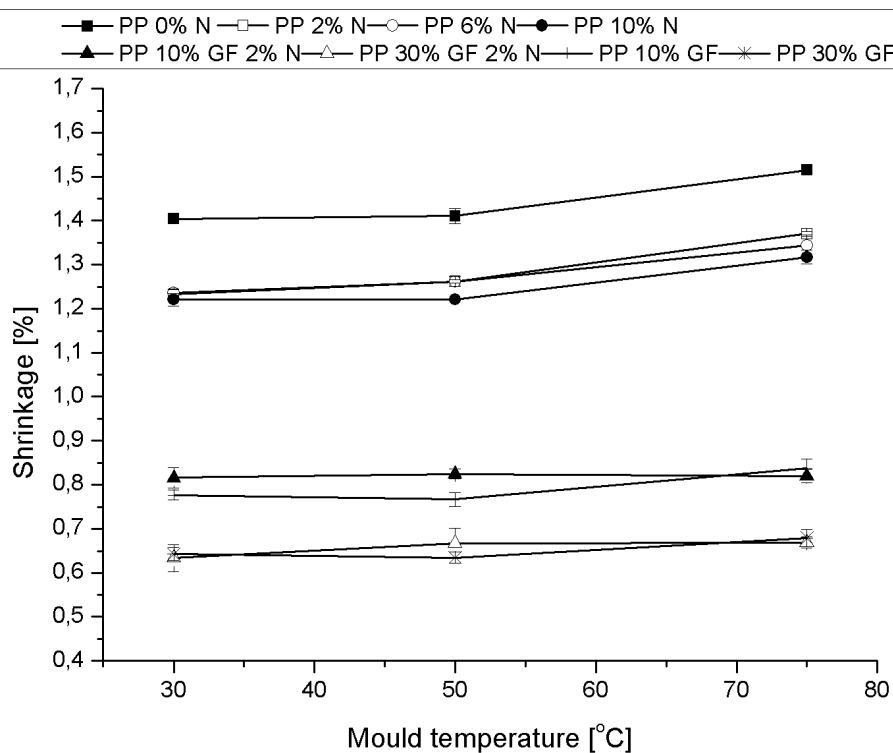


Figure 5.15 - Shrinkage of the external diameter of different mould temperatures

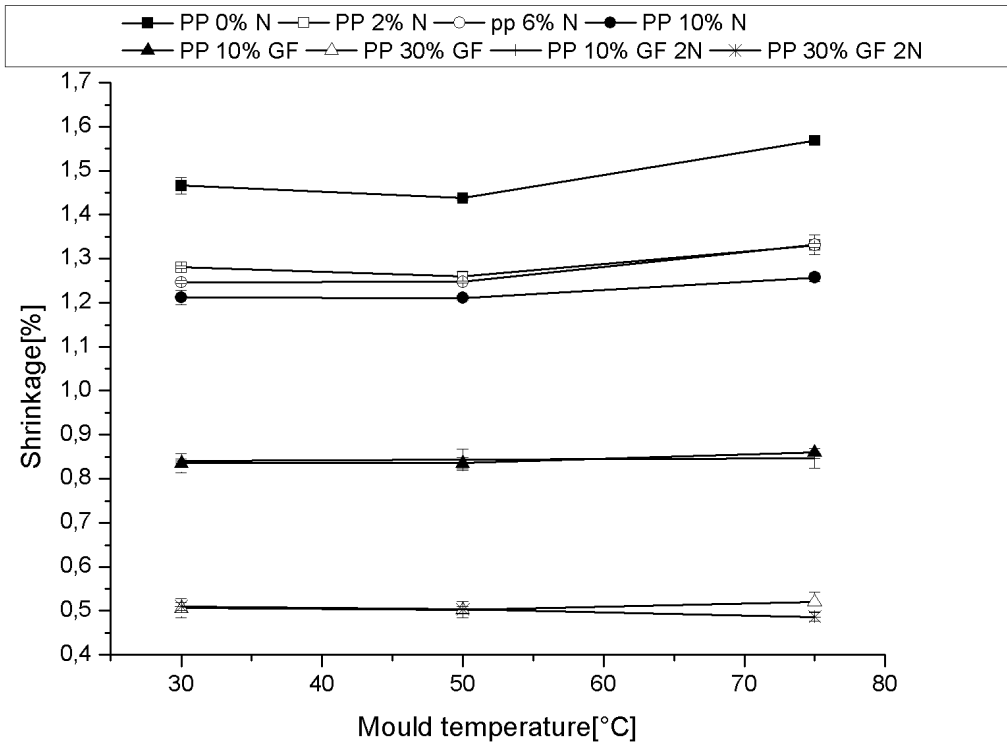


Figure 5.16 - Shrinkage of the internal diameter with various mould temperatures

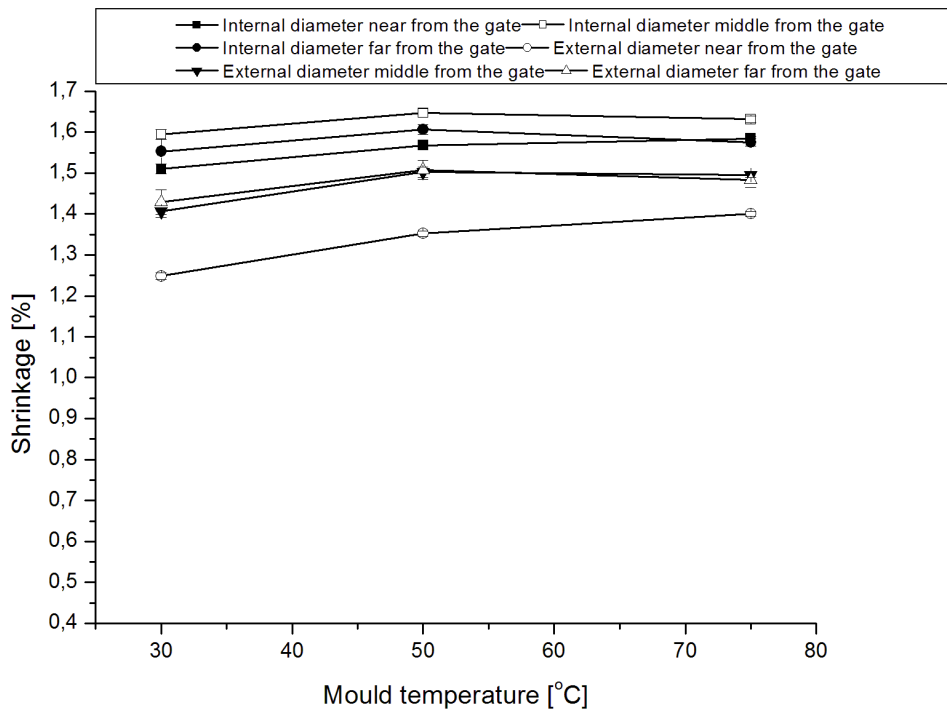


Figure 5.17 - Shrinkage dependence of the mould temperature for PP without reinforcement in several positions along the flow path

5.2.4 Effect of the content of glass fibre

The thermal expansion coefficient of the glass fibre is a key factor in mould shrinkage owing to possessing higher magnitude than matrix thermal expansion coefficient, Figure 5.18 and Figure 5.19. Thus, as far as glass fibre content is elevated, the shrinkage would decrease. In relation to the mould temperature effect, it was explained in the previous section 5.2.3.

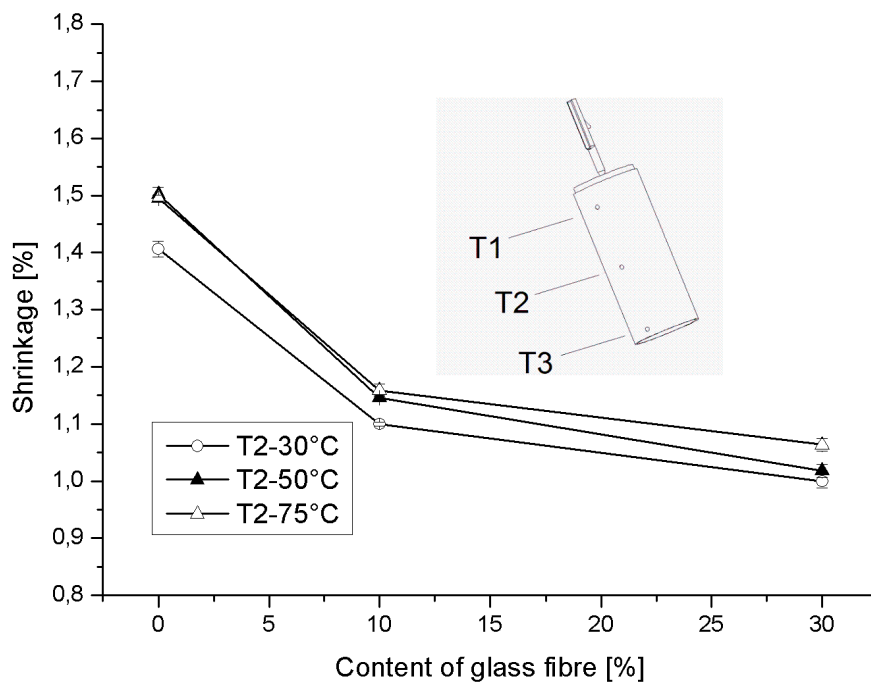


Figure 5.18 – Shrinkage of external diameter at the position T2 for different glass fibre content and different mould temperatures

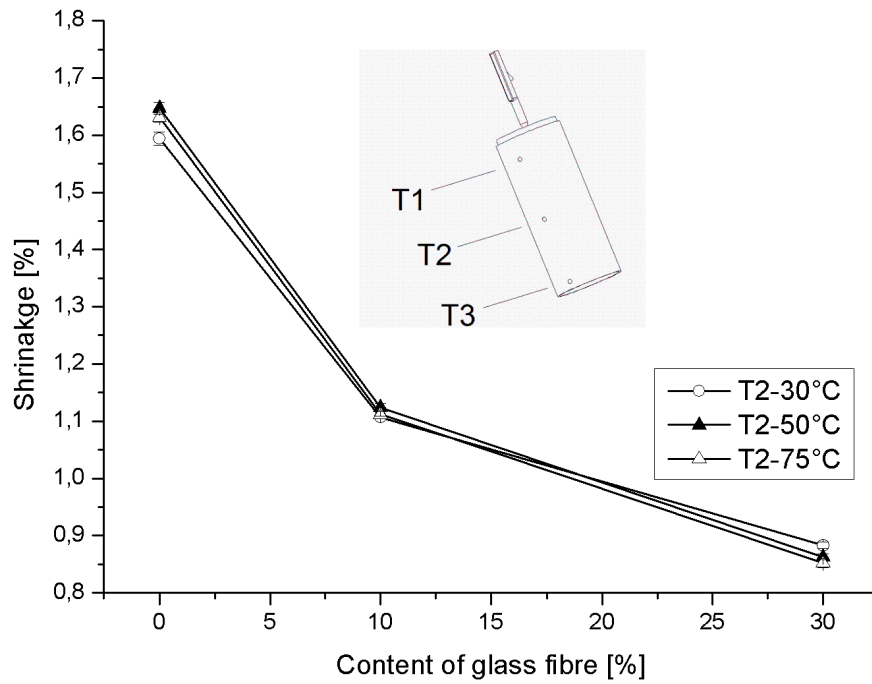


Figure 5.19 – Shrinkage of internal diameter at position T2 for different glass fibre content for different mould temperatures

5.2.5 Effect of content of nanoclays

In the Figure 5.20 and Figure 5.21, it is presented the internal and external shrinkage diameter, respectively, at position T2 with different mould temperatures. As it can be seen the shrinkage decreases with the nanoclay content. This behaviour is due to the constraining effect of the nanoclays and the lower thermal expansion coefficient.

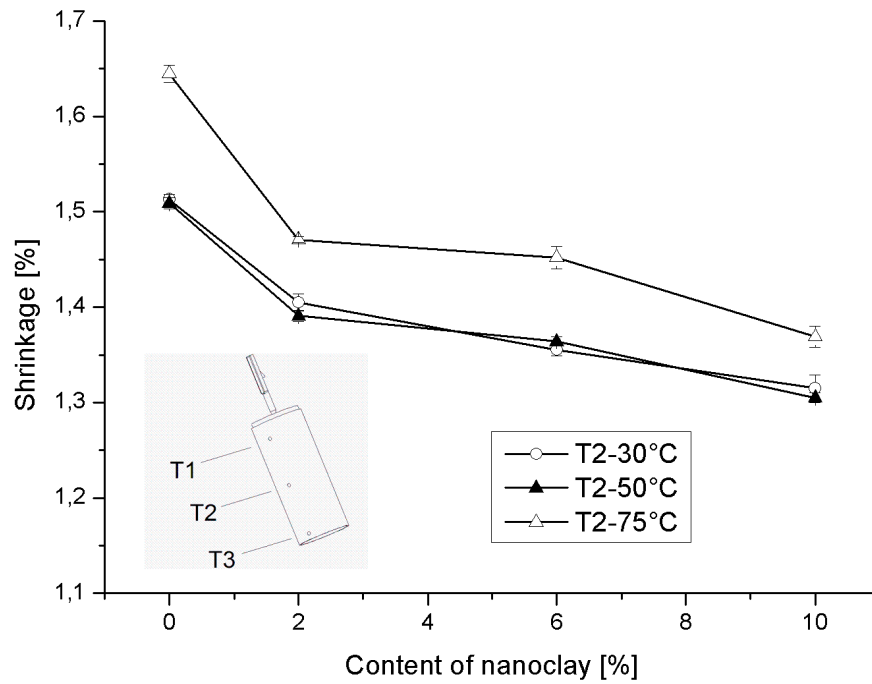


Figure 5.20 – Internal diameter at position T2 for different content of nanoclays at different mould temperatures

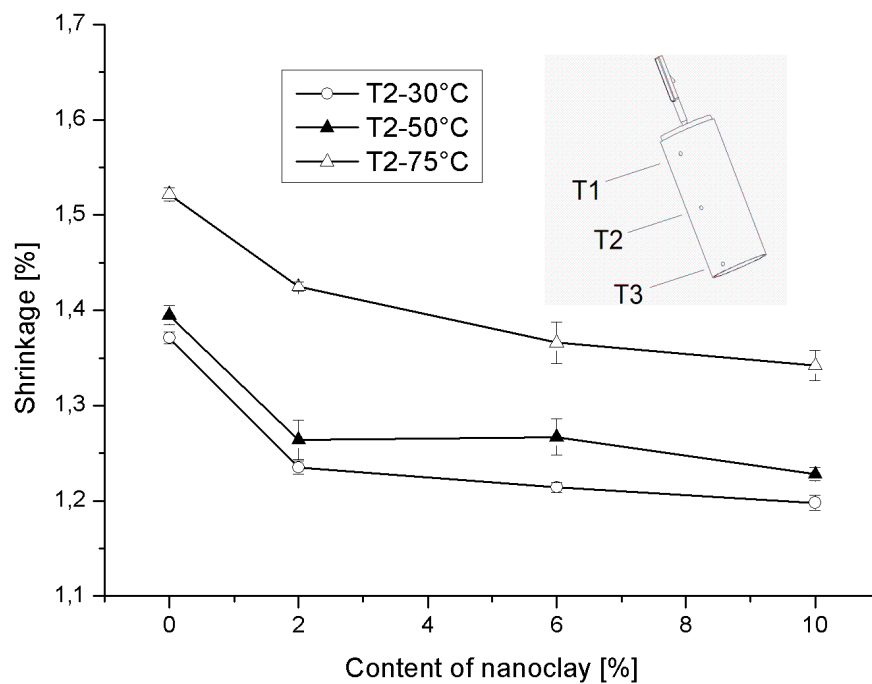


Figure 5.21 – External shrinkage diameter of position T2 for different content of nanoclays at different mould temperatures

5.3 Ejection force

It can be observed in the Figure 5.22 and Figure 5.23 that the ejection force decreases with the increase of mould temperature. The ejection force also increases with the increase of the glass fibres content, due to the higher elastic modulus. In contrary the nanoclays decrease the ejection force when compared with glass fibres and pure PP. When nanoclays are added to PP with glass fibre the ejection forces decreases slightly in comparison with the ejection forces of the mouldings produced with the material without nanoclays. This behaviour is in agreement with the nanoclays reducing the shrinkage and also the coefficient of friction and consequently reduce the ejection force.

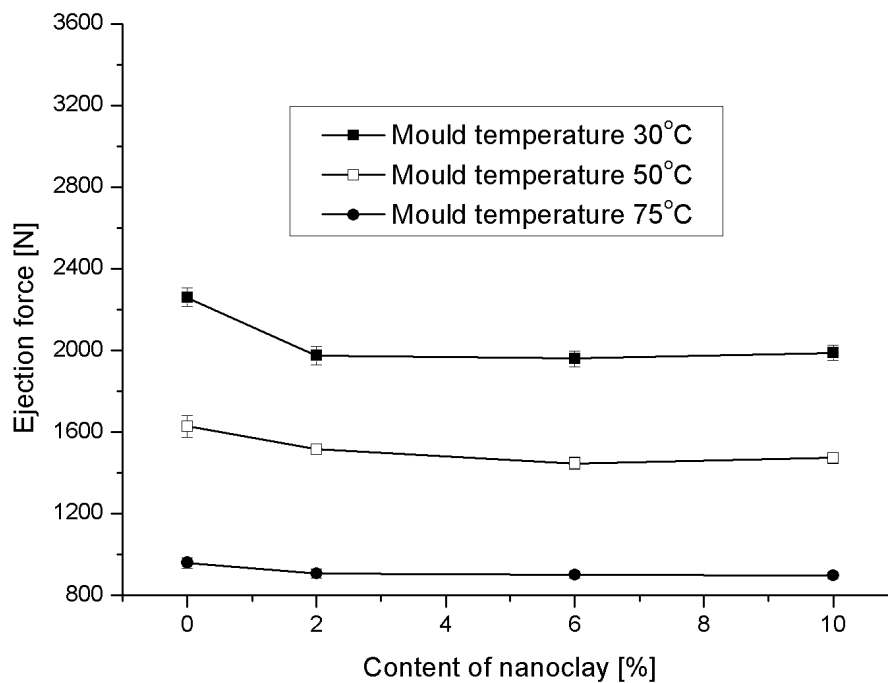


Figure 5.22 - Ejection forces in relation to content of nanoclays for mould temperatures of 30°C, 50°C and 75°C

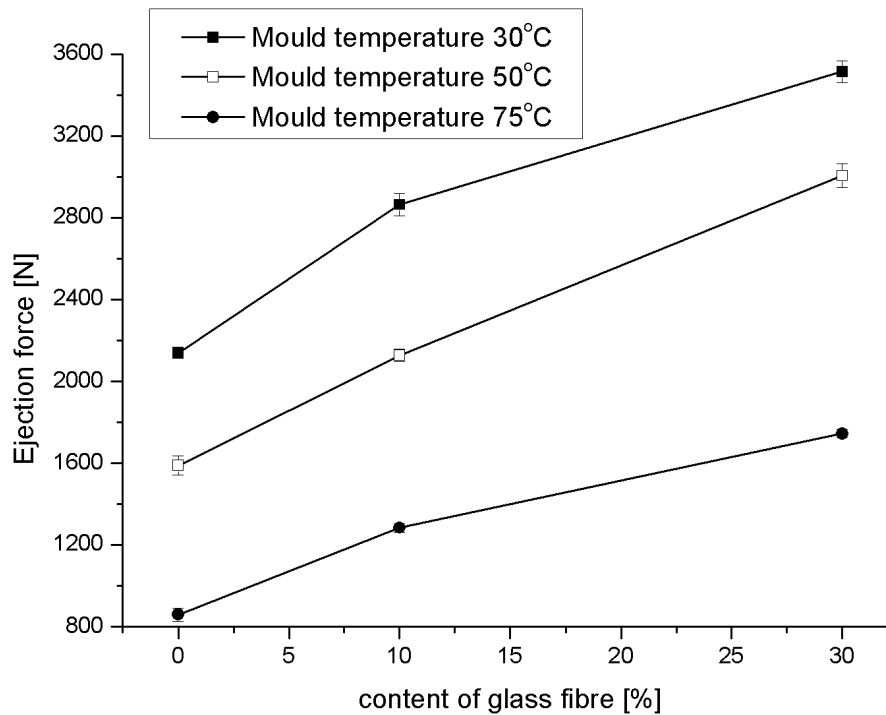


Figure 5.23 - Ejection forces in relation to content of glass fibre for mould temperatures of 30°C, 50°C and 75°C

5.4 Fibre Orientation Measurement data

According to the procedure described in the previous chapter, the orientations of fibres were obtained. Considering the measurement data, the tensors a_{11} , a_{22} and a_{33} represent the orientation of fibres along the thickness of the part. The tensor a_{11} describes the orientation in the direction of flow, the tensor a_{22} shows the orientation in the transversal direction of the flow and the tensor a_{33} represents the orientation in the thickness direction of the part.

In the Figure 5.24 and Figure 5.25 are presented the results for PP with 10% of glass fibre at the mould temperature of 50°C, in the position near to the gate and far away from the gate, respectively. In the Figure 5.26 and Figure 5.27 is present the tensors for PP with 30% of glass fibre.

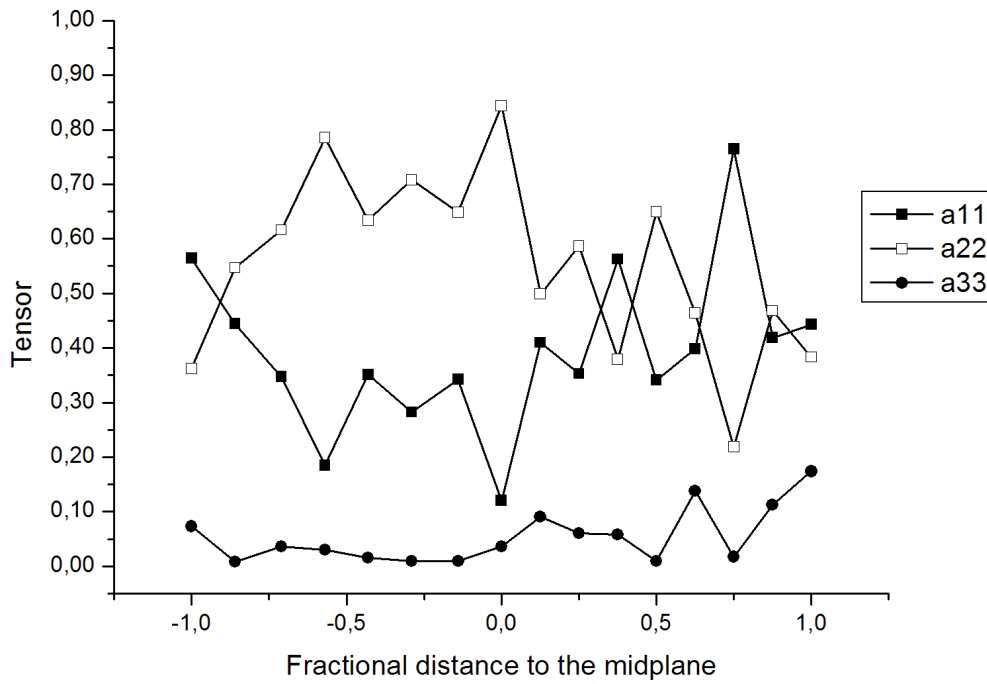


Figure 5.24 - Tensors for PP with 10% of glass fibre for mould temperature of 50°C near from the gate

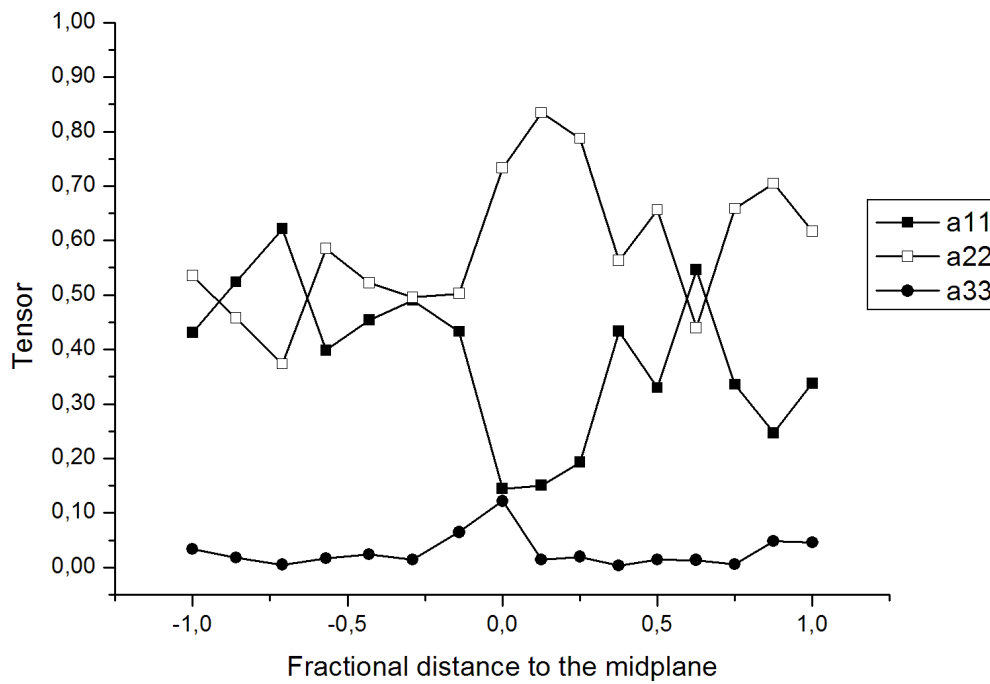


Figure 5.25 - Tensors for PP with 10% of glass fibre for mould temperature of 50°C far from the gate

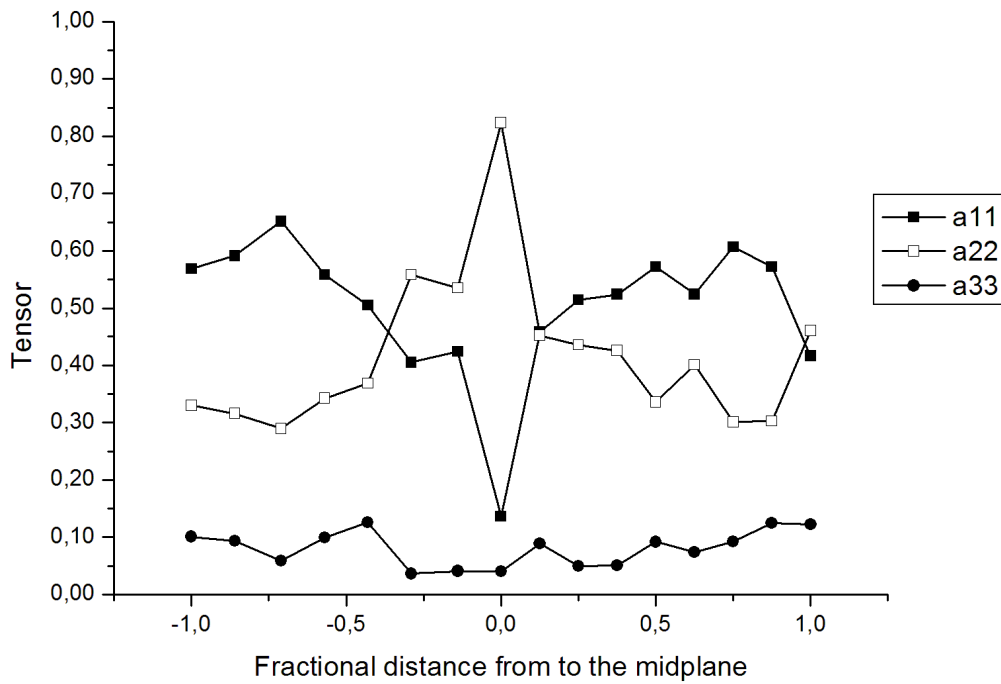


Figure 5.26 - Tensors for PP with 30% of glass fibre for mould temperature of 50°C near from the gate

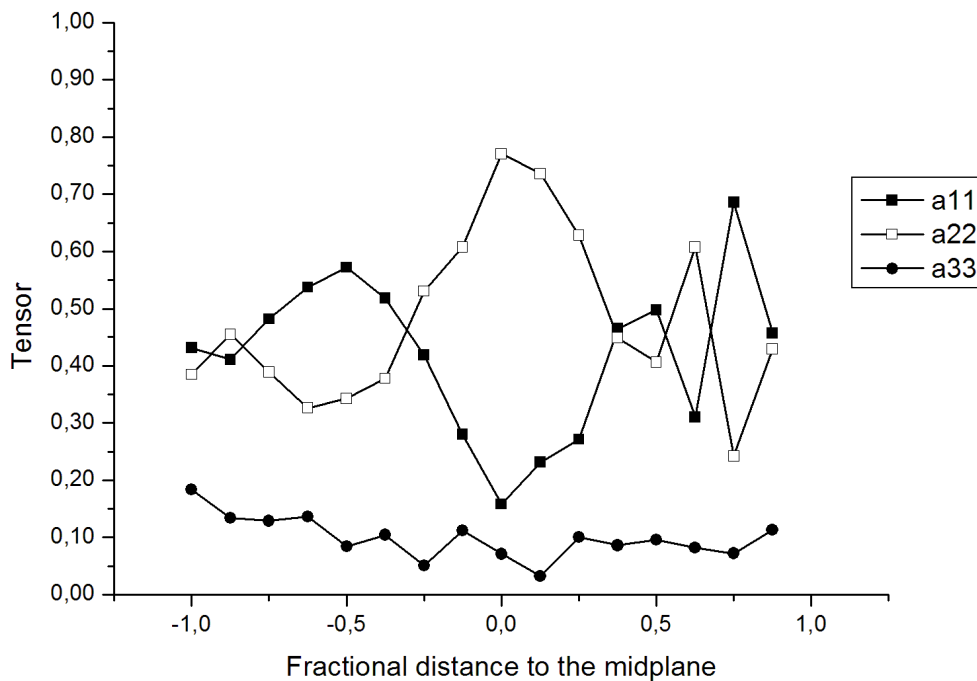


Figure 5.27 - Tensors for PP with 30% of glass fibre for mould temperature of 50°C far from the gate

The tensors a_{11} and a_{22} are approximately symmetric, in other words, when a_{11} increases, a_{22} decreases and vice versa. In relation to the orientation of the fibres this means that

when a_{11} is higher the orientation of the fibres is predominant in the flow direction and when a_{22} is higher the orientation of the fibres is predominant in the circumferential direction. Other important point to be observed is the value of the tensor in the thickness direction. The tensor in this direction is, a_{33} , and is usually very low.

Analysing the tensors a_{11} and a_{22} for polymer with 10% of glass fibre it is noticeable that there is a higher orientation of fibres in the circumferential direction, and thus the tensor a_{22} is higher than a_{11} . The inverse is observed for PP with 30% of glass fibre. The tensor a_{22} also increases with the flow path, is higher away from the gate.

The mould temperature does not cause significant influence in the glass fibre orientation.

5.5 Model implementation

In the chapter 3, the data needed to apply the model and to evaluate the shrinkage and ejection force for tubular part was mentioned.

The polymer matrix data, namely PP, are described in the Table 5.1 according to the mould temperature.

Table 5.1 - Parameters of the models used for unreinforced PP

Polypropylene (PP0)					
Parameter	Tm 30°C	Tm 50°C	Tm 75°C	Unit	source
Elastic modulus, E	0.70	0.65	0.60	GPa	*
Poisson coefficient, ν	0.38	0.38	0.38	-	
Thermal expansion coefficient, α	1.7×10^{-4}	1.7×10^{-4}	1.7×10^{-4}	K^{-1}	
linear compressibility, β	1.64×10^{-10}	1.64×10^{-10}	1.64×10^{-10}	MPa^{-1}	[3]
Friction coefficient, μ	0.13	0.17	0.25	-	*
Solidification temperature, T_s	111	111	111	°C	
Ejection average temperature, T_e	42	61	76	°C	
Solidification pressure near ₁ , P_s	26.4	26.9	28.3	MPa	⊕
Solidification pressure far ₂ , P_s	12.3	15.2	18.3	MPa	

1 The solidification pressure near from the gate and 2 far from the gate

* Parameter obtained by experimental test

⊕ Parameter obtained by simulation

The solidification pressure was obtained according to the simulated temperature. When a layer reached the solidification temperature, the pressure in this moment was considered as the solidification pressure.

The data for glass fibre are presented in the Table 5.2.

Table 5.2 - Glass fibre parameters

Glass fibre			
Parameter	Value	Unit	Source
Elastic modulus, E	73	GPa	[94]
Poisson coefficient, ν	0.18	-	
Thermal expansion coefficient, α	4.6×10^{-6}	K^{-1}	
Fibre average length for PP with 10% GF, l	530	μm	*
Fibre average diameter for PP with 10% GF, d	16	μm	
Fibre average length for PP with 30% GF, l	440	μm	
Fibre average diameter for PP with 30% GF, d	16	μm	

* Parameter obtained by experimental test

For the other materials used in this work, the parameters of the models used to predict the shrinkage and ejection forces can be found in the appendix A.7.

The prediction of shrinkage for neat PP and PP with nanoclays, in the flow direction and transversal to the flow direction, were done using the Jansen equations (3.117 and 3.118). The nanoclays at the microscale can be considered an isotropic material, but at the nanoscale it is known that the nanoclays have some orientation, depending on various factors.

In the case of PP with glass fibres (due to its anisotropic shrinkage) it is necessary to apply the thickness shrinkage equation (3.164). If this contribution is neglected, the ejection forces are underestimated.

The equation to predict the ejection force developed in this work, when applied to unreinforced material becomes the equation (3.45) developed by Pontes [173]–[175].

5.6 Assessment of the model accuracy

5.6.1 Shrinkage

In this section is presented the comparison results when the model is applied to glass fibre and nanoclay composites and the experimental data. As previously mentioned the shrinkage has influence in the ejection force. In Figure 5.28 it is shown the shrinkage of the neat PP mouldings (PP0) in the flow direction of the part at various mould temperatures. The behaviour of the shrinkage in the flow direction does not change with the materials in this study. For this reason just the PP0 data is shown. The model predicts higher shrinkage comparing with the experimental data.

The overestimation by the model is attributable to the solidification pressure, obtained by simulated temperature.

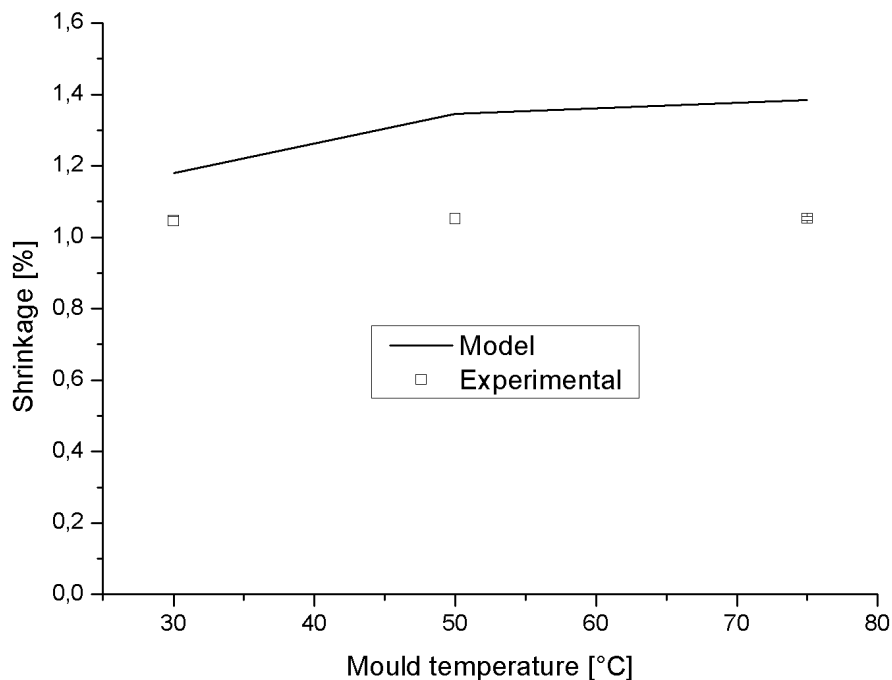


Figure 5.28 - Comparison between the model and experimental shrinkage in the flow direction at different mould temperature for PP0

In the Figure 5.29 the diametrical shrinkage of PP0 mouldings in relation to the mould temperature is shown. It is necessary to remember that the shrinkage was assessed at two locations of the part. The pressure is higher in the near to the gate region than far away

from it, and the prediction for these regions is more inaccurate due to the detachment of the part that, tend to could occur during solidification therefore changing the temperature profile.

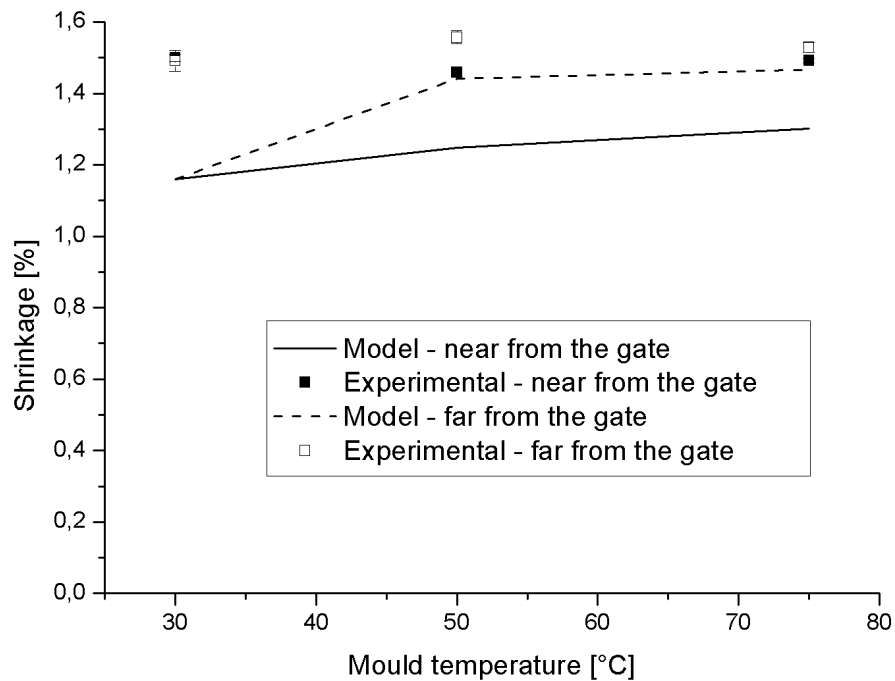


Figure 5.29 - Comparison between the model and experimental average diametrical shrinkage in relation to the mould temperature for PP0

In the Figure 5.30 it is made the comparison of the composites with various contents of nanoclay with the mould temperature at 75°C. It is observed that the content of nanoclay causes the diametrical shrinkage to decrease in relation to the material without nanoclays. The results of the model and experimental data are in a good agreement. The shrinkage reduction could be attributed to the nanoscale dispersion of the clay [155] and the lower expansion thermal coefficient than neat PP.

The assessment of using different amount of glass fibre is also carried out and presented in the Figure 5.31. Because of the content of glass fibre and the lower thermal expansion of the composite it is expectable that the shrinkage is lower for the material with higher content of glass fibre. The model is able to describe this behaviour with better results for lower mould temperature. Furthermore, the model also follows the same trend in predicting more shrinkage far from the gate than near from the gate.

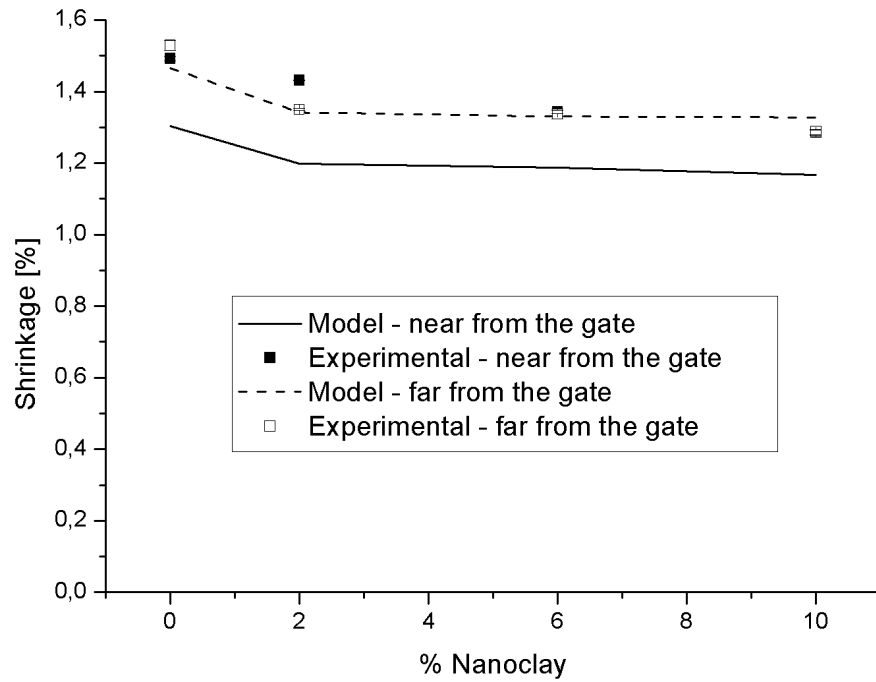


Figure 5.30 - Comparison between the model and experimental average diametrical shrinkage for different content of nanoclay near to the gate and far from the gate at the mould temperature of 75°C

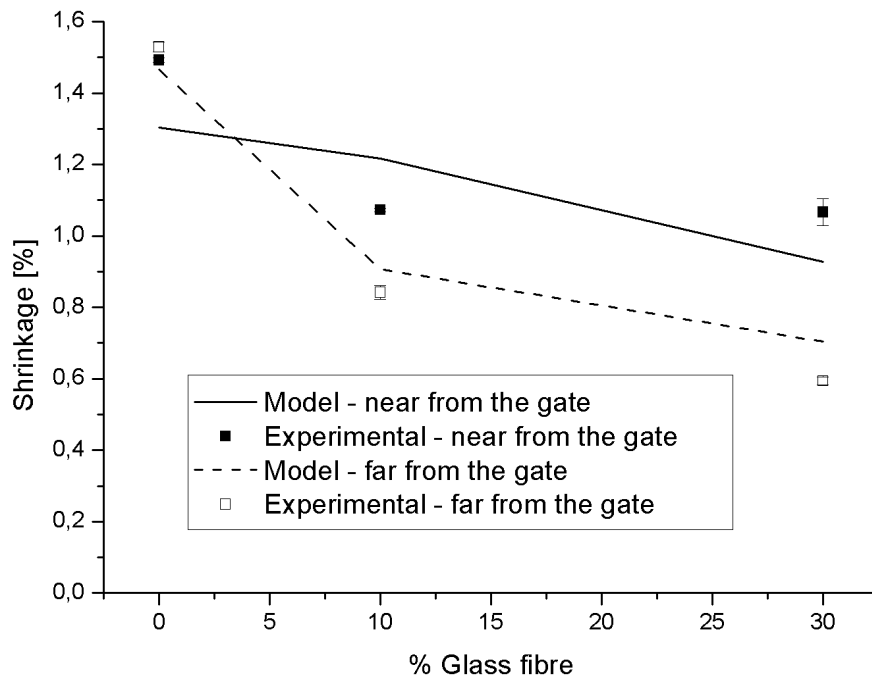


Figure 5.31 - Comparison between the model and experimental diametrical shrinkage in relation to the content of glass fibre near from the gate and far from the gate for the mould temperature of 75°C

An important aspect to investigate is the influence of nanoclay in the material with glass fibres. It can be noted in the Figure 5.32, that the material with nanoclay and glass fibre shrinks less than the material with only glass fibre. The difference is bigger in the comparing with pure PP. This can be explained by the thermal expansion as previously reported.

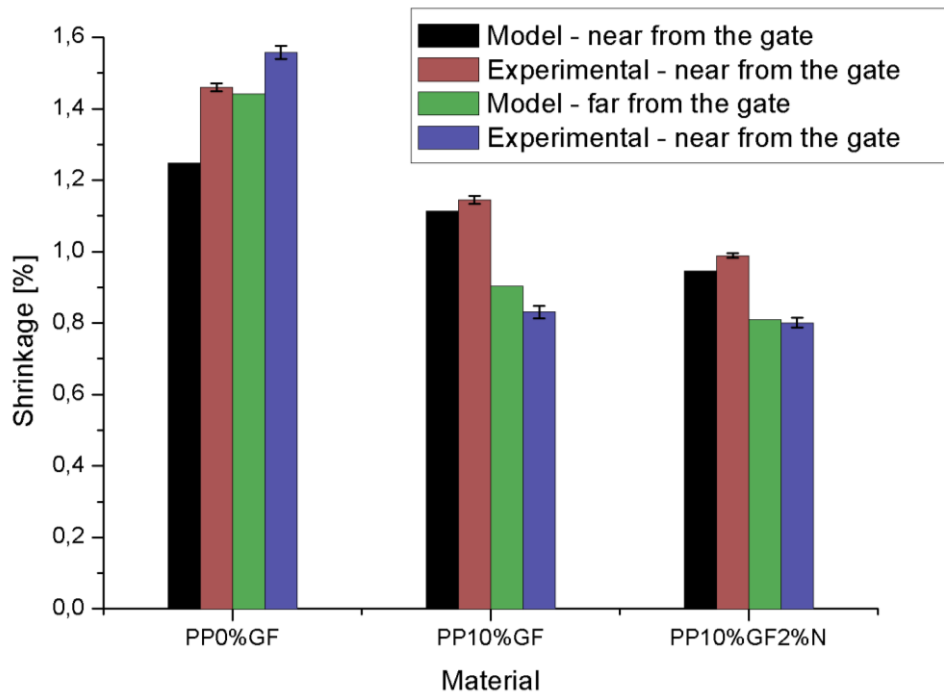


Figure 5.32 - Comparison between the model and experimental diametrical shrinkage in relation to the content of glass fibre 10% and nanoclay 2% added simultaneously near from the gate and far from the gate for the mould temperature of 50°C

Similar situation occurs with material with 30% of glass fibre and 2% of nanoclay as shown in the Figure 5.33.

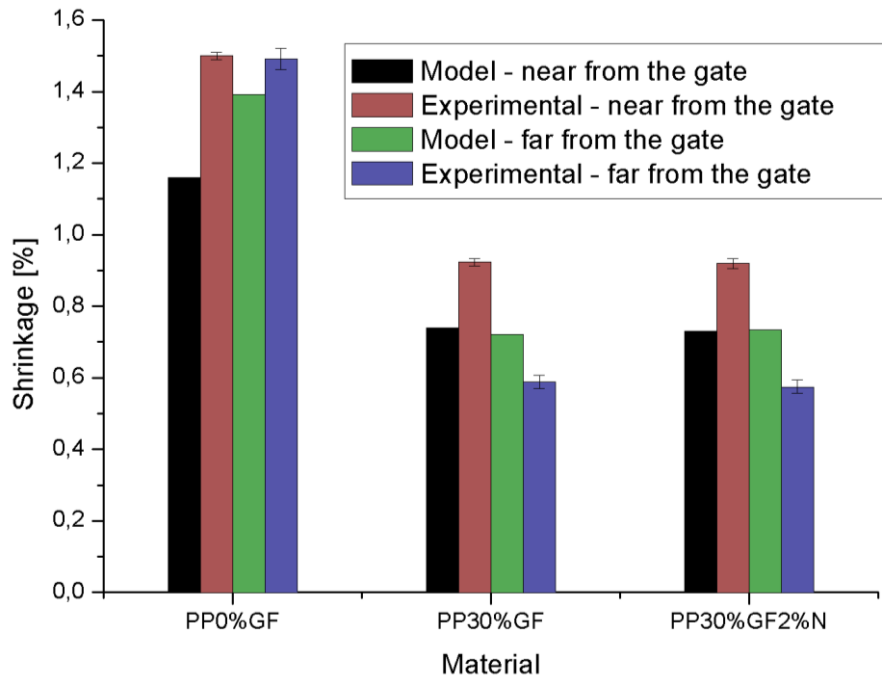


Figure 5.33 - Comparison between the model and experimental diametrical shrinkage in relation to the content of glass fibre 30% and nanoclay 2% added simultaneously near from the gate and far from the gate for the mould temperature of 30°C

5.6.2 Ejection force

Generally, the model can predict the ejection force for all the conditions that were experimentally tested. In the sequence of the Figure 5.34 and Figure 5.35 several situations for ejection force in relation to the mould temperature for several materials are presented. The agreement for all materials is clearly shown mainly at higher mould temperatures. The model is less precise in lower mould temperature, it happens, probably because the problems with solidification pressure obtained by the simulated temperature as described previously.

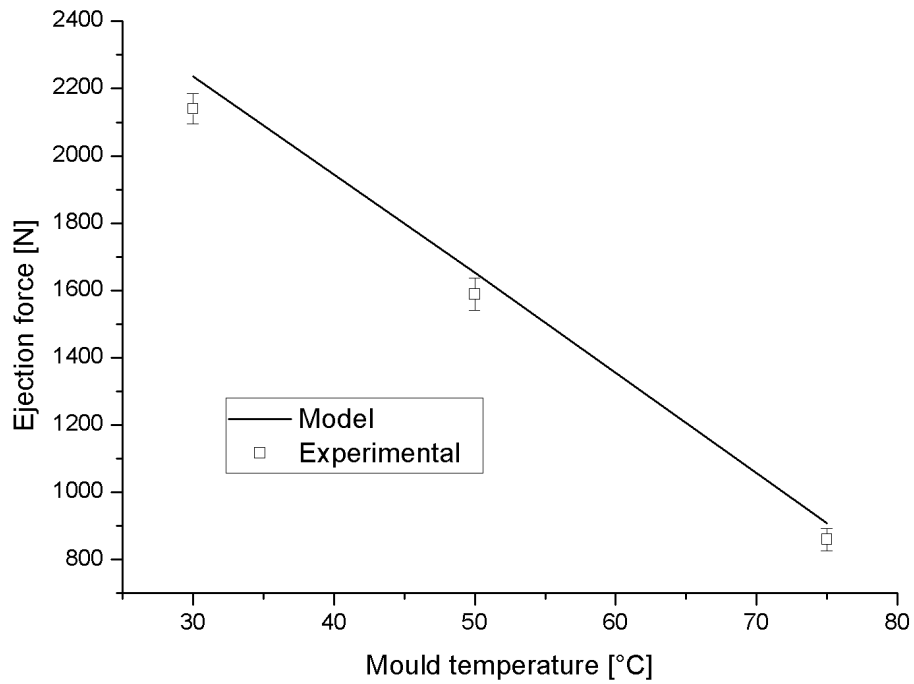


Figure 5.34 - Comparison between the model and experimental ejection force in relation to the mould temperature for PPO

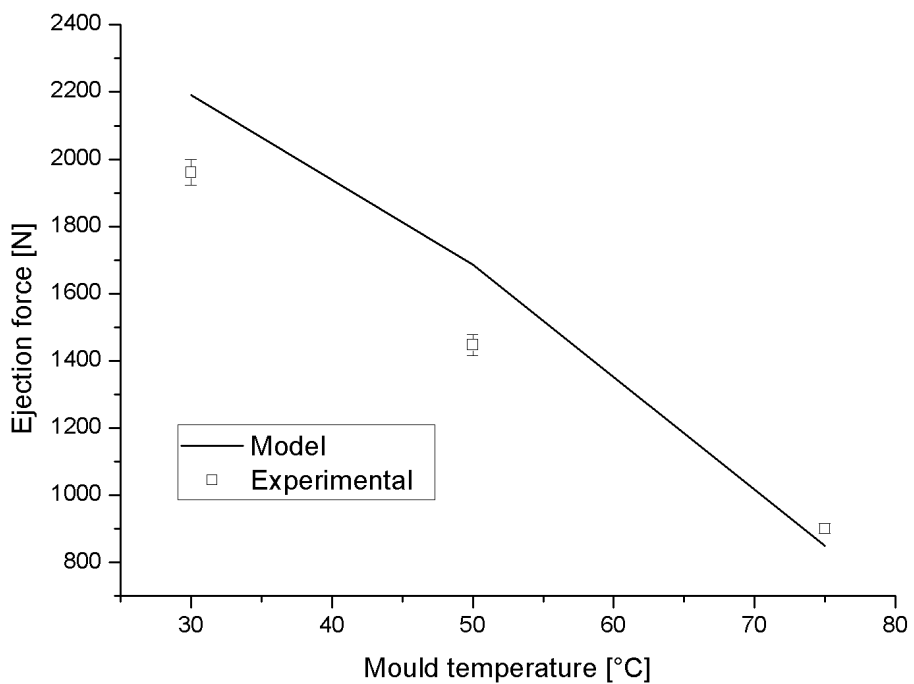


Figure 5.35 - Comparison between the model and experimental ejection force in relation to the mould temperature for PP6N

The content of nanoclays influences the shrinkage and the elastic modulus. In relation to the elastic modulus it is unlikely to affect the predictions as the modulus does not vary with the various materials with nanoclay. The difference in the results of the model is therefore due to the solidification pressure.

The same analysis is done for the mouldings material with glass fibre and glass fibre with nanoclay. The model can reproduce the ejection forces also for these materials.

In relation to the material with glass fibre, the model yields better results when the percentage of glass fibre is higher. It can be explained because the thermal stability is higher with the increase of content of glass fibre, Figure 5.36.

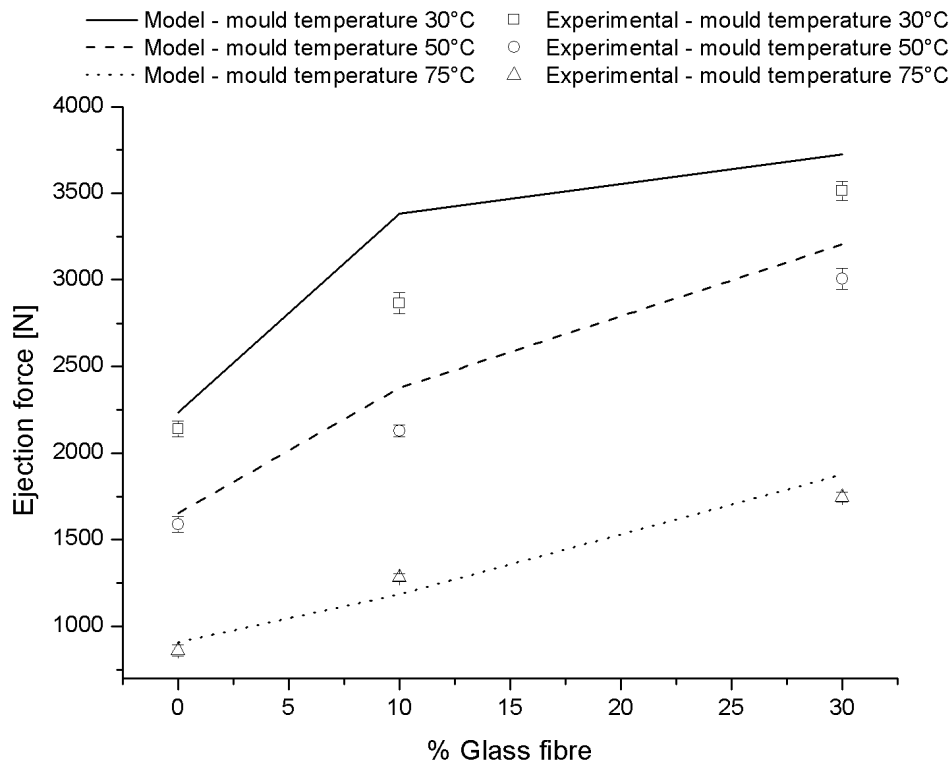


Figure 5.36 - Comparison between model and experimental results for ejection force in relation to the content of glass fibre in different mould temperatures

An important remark can be done if the content of glass fibre without nanoclay and with nanoclay are considered, Figure 5.37.

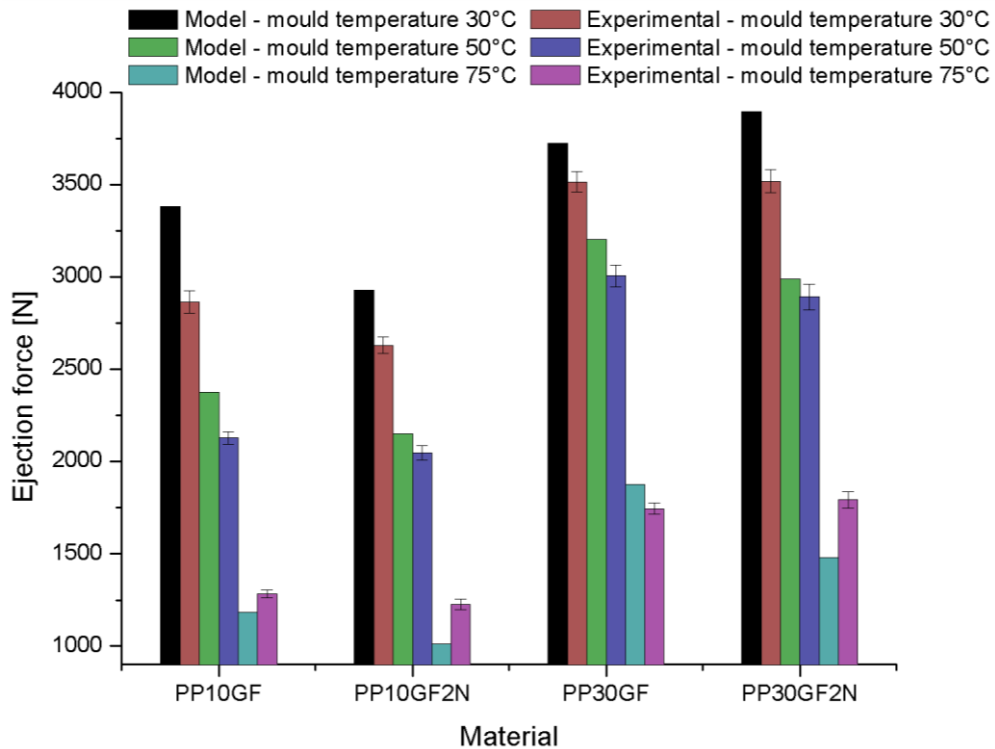


Figure 5.37 - Comparison between model and experimental results for ejection force for material with glass fibre and glass fibre with addition of nanoclay

In the Table 5.3 is presented a brief comparison among the results of the model and the experimental data with the difference in percentage for each material and with the mould temperature.

Table 5.3 - Comparison among the results of the model and experimental data of ejection force for materials in relation of the mould temperature

Material	Ejection force (N)								
	Mould temperature								
	Tm=30 °C			Tm=50 °C			Tm=75 °C		
	Model	Exp.	% Dif.	Model	Exp.	% Dif.	Model	Exp.	% Dif.
PP0	2305	2138	8	1653	1589	4	909	860	6
PP2N	2167	1976	10	1728	1516	14	892	908	-2
PP6N	2191	1960	12	1685	1447	16	850	901	-6
PP10N	2242	1989	13	1744	1479	18	810	898	-10
PP10GF	3383	2865	18	2376	2128	11	1185	1284	-8
PP30GF	3724	3515	6	3204	3006	7	1875	1745	7
PP10GF2N	2928	2630	11	2151	2047	5	1013	1227	-17
PP30GF2N	3895	3520	11	2988	2892	3	1480	1792	-17

6 Conclusions

In the context of this research work a major contribution was given to the extension of a thermo-mechanical model to describe the shrinkage and ejection forces to the case of reinforced PP with different reinforcements (glass fibres and nanoclays) and contents. The assessment of the data from the experimental work was also done in controlled processing conditions of temperature and pressure. Consequently, aspects such as detailed consideration of the crystallinity process in injection moulding, or the fibre orientation are aside from the body of this research. The predictions were compared with experimental data (shrinkage and ejection forces) in order to validate the model.

Shrinkage

Experimental data

- The mould temperature affects the shrinkage. The increase of the mould temperature increases also the shrinkage because the material has no constraint and can shrink freely.
- The effect of glass fibre in the shrinkage during the moulding process is significant. The final shrinkage is smaller with the increase of the fibre content in the case of free shrinkage.
- The shrinkage seems to be affected by the nanoclays in the same way of the glass fibre.

Prediction of the shrinkage

Within this work a thermomechanical model was developed for a more precise description of the shrinkage mechanism in reinforced PP.

- The thermo-mechanical model developed in this work gives a satisfactory description of the shrinkage in the case of PP composites.

- The precision of results depends of the determination of several input data that was gotten in many experimental tests

Ejection force

The main objective of the work was the assessment and the prediction of the ejection forces in the case of tubular moulding. The effect of processing parameters on the ejection forces of a tubular moulding was analysed and a thermo-mechanical model was developed to estimate those forces. The model developed in this work describes the case of semi-crystalline materials with reinforcements.

Experimental data

Effect of the mould temperature

- The results indicate that the temperature of the mould influences substantially the ejection force. In particular, this force decreases when the mould temperature increases. This is an expected result of the concurrent effect of the reduction of the modulus and of the shrinkage at ejection, both having an influence in that sense.

Effect of the glass fibre

- The ejection force changes directly with respect to the glass fibre content. The increase of the mechanical modulus of the material at ejection is responsible for this behaviour.

Prediction of the ejection force

- The prediction of the ejection force is in close agreement with the experimental data, it was shown in the Table 5.3.
- The decrease of the ejection force with the rise of the mould temperature is an expected result and it derives from the concurrent effect of the reduction of the modulus and the volumetric shrinkage at ejection, pointing together in that direction

- The thermo-mechanical model results agree well with the experimental data when the nanoclays and glass fibre is analyzed as reinforcement.

7 Further work

This work presents an advance of thermomechanical model in relation to the several materials used. Many possibilities arise to improve the comprehension of the phenomena related to the shrinkage and ejection forces. By the way, in the final of the work it is possible to sight many forms to develop knowledge in this field. Some items can be reported below:

- To work with other polymer matrix and change the sort and percentages of reinforcements materials of the interest of the industries.
- To developed a thermomechanical model to predict shrinkage for more complex shapes of parts as ribs and boss.
- To study the behaviour of nanoclay to built a model to predict shrinkage for nanoclay and don't consider this material as isotropic, because the nanoclay is not isotropic in nanoscale. To determine the orientation of nanoclay and its influence on the shrinkage.
- To aggregate the evaluation of ejection force with the simulation of the mould and part.
- To develop a FEM model to predict the shrinkage and ejection force for the entire part.
- To try to understand better the mechanism of shrinkage in the thickness of the part and to improve the results in this region of the moulded product.
- To obtain characterisation data of the glass fibre to refine the results of the model.
- To use the mesh generator to obtain more accurate nodes side by side along of the thickness of the part.

8 References

- [1] J. F. Chabot and R. A. Malloy, "A History of Thermoplastic Injection Molding . Part I : The Birth of an Industry," *J. Inject. Molding Technol.*, vol. 1, no. 1, pp. 1–9, 1997.
- [2] F. Johannaber, *Injection Molding Machines: A User's Guide*. Hanser Verlag, 2008.
- [3] A. J. V. Pontes, "Shrinkage and ejection forces in injection moulded products," Universidade do Minho, 2002.
- [4] Z. Tadmor and C. G. Gogos, *Principles of polymer processing*. Wiley, 2006.
- [5] D. V. Rosato, D. V. Rosato, and M. G. Rosato, *Injection molding handbook*. Springer, 2000.
- [6] T. Osswald, L.-S. Turng, and P. Gramann, *Injection Molding Handbook*. Hanser Publications, 2008, p. 764.
- [7] G. Pötsch and W. Michaeli, *Injection molding: an introduction*. Hanser Verlag, 2008.
- [8] W. Michaeli, *Plastics processing: An introduction*. Hanser Munchen, 1995.
- [9] J. C. Viana, "Mechanical Characterisation of Injection Moulded Plates," Universidade do Minho, 1999.
- [10] F. L. Peixoto, "Aplicação do processo de sobreinjeção em insertos de termoplástico utilizando moldes de fabricação rápida." Universidade Federal de Santa Catarina, Florianópolis, p. 200, 2009.
- [11] L. R. Schmidt, "The Fountain Flow in Injection Molding," *Polym. Eng. Sci.*, vol. 26, no. 20, pp. 1457–1466, 1986.
- [12] M. R. Kamal and S. Kenigo, "The Injection Molding of Thermoplastics Part I: Theoretical Model," *Polym. Eng. Sci.*, vol. 12, no. 4, pp. 294–301, 1972.
- [13] K. Nguyen and M. Kamal, "Analysis of the packing stage of a viscoelastic melt," *Polym. Eng. Sci.*, vol. 33, no. 11, pp. 665–674, 1993.
- [14] H. Zhou, *Computer Modeling for Injection Molding: Simulation, Optimization, and Control*. Wiley-Blackwell, 2013, p. 416.
- [15] R. Pantani, I. Coccorullo, V. Speranza, and G. Titomanlio, "Modeling of morphology evolution in the injection molding process of thermoplastic polymers," *Prog. Polym. Sci.*, vol. 30, no. 12, pp. 1185–1222, Dec. 2005.

- [16] P. G. Lafleur and M. R. Kamal, "A structure-oriented computer simulation of the injection molding of viscoelastic crystalline polymers part I: Model with fountain flow, packing, solidification," *Polym. Eng. Sci.*, vol. 26, no. 1, pp. 92–102, Jan. 1986.
- [17] M. Kamal and P. Laflur, "Computer simulation of injection molding," *Polym. Eng. Sci.*, vol. 22, no. 17, 1982.
- [18] D. H. Harry and R. G. Parrott, "Numerical simulation of injection mold filling," *Polym. Eng. Sci.*, vol. 10, no. 4, pp. 209–214, Jul. 1970.
- [19] J. L. Berger and C. G. Gogos, "A numerical simulation of the cavity filling process with PVC in injection molding," *Polym. Eng. Sci.*, vol. 13, no. 2, pp. 102–112, Mar. 1973.
- [20] Z. Tadmor, E. Broyer, and C. Gutfinger, "Flow analysis network (FAN)—A method for solving flow problems in polymer processing," *Polym. Eng. Sci.*, vol. 14, no. 9, pp. 660–665, Sep. 1974.
- [21] H. A. Lord and G. Williams, "Mold- filling studies for the injection molding of thermoplastic materials. Part II: The transient flow of plastic materials in the cavities of injection- molding dies," *Polym. Eng. Sci.*, vol. 15, no. 8, pp. 569–582, 1975.
- [22] G. Williams and H. A. Lord, "Mold- filling studies for the injection molding of thermoplastic materials. Part I: The flow of plastic materials in hot- and cold-walled circular channels," *Polym. Eng. Sci.*, vol. 15, no. 8, pp. 553–568, 1975.
- [23] C. A. Hieber and S. F. Shen, "A finite-element/finite-difference simulation of the injection-molding filling process," *J. Nonnewton. Fluid Mech.*, vol. 7, no. 1, pp. 1–32, 1980.
- [24] A. Isayev and C. Hieber, "Toward a viscoelastic modelling of the injection molding of polymers," *Rheol. Acta*, vol. 19, pp. 168–182, 1980.
- [25] M. Sanouf, B. I. N. Chung, and C. Cohen, "Glass Fiber-Filled Thermoplastics.," *Polym. Eng. Sci.*, vol. 25, no. 16, pp. 1008–1016, 1985.
- [26] M. R. Kamal, E. Chu, P. G. Lafleur, and M. E. Ryan, "Computer simulation of injection mold filling for viscoelastic melts with fountain flow," *Polym. Eng. Sci.*, vol. 26, no. 3, pp. 190–196, 1986.
- [27] H. Mavridis, A. N. Hrymak, and J. Vlachopoulos, "Finite element simulation of fountain flow in injection molding," *Polym. Eng. Sci.*, vol. 26, no. 7, pp. 449–454, 1986.
- [28] C. G. Gogos, C. Huang, and L. R. Schmidt, "The process of cavity filling including the fountain flow in injection molding," *Polym. Eng. Sci.*, vol. 26, no. 20, pp. 1457–1466, 1986.

- [29] B. S. Chen and W. H. Liu, "Numerical simulation and experimental investigation of injection mold filling with melt solidification," *Polym. Eng. Sci.*, vol. 29, no. 15, pp. 1039–1050, 1989.
- [30] T. D. Papathanasiou and M. R. Kamal, "Filling of a complex- shaped mold with a viscoelastic polymer. Part I: The mathematical model," *Polym. Eng. Sci.*, vol. 33, no. 7, pp. 400–409, 1993.
- [31] M. R. Kamal and T. D. Papathanasiou, "Filling of a complex- shaped mold with a viscoelastic polymer. Part II: Comparison with experimental data," *Polym. Eng. Sci.*, vol. 33, no. 7, pp. 410–417, 1993.
- [32] B. Friedrichs and S. I. Güçeri, "A novel hybrid numerical technique to model 3-D fountain flow in injection molding processes," *J. Nonnewton. Fluid Mech.*, vol. 49, no. 2, pp. 141–173, 1993.
- [33] E. Pichelin and T. Coupez, "Finite element solution of the 3D mold filling problem for viscous incompressible fluid," *Comput. Methods Appl. Mech. Eng.*, vol. 163, no. 1, pp. 359–371, 1998.
- [34] J. Hétu, D. M. Gao, A. Garcia- Rejon, and G. Salloum, "3D finite element method for the simulation of the filling stage in injection molding," *Polym. Eng. Sci.*, vol. 38, no. 2, pp. 223–236, 1998.
- [35] A. Kumar, P. S. Ghoshdastidar, and M. K. Muju, "Computer simulation of transport processes during injection mold-filling and optimization of the molding conditions," *J. Mater. Process. Technol.*, vol. 120, no. 1, pp. 438–449, 2002.
- [36] L. M. Galantucci and R. Spina, "Evaluation of filling conditions of injection moulding by integrating numerical simulations and experimental tests," *J. Mater. Process. Technol.*, vol. 141, no. 2, pp. 266–275, 2003.
- [37] S. Kim and L. Turng, "Three- dimensional numerical simulation of injection molding filling of optical lens and multiscale geometry using finite element method," *Polym. Eng. Sci.*, vol. 46, no. 9, pp. 1263–1274, 2006.
- [38] T. Chung and M. E. Ryan, "Analysis of the packing stage in injection molding," *Polym. Eng. Sci.*, vol. 21, no. 5, pp. 271–275, 1981.
- [39] T. Chung, "Pressure build- up during the packing stage of injection molding," *Polym. Eng. Sci.*, vol. 25, no. 12, pp. 772–777, 1985.
- [40] J. Greener, "General consequences of the packing phase in injection molding," *Polym. Eng. Sci.*, vol. 26, no. 12, pp. 886–892, 1986.
- [41] D. Huilier, C. Lenfant, J. Terrisse, and R. Deterre, "Modeling the packing stage in injection molding of thermoplastics," *Polym. Eng. Sci.*, vol. 28, no. 24, pp. 1637–1643, 1988.

- [42] K. T. Nguyen and M. R. Kamal, "Analysis of the packing stage of a viscoelastic melt," *Polym. Eng. Sci.*, vol. 33, no. 11, pp. 665–674, 1993.
- [43] B. S. Chen and W. H. Liu, "Numerical simulation of the post-filling stage in injection molding with a two-phase model," *Polym. Eng. Sci.*, vol. 34, no. 10, pp. 835–846, 1994.
- [44] H. Zhou and D. Li, "Residual stress analysis of the post-filling stage in injection moulding," *Int. J. Adv. Manuf. Technol.*, vol. 25, no. 7–8, pp. 700–704, 2005.
- [45] M. R. Kamal and S. Kenig, "The injection molding of thermoplastics part I: Theoretical model," *Polym. Eng. Sci.*, vol. 12, no. 4, pp. 294–301, 1972.
- [46] M. R. Kamal, Y. Kuo, and P. H. Doan, "The injection molding behavior of thermoplastics in thin rectangular cavities," *Polym. Eng. Sci.*, vol. 15, no. 12, pp. 863–868, 1975.
- [47] M. R. Kamal and P. G. Laflur, "Computer simulation of injection molding," *Polym. Eng. Sci.*, vol. 22, no. 17, pp. 1066–1074, 1982.
- [48] P. G. Lafleur and M. R. Kamal, "A structure-oriented computer simulation of the injection molding of viscoelastic crystalline polymers part I: Model with fountain flow, packing, solidification," *Polym. Eng. Sci.*, vol. 26, no. 1, pp. 92–102, 1986.
- [49] H. H. Chiang, C. A. Hieber, and K. K. Wang, "A unified simulation of the filling and postfilling stages in injection molding. Part I: Formulation," *Polym. Eng. Sci.*, vol. 31, no. 2, pp. 116–124, 1991.
- [50] H. H. Chiang, C. A. Hieber, and K. K. Wang, "A unified simulation of the filling and postfilling stages in injection molding. Part II: Experimental verification," *Polym. Eng. Sci.*, vol. 31, no. 2, pp. 125–139, 1991.
- [51] K.-H. Han and Y.-T. Im, "Compressible flow analysis of filling and postfilling in injection molding with phase-change effect," *Compos. Struct.*, vol. 38, no. 1, pp. 179–190, 1997.
- [52] C. A. Hieber, "Modeling/simulating the injection molding of isotactic polypropylene," *Polym. Eng. Sci.*, vol. 42, no. 7, pp. 1387–1409, 2002.
- [53] L. F. A. Douven, F. P. T. Baaijens, and H. E. H. Meijer, "The computation of properties of injection-moulded products," *Prog. Polym. Sci.*, vol. 20, no. 3, pp. 403–457, 1995.
- [54] A. Bikas, N. Pantelelis, and A. Kanarachos, "Computational tools for the optimal design of the injection moulding process," *J. Mater. Process. Technol.*, vol. 122, no. 1, pp. 112–126, 2002.
- [55] L. S. Turng and M. Peić, "Computer aided process and design optimization for injection moulding," *Proc. Inst. Mech. Eng. Part B J. Eng. Manuf.*, vol. 216, no. 12, pp. 1523–1532, 2002.

- [56] Y. C. Lam, G. A. Britton, and Y.-M. Deng, "A computer-aided system for an optimal moulding conditions design using a simulation-based approach," *Int. J. Adv. Manuf. Technol.*, vol. 22, no. 7–8, pp. 574–586, 2003.
- [57] S.-W. Kim and L.-S. Turng, "Developments of three-dimensional computer-aided engineering simulation for injection moulding," *Model. Simul. Mater. Sci. Eng.*, vol. 12, no. 3, p. S151, 2004.
- [58] B. Ozcelik and T. Erzurumlu, "Comparison of the warpage optimization in the plastic injection molding using ANOVA, neural network model and genetic algorithm," *J. Mater. Process. Technol.*, vol. 171, no. 3, pp. 437–445, 2006.
- [59] C. Shen, L. Wang, and Q. Li, "Optimization of injection molding process parameters using combination of artificial neural network and genetic algorithm method," *J. Mater. Process. Technol.*, vol. 183, no. 2, pp. 412–418, 2007.
- [60] S. H. Tang, Y. J. Tan, S. M. Sapuan, S. Sulaiman, N. Ismail, and R. Samin, "The use of Taguchi method in the design of plastic injection mould for reducing warpage," *J. Mater. Process. Technol.*, vol. 182, no. 1, pp. 418–426, 2007.
- [61] J. Zhou and L. Turng, "Process optimization of injection molding using an adaptive surrogate model with Gaussian process approach," *Polym. Eng. Sci.*, vol. 47, no. 5, pp. 684–694, 2007.
- [62] H. Zhou, S. Shi, and B. Ma, "A virtual injection molding system based on numerical simulation," *Int. J. Adv. Manuf. Technol.*, vol. 40, no. 3–4, pp. 297–306, 2009.
- [63] C.-P. Chen, M.-T. Chuang, Y.-H. Hsiao, Y.-K. Yang, and C.-H. Tsai, "Simulation and experimental study in determining injection molding process parameters for thin-shell plastic parts via design of experiments analysis," *Expert Syst. Appl.*, vol. 36, no. 7, pp. 10752–10759, 2009.
- [64] I. Ferreira, O. de Weck, P. Saraiva, and J. Cabral, "Multidisciplinary optimization of injection molding systems," *Struct. Multidiscip. Optim.*, vol. 41, no. 4, pp. 621–635, 2010.
- [65] C. Fernandes, A. J. Pontes, J. C. Viana, and A. Gaspar-Cunha, "Using multiobjective evolutionary algorithms in the optimization of operating conditions of polymer injection molding," *Polym. Eng. Sci.*, vol. 50, no. 8, pp. 1667–1678, 2010.
- [66] R. Zheng, R. I. Tanner, and X.-J. Fan, *Injection Molding: Integration of Theory and Modeling Methods*. Springer, 2011, p. 250.
- [67] J. Greener and R. Wimberger-Friedl, *Precision Injection Molding: Process, Materials and Applications*. Hanser Gardner Publications, 2006, p. 328.
- [68] J. Fischer, *Handbook of molded part shrinkage and warpage*, 2^a ed. London: Elsevier, 2013, p. 261.

- [69] “ASTM D955 - 08 Standard Test Method of Measuring Shrinkage from Mold Dimensions of Thermoplastics.” [Online]. Available: <http://www.astm.org/Standards/D955.htm>. [Accessed: 22-Aug-2013].
- [70] W. Michaeli, G. Menges, and P. Mohren, *How to Make Injection Molds*. Carl Hanser Verlag GmbH & Co, 2001, p. 631.
- [71] A. Mamat, T. F. Trochu, and B. Sanschagrín, “Analysis of shrinkage by dual kriging for filled and unfilled polypropylene molded parts,” *Polym. Eng. Sci.*, vol. 35, no. 19, pp. 1511–1520, 1995.
- [72] K. M. B. Jansen, R. Pantani, and G. Titomanlio, “As-molded shrinkage measurements on polystyrene injection molded products,” *Polym. Eng. Sci.*, vol. 38, no. 2, pp. 254–264, 1998.
- [73] K. M. B. Jansen, D. J. Van Dijk, and M. H. Husselman, “Effect of processing conditions on shrinkage in injection molding,” *Polym. Eng. Sci.*, vol. 38, no. 5, pp. 838–846, 1998.
- [74] Tao C . Chang and Ernest Faison, “A Study of the Effects of Process Conditions on the Shrinkage of Plastic Parts in Injection Molding by the Taguchi Method,” *Proc. 58th Annu. Tech. Conf. Exhib.*, vol. XLVI, pp. 3068–3073, 2000.
- [75] T. C. Chang and E. Faison, “Shrinkage behavior and optimization of injection molded parts studied by the Taguchi method,” *Polym. Eng. Sci.*, vol. 41, no. 5, pp. 703–710, 2001.
- [76] T. . J. Wang and C. . K. . Yoon, “Effects of process Conditions on shrinkage and warpage in the injection molding process,” *Proc. 57th Annu. Tech. Conf. Exhib.*, vol. I, pp. 584–588, 1999.
- [77] P. Postawa and J. Koszkul, “Change in injection moulded parts shrinkage and weight as a function of processing conditions,” *J. Mater. Process. Technol.*, vol. 162–163, pp. 109–115, 2005.
- [78] A. Kramschuster, R. Cavitt, D. Ermer, Z. B. Chen, and L.-S. Turng, “Effect of processing conditions on shrinkage and warpage and morphology of injection moulded parts using microcellular injection moulding,” *Plast. rubber Compos.*, vol. 35, no. 5, pp. 198–209, 2006.
- [79] M. Kurt, Y. Kaynak, O. S. Kamber, B. Mutlu, B. Bakir, and U. Koklu, “Influence of molding conditions on the shrinkage and roundness of injection molded parts,” *Int. J. Adv. Manuf. Technol.*, vol. 46, no. 5–8, pp. 571–578, 2010.
- [80] E. Hakimian and A. B. Sulong, “Analysis of warpage and shrinkage properties of injection-molded micro gears polymer composites using numerical simulations assisted by the Taguchi method,” *Mater. Des.*, vol. 42, pp. 62–71, 2012.
- [81] A. Gordillo, D. Ariza, M. Sanchez-Soto, and M. L. I. Maspocho, “Shrinkage predictions of injection moulded parts in semi-crystalline polymers: experimental

- verification,” in *Emerging Technologies and Factory Automation, 1999. Proceedings. ETFA '99. 1999 7th IEEE International Conference on*, 1999, vol. 2, pp. 1281–1287.
- [82] S. J. Liao, D. Y. Chang, H. J. Chen, L. S. Tsou, J. R. Ho, H. T. Yau, W. H. Hsieh, J. T. Wang, and Y. C. Su, “Optimal process conditions of shrinkage and warpage of thin wall parts,” *Polym. Eng. Sci.*, vol. 44, no. 5, pp. 917–928, 2004.
- [83] S. J. Liao, W. H. Hsieh, J. T. Wang, and Y. C. Su, “Shrinkage and warpage prediction of injection- molded thin- wall parts using artificial neural networks,” *Polym. Eng. Sci.*, vol. 44, no. 11, pp. 2029–2040, 2004.
- [84] A. R. Jafarian and M. Shakeri, “Investigating the Influence of Different Process Parameters on Shrinkage of Injection-Molded Parts,” *Am. J. Appl. Sci.*, vol. 2, no. 3, pp. 688–700, 2005.
- [85] C.-H. Wu and Y.-J. Huang, “The influence of cavity deformation on the shrinkage and warpage of an injection-molded part,” *Int. J. Adv. Manuf. Technol.*, vol. 32, no. 11–12, pp. 1144–1154, 2007.
- [86] S. Fathi and A. H. Behravesh, “Visualization of in- mold shrinkage in injection molding process,” *Polym. Eng. Sci.*, vol. 47, no. 5, pp. 750–756, 2007.
- [87] A. E. Resler, “Cooling rate effects on shrinkage,” *Proc. 57th Annu. Tech. Conf. Exhib.*, vol. III, pp. 3665–3669, 1999.
- [88] D. A. Velarde and M. J. Yeagley, “Linear shrinkage differences in plastics injection molded parts,” *Proc. 58th Annu. Tech. Conf. Exhib.*, vol. XLVI, pp. 506–510, 2000.
- [89] J. Pomerleau and B. Sanschagrín, “Injection molding shrinkage of PP: Experimental progress,” *Polym. Eng. Sci.*, vol. 46, no. 9, pp. 1275–1283, 2006.
- [90] K. Shelesh-Nezhad and A. Taghizadeh, “Shrinkage behavior and mechanical performances of injection molded polypropylene/talc composites,” *Polym. Eng. Sci.*, vol. 47, no. 12, pp. 2124–2128, 2007.
- [91] F. De Santis, R. Pantani, V. Speranza, and G. Titomanlio, “As-molded shrinkage on industrial polypropylene injection molded parts: experiments and analysis,” *Int. J. Mater. Form.*, vol. 1, no. 1, pp. 719–722, 2008.
- [92] A. L. Gershon, L. S. Gyger Jr, H. A. Bruck, and S. K. Gupta, “Thermoplastic Polymer Shrinkage in Emerging Molding Processes,” *Exp. Mech.*, vol. 48, no. 6, pp. 789–798, 2008.
- [93] K. M. B. Jansen, “Measurement and prediction of anisotropy in injection moulded PP products,” *Int. Polym. Process.*, vol. 13, no. 3, pp. 309–317, 1998.

- [94] K. M. B. Jansen, D. J. Van Dijk, and M. J. A. Freriksen, "Shrinkage anisotropy in fiber reinforced injection molded products," *Polym. Compos.*, vol. 19, no. 4, pp. 325–334, 1998.
- [95] K. H. K. and C. van S. Keehae Kwon, A.I. Isayev, "Anisotropic shrinkage in injection moldings of semicrystalline and amorphous polymers: Simulation and experiment," in *Proceedings of the 63rd Annual Technical Conference & Exhibition*, 2005, pp. 506–510.
- [96] K. Kwon, A. I. Isayev, and K. H. Kim, "Toward a viscoelastic modeling of anisotropic shrinkage in injection molding of amorphous polymers," *J. Appl. Polym. Sci.*, vol. 98, no. 5, pp. 2300–2313, 2005.
- [97] P. Postawa and A. Gnatowski, "Anisotropy of physical properties injection moulded parts and its analysis," *J. Achiev. Mater. Manuf. Eng.*, vol. 23, no. 2, pp. 35–38, 2007.
- [98] M. Xia, H. Hamada, and Z. Maekawa, "Flexural Stiffness of injection-Molded glass-fiber-reinforced thermoplastics," *Int. Polym. Process.*, vol. 10, no. 1, pp. 74–81, 1995.
- [99] B. Mlekusch, "Thermoelastic properties of short-fibre-reinforced thermoplastics," *Compos. Sci. Technol.*, vol. 59, no. 6, pp. 911–923, 1999.
- [100] N. M. Neves, A. J. Pontes, and A. S. Pouzada, "Experimental validation of morphology simulation in glass fibre reinforced polycarbonate discs," *J. Reinf. Plast. Compos.*, vol. 20, no. 6, pp. 452–465, 2001.
- [101] P. J. Hine, H. Rudolf Lusti, and A. A. Gusev, "Numerical simulation of the effects of volume fraction, aspect ratio and fibre length distribution on the elastic and thermoelastic properties of short fibre composites," *Compos. Sci. Technol.*, vol. 62, no. 10, pp. 1445–1453, 2002.
- [102] J. L. Thomason, "Micromechanical parameters from macromechanical measurements on glass reinforced polypropylene," *Compos. Sci. Technol.*, vol. 62, no. 10, pp. 1455–1468, 2002.
- [103] S. Han and K. K. Wang, "Shrinkage prediction for slowly-crystallizing thermoplastic polymers in injection molding," *Int. Polym. Process.*, vol. 12, no. 3, pp. 228–237, 1997.
- [104] D.-S. Choi and Y.-T. Im, "Prediction of shrinkage and warpage in consideration of residual stress in integrated simulation of injection molding," *Compos. Struct.*, vol. 47, no. 1, pp. 655–665, 1999.
- [105] C. Lotti, M. M. Ueki, and R. E. S. Bretas, "Prediction of the shrinkage of injection molded iPP plaques using artificial neural networks," *J. Inject. molding Technol.*, vol. 6, no. 3, pp. 157–176, 2002.

- [106] S. S. Yang and T. H. Kwon, "A study of birefringence, residual stress and final shrinkage for precision injection molded parts," *Korea-Australia Rheol. J.*, vol. 19, no. 4, pp. 191–199, 2007.
- [107] V. Speranza, R. Pantani, G. B. Besana, and G. Titomanlio, "Anisotropic shrinkage of injection molded poly vinylidene fluoride samples," *Polym. Eng. Sci.*, vol. 47, no. 11, pp. 1788–1795, 2007.
- [108] S. S. Yang and T. H. Kwon, "Numerical and experimental investigation of shrinkage behavior of precision injection molded articles. II. Results and discussion," *Polym. Eng. Sci.*, vol. 48, no. 8, pp. 1569–1583, 2008.
- [109] M. Altan, "Reducing shrinkage in injection moldings via the Taguchi, ANOVA and neural network methods," *Mater. Des.*, vol. 31, no. 1, pp. 599–604, 2010.
- [110] A. I. Isayev and T.-H. Lin, "Frozen-in birefringence and anisotropic shrinkage in optical moldings: I. Theory and simulation scheme," *Polymer (Guildf.)*, vol. 51, no. 1, pp. 316–327, 2010.
- [111] T. Lucyshyn, G. Knapp, M. Kipperer, and C. Holzer, "Determination of the transition temperature at different cooling rates and its influence on prediction of shrinkage and warpage in injection molding simulation," *J. Appl. Polym. Sci.*, vol. 123, no. 2, pp. 1162–1168, 2012.
- [112] S. F. Walsh, "Shrinkage and warpage prediction for injection molded components," *J. Reinf. Plast. Compos.*, vol. 12, no. 7, pp. 769–777, 1993.
- [113] R. Pantani, "Analysis of shrinkage development in injection moulding samples," Università Degli Studi di Salerno, 1999.
- [114] H. Hassan, N. Regnier, C. Pujos, E. Arquis, and G. Defaye, "Modeling the effect of cooling system on the shrinkage and temperature of the polymer by injection molding," *Appl. Therm. Eng.*, vol. 30, no. 13, pp. 1547–1557, 2010.
- [115] W. C. Bushko and V. K. Stokes, "Solidification of thermoviscoelastic melts. Part II: Effects of processing conditions on shrinkage and residual stresses," *Polym. Eng. Sci.*, vol. 35, no. 4, pp. 365–383, 1995.
- [116] W. C. Bushko and V. K. Stokes, "Solidification of thermoviscoelastic melts. Part 4: Effects of boundary conditions on shrinkage and residual stresses," *Polym. Eng. Sci.*, vol. 36, no. 5, pp. 658–675, 1996.
- [117] K. M. B. Jansen and G. Titomanlio, "Effect of pressure history on shrinkage and residual stresses— injection molding with constrained shrinkage," *Polym. Eng. Sci.*, vol. 36, no. 15, pp. 2029–2040, 1996.
- [118] G. Titomanlio and K. M. B. Jansen, "In-mold shrinkage and stress prediction in injection molding," *Polym. Eng. Sci.*, vol. 36, no. 15, pp. 2041–2049, 1996.

- [119] K. K. Kabanemi, H. Vaillancourt, H. Wang, and G. Salloum, "Residual stresses, shrinkage, and warpage of complex injection molded products: numerical simulation and experimental validation," *Polym. Eng. Sci.*, vol. 38, no. 1, pp. 21–37, 1998.
- [120] T. Azdast and A. H. Behraves, "An Analytical Study of Constrained Shrinkage of Injection Molded Semi-Crystalline Plastic Parts," *Polym. Plast. Technol. Eng.*, vol. 47, no. 12, pp. 1265–1272, 2008.
- [121] F. De Santis, R. Pantani, V. Speranza, and G. Titomanlio, "Analysis of shrinkage development of a semicrystalline polymer during injection molding," *Ind. Eng. Chem. Res.*, vol. 49, no. 5, pp. 2469–2476, 2010.
- [122] S. G. Advani, *Flow and Rheology in Polymer Composites Manufacturing, Volume 10 (Composite Materials Series)*. Elsevier Science, 1994, p. 626.
- [123] A. K. Kaw, *Mechanics of Composite Materials*. CRC Press, 2005, p. 490.
- [124] G. B. Jeffery, "The rotation of two circular cylinders in a viscous fluid," *Proc. R. Soc. London. Ser. A*, vol. 101, no. 709, pp. 169–174, 1922.
- [125] S. G. Advani and C. Tucker, "A tensor description of Fiber orientation in short fiber composites," in *43 rd Annual Technical Conference, Society of Plastics Engineers, Inc*, 1985, pp. 1113–1118.
- [126] S. G. Advani and C. L. Tucker III, "The use of tensors to describe and predict fiber orientation in short fiber composites," *J. Rheol. (N. Y. N. Y.)*, vol. 31, p. 751, 1987.
- [127] S. F. Xavier, D. Tyagi, and A. Misra, "Influence of injection- molding parameters on the morphology and mechanical properties of glass fiber- reinforced polypropylene composites," *Polym. Compos.*, vol. 3, no. 2, pp. 88–96, 1982.
- [128] R. Byron Pipes, R. L. McCullough, and D. G. Taggart, "Behavior of discontinuous fiber composites: Fiber orientation," *Polym. Compos.*, vol. 3, no. 1, pp. 34–39, 1982.
- [129] M. Vincent and J. F. Agassant, "Experimental study and calculations of short glass fiber orientation in a center gated molded disc," *Polym. Compos.*, vol. 7, no. 2, pp. 76–83, 1986.
- [130] M. C. Altan, S. Subbiah, S. I. Güçeri, and R. B. Pipes, "Numerical prediction of three- dimensional fiber orientation in Hele- Shaw flows," *Polym. Eng. Sci.*, vol. 30, no. 14, pp. 848–859, 1990.
- [131] T. Matsuoka, J. Takabatake, Y. Inoue, and H. Takahashi, "Prediction of fiber orientation in injection molded parts of short- fiber- reinforced thermoplastics," *Polym. Eng. Sci.*, vol. 30, no. 16, pp. 957–966, 1990.

- [132] M. Akay and D. Barkley, "Fibre orientation and mechanical behaviour in reinforced thermoplastic injection mouldings," *J. Mater. Sci.*, vol. 26, no. 10, pp. 2731–2742, 1991.
- [133] R. S. Bay and C. L. Tucker, "Fiber orientation in simple injection moldings. Part I: Theory and numerical methods," *Polym. Compos.*, vol. 13, no. 4, pp. 317–331, 1992.
- [134] R. S. Bay and C. L. Tucker, "Fiber orientation in simple injection moldings. Part II: Experimental results," *Polym. Compos.*, vol. 13, no. 4, pp. 332–341, 1992.
- [135] R. S. Bay and C. L. Tucker, "Stereological measurement and error estimates for three-dimensional fiber orientation," *Polym. Eng. Sci.*, vol. 32, no. 4, pp. 240–253, 1992.
- [136] L. G. Reifschneider and H. U. Akay, "Applications of a fiber orientation prediction algorithm for compression molded parts with multiple charges," *Polym. Compos.*, vol. 15, no. 4, pp. 261–269, 1994.
- [137] J. S. Cintra Jr and C. L. Tucker III, "Orthotropic closure approximations for flow-induced fiber orientation," *J. Rheol. (N. Y. N. Y.)*, vol. 39, p. 1095, 1995.
- [138] N. C. Davidson, A. R. Clarke, and G. Archenhold, "Large-area, high-resolution image analysis of composite materials," *J. Microsc.*, vol. 185, no. 2, pp. 233–242, 2003.
- [139] N. M. Neves, G. Isdell, A. S. Pouzada, and P. C. Powell, "On the effect of the fiber orientation on the flexural stiffness of injection molded short fiber reinforced polycarbonate plates," *Polym. Compos.*, vol. 19, no. 5, pp. 640–651, 1998.
- [140] L. Zhang, L. J. Ernst, and H. R. Brouwer, "Transverse behaviour of a unidirectional composite (glass fibre reinforced unsaturated polyester). Part I. Influence of fibre packing geometry," *Mech. Mater.*, vol. 27, no. 1, pp. 13–36, 1998.
- [141] N.-J. Lee and J. Jang, "The effect of fibre content on the mechanical properties of glass fibre mat/polypropylene composites," *Compos. Part A Appl. Sci. Manuf.*, vol. 30, no. 6, pp. 815–822, 1999.
- [142] R. Zheng, P. Kennedy, N. Phan-Thien, and X. J. Fan, "Thermoviscoelastic simulation of thermally and pressure-induced stresses in injection moulding for the prediction of shrinkage and warpage for fibre-reinforced thermoplastics," *J. Nonnewton. Fluid Mech.*, vol. 84, no. 2, pp. 159–190, 1999.
- [143] S.-Y. Fu, B. Lauke, E. Mäder, C.-Y. Yue, and X. Hu, "Tensile properties of short-glass-fiber-and short-carbon-fiber-reinforced polypropylene composites," *Compos. Part A Appl. Sci. Manuf.*, vol. 31, no. 10, pp. 1117–1125, 2000.
- [144] C. Eberhardt and A. Clarke, "Fibre-orientation measurements in short-glass-fibre composites. Part I: automated, high-angular-resolution measurement by confocal microscopy," *Compos. Sci. Technol.*, vol. 61, no. 10, pp. 1389–1400, 2001.

- [145] A. J. Pontes, N. M. Neves, and A. S. Pouzada, "The role of the interaction coefficient in the prediction of the fiber orientation in planar injection moldings," *Polym. Compos.*, vol. 24, no. 3, pp. 358–366, 2003.
- [146] M. Vincent, T. Giroud, A. Clarke, and C. Eberhardt, "Description and modeling of fiber orientation in injection molding of fiber reinforced thermoplastics," *Polymer (Guildf)*, vol. 46, no. 17, pp. 6719–6725, 2005.
- [147] M. W. E. Toledo, L. G. Nallim, and B. M. Luccioni, "A micro-macromechanical approach for composite laminates," *Mech. Mater.*, vol. 40, no. 11, pp. 885–906, 2008.
- [148] J. H. Phelps and C. L. Tucker III, "An anisotropic rotary diffusion model for fiber orientation in short-and long-fiber thermoplastics," *J. Nonnewton. Fluid Mech.*, vol. 156, no. 3, pp. 165–176, 2009.
- [149] H. Miled, L. Silva, T. Coupez, and J.-F. Agassant, "Injection moulding of fibre reinforced thermoplastics: integration of fibre orientation and mechanical properties computations," in *Proceedings of the 27th World Congress of the Polymer Processing Society*, 2011.
- [150] J. Koo, *Polymer Nanocomposites: Processing, Characterization, And Applications (Mcgraw-Hill Nanoscience and Technology Series)*. McGraw-Hill Professional, 2006, p. 272.
- [151] S. G. Advani, *Processing and Properties of Nanocomposites*. World Scientific Pub Co Inc, 2006, p. 460.
- [152] A. Esfandiari, H. Nazokdast, A.-S. Rashidi, and M.-E. Yazdanshenas, "Review of polymer-organoclay nanocomposites," *J. Appl. Sci.*, vol. 8, no. 3, pp. 545–561, 2008.
- [153] E. T. Thostenson, C. Li, and T.-W. Chou, "Nanocomposites in context," *Compos. Sci. Technol.*, vol. 65, no. 3, pp. 491–516, 2005.
- [154] S. G. Lei, S. V Hoa, and M.-T. Ton-That, "Effect of clay types on the processing and properties of polypropylene nanocomposites," *Compos. Sci. Technol.*, vol. 66, no. 10, pp. 1274–1279, 2006.
- [155] R. Revilla Díaz, S. Sánchez Valdés, F. López Campos, F. J. Medellín Rodríguez, and M. L. López Quintanilla, "Comparative Characterization of PP Nano- and Microcomposites by In-Mold Shrinkage Measurements and Structural Characteristics," *Macromol. Mater. Eng.*, vol. 292, no. 6, pp. 762–768, 2007.
- [156] L. B. de Paiva, A. R. Morales, and F. R. Valenzuela Díaz, "Organoclays: properties, preparation and applications," *Appl. Clay Sci.*, vol. 42, no. 1, pp. 8–24, 2008.

- [157] K. Kanny, P. Jawahar, and V. K. Moodley, "Mechanical and tribological behavior of clay–polypropylene nanocomposites," *J. Mater. Sci.*, vol. 43, no. 22, pp. 7230–7238, 2008.
- [158] F. J. Carrión, A. Arribas, M.-D. Bermúdez, and A. Guillamon, "Physical and tribological properties of a new polycarbonate-organoclay nanocomposite," *Eur. Polym. J.*, vol. 44, no. 4, pp. 968–977, 2008.
- [159] D. W. Litchfield and D. G. Baird, "The role of nanoclay in the generation of poly (ethylene terephthalate) fibers with improved modulus and tenacity," *Polymer (Guildf)*, vol. 49, no. 23, pp. 5027–5036, 2008.
- [160] D. R. Paul and L. M. Robeson, "Polymer nanotechnology: nanocomposites," *Polymer (Guildf)*, vol. 49, no. 15, pp. 3187–3204, 2008.
- [161] K. S. Santos, S. A. Liberman, M. A. S. Oviedo, and R. S. Mauler, "Optimization of the mechanical properties of polypropylene-based nanocomposite via the addition of a combination of organoclays," *Compos. Part A Appl. Sci. Manuf.*, vol. 40, no. 8, pp. 1199–1209, 2009.
- [162] R. G. W. Pye, *Injection Mould Design*, 4^a ed. Longman Scientific & Technical, 1989, p. 754.
- [163] Z. Wang, K. S. Lee, J. Y. H. Fuh, Z. Li, Y. F. Zhang, A. Y. C. Nee, and D. C. H. Yang, "Optimum ejector system design for plastic injection mould," *Int. J. Mater. Prod. Technol.*, vol. 11, no. 5–6, pp. 371–385, 1996.
- [164] C. J. Yu and J. E. Sunderland, "Determination of ejection temperature and cooling time in injection molding," *Polym. Eng. Sci.*, vol. 32, no. 3, pp. 191–197, 1992.
- [165] C. Burke and R. Malloy, "An experimental study of the ejection forces encountered during injection molding," *ANTEC 1991*, pp. 1781–1787, 1991.
- [166] K. Shen, L.-M. Chen, and L. Jiang, "Calculation of ejection force of hollow, thin walled, and injection moulded cones," *Plast. rubber Compos.*, vol. 28, no. 7, pp. 341–345, 1999.
- [167] T. Sasaki, N. Koga, K. Shirai, Y. Kobayashi, and A. Toyoshima, "An experimental study on ejection forces of injection molding," *Precis. Eng.*, vol. 24, no. 3, pp. 270–273, 2000.
- [168] D. Delaunay, P. Le Bot, R. Fulchiron, J. F. Luye, and G. Regnier, "Nature of contact between polymer and mold in injection molding. Part I: Influence of a non- perfect thermal contact," *Polym. Eng. Sci.*, vol. 40, no. 7, pp. 1682–1691, 2000.
- [169] D. Delaunay, P. Le Bot, R. Fulchiron, J. F. Luye, and G. Regnier, "Nature of contact between polymer and mold in injection molding. Part II: Influence of mold deflection on pressure history and shrinkage," *Polym. Eng. Sci.*, vol. 40, no. 7, pp. 1692–1700, 2000.

- [170] N. Hopkinson and P. Dickens, "Predicting stereolithography injection mould tool behaviour using models to predict ejection force and tool strength," *Int. J. Prod. Res.*, vol. 38, no. 16, pp. 3747–3757, 2000.
- [171] H. Wang, K. K. Kabanemi, and G. Salloum, "Numerical and experimental studies on the ejection of injection- molded plastic products," *Polym. Eng. Sci.*, vol. 40, no. 3, pp. 826–840, 2000.
- [172] G. T. Pham and J. S. Colton, "Ejection force modeling for stereolithography injection molding tools," *Polym. Eng. Sci.*, vol. 42, no. 4, pp. 681–693, 2002.
- [173] A. J. Pontes, A. M. Brito, and A. S. Pouzada, "Assessment of the ejection force in tubular injection moldings," *J. Inject. molding Technol.*, vol. 6, no. 4, pp. 343–352, 2002.
- [174] A. J. Pontes and A. S. Pouzada, "Ejection force in tubular injection moldings. Part I: effect of processing conditions," *Polym. Eng. Sci.*, vol. 44, no. 5, pp. 891–897, 2004.
- [175] A. J. Pontes, A. S. Pouzada, R. Pantani, and G. Titomanlio, "Ejection force of tubular injection moldings. Part II: a prediction model," *Polym. Eng. Sci.*, vol. 45, no. 3, pp. 325–332, 2005.
- [176] N. Bhagavatula, D. Michalski, B. Lilly, and G. Glozer, "Modelling and verification of ejection forces in thermoplastic injection moulding," *Model. Simul. Mater. Sci. Eng.*, vol. 12, no. 3, p. S239, 2004.
- [177] Y. B. Jean-Yves Charmeau 1, Mikaël Chailly, Vincent Gilbert, "Influence of mold surface coatings in injection molding: Application to the ejection stage," *Int. J. Mater. Form.*, vol. 1, no. 1 Supplement, pp. 699–702, 2008.
- [178] J. C. Halpin, *Primer on Composite Materials Analysis*, 2^a ed. New York: CRC Press, 1992, p. 240.
- [179] J. M. Whitney and R. L. McCullough, *Delaware Composites Design Encyc: Micromechanical Materials Modeling - Volume II*. CRC Press, 1990, p. 231.
- [180] R. . J. Crawford, *Plastics Engineering*. Oxford: Butterworth-Heinemann, 2002, p. 505.
- [181] Domo Chemicals, "Data sheet Domolen 1100L," 2007.
- [182] H. Wiebeck and J. Harada, *Plásticos de engenharia: Tecnologia e Aplicações*. São Paulo: Artliber, 2005, p. 349.
- [183] Domo Chemicals, "Data sheet Domolen P1-013-V10-N," 2006.
- [184] Domo Chemicals, "Data sheet Domolen P1-102-V30-N," 2006.

- [185] “NanoMax Polyolefin Masterbatch - Data sheet P-802.”: [Online]. Available: http://www.nanocor.com/tech_sheets/P802.pdf
- [186] J. Scheirs, *Compositional and Failure Analysis of Polymers: A Practical Approach*. Wiley, 2000, p. 806.
- [187] A. Naranjo, M. del P. Noriega, T. Osswald, A. Roldan-Alzate, and J. D. Sierra, *Plastics Testing and Characterization: Industrial Applications*. Hanser Publications, 2008, p. 363.
- [188] PerkinElmer, “Differential Scanning Calorimetry (DSC),” 2010.
- [189] PerkinElmer, “Introduction to dynamic mechanical analysis (DMA),” 2008.
- [190] G. W. Ehrenstein, G. Riedel, and P. Trawiel, *Thermal Analysis Of Plastics: Theory and Practice*. Hanser Gardner Pubns, 2004, p. 368.
- [191] T. Hatakeyama and F. X. Quinn, *Thermal Analysis: Fundamentals and Applications to Polymer Science*. Wiley, 1999, p. 190.
- [192] Malvern Instruments Ltd, “Operator/Installation Manual for the Rosand RH7/10 Rheometers,” 2004.
- [193] E. C. Ferreira, N. M. Neves, R. Muschalle, and A. S. Pouzada, “Friction properties of thermoplastics in injection molding,” in *ANTEC 2001 Conference Proceedings*, 2001, p. 5.
- [194] A. S. Pouzada, E. C. Ferreira, and A. J. Pontes, “Friction properties of moulding thermoplastics,” *Polym. Test.*, vol. 25, no. 8, pp. 1017–1023, 2006.
- [195] K. Delaney, D. Kennedy, and G. Bissacco, “A Study of Friction Testing Methods Applicable to Demoulding Force Prediction for Micro Replicated Parts,” in *Matrib 2010*, 2010.
- [196] M. W. Gonçalves, G. V Salmoria, C. H. Ahrens, and A. S. Pouzada, “Study of tribological properties of moulds obtained by stereolithography,” *Virtual Phys. Prototyp.*, vol. 2, no. 1, pp. 29–36, 2007.
- [197] A. da C. S. Netto, “Desenvolvimento de compósito de resina epóxi e fibras curtas de aço para fabricação rápida de moldes para injeção de termoplásticos,” UFSC, 2008.
- [198] J. S. V. Canevarolo, *Técnicas de caracterização de polímeros*. São Paulo: Artliber, 2003, p. 448.
- [199] S. M. Lee, *Handbook of Composite Reinforcements Stuart M. Lee*. Wiley-VCH, 1992, p. 715.

- [200] S.-Y. Fu and B. Lauke, "Effects of fiber length and fiber orientation distributions on the tensile strength of short-fiber-reinforced polymers," *Compos. Sci. Technol.*, vol. 56, no. 10, pp. 1179–1190, 1996.
- [201] M. C. Ferreira, "Avaliação da contracção e força de extracção em moldações tubulares de PP reforçado com fibra de vidro," Universidade do Minho, 2010.
- [202] H. Shin and E. Park, "Analysis of crack phenomenon for injection- molded screw using moldflow simulation," *J. Appl. Polym. Sci.*, vol. 113, no. 4, pp. 2702–2708, 2009.
- [203] C.-Y. Wu, C.-C. Ku, and H.-Y. Pai, "Injection molding optimization with weld line design constraint using distributed multi-population genetic algorithm," *Int. J. Adv. Manuf. Technol.*, vol. 52, no. 1–4, pp. 131–141, 2011.
- [204] R. A. Tataru, R. M. Sievers, and V. Hierzer, "Modeling the injection molding processing of a polypropylene closure having an integral hinge," *J. Mater. Process. Technol.*, vol. 176, no. 1, pp. 200–204, 2006.
- [205] P. Kennedy, *Flow Analysis of Injection Molds*. Hanser Gardner Publications, 1995, p. 237.
- [206] R. Bretas and M. D'ávila, *Reologia de polímeros fundidos*. São Paulo, 2010, p. 257.
- [207] M. Leite, *Scilab: uma abordagem pratica e didática*. Rio de Janeiro: Editora Ciência Moderna, 2009, p. 601.
- [208] [Online]. Available: <http://www.scilab.org>. [Accessed: 23-Aug-2012].
- [209] "International Workshop on Open Source Software Scilab and its Engineering Application (OSSS-EA'06)," 2006.
- [210] P. Thienel and G. Menges, "Mathematical and experimental determination of temperature, velocity, and pressure fields in flat molds during the filling process in injection molding of thermoplastics," *Polym. Eng. Sci.*, vol. 18, no. 4, pp. 314–320, 1978.

9 Appendix

A1 – Material

Table A1. 1 - Property typical value for Domolen 1100L [181]

Properties	Unit	Test Method	Value
Melt flow rate (MFR 230/2.16)	g/10 m	ISO 1133	6
Technical properties			
Tensile modulus of elasticity (v=1mm/min)	MPa	ISO 527-2	1500
Tensile yield stress (v=50mm/min)	MPa	ISO 527-2	34
Tensile yield strain (v=50mm/min)	%	ISO 527-2	9
Tensile strain at break (v=50mm/min)	%	ISO 527-2	>50
Tensile creep modulus (1000h, elongation ≤0.5%)	MPa	ISO 899-1	380
Shear modulus	MPa	ISO 6721-2	750
Charpy impact strength notched +23°C	kJ/m ²	ISO 179/1eA	3.5
Charpy impact strength notched -30°C	kJ/m ²	ISO 179/1eA	1.5
Charpy impact strength unnotched +23°C	kJ/m ²	ISO 179/1eU	140
Charpy impact strength unnotched -30°C	kJ/m ²	ISO 179/1eU	16
Izod impact strength unnotched +23°C	kJ/m ²	ISO 180/1A	3.5
Izod impact strength unnotched -30°C	kJ/m ²	ISO 180/1A	1.3
Ball indentation hardness (H 132/30 – H358-/30)	MPa	ISO 2039-1	74
Thermal properties			
Melting point, DSC	°C	ISO 3146	163
Heat deflection temperature			
- HDT / A (1.8 MPa)	°C	ISO 75-2	55
- HDT / B (0.45 MPa)	°C	ISO 75-2	85
Vicat softening temperature			
- VST / A (10N)	°C	ISO 306	154
- VST / B (50N)	°C	ISO 306	90
Other properties			
Haze	%	ASTM D 1003	60
Density	g/cm ³	ISO 1183	0.91
Applications			
Closures, housewares, general injection moulding			

Table A1. 2 - Property typical value for Domolen P1-013-V10-N [183]

Properties	Unit	Test	Value
General properties			
Density	g/cm ³	ISO 1183/A	0.96
Ash content (600°C)	%	ISO 3451	10
Melt Flow Rate – MFR (230°C/2.16kg)	g/10min	ISO 1133	8
Moulding shrinkage (after 120h, 23°C, 50% RH)			
- Length	%	ISO 2577	-
- Width	%	ISO 2577	-
Mechanical properties			
Tensile modulus of elasticity (v=1mm/min)	MPa	ISO 527-1A	3500
Tensile yield stress (v=50mm/min)	MPa	ISO 527-1A	-
Tensile yield strain (v=50mm/min)	%	ISO 527-1A	-
Tensile stress at break (v=50mm/min)	MPa	ISO 527-1A	60
Tensile strain at break (v=50mm/min)	%	ISO 527-1A	3.6
Charpy impact strength notched +23°C	kJ/m ²	ISO 179/1eA	5
Charpy impact strength notched -30°C	kJ/m ²	ISO 179/1eA	-
Charpy impact strength unnotched +23°C	kJ/m ²	ISO 179/1eU	40
Charpy impact strength unnotched -30°C	kJ/m ²	ISO 179/1eU	-
Thermal properties			
Melting point, DSC	°C	ISO 3146	166
Heat deflection temperature:			
- HDT/A (1.8 MPa)	°C	ISO 75-2	130
- HDT/B (0.45 MPa)	°C	ISO 75-2	157
Vicat softening temperature:			
- VST/A/50 (10N)	°C	ISO 306	-
- VST/B/50 (50N)	°C	ISO 306	-

Table A1. 3 - Property typical value for Domolen P1-102-V30-N [184]

Properties	Unit	Test	Value
General properties			
Density	g/cm ³	ISO 1183/A	1.12
Ash content (600°C)	%	ISO 3451	30
Melt Flow Rate – MFR (230°C/2.16kg)	g/10min	ISO 1133	7.5
Moulding shrinkage (after 120h, 23°C, 50% RH)			
- Length	%	ISO 2577	-
- Width	%	ISO 2577	-
Mechanical properties			
Tensile modulus of elasticity (v=1mm/min)	MPa	ISO 527-1A	6700
Tensile yield stress (v=50mm/min)	MPa	ISO 527-1A	93
Tensile yield strain (v=50mm/min)	%	ISO 527-1A	-
Tensile stress at break (v=50mm/min)	MPa	ISO 527-1A	-
Tensile strain at break (v=50mm/min)	%	ISO 527-1A	3
Charpy impact strength notched +23°C	kJ/m ²	ISO 179/1eA	8
Charpy impact strength notched -30°C	kJ/m ²	ISO 179/1eA	-
Charpy impact strength unnotched +23°C	kJ/m ²	ISO 179/1eU	50
Charpy impact strength unnotched -30°C	kJ/m ²	ISO 179/1eU	-
Thermal properties			
Melting point, DSC	°C	ISO 3146	167
Heat deflection temperature:			
- HDT/A (1.8 MPa)	°C	ISO 75-2	145
- HDT/B (0.45 MPa)	°C	ISO 75-2	158
Vicat softening temperature:			
- VST/A/50 (10N)	°C	ISO 306	163
- VST/B/50 (50N)	°C	ISO 306	130

A2 – Shrinkage tables

Table A2. 1 - Shrinkage for PP - mould temperature 30°C

Measurement	Mould dimension [mm]	Sample 3		Sample 6		Sample 9		Average shrinkage among samples [%]
		Dimension [mm]	Shrinkage [%]	Dimension [mm]	Shrinkage [%]	Dimension [mm]	Shrinkage [%]	
Int. diameter (D3)	59,880	58,968	1,523	58,950	1,553	58,932	1,583	1,553
Int. diameter (D2)	58,830	57,898	1,584	57,894	1,591	57,884	1,608	1,594
Int. diameter (D1)	57,820	56,952	1,501	56,950	1,505	56,939	1,524	1,510
Ext. diameter (D3)	63,870	62,940	1,456	62,953	1,436	62,978	1,397	1,429
Ext. diameter (D2)	62,810	61,923	1,412	61,920	1,417	61,937	1,390	1,406
Ext. diameter (D1)	61,820	61,050	1,246	61,043	1,257	61,052	1,242	1,248
Height of part	146,000	144,503	1,025	144,480	1,041	144,481	1,040	1,036

Table A2. 2 - Shrinkage for PP - mould temperature 50°C

Measurement	Mould dimension [mm]	Sample 3		Sample 6		Sample 9		Average shrinkage among samples [%]
		Dimension [mm]	Shrinkage [%]	Dimension [mm]	Shrinkage [%]	Dimension [mm]	Shrinkage [%]	
Int. diameter (D3)	59,880	58,912	1,617	58,926	1,593	58,917	1,608	1,606
Int. diameter (D2)	58,830	57,854	1,659	57,864	1,642	57,865	1,640	1,647
Int. diameter (D1)	57,820	56,910	1,574	56,911	1,572	56,920	1,557	1,568
Ext. diameter (D3)	63,870	62,913	1,498	62,890	1,534	62,918	1,491	1,508
Ext. diameter (D2)	62,810	61,871	1,495	61,858	1,516	61,870	1,497	1,502
Ext. diameter (D1)	61,820	60,988	1,346	60,985	1,351	60,980	1,359	1,352
Height of part	146,000	144,480	1,041	144,480	1,041	144,480	1,041	1,041

Table A2. 3 - Shrinkage for PP - mould temperature 75°C

Measurement	Mould dimension [mm]	Sample 3		Sample 6		Sample 9		Average shrinkage among samples [%]
		Dimension [mm]	Shrinkage [%]	Dimension [mm]	Shrinkage [%]	Dimension [mm]	Shrinkage [%]	
Int. diameter (D3)	59,880	58,931	1,585	58,940	1,570	58,940	1,570	1,575
Int. diameter (D2)	58,830	57,866	1,639	57,875	1,623	57,870	1,632	1,631
Int. diameter (D1)	57,820	56,902	1,588	56,908	1,577	56,902	1,588	1,584
Ext. diameter (D3)	63,870	62,930	1,472	62,929	1,473	62,910	1,503	1,483
Ext. diameter (D2)	62,810	61,868	1,500	61,875	1,489	61,870	1,497	1,495
Ext. diameter (D1)	61,820	60,953	1,402	60,961	1,390	60,950	1,407	1,400
Height of part	146,000	144,474	1,045	144,483	1,039	144,480	1,041	1,042

Table A2. 4 - Shrinkage for PP10GF - mould temperature 30°C

Measurement	Mould dimension [mm]	Sample 3		Sample 6		Sample 9		Average shrinkage among samples [%]
		Dimension [mm]	Shrinkage [%]	Dimension [mm]	Shrinkage [%]	Dimension [mm]	Shrinkage [%]	
Int. diameter (D3)	59,880	59,380	0,835	59,376	0,842	59,374	0,845	0,841
Int. diameter (D2)	58,830	58,180	1,105	58,178	1,108	58,179	1,107	1,107
Int. diameter (D1)	57,820	57,206	1,062	57,146	1,166	57,206	1,062	1,097
Ext. diameter (D3)	63,870	63,349	0,816	63,373	0,778	63,347	0,819	0,804
Ext. diameter (D2)	62,810	62,117	1,103	62,122	1,095	62,118	1,102	1,100
Ext. diameter (D1)	61,820	61,225	0,962	61,226	0,961	61,224	0,964	0,962
Height of part	146,000	144,379	1,110	144,477	1,043	144,476	1,044	1,066

Table A2. 5 - Shrinkage for PP10GF - mould temperature 50°C

Measurement	Mould dimension [mm]	Sample 3		Sample 6		Sample 9		Average shrinkage among samples [%]
		Dimension [mm]	Shrinkage [%]	Dimension [mm]	Shrinkage [%]	Dimension [mm]	Shrinkage [%]	
Int. diameter (D3)	59,880	59,389	0,820	59,360	0,868	59,375	0,843	0,844
Int. diameter (D2)	58,830	58,169	1,124	58,165	1,130	58,173	1,117	1,124
Int. diameter (D1)	57,820	57,104	1,238	57,197	1,077	56,955	1,496	1,271
Ext. diameter (D3)	63,870	63,343	0,825	63,345	0,822	63,356	0,805	0,817
Ext. diameter (D2)	62,810	62,093	1,142	62,088	1,149	62,090	1,146	1,146
Ext. diameter (D1)	61,820	61,197	1,008	61,188	1,022	61,183	1,030	1,020
Height of part	146,000	144,476	1,044	144,477	1,043	144,475	1,045	1,044

Table A2. 6 - Shrinkage for PP10GF - mould temperature 75°C

Measurement	Mould dimension [mm]	Sample 3		Sample 6		Sample 9		Average shrinkage among samples [%]
		Dimension [mm]	Shrinkage [%]	Dimension [mm]	Shrinkage [%]	Dimension [mm]	Shrinkage [%]	
Int. diameter (D3)	59,880	59,361	0,867	59,370	0,852	59,388	0,822	0,847
Int. diameter (D2)	58,830	58,172	1,118	58,180	1,105	58,176	1,112	1,112
Int. diameter (D1)	57,820	57,200	1,072	57,212	1,052	57,136	1,183	1,102
Ext. diameter (D3)	63,870	63,346	0,820	63,329	0,847	63,331	0,844	0,837
Ext. diameter (D2)	62,810	62,090	1,146	62,079	1,164	62,077	1,167	1,159
Ext. diameter (D1)	61,820	61,188	1,022	61,170	1,051	61,167	1,056	1,043
Height of part	146,000	144,473	1,046	144,483	1,039	144,478	1,042	1,042

Table A2. 7 - Shrinkage for PP30GF - mould temperature 30°C

Measurement	Mould dimension [mm]	Sample 3		Sample 6		Sample 9		Average shrinkage among samples [%]
		Dimension [mm]	Shrinkage [%]	Dimension [mm]	Shrinkage [%]	Dimension [mm]	Shrinkage [%]	
Int. diameter (D3)	59,880	59,577	0,506	59,578	0,504	59,569	0,519	0,510
Int. diameter (D2)	58,830	58,306	0,891	58,312	0,881	58,313	0,879	0,883
Int. diameter (D1)	57,820	57,278	0,937	57,296	0,906	57,284	0,927	0,924
Ext. diameter (D3)	63,870	63,465	0,634	63,426	0,695	63,444	0,667	0,665
Ext. diameter (D2)	62,810	62,190	0,987	62,181	1,001	62,175	1,011	1,000
Ext. diameter (D1)	61,820	61,252	0,919	61,246	0,929	61,248	0,925	0,924
Height of part	146,000	144,478	1,042	144,477	1,043	144,476	1,044	1,043

Table A2. 8 - Shrinkage for PP30GF - mould temperature 50°C

Measurement	Mould dimension [mm]	Sample 3		Sample 6		Sample 9		Average shrinkage among samples [%]
		Dimension [mm]	Shrinkage [%]	Dimension [mm]	Shrinkage [%]	Dimension [mm]	Shrinkage [%]	
Int. diameter (D3)	59,880	59,585	0,493	59,585	0,493	59,566	0,524	0,503
Int. diameter (D2)	58,830	58,323	0,862	58,325	0,858	58,319	0,869	0,863
Int. diameter (D1)	57,820	57,305	0,891	57,302	0,896	57,303	0,894	0,894
Ext. diameter (D3)	63,870	63,444	0,667	63,447	0,662	63,483	0,606	0,645
Ext. diameter (D2)	62,810	62,166	1,025	62,166	1,025	62,179	1,005	1,018
Ext. diameter (D1)	61,820	61,232	0,951	61,228	0,958	61,244	0,932	0,947
Height of part	146,000	144,476	1,044	144,482	1,040	144,478	1,042	1,042

Table A2. 9 - Shrinkage for PP30GF - mould temperature 75°C

Measurement	Mould dimension [mm]	Sample 3		Sample 6		Sample 9		Average shrinkage among samples [%]
		Dimension [mm]	Shrinkage [%]	Dimension [mm]	Shrinkage [%]	Dimension [mm]	Shrinkage [%]	
Int. diameter (D3)	59,880	59,593	0,479	59,591	0,483	59,582	0,498	0,487
Int. diameter (D2)	58,830	58,332	0,847	58,331	0,848	58,323	0,862	0,852
Int. diameter (D1)	57,820	57,316	0,872	57,008	1,404	57,131	1,192	1,156
Ext. diameter (D3)	63,870	63,429	0,690	63,424	0,698	63,413	0,716	0,701
Ext. diameter (D2)	62,810	62,136	1,073	62,140	1,067	62,150	1,051	1,064
Ext. diameter (D1)	61,820	61,210	0,987	61,219	0,972	61,216	0,977	0,979
Height of part	146,000	144,474	1,045	144,477	1,043	144,474	1,045	1,045

Table A2. 10 - Shrinkage for PP2N - mould temperature 30°C

Measurement	Mould dimension [mm]	Sample 3		Sample 6		Sample 9		Average shrinkage among samples [%]
		Dimension [mm]	Shrinkage [%]	Dimension [mm]	Shrinkage [%]	Dimension [mm]	Shrinkage [%]	
Int. diameter (D3)	59,880	59,111	1,284	59,113	1,281	59,115	1,278	1,281
Int. diameter (D2)	58,830	57,997	1,416	58,007	1,399	58,006	1,401	1,405
Int. diameter (D1)	57,820	56,987	1,441	56,997	1,423	56,998	1,422	1,429
Ext. diameter (D3)	63,870	63,075	1,245	63,084	1,231	63,089	1,223	1,233
Ext. diameter (D2)	62,810	62,029	1,243	62,036	1,232	62,037	1,231	1,235
Ext. diameter (D1)	61,820	61,094	1,174	61,105	1,157	61,100	1,165	1,165
Height of part	146,000	144,481	1,040	144,479	1,042	144,479	1,042	1,041

Table A2. 11 - Shrinkage for PP2N - mould temperature 50°C

Measurement	Mould dimension [mm]	Sample 3		Sample 6		Sample 9		Average shrinkage among samples [%]
		Dimension [mm]	Shrinkage [%]	Dimension [mm]	Shrinkage [%]	Dimension [mm]	Shrinkage [%]	
Int. diameter (D3)	59,880	59,121	1,268	59,123	1,264	59,133	1,247	1,260
Int. diameter (D2)	58,830	58,009	1,396	58,010	1,394	58,016	1,384	1,391
Int. diameter (D1)	57,820	56,972	1,467	56,974	1,463	56,978	1,456	1,462
Ext. diameter (D3)	63,870	63,066	1,259	63,061	1,267	63,065	1,260	1,262
Ext. diameter (D2)	62,810	62,006	1,280	62,012	1,270	62,031	1,240	1,264
Ext. diameter (D1)	61,820	61,063	1,225	61,077	1,202	61,099	1,166	1,198
Height of part	146,000	144,479	1,042	144,485	1,038	144,480	1,041	1,040

Table A2. 12 - Shrinkage for PP2N - mould temperature 75°C

Measurement	Mould dimension [mm]	Sample 3		Sample 6		Sample 9		Average shrinkage among samples [%]
		Dimension [mm]	Shrinkage [%]	Dimension [mm]	Shrinkage [%]	Dimension [mm]	Shrinkage [%]	
Int. diameter (D3)	59,880	59,082	1,333	59,086	1,326	59,082	1,333	1,330
Int. diameter (D2)	58,830	57,963	1,474	57,965	1,470	57,966	1,469	1,471
Int. diameter (D1)	57,820	56,938	1,525	56,938	1,525	56,937	1,527	1,526
Ext. diameter (D3)	63,870	62,992	1,375	62,998	1,365	62,995	1,370	1,370
Ext. diameter (D2)	62,810	61,913	1,428	61,913	1,428	61,918	1,420	1,425
Ext. diameter (D1)	61,820	60,995	1,335	60,994	1,336	60,994	1,336	1,336
Height of part	146,000	144,477	1,043	144,484	1,038	144,483	1,039	1,040

Table A2. 13 - Shrinkage for PP6N - mould temperature 30°C

Measurement	Mould dimension [mm]	Sample 3		Sample 6		Sample 9		Average shrinkage among samples [%]
		Dimension [mm]	Shrinkage [%]	Dimension [mm]	Shrinkage [%]	Dimension [mm]	Shrinkage [%]	
Int. diameter (D3)	59,880	59,136	1,242	59,132	1,249	59,132	1,249	1,247
Int. diameter (D2)	58,830	58,033	1,355	58,029	1,362	58,036	1,350	1,355
Int. diameter (D1)	57,820	57,039	1,351	57,035	1,358	57,042	1,346	1,351
Ext. diameter (D3)	63,870	63,086	1,227	63,075	1,245	63,080	1,237	1,236
Ext. diameter (D2)	62,810	62,048	1,213	62,044	1,220	62,050	1,210	1,214
Ext. diameter (D1)	61,820	61,139	1,102	61,134	1,110	61,137	1,105	1,105
Height of part	146,000	144,481	1,040	144,482	1,040	144,480	1,041	1,040

Table A2. 14 - Shrinkage for PP6N - mould temperature 50°C

Measurement	Mould dimension [mm]	Sample 3		Sample 6		Sample 9		Average shrinkage among samples [%]
		Dimension [mm]	Shrinkage [%]	Dimension [mm]	Shrinkage [%]	Dimension [mm]	Shrinkage [%]	
Int. diameter (D3)	59,880	59,132	1,249	59,133	1,247	59,134	1,246	1,247
Int. diameter (D2)	58,830	58,028	1,363	58,024	1,370	58,030	1,360	1,364
Int. diameter (D1)	57,820	57,028	1,370	57,025	1,375	57,032	1,363	1,369
Ext. diameter (D3)	63,870	63,072	1,249	63,059	1,270	63,061	1,267	1,262
Ext. diameter (D2)	62,810	62,028	1,245	62,007	1,278	62,008	1,277	1,267
Ext. diameter (D1)	61,820	61,110	1,148	61,095	1,173	61,091	1,179	1,167
Height of part	146,000	144,477	1,043	144,476	1,044	144,475	1,045	1,044

Table A2. 15 - - Shrinkage for PP6N - mould temperature 75°C

Measurement	Mould dimension [mm]	Sample 3		Sample 6		Sample 9		Average shrinkage among samples [%]
		Dimension [mm]	Shrinkage [%]	Dimension [mm]	Shrinkage [%]	Dimension [mm]	Shrinkage [%]	
Int. diameter (D3)	59,880	59,067	1,358	59,090	1,319	59,091	1,318	1,332
Int. diameter (D2)	58,830	57,968	1,465	57,978	1,448	57,982	1,441	1,452
Int. diameter (D1)	57,820	56,980	1,453	56,971	1,468	56,978	1,456	1,459
Ext. diameter (D3)	63,870	63,002	1,359	63,004	1,356	63,029	1,317	1,344
Ext. diameter (D2)	62,810	61,943	1,380	61,945	1,377	61,968	1,341	1,366
Ext. diameter (D1)	61,820	61,060	1,229	61,059	1,231	61,067	1,218	1,226
Height of part	146,000	144,480	1,041	144,480	1,041	144,481	1,040	1,041

Table A2. 16 - Shrinkage for PP10N - mould temperature 30°C

Measurement	Mould dimension [mm]	Sample 3		Sample 6		Sample 9		Average shrinkage among samples [%]
		Dimension [mm]	Shrinkage [%]	Dimension [mm]	Shrinkage [%]	Dimension [mm]	Shrinkage [%]	
Int. diameter (D3)	59,880	59,143	1,231	59,161	1,201	59,159	1,204	1,212
Int. diameter (D2)	58,830	58,047	1,331	58,059	1,311	58,063	1,304	1,315
Int. diameter (D1)	57,820	57,063	1,309	57,075	1,288	57,073	1,292	1,297
Ext. diameter (D3)	63,870	63,080	1,237	63,095	1,213	63,096	1,212	1,221
Ext. diameter (D2)	62,810	62,052	1,207	62,060	1,194	62,061	1,192	1,198
Ext. diameter (D1)	61,820	61,143	1,095	61,150	1,084	61,150	1,084	1,088
Height of part	146,000	144,482	1,040	144,480	1,041	144,482	1,040	1,040

Table A2. 17 - Shrinkage for PP10N - mould temperature 50°C

Measurement	Mould dimension [mm]	Sample 3		Sample 6		Sample 9		Average shrinkage among samples [%]
		Dimension [mm]	Shrinkage [%]	Dimension [mm]	Shrinkage [%]	Dimension [mm]	Shrinkage [%]	
Int. diameter (D3)	59,880	59,156	1,209	59,151	1,217	59,157	1,207	1,211
Int. diameter (D2)	58,830	58,065	1,300	58,062	1,305	58,059	1,311	1,305
Int. diameter (D1)	57,820	57,067	1,302	57,065	1,306	57,069	1,299	1,302
Ext. diameter (D3)	63,870	63,088	1,224	63,092	1,218	63,091	1,220	1,221
Ext. diameter (D2)	62,810	62,036	1,232	62,036	1,232	62,044	1,220	1,228
Ext. diameter (D1)	61,820	61,131	1,115	61,126	1,123	61,137	1,105	1,114
Height of part	146,000	144,482	1,040	144,481	1,040	144,482	1,040	1,040

Table A2. 18 - Shrinkage for PP10N - mould temperature 75°C

Measurement	Mould dimension [mm]	Sample 3		Sample 6		Sample 9		Average shrinkage among samples [%]
		Dimension [mm]	Shrinkage [%]	Dimension [mm]	Shrinkage [%]	Dimension [mm]	Shrinkage [%]	
Int. diameter (D3)	59,880	59,123	1,264	59,124	1,263	59,134	1,246	1,258
Int. diameter (D2)	58,830	58,022	1,373	58,020	1,377	58,032	1,356	1,369
Int. diameter (D1)	57,820	57,026	1,373	57,024	1,377	57,038	1,352	1,367
Ext. diameter (D3)	63,870	63,024	1,325	63,022	1,328	63,041	1,298	1,317
Ext. diameter (D2)	62,810	61,961	1,352	61,962	1,350	61,979	1,323	1,342
Ext. diameter (D1)	61,820	61,069	1,215	61,076	1,203	61,084	1,191	1,203
Height of part	146,000	144,477	1,043	144,478	1,042	144,480	1,041	1,042

Table A2. 19 - Shrinkage for PP10GF2N - mould temperature 30°C

Measurement	Mould dimension [mm]	Sample 3		Sample 6		Sample 9		Average shrinkage among samples [%]
		Dimension [mm]	Shrinkage [%]	Dimension [mm]	Shrinkage [%]	Dimension [mm]	Shrinkage [%]	
Int. diameter (D3)	59,880	59,394	0,812	59,375	0,843	59,370	0,852	0,836
Int. diameter (D2)	58,830	58,202	1,067	58,192	1,084	58,192	1,084	1,079
Int. diameter (D1)	57,820	57,233	1,015	57,229	1,022	57,228	1,024	1,020
Ext. diameter (D3)	63,870	63,376	0,773	63,366	0,789	63,379	0,769	0,777
Ext. diameter (D2)	62,810	62,164	1,028	62,159	1,036	62,169	1,021	1,028
Ext. diameter (D1)	61,820	61,256	0,912	61,249	0,924	61,263	0,901	0,912
Height of part	146,000	144,481	1,040	144,478	1,042	144,479	1,042	1,042

Table A2. 20 - Shrinkage for PP10GF2N - mould temperature 50°C

Measurement	Mould dimension [mm]	Sample 3		Sample 6		Sample 9		Average shrinkage among samples [%]
		Dimension [mm]	Shrinkage [%]	Dimension [mm]	Shrinkage [%]	Dimension [mm]	Shrinkage [%]	
Int. diameter (D3)	59,880	59,394	0,812	59,375	0,843	59,370	0,852	0,836
Int. diameter (D2)	58,830	58,202	1,067	58,192	1,084	58,192	1,084	1,079
Int. diameter (D1)	57,820	57,233	1,015	57,229	1,022	57,228	1,024	1,020
Ext. diameter (D3)	63,870	63,376	0,773	63,366	0,789	63,379	0,769	0,777
Ext. diameter (D2)	62,810	62,164	1,028	62,159	1,036	62,169	1,021	1,028
Ext. diameter (D1)	61,820	61,256	0,912	61,249	0,924	61,263	0,901	0,912
Height of part	146,000	144,481	1,040	144,478	1,042	144,479	1,042	1,042

Table A2. 21 - Shrinkage for PP10GF2N - mould temperature 75°C

Measurement	Mould dimension [mm]	Sample 3		Sample 6		Sample 9		Average shrinkage among samples [%]
		Dimension [mm]	Shrinkage [%]	Dimension [mm]	Shrinkage [%]	Dimension [mm]	Shrinkage [%]	
Int. diameter (D3)	59,880	59,385	0,827	59,371	0,850	59,383	0,830	0,836
Int. diameter (D2)	58,830	58,200	1,071	58,191	1,086	58,190	1,088	1,082
Int. diameter (D1)	57,820	57,224	1,031	57,218	1,041	57,213	1,050	1,041
Ext. diameter (D3)	63,870	63,371	0,781	63,378	0,770	63,391	0,750	0,767
Ext. diameter (D2)	62,810	62,151	1,049	62,156	1,041	62,165	1,027	1,039
Ext. diameter (D1)	61,820	61,241	0,937	61,239	0,940	61,243	0,933	0,937
Height of part	146,000	144,481	1,040	144,481	1,040	144,475	1,045	1,042

Table A2. 22 - Shrinkage for PP30GF2N - mould temperature 30°C

Measurement	Mould dimension [mm]	Sample 3		Sample 6		Sample 9		Average shrinkage among samples [%]
		Dimension [mm]	Shrinkage [%]	Dimension [mm]	Shrinkage [%]	Dimension [mm]	Shrinkage [%]	
Int. diameter (D3)	59,880	59,562	0,531	59,581	0,499	59,587	0,489	0,507
Int. diameter (D2)	58,830	58,289	0,920	58,293	0,913	58,299	0,903	0,912
Int. diameter (D1)	57,820	57,279	0,936	57,280	0,934	57,291	0,915	0,928
Ext. diameter (D3)	63,870	63,455	0,650	63,453	0,653	63,470	0,626	0,643
Ext. diameter (D2)	62,810	62,190	0,987	62,193	0,982	62,200	0,971	0,980
Ext. diameter (D1)	61,820	61,248	0,925	61,254	0,916	61,267	0,895	0,912
Height of part	146,000	144,481	1,040	144,483	1,039	144,475	1,045	1,041

Table A2. 23 - Shrinkage for PP30GF2N - mould temperature 50°C

Measurement	Mould dimension [mm]	Sample 3		Sample 6		Sample 9		Average shrinkage among samples [%]
		Dimension [mm]	Shrinkage [%]	Dimension [mm]	Shrinkage [%]	Dimension [mm]	Shrinkage [%]	
Int. diameter (D3)	59,880	59,581	0,499	59,574	0,511	59,583	0,496	0,502
Int. diameter (D2)	58,830	58,311	0,882	58,304	0,894	58,310	0,884	0,887
Int. diameter (D1)	57,820	57,295	0,908	57,291	0,915	57,293	0,911	0,911
Ext. diameter (D3)	63,870	63,473	0,622	63,457	0,647	63,463	0,637	0,635
Ext. diameter (D2)	62,810	62,200	0,971	62,193	0,982	62,190	0,987	0,980
Ext. diameter (D1)	61,820	61,256	0,912	61,257	0,911	61,247	0,927	0,917
Height of part	146,000	144,479	1,042	144,476	1,044	144,480	1,041	1,042

Table A2. 24- Shrinkage for PP30GF2N - mould temperature 75°C

Measurement	Mould dimension [mm]	Sample 3		Sample 6		Sample 9		Average shrinkage among samples [%]
		Dimension [mm]	Shrinkage [%]	Dimension [mm]	Shrinkage [%]	Dimension [mm]	Shrinkage [%]	
Int. diameter (D3)	59,880	59,584	0,494	59,560	0,534	59,561	0,533	0,520
Int. diameter (D2)	58,830	58,309	0,886	58,289	0,920	58,281	0,933	0,913
Int. diameter (D1)	57,820	57,299	0,901	57,282	0,930	57,275	0,943	0,925
Ext. diameter (D3)	63,870	63,422	0,701	63,444	0,667	63,443	0,669	0,679
Ext. diameter (D2)	62,810	62,152	1,048	62,156	1,041	62,158	1,038	1,042
Ext. diameter (D1)	61,820	61,213	0,982	61,216	0,977	61,219	0,972	0,977
Height of part	146,000	144,477	1,043	144,480	1,041	144,487	1,036	1,040

A3 – Ejection force tables

Table A3. 1 - Ejection force for PP0

MOULD TEMPERATURE 30°C							
Part	LOAD CELL 1			LOAD CELL 2			EJECTION FORCE
	BASE	MAX.	ΔF EJECTION	BASE	MAX.	ΔF EJECTION	
PP0-30-1	903,89	1953,13	1049,24	1133,27	2237,01	1103,74	2152,98
PP0-30-2	1183,23	2286,97	1103,74	1085,57	2123,46	1037,89	2141,63
PP0-30-3	1183,23	2289,24	1106,01	1003,82	2050,78	1046,96	2152,97
PP0-30-4	1167,33	2268,80	1101,47	962,94	1998,55	1035,61	2137,08
PP0-30-5	1180,96	2298,33	1117,37	1071,95	2121,18	1049,23	2166,60
PP0-30-6	1165,06	2282,43	1117,37	1031,07	2084,85	1053,78	2171,15
PP0-30-7	1160,52	2252,91	1092,39	1024,26	2066,68	1042,42	2134,81
PP0-30-8	1180,96	2275,62	1094,66	1033,34	2059,87	1026,53	2121,19
PP0-30-9	1199,13	2291,52	1092,39	1049,24	2091,66	1042,42	2134,81
PP0-30-10	1190,04	2252,91	1062,87	1024,26	2041,70	1017,44	2080,31
AVERAGE CEL 1			1093,75	AVERAGE CEL 2			1045,60
STD. DEVIATION			22,02	STD. DEVIATION			23,09
AVERAGE EJECTION FORCE (N)	2139,35			STANDARD DEVIATION			45,11
MOULD TEMPERATURE 50°C							
PP0-50-1	851,65	1680,60	828,95	1203,67	2066,68	863,01	1691,96
PP0-50-2	806,23	1594,30	788,07	1233,19	2071,22	838,03	1626,10
PP0-50-3	813,05	1587,48	774,43	1224,11	2059,87	835,76	1610,19
PP0-50-4	817,59	1562,50	744,91	1253,63	2068,95	815,32	1560,23
PP0-50-5	819,86	1592,02	772,16	1244,55	2075,76	831,21	1603,37
PP0-50-6	819,86	1580,67	760,81	1242,28	2057,59	815,31	1576,12
PP0-50-7	808,50	1537,52	729,02	1228,65	2034,88	806,23	1535,25
PP0-50-8	828,94	1567,04	738,10	1240,01	2039,43	799,42	1537,52
PP0-50-9	831,21	1585,21	754,00	1208,21	2018,99	810,78	1564,78
PP0-50-10	815,32	1573,86	758,54	1183,23	2005,36	822,13	1580,67
AVERAGE CEL 1			764,90	AVERAGE CEL 2			823,72
STD. DEVIATION			28,60	STD. DEVIATION			18,73
AVERAGE EJECTION FORCE (N)	1588,62			STANDARD DEVIATION			47,33
MOULD TEMPERATURE 75°C							
PP0-75-1	1230,92	1701,04	470,12	1140,08	1548,87	408,79	878,91
PP0-75-2	1249,09	1719,20	470,11	1060,59	1467,11	406,52	876,63
PP0-75-3	1221,84	1710,12	488,28	1062,86	1507,99	445,13	933,41
PP0-75-4	1253,63	1707,85	454,22	1060,59	1473,93	413,34	867,56
PP0-75-5	1226,38	1680,60	454,22	1253,47	1639,72	386,25	840,47
PP0-75-6	1237,74	1687,41	449,67	1108,28	1512,54	404,26	853,93
PP0-75-7	1253,63	1698,76	445,13	1094,66	1496,64	401,98	847,11
PP0-75-8	1249,09	1703,31	454,22	1119,64	1507,99	388,35	842,57
PP0-75-9	1240,01	1682,87	442,86	1065,13	1446,68	381,55	824,41
PP0-75-10	1230,92	1666,97	436,05	1124,18	1523,89	399,71	835,76
AVERAGE CEL 1			456,49	AVERAGE CEL 2			403,59
STD. DEVIATION			15,55	STD. DEVIATION			17,93
AVERAGE EJECTION FORCE (N)	860,08			STANDARD DEVIATION			33,48

Table A3. 2 - Ejection force for PP10GF

MOULD TEMPERATURE 30°C							
Part	LOAD CELL 1			LOAD CELL 2			EJECTION FORCE
	BASE	MAX.	ΔF EJECTION	BASE	MAX.	ΔF EJECTION	
PPO-30-1	1183,2	2791,15	1607,92	1135,84	2432,32	1296,48	2904,40
PPO-30-2	1169,60	2770,71	1601,11	1021,98	2307,41	1285,43	2886,54
PPO-30-3	1162,79	2752,54	1589,75	978,83	2266,53	1287,70	2877,45
PPO-30-4	1151,44	2716,21	1564,77	1067,41	2327,85	1260,44	2825,21
PPO-30-5	1144,62	2743,46	1598,84	969,75	2264,26	1294,51	2893,35
PPO-30-6	1153,71	2720,75	1567,04	1026,53	2277,89	1251,36	2818,40
PPO-30-7	1183,23	2750,27	1567,04	1090,12	2352,83	1262,71	2829,75
PPO-30-8	1174,15	2766,17	1592,02	874,29	2266,53	1392,24	2984,26
PPO-30-9	1146,89	2711,66	1564,77	1056,05	2316,50	1260,45	2825,22
PPO-30-10	1162,79	2741,19	1578,40	1106,01	2332,39	1226,38	2804,78
AVERAGE CEL 1			1583,17	AVERAGE CEL 2			1281,77
STD. DEVIATION			16,74	STD. DEVIATION			44,59
AVERAGE EJECTION FORCE (N)			2864,94	STANDARD DEVIATION			61,33
MOULD TEMPERATURE 50°C							
PPO-50-1	826,67	1800,96	974,29	1285,43	2500,45	1215,02	2189,31
PPO-50-2	783,52	1728,29	944,77	1240,01	2418,70	1178,69	2123,46
PPO-50-3	749,45	1678,32	928,87	1226,38	2391,44	1165,06	2093,93
PPO-50-4	774,44	1710,12	935,68	1233,19	2423,24	1190,05	2125,73
PPO-50-5	749,45	1680,60	931,15	1215,03	2386,90	1171,87	2103,02
PPO-50-6	810,77	1778,25	967,48	1278,62	2464,12	1185,50	2152,98
PPO-50-7	769,89	1732,83	962,94	1210,48	2400,53	1190,05	2152,99
PPO-50-8	769,89	1696,49	926,60	1205,94	2384,63	1178,69	2105,29
PPO-50-9	781,25	1710,12	928,87	1230,92	2393,71	1162,79	2091,66
PPO-50-10	849,38	1798,69	949,31	1278,62	2475,47	1196,85	2146,16
AVERAGE CEL 1			945,00	AVERAGE CEL 2			1183,46
STD. DEVIATION			17,77	STD. DEVIATION			15,68
AVERAGE EJECTION FORCE (N)			2128,45	STANDARD DEVIATION			33,45
MOULD TEMPERATURE 75°C							
PPO-75-1	1255,90	2000,82	744,92	981,10	1519,35	538,25	1283,17
PPO-75-2	1276,34	2030,34	754,00	1040,15	1594,30	554,15	1308,15
PPO-75-3	1258,18	1998,55	740,37	1056,05	1603,38	547,33	1287,70
PPO-75-4	1267,26	1998,55	731,29	1074,22	1596,57	522,35	1253,64
PPO-75-5	1274,07	2018,99	744,92	1033,34	1573,86	540,52	1285,44
PPO-75-6	1296,78	2039,43	742,65	981,10	1514,81	533,71	1276,36
PPO-75-7	1294,51	2021,26	726,75	1110,56	1637,45	526,89	1253,64
PPO-75-8	1280,89	2021,26	740,37	1103,74	1651,07	547,33	1287,70
PPO-75-9	1264,99	2007,63	742,64	1042,42	1582,94	540,52	1283,16
PPO-75-10	1260,45	2023,53	763,08	1008,36	1564,77	556,41	1319,49
AVERAGE CEL 1			743,10	AVERAGE CEL 2			540,75
STD. DEVIATION			10,26	STD. DEVIATION			11,05
AVERAGE EJECTION FORCE (N)			1283,85	STANDARD DEVIATION			21,30

Table A3. 3 - Ejection force for PP30GF

MOULD TEMPERATURE 30°C							
Part	LOAD CELL 1			LOAD CELL 2			EJECTION FORCE
	BASE	MAX.	ΔF EJECTION	BASE	MAX.	ΔF EJECTION	
PPO-30-1	1192,3	3088,66	1896,35	1078,76	2636,72	1557,96	3454,31
PPO-30-2	1155,98	3097,75	1941,77	1074,22	2684,41	1610,19	3551,96
PPO-30-3	1171,88	3147,71	1975,83	1074,22	2686,68	1612,46	3588,29
PPO-30-4	1187,77	3143,17	1955,40	1028,80	2645,80	1617,00	3572,40
PPO-30-5	1185,50	3093,90	1908,40	1028,80	2582,21	1553,41	3461,81
PPO-30-6	1169,60	3113,64	1944,04	956,12	2529,28	1573,16	3517,20
PPO-30-7	1169,60	3113,64	1944,04	1058,32	2641,26	1582,94	3526,98
PPO-30-8	1183,23	3127,70	1944,47	1106,01	2711,66	1605,65	3550,12
PPO-30-9	1151,44	3086,39	1934,95	937,95	2493,64	1555,69	3490,64
PPO-30-10	1167,33	3070,49	1903,16	1090,12	2620,82	1530,70	3433,86
AVERAGE CEL 1			1934,84	AVERAGE CEL 2			1579,92
STD. DEVIATION			24,94	STD. DEVIATION			30,30
AVERAGE EJECTION FORCE (N)			3514,76	STANDARD DEVIATION			55,24
MOULD TEMPERATURE 50°C							
PPO-50-1	772,17	2207,49	1435,32	1244,55	2904,71	1660,16	3095,48
PPO-50-2	799,42	2134,81	1335,39	1249,09	2841,12	1592,03	2927,42
PPO-50-3	778,98	2150,71	1371,73	1230,92	2847,93	1617,01	2988,74
PPO-50-4	774,44	2118,91	1344,47	1221,84	2838,84	1617,00	2961,47
PPO-50-5	803,96	2146,17	1342,21	1242,28	2854,74	1612,46	2954,67
PPO-50-6	881,18	2246,09	1364,91	1219,57	2843,39	1623,82	2988,73
PPO-50-7	778,98	2191,59	1412,61	1217,30	2870,64	1653,34	3065,95
PPO-50-8	792,61	2212,03	1419,42	1196,86	2850,20	1653,34	3072,76
PPO-50-9	783,52	2177,96	1394,44	1212,75	2863,83	1651,08	3045,52
PPO-50-10	790,33	2128,00	1337,67	1210,48	2834,30	1623,82	2961,49
AVERAGE CEL 1			1375,82	AVERAGE CEL 2			1630,41
STD. DEVIATION			37,24	STD. DEVIATION			22,62
AVERAGE EJECTION FORCE (N)			3006,22	STANDARD DEVIATION			59,86
MOULD TEMPERATURE 75°C							
PPO-75-1	1251,36	2241,55	990,19	983,38	1732,83	749,45	1739,64
PPO-75-2	1262,72	2257,45	994,73	999,27	1741,91	742,64	1737,37
PPO-75-3	1269,53	2255,18	985,65	1001,54	1771,44	769,90	1755,55
PPO-75-4	1255,90	2264,26	1008,36	1051,17	1773,71	722,54	1730,90
PPO-75-5	1283,16	2271,08	987,92	931,14	1682,87	751,73	1739,65
PPO-75-6	1271,80	2248,36	976,56	1015,17	1778,25	763,08	1739,64
PPO-75-7	1262,72	2261,99	999,27	1021,98	1807,78	785,80	1785,07
PPO-75-8	1262,72	2246,09	983,37	1031,07	1796,42	765,35	1748,72
PPO-75-9	1251,36	2234,74	983,38	972,02	1746,46	774,44	1757,82
PPO-75-10	1280,89	2255,18	974,29	981,01	1726,02	745,01	1719,30
AVERAGE CEL 1			988,37	AVERAGE CEL 2			756,99
STD. DEVIATION			10,31	STD. DEVIATION			18,35
AVERAGE EJECTION FORCE (N)			1745,37	STANDARD DEVIATION			28,66

Table A3. 4 - Ejection force for PP2N

MOULD TEMPERATURE 30°C							
Part	LOAD CELL 1			LOAD CELL 2			EJECTION FORCE
	BASE	MAX.	ΔF EJECTION	BASE	MAX.	ΔF EJECTION	
PPO-30-1	1106	2114,37	1008,36	1085,57	2152,98	1067,41	2075,77
PPO-30-2	1192,31	2150,71	958,40	1124,18	2146,17	1021,99	1980,39
PPO-30-3	1112,83	2089,39	976,56	1106,01	2148,44	1042,43	2018,99
PPO-30-4	1153,71	2107,56	953,85	1121,91	2157,52	1035,61	1989,46
PPO-30-5	1235,47	2168,88	933,41	1137,81	2148,44	1010,63	1944,04
PPO-30-6	1140,08	2096,20	956,12	1126,45	2143,90	1017,45	1973,57
PPO-30-7	1090,12	2018,99	928,87	1103,74	2107,56	1003,82	1932,69
PPO-30-8	1119,64	2046,24	926,60	1110,56	2112,10	1001,54	1928,14
PPO-30-9	1112,83	2068,95	956,12	1110,56	2130,27	1019,71	1975,83
PPO-30-10	1099,20	2034,88	935,68	1106,01	2107,56	1001,55	1937,23
AVERAGE CEL 1			953,40	AVERAGE CEL 2		1022,21	
STD. DEVIATION			25,01	STD. DEVIATION		21,05	
AVERAGE EJECTION FORCE (N)			1975,61	STANDARD DEVIATION			46,06
MOULD TEMPERATURE 50°C							
PPO-50-1	1217,30	1953,13	735,83	1110,56	1912,25	801,69	1537,52
PPO-50-2	1078,76	1805,51	726,75	1101,47	1887,26	785,79	1512,54
PPO-50-3	1183,23	1925,87	742,64	1131,00	1921,33	790,33	1532,97
PPO-50-4	1060,59	1807,78	747,19	1096,93	1884,99	788,06	1535,25
PPO-50-5	1065,13	1785,07	719,94	1094,66	1860,01	765,35	1485,29
PPO-50-6	1051,51	1789,61	738,10	1083,30	1864,55	781,25	1519,35
PPO-50-7	1076,49	1796,42	719,93	1108,28	1884,99	776,71	1496,64
PPO-50-8	1049,24	1782,79	733,55	1085,57	1853,20	767,63	1501,18
PPO-50-9	1019,71	1769,17	749,46	1096,93	1853,20	756,27	1505,73
PPO-50-10	1035,61	1796,42	760,81	1103,74	1880,45	776,71	1537,52
AVERAGE CEL 1			737,42	AVERAGE CEL 2		778,98	
STD. DEVIATION			13,16	STD. DEVIATION		13,41	
AVERAGE EJECTION FORCE (N)			1516,40	STANDARD DEVIATION			26,57
MOULD TEMPERATURE 75°C							
PPO-75-1	1049,24	1489,83	440,59	1083,30	1594,30	511,00	951,59
PPO-75-2	1076,49	1505,72	429,23	1083,30	1587,48	504,18	933,41
PPO-75-3	1087,85	1507,99	420,14	1101,47	1594,30	492,83	912,97
PPO-75-4	1183,23	1603,38	420,15	1121,91	1605,65	483,74	903,89
PPO-75-5	1085,57	1512,54	426,97	1124,18	1605,65	481,47	908,44
PPO-75-6	1128,72	1544,33	415,61	1115,10	1598,84	483,74	899,35
PPO-75-7	1094,66	1505,72	411,06	1115,10	1598,84	483,74	894,80
PPO-75-8	1151,44	1569,31	417,87	1110,56	1592,02	481,46	899,33
PPO-75-9	1128,72	1553,42	424,70	1103,74	1571,58	467,84	892,54
PPO-75-10	1106,01	1510,27	404,26	1124,18	1607,92	483,74	888,00
AVERAGE CEL 1			421,06	AVERAGE CEL 2		487,37	
STD. DEVIATION			10,11	STD. DEVIATION		12,36	
AVERAGE EJECTION FORCE (N)			908,43	STANDARD DEVIATION			22,47

Table A3. 5 - Ejection force for PP6N

MOULD TEMPERATURE 30°C							
Part	LOAD CELL 1			LOAD CELL 2			EJECTION FORCE
	BASE	MAX.	ΔF EJECTION	BASE	MAX.	ΔF EJECTION	
PPO-30-1	1053,8	2016,72	962,94	1094,66	2132,54	1037,88	2000,82
PPO-30-2	1128,72	2091,66	962,94	1142,35	2166,61	1024,26	1987,20
PPO-30-3	1067,41	1996,28	928,87	1112,83	2103,02	990,19	1919,06
PPO-30-4	1085,57	2016,72	931,15	1119,64	2118,91	999,27	1930,42
PPO-30-5	1040,15	2007,63	967,48	1110,56	2130,27	1019,71	1987,19
PPO-30-6	1042,42	2009,90	967,48	1096,93	2137,08	1040,15	2007,63
PPO-30-7	1242,28	2180,23	937,95	1208,21	2216,57	1008,36	1946,31
PPO-30-8	1040,15	1984,92	944,77	1103,74	2093,93	990,19	1934,96
PPO-30-9	1058,32	1991,73	933,41	1126,45	2103,02	976,57	1909,98
PPO-30-10	1058,32	2032,61	974,29	1117,37	2123,46	1006,09	1980,38
AVERAGE CEL 1			951,13	AVERAGE CEL 2		1009,27	
STD. DEVIATION			17,55	STD. DEVIATION		21,12	
AVERAGE EJECTION FORCE (N)			1960,40	STANDARD DEVIATION			38,67
MOULD TEMPERATURE 50°C							
PPO-50-1	1071,95	1782,79	710,84	1124,18	1925,87	801,69	1512,53
PPO-50-2	1031,07	1723,75	692,68	1135,54	1898,62	763,08	1455,76
PPO-50-3	1058,32	1751,00	692,68	1121,91	1900,89	778,98	1471,66
PPO-50-4	1085,57	1764,63	679,06	1160,52	1921,33	760,81	1439,87
PPO-50-5	1051,51	1737,37	685,86	1155,98	1912,25	756,27	1442,13
PPO-50-6	1056,05	1730,56	674,51	1171,88	1909,97	738,09	1412,60
PPO-50-7	1140,08	1816,86	676,78	1174,15	1925,87	751,72	1428,50
PPO-50-8	1081,03	1757,81	676,78	1165,06	1916,79	751,73	1428,51
PPO-50-9	1049,24	1741,91	692,67	1158,25	1928,14	769,89	1462,56
PPO-50-10	1131,00	1803,23	672,23	1185,50	1928,14	742,64	1414,87
AVERAGE CEL 1			685,41	AVERAGE CEL 2		761,49	
STD. DEVIATION			11,96	STD. DEVIATION		18,61	
AVERAGE EJECTION FORCE (N)			1446,90	STANDARD DEVIATION			30,57
MOULD TEMPERATURE 75°C							
PPO-75-1	1142,35	1560,23	417,88	1101,47	1612,46	510,99	928,87
PPO-75-2	1171,88	1585,21	413,33	1124,18	1610,19	486,01	899,34
PPO-75-3	1060,59	1476,20	415,61	1140,08	1628,36	488,28	903,89
PPO-75-4	1069,68	1476,20	406,52	1140,08	1639,72	499,64	906,16
PPO-75-5	1094,66	1501,18	406,52	1140,08	1628,36	488,28	894,80
PPO-75-6	1101,47	1505,72	404,25	1137,81	1630,63	492,82	897,07
PPO-75-7	1051,51	1464,84	413,33	1158,25	1648,80	490,55	903,88
PPO-75-8	1112,83	1514,81	401,98	1146,89	1623,82	476,93	878,91
PPO-75-9	1062,86	1476,20	413,34	1149,16	1628,36	479,20	892,54
PPO-75-10	1074,22	1483,01	408,79	1140,08	1632,90	492,82	901,61
AVERAGE CEL 1			410,16	AVERAGE CEL 2		490,55	
STD. DEVIATION			5,27	STD. DEVIATION		9,75	
AVERAGE EJECTION FORCE (N)			900,71	STANDARD DEVIATION			15,02

Table A3. 6 - Ejection force for PP10N

MOULD TEMPERATURE 30°C							
Part	LOAD CELL 1			LOAD CELL 2			EJECTION FORCE
	BASE	MAX.	ΔF EJECTION	BASE	MAX.	ΔF EJECTION	
PPO-30-1	1015,2	1959,94	944,77	1083,30	2157,52	1074,22	2018,99
PPO-30-2	1037,88	1991,73	953,85	1115,10	2187,05	1071,95	2025,80
PPO-30-3	1135,54	2071,22	935,68	1115,10	2168,88	1053,78	1989,46
PPO-30-4	1017,44	1987,19	969,75	1099,20	2184,77	1085,57	2055,32
PPO-30-5	1035,61	1971,29	935,68	1108,28	2173,42	1065,14	2000,82
PPO-30-6	1060,59	1998,55	937,96	1112,83	2155,25	1042,42	1980,38
PPO-30-7	1155,98	2073,49	917,51	1167,33	2209,76	1042,43	1959,94
PPO-30-8	1096,93	2018,99	922,06	1140,08	2177,96	1037,88	1959,94
PPO-30-9	1042,42	1966,75	924,33	1115,10	2148,44	1033,34	1957,67
PPO-30-10	1108,28	2021,26	912,98	1137,81	2168,88	1031,07	1944,05
AVERAGE CEL 1			935,46	AVERAGE CEL 2			1053,78
STD. DEVIATION			17,44	STD. DEVIATION			19,24
AVERAGE EJECTION FORCE (N)			1989,24	STANDARD DEVIATION			36,68
MOULD TEMPERATURE 50°C							
PPO-50-1	1094,66	1805,51	710,85	1108,28	1928,14	819,86	1530,71
PPO-50-2	1149,16	1835,03	685,87	1142,35	1941,77	799,42	1485,29
PPO-50-3	1103,74	1798,69	694,95	1140,08	1930,41	790,33	1485,28
PPO-50-4	1081,03	1775,98	694,95	1137,81	1928,14	790,33	1485,28
PPO-50-5	1094,66	1766,90	672,24	1137,81	1923,60	785,79	1458,03
PPO-50-6	1087,85	1775,98	688,13	1140,08	1937,23	797,15	1485,28
PPO-50-7	1090,12	1773,71	683,59	1144,62	1928,14	783,52	1467,11
PPO-50-8	1092,39	1769,17	676,78	1137,81	1919,06	781,25	1458,03
PPO-50-9	1119,64	1791,88	672,24	1146,89	1923,60	776,71	1448,95
PPO-50-10	1083,30	1746,46	663,16	1142,35	1916,79	774,44	1437,60
AVERAGE CEL 1			684,28	AVERAGE CEL 2			789,88
STD. DEVIATION			13,92	STD. DEVIATION			13,28
AVERAGE EJECTION FORCE (N)			1474,16	STANDARD DEVIATION			27,20
MOULD TEMPERATURE 75°C							
PPO-75-1	1017,44	1444,40	426,96	1158,25	1653,34	495,09	922,05
PPO-75-2	1051,51	1458,03	406,52	1158,25	1655,61	497,36	903,88
PPO-75-3	1058,32	1462,57	404,25	1165,06	1648,80	483,74	887,99
PPO-75-4	1067,41	1473,93	406,52	1160,52	1641,99	481,47	887,99
PPO-75-5	1131,00	1542,06	411,06	1160,52	1646,53	486,01	897,07
PPO-75-6	1092,39	1494,37	401,98	1158,25	1646,53	488,28	890,26
PPO-75-7	1117,37	1526,16	408,79	1165,06	1651,07	486,01	894,80
PPO-75-8	1115,10	1510,27	395,17	1176,42	1657,89	481,47	876,64
PPO-75-9	1108,28	1526,16	417,88	1199,13	1698,76	499,63	917,51
PPO-75-10			0,00			0,00	0,00
AVERAGE CEL 1			408,79	AVERAGE CEL 2			488,78
STD. DEVIATION			9,22	STD. DEVIATION			6,88
AVERAGE EJECTION FORCE (N)			897,58	STANDARD DEVIATION			16,11

Table A3. 7 - Ejection force for PP10GF2N

MOULD TEMPERATURE 30°C							
Part	LOAD CELL 1			LOAD CELL 2			EJECTION FORCE
	BASE	MAX.	ΔF EJECTION	BASE	MAX.	ΔF EJECTION	
PPO-30-1	1162,8	2371,00	1208,21	1124,18	2634,45	1510,27	2718,48
PPO-30-2	1131,00	2298,33	1167,33	1137,81	2586,76	1448,95	2616,28
PPO-30-3	1271,80	2443,68	1171,88	1212,75	2675,33	1462,58	2634,46
PPO-30-4	1090,12	2237,01	1146,89	1133,27	2577,67	1444,40	2591,29
PPO-30-5	1092,39	2237,01	1144,62	1126,45	2550,42	1423,97	2568,59
PPO-30-6	1230,92	2400,53	1169,61	1194,59	2695,77	1501,18	2670,79
PPO-30-7	1135,54	2286,97	1151,43	1167,33	2618,55	1451,22	2602,65
PPO-30-8	1117,37	2289,24	1171,87	1160,52	2625,36	1464,84	2636,71
PPO-30-9	1074,22	2234,74	1160,52	1094,66	2541,33	1446,67	2607,19
PPO-30-10	1187,77	2371,00	1183,23	1185,50	2652,62	1467,12	2650,35
AVERAGE CEL 1			1167,56	AVERAGE CEL 2			1462,12
STD. DEVIATION			18,86	STD. DEVIATION			26,20
AVERAGE EJECTION FORCE (N)			2629,68	STANDARD DEVIATION			45,06
MOULD TEMPERATURE 50°C							
PPO-50-1	1203,67	2132,54	928,87	1162,79	2352,83	1190,04	2118,91
PPO-50-2	1081,03	1966,75	885,72	1142,35	2268,80	1126,45	2012,17
PPO-50-3	1071,95	1941,77	869,82	1149,16	2334,67	1185,51	2055,33
PPO-50-4	1060,59	1957,67	897,08	1144,62	2309,68	1165,06	2062,14
PPO-50-5	1031,07	1907,70	876,63	1103,74	2255,18	1151,44	2028,07
PPO-50-6	1085,57	1969,02	883,45	1151,44	2316,50	1165,06	2048,51
PPO-50-7	1062,86	1957,67	894,81	1158,25	2332,39	1174,14	2068,95
PPO-50-8	1085,57	1971,29	885,72	1146,89	2296,06	1149,17	2034,89
PPO-50-9	1149,16	2034,88	885,72	1167,33	2323,31	1155,98	2041,70
PPO-50-10	1228,65	2098,47	869,82	1194,59	2323,31	1128,72	1998,54
AVERAGE CEL 1			887,76	AVERAGE CEL 2			1159,16
STD. DEVIATION			17,08	STD. DEVIATION			21,36
AVERAGE EJECTION FORCE (N)			2046,92	STANDARD DEVIATION			38,44
MOULD TEMPERATURE 75°C							
PPO-75-1	1115,10	1646,53	531,43	1137,81	1905,43	767,62	1299,05
PPO-75-2	1035,61	1537,52	501,91	1128,72	1839,57	710,85	1212,76
PPO-75-3	1046,97	1542,06	495,09	1142,35	1855,47	713,12	1208,21
PPO-75-4	1126,45	1619,28	492,83	1155,98	1884,99	729,01	1221,84
PPO-75-5	1037,88	1539,79	501,91	1158,25	1884,99	726,74	1228,65
PPO-75-6	1033,34	1542,06	508,72	1158,25	1884,99	726,74	1235,46
PPO-75-7	1053,78	1555,69	501,91	1151,44	1855,47	704,03	1205,94
PPO-75-8	1062,86	1569,31	506,45	1151,44	1873,64	722,20	1228,65
PPO-75-9	1049,24	1551,14	501,90	1151,44	1857,74	706,30	1208,20
PPO-75-10	1056,05	1562,50	506,45	1158,25	1871,37	713,12	1219,57
AVERAGE CEL 1			504,86	AVERAGE CEL 2			721,97
STD. DEVIATION			10,55	STD. DEVIATION			18,34
AVERAGE EJECTION FORCE (N)			1226,83	STANDARD DEVIATION			28,88

Table A3. 8 - Ejection force for PP30GF2N

MOULD TEMPERATURE 30°C							
Part	LOAD CELL 1			LOAD CELL 2			EJECTION FORCE
	BASE	MAX.	ΔF EJECTION	BASE	MAX.	ΔF EJECTION	
PPO-30-1	1230,9	2854,74	1623,82	1153,71	3138,63	1984,92	3608,74
PPO-30-2	1260,45	2877,45	1617,00	1171,88	3131,81	1959,93	3576,93
PPO-30-3	1301,33	2936,50	1635,17	1167,33	3156,80	1989,47	3624,64
PPO-30-4	1242,28	2832,03	1589,75	1199,13	3111,37	1912,24	3501,99
PPO-30-5	1106,01	2698,04	1592,03	1133,27	3050,05	1916,78	3508,81
PPO-30-6	1274,07	2834,30	1560,23	1183,23	3097,75	1914,52	3474,75
PPO-30-7	1103,74	2659,43	1555,69	1151,44	3047,78	1896,34	3452,03
PPO-30-8	1169,60	2748,00	1578,40	1171,88	3106,83	1934,95	3513,35
PPO-30-9	1103,74	2666,24	1562,50	1133,27	3038,70	1905,43	3467,93
PPO-30-10	1158,25	2729,83	1571,58	1155,98	3054,60	1898,62	3470,20
AVERAGE CEL 1			1588,62	AVERAGE CEL 2			1931,32
STD. DEVIATION			28,27	STD. DEVIATION			34,81
AVERAGE EJECTION FORCE (N)			3519,94	STANDARD DEVIATION			63,08
MOULD TEMPERATURE 50°C							
PPO-50-1	1224,11	2589,03	1364,92	1108,28	2772,98	1664,70	3029,62
PPO-50-2	1251,36	2507,27	1255,91	1115,10	2688,95	1573,85	2829,76
PPO-50-3	1069,68	2332,39	1262,71	1112,83	2727,56	1614,73	2877,44
PPO-50-4	1260,45	2548,15	1287,70	1135,54	2695,77	1560,23	2847,93
PPO-50-5	1571,58	2832,03	1260,45	1494,37	3077,31	1582,94	2843,39
PPO-50-6	1319,49	2557,23	1237,74	1167,33	2738,92	1571,59	2809,33
PPO-50-7	1185,50	2482,29	1296,79	1142,35	2782,07	1639,72	2936,51
PPO-50-8	1324,04	2614,01	1289,97	1137,81	2759,36	1621,55	2911,52
PPO-50-9	1085,57	2368,73	1283,16	1121,91	2770,71	1648,80	2931,96
PPO-50-10	1251,36	2550,42	1299,06	1128,72	2732,10	1603,38	2902,44
AVERAGE CEL 1			1283,84	AVERAGE CEL 2			1608,15
STD. DEVIATION			34,84	STD. DEVIATION			35,80
AVERAGE EJECTION FORCE (N)			2891,99	STANDARD DEVIATION			70,65
MOULD TEMPERATURE 75°C							
PPO-75-1	1187,77	2021,26	833,49	1101,47	2171,15	1069,68	1903,17
PPO-75-2	1140,08	1925,87	785,79	1133,27	2168,88	1035,61	1821,40
PPO-75-3	1071,95	1828,22	756,27	1126,45	2152,98	1026,53	1782,80
PPO-75-4	1158,25	1932,69	774,44	1137,81	2148,44	1010,63	1785,07
PPO-75-5	1137,81	1914,52	776,71	1124,18	2137,08	1012,90	1789,61
PPO-75-6	1199,13	1966,75	767,62	1140,08	2137,08	997,00	1764,62
PPO-75-7	1242,28	2007,63	765,35	1137,81	2132,54	994,73	1760,08
PPO-75-8	1103,74	1871,37	767,63	1146,89	2134,81	987,92	1755,55
PPO-75-9	1117,37	1882,72	765,35	1137,81	2155,25	1017,44	1782,79
PPO-75-10	1121,91	1889,53	767,62	1140,08	2148,44	1008,36	1775,98
AVERAGE CEL 1			776,03	AVERAGE CEL 2			1016,08
STD. DEVIATION			21,68	STD. DEVIATION			23,75
AVERAGE EJECTION FORCE (N)			1792,11	STANDARD DEVIATION			45,43

A4 – Crystallization temperature curves

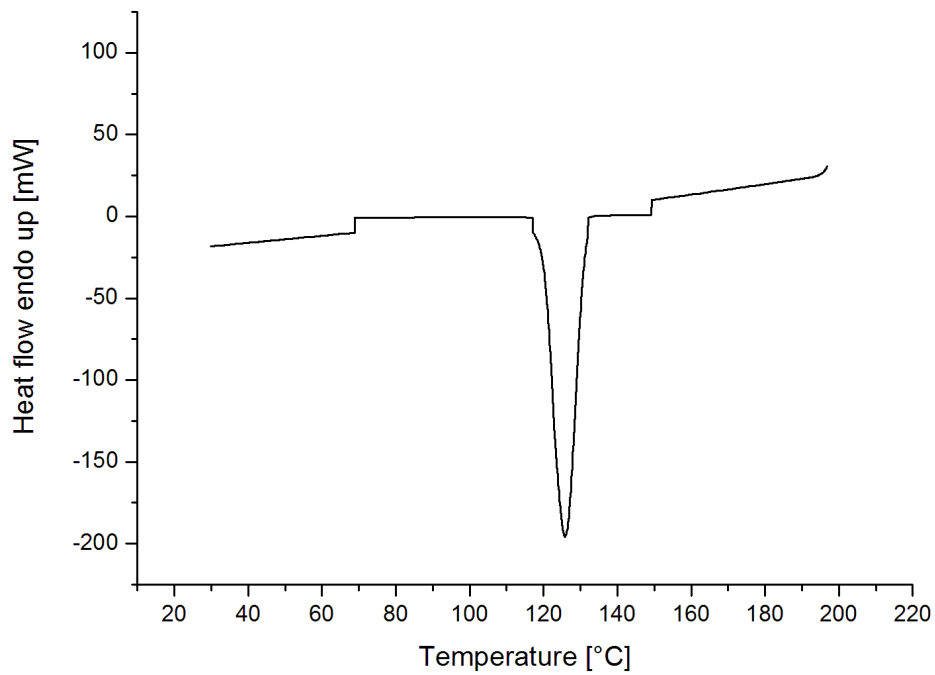


Figure A4. 1 - Crystallization curve for PP2N

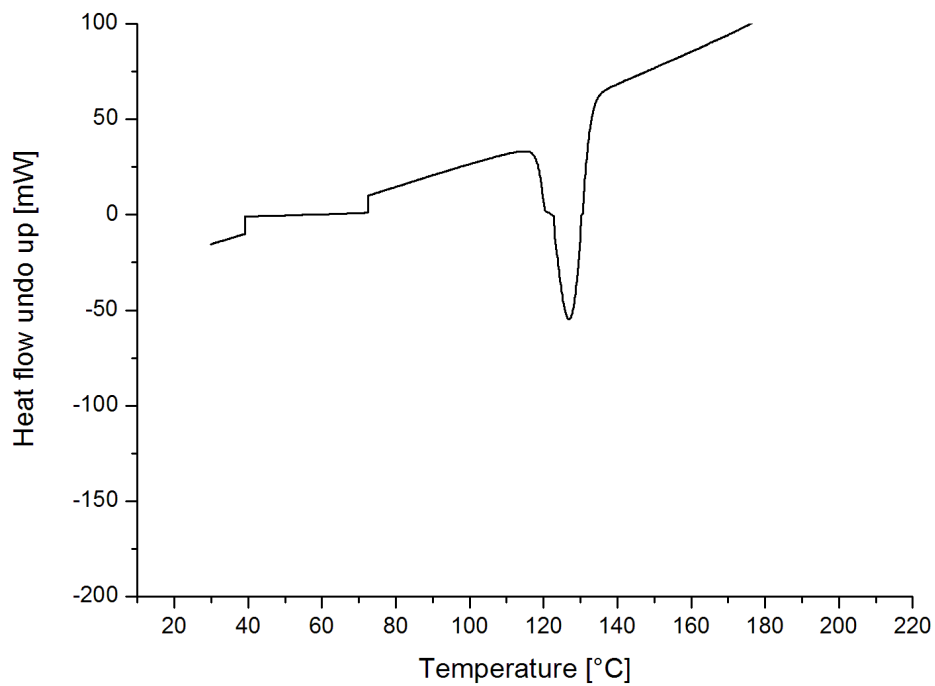


Figure A4. 2 - Crystallization curve for PP6N

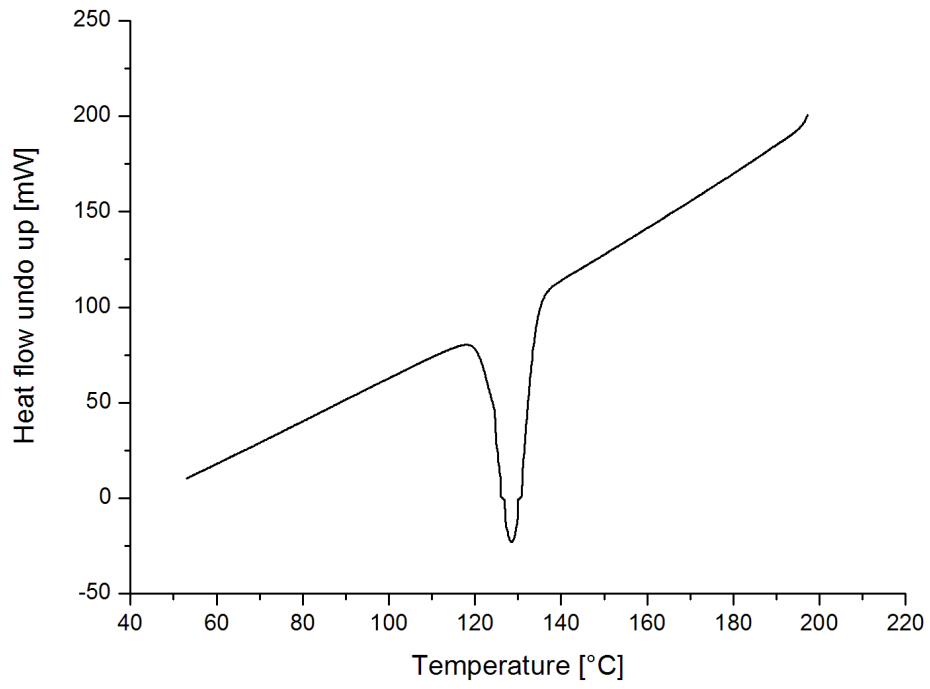


Figure A4. 3 - Crystallization curve for PP10N

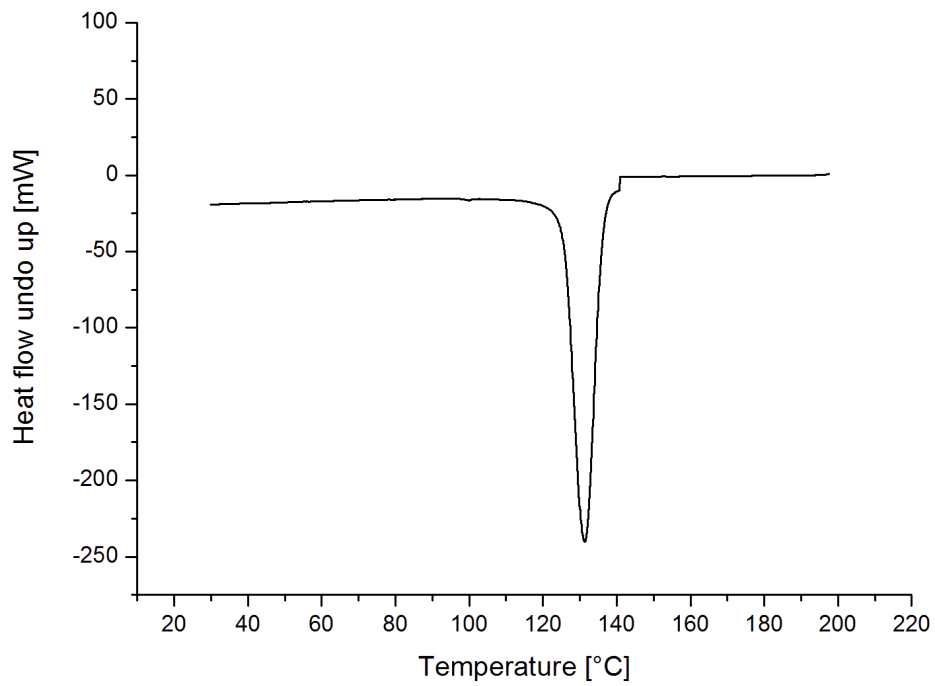


Figure A4. 4 - Crystallization curve for PP10GF

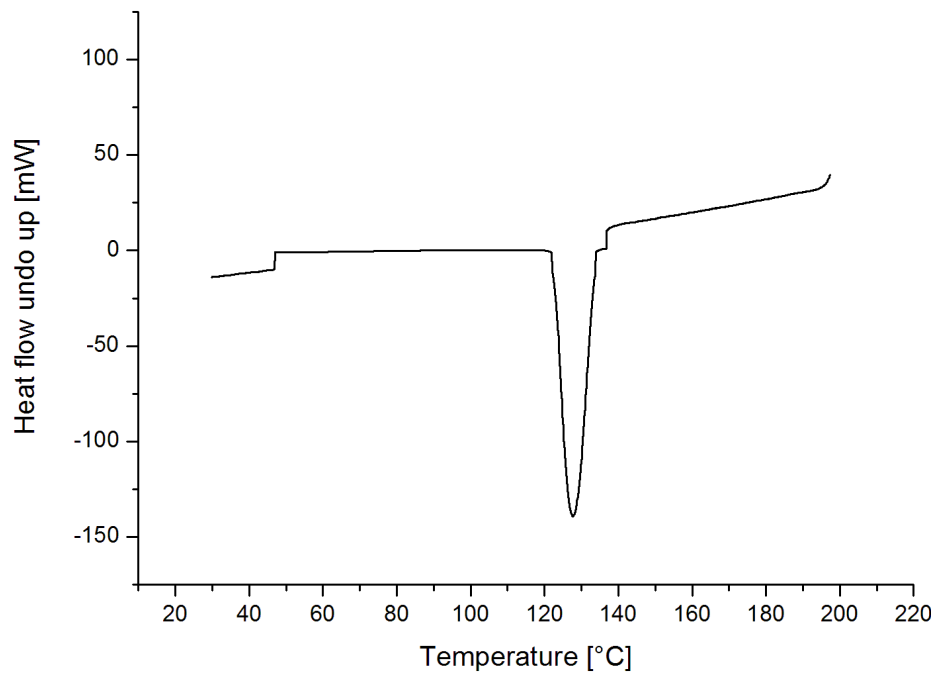


Figure A4. 5 - Crystallization curve for PP30GF

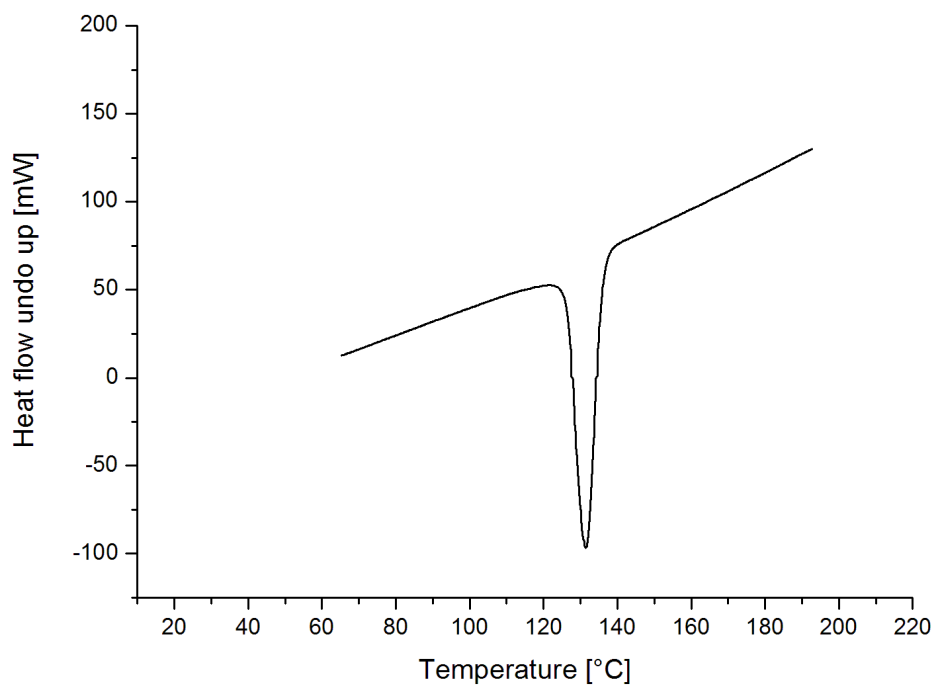


Figure A4. 6 - Crystallization curve for PP10GF2N

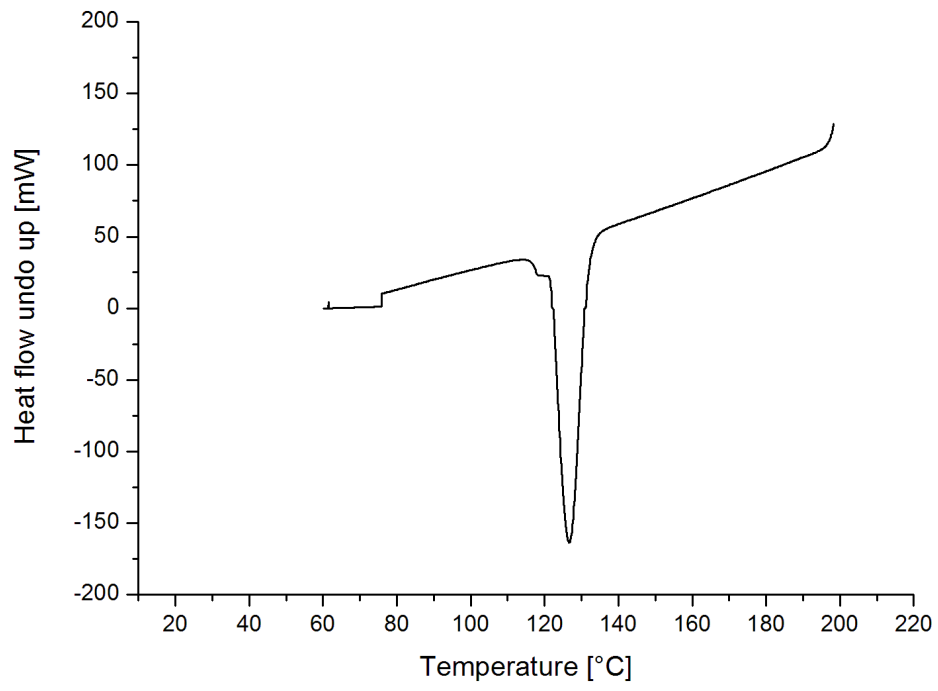


Figure A4. 7 - Crystallization curve for PP30GF2N

A5 – DMA curves

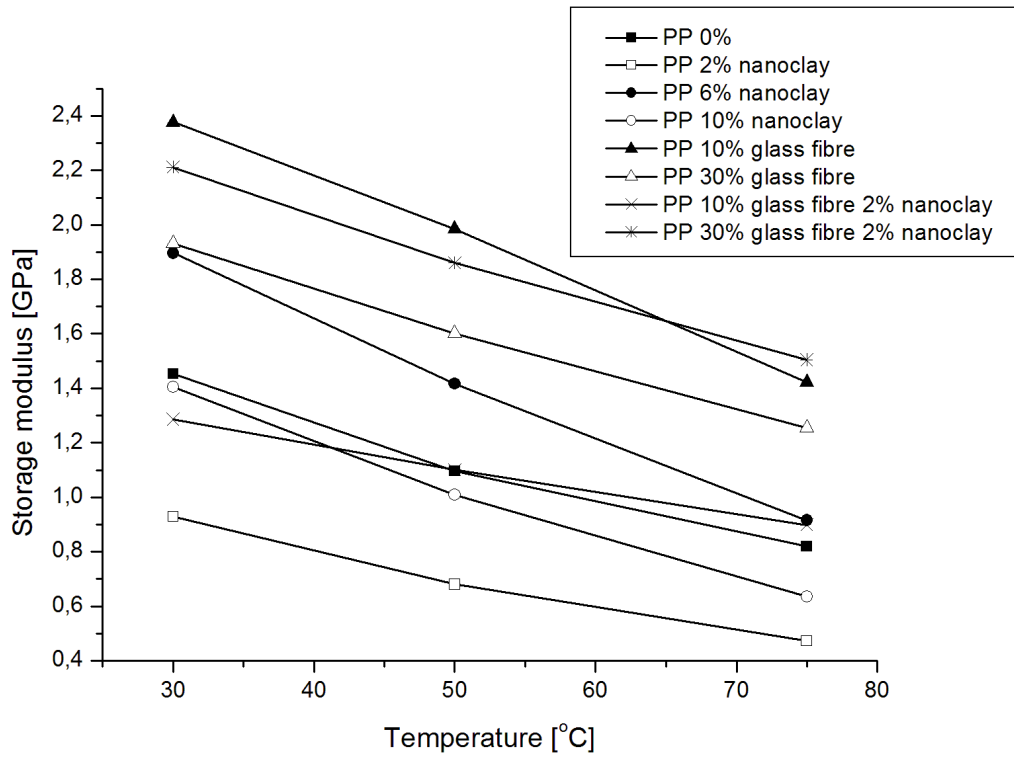


Figure A5. 1 - Storage modulus for several materials relation to the temperature

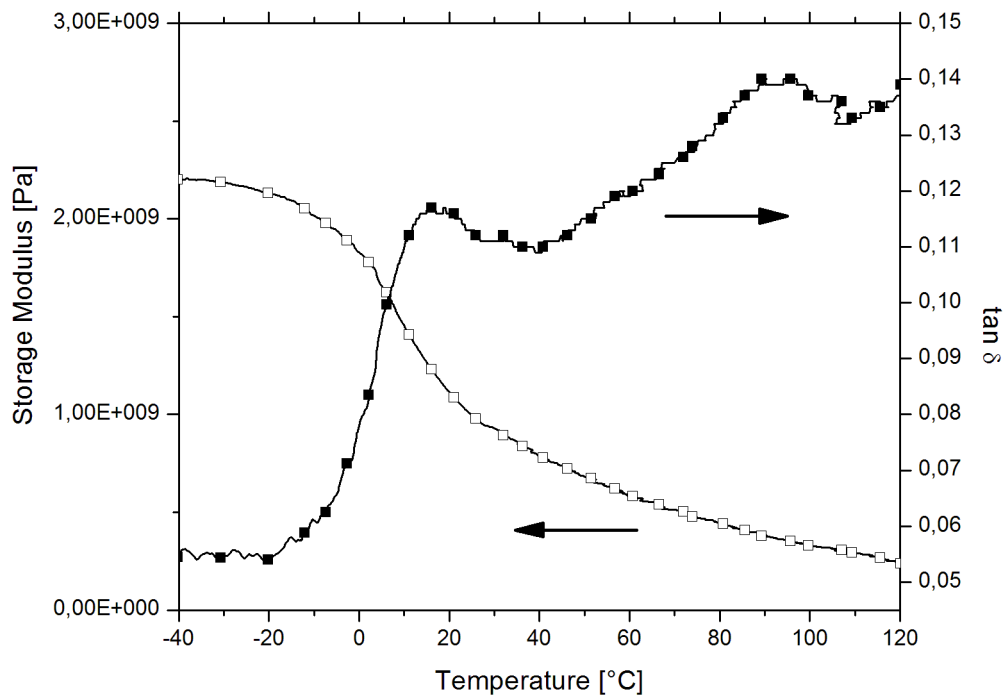


Figure A5. 2 - DMA curves for PP with 2% of nanoclay

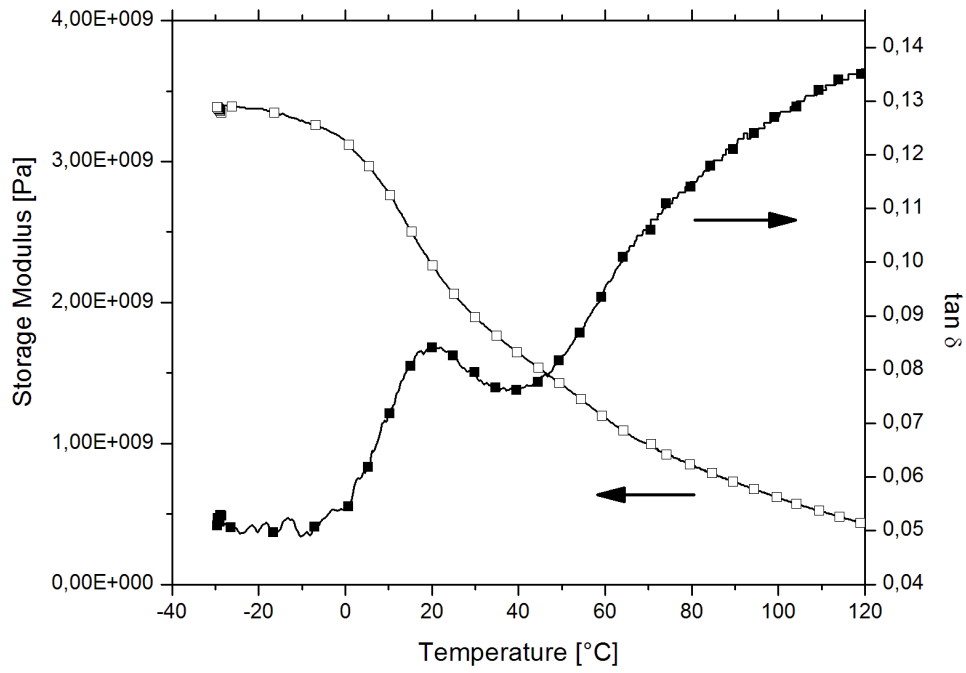


Figure A5. 3 - DMA curves for PP with 6% of nanoclay

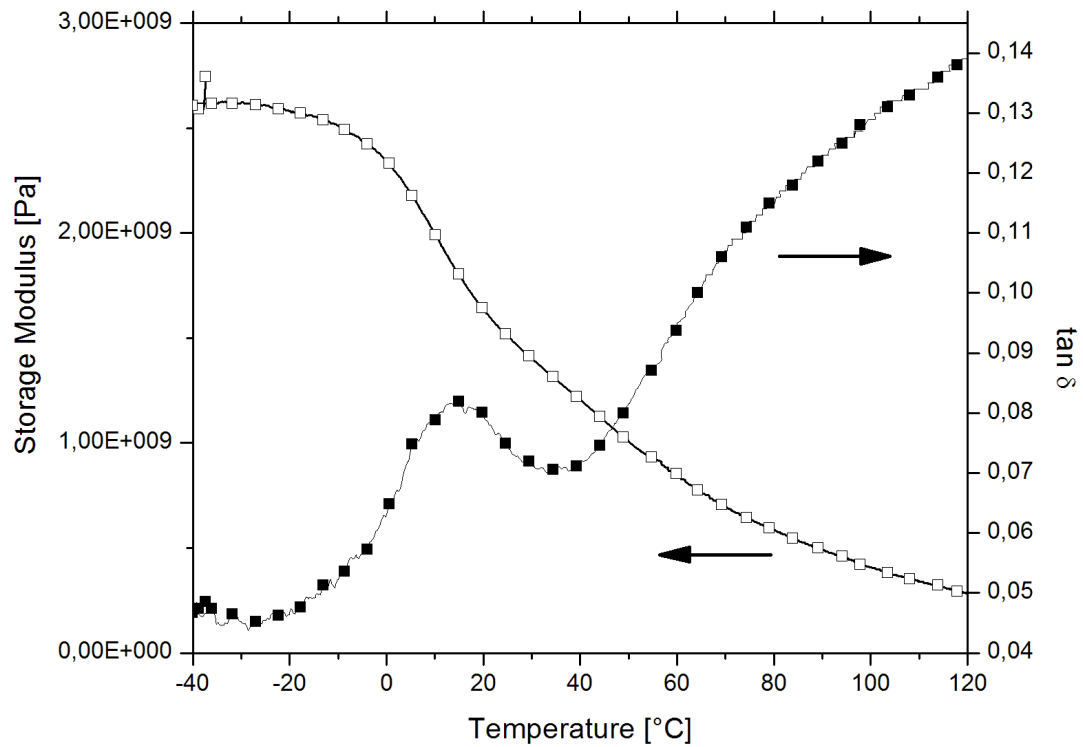


Figure A5. 4 - DMA curves for PP with 10% of nanoclay

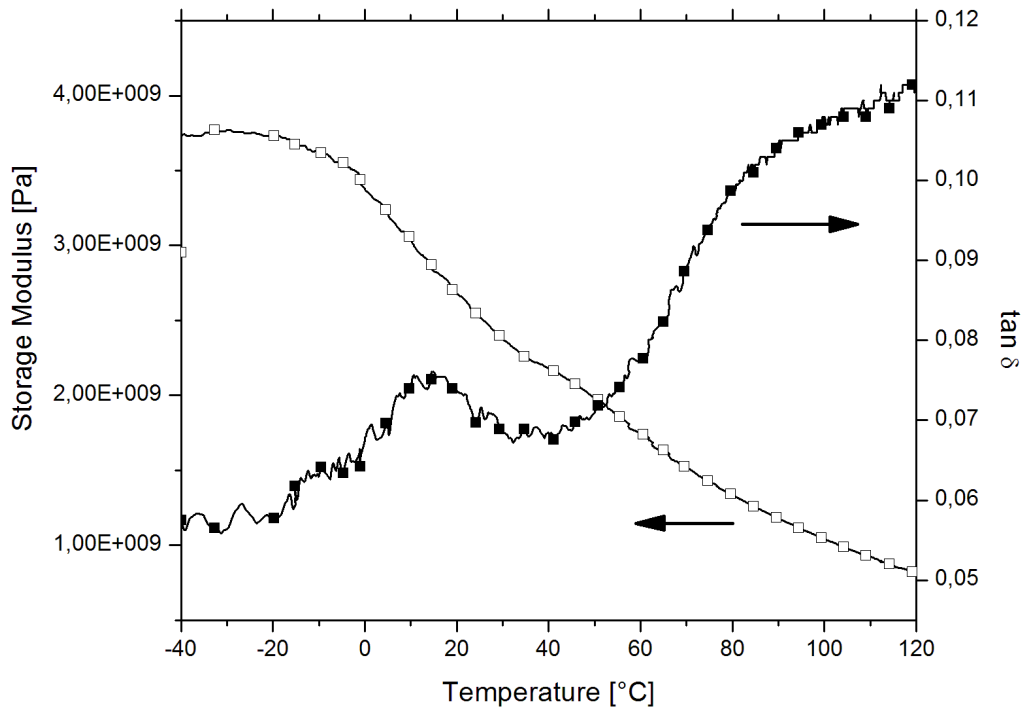


Figure A5. 5 - DMA curves for PP with 10% of glass fibre

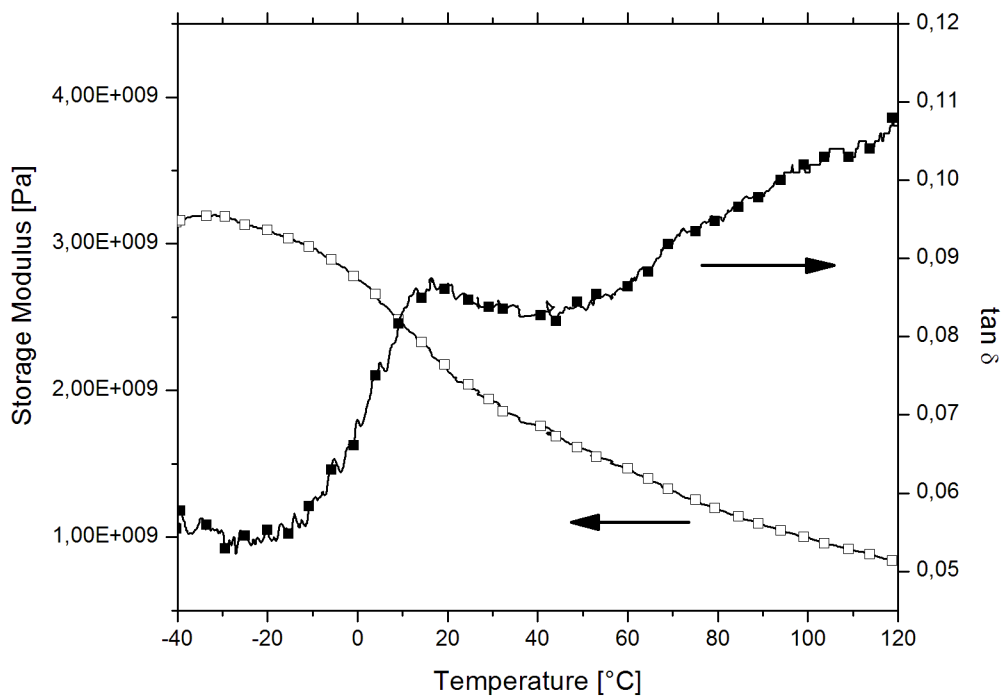


Figure A5. 6 - DMA curves for PP with 30% of glass fibre

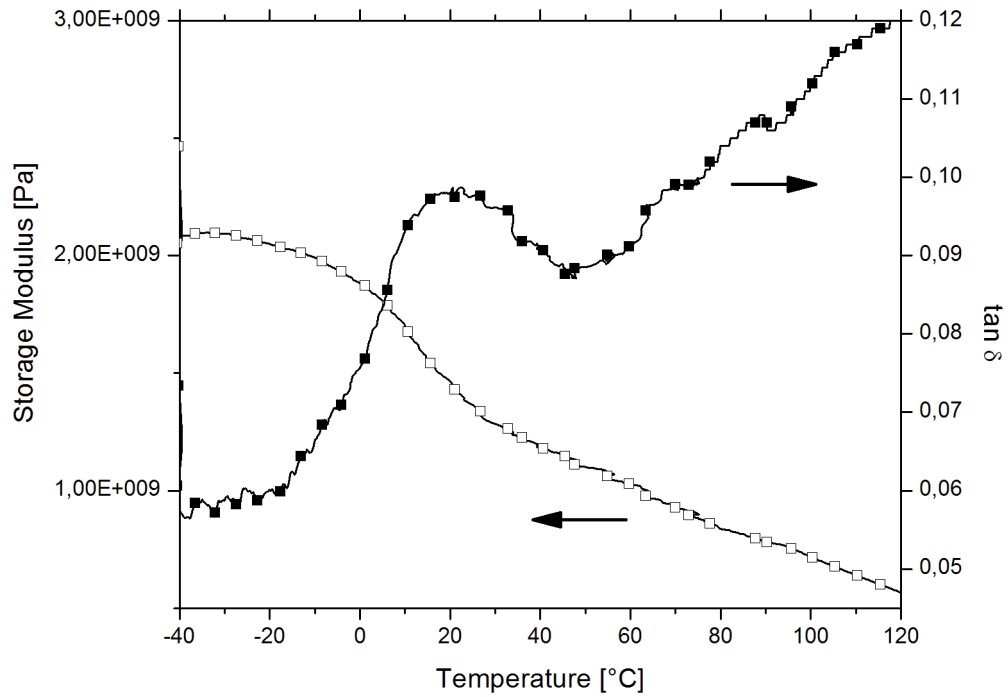


Figure A5. 7 - DMA curves for PP with 10% of glass fibre and 2% of nanoclay

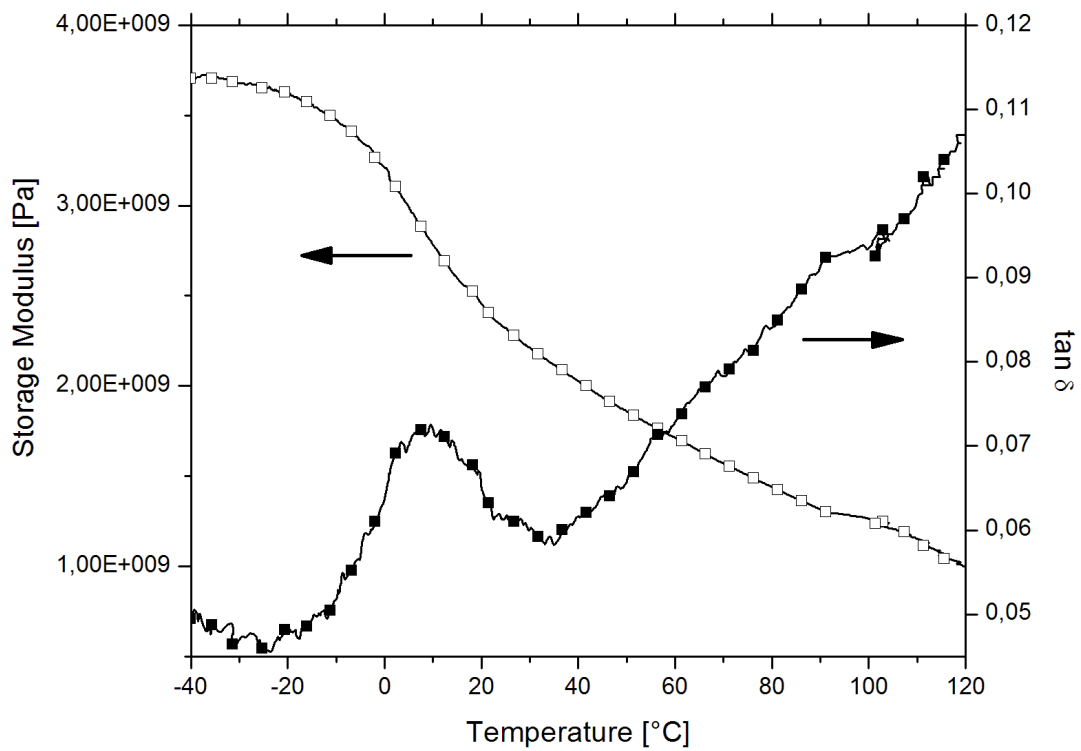


Figure A5. 8 - DMA curves for PP with 30% of glass fibre and 2% of nanoclay

A6 – Curves for Thermal expansion coefficient

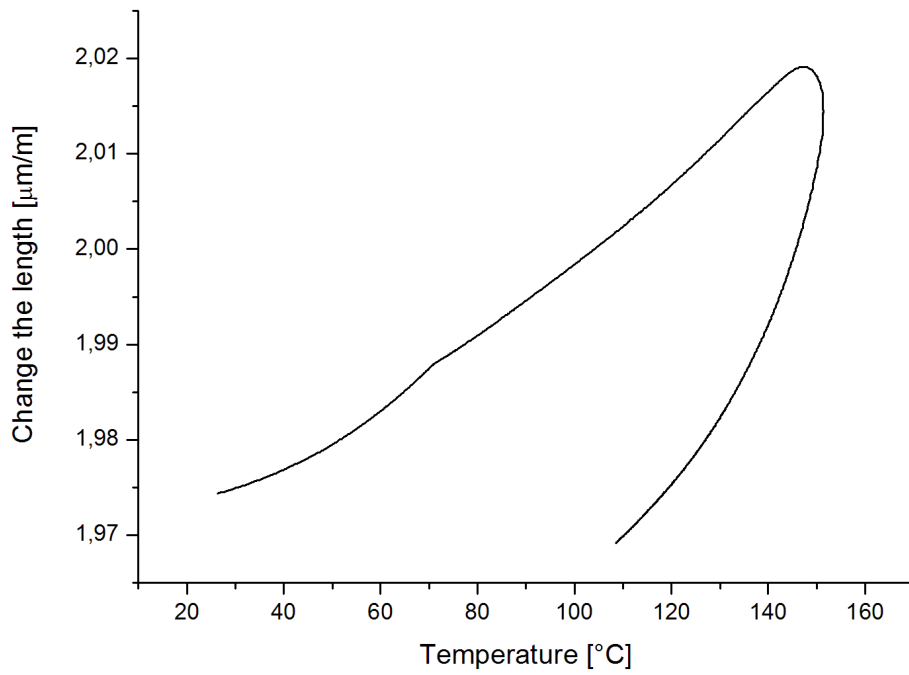


Figure A6. 1 - Curve for thermal expansion coefficient for PP2N

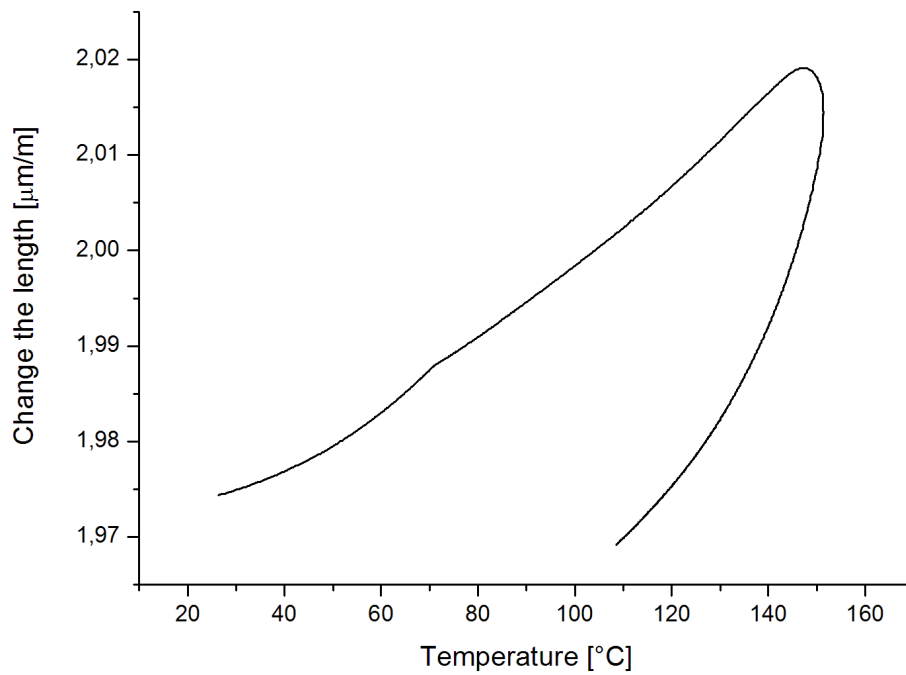


Figure A6. 2 - Curve for thermal expansion coefficient for PP6N

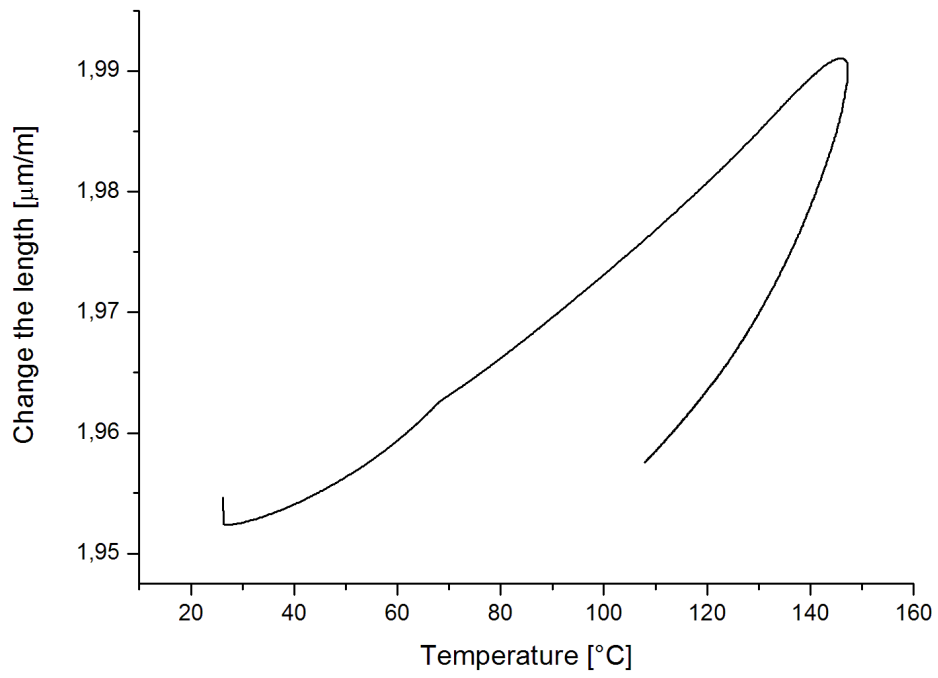


Figure A6. 3 - Curve for thermal expansion coefficient for PP10N

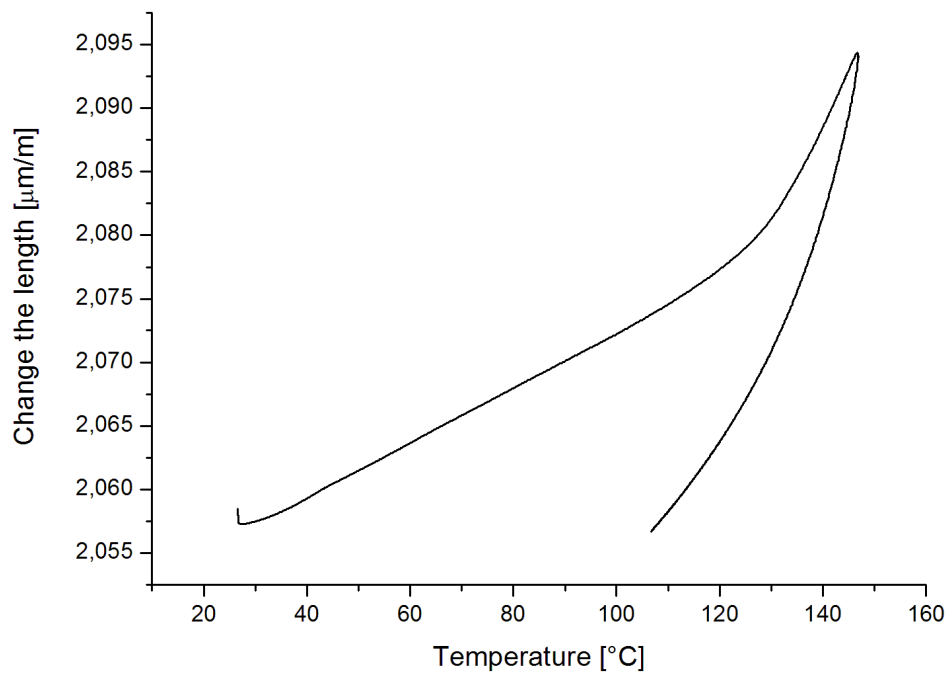


Figure A6. 4 - Curve for thermal expansion coefficient for PP10GF

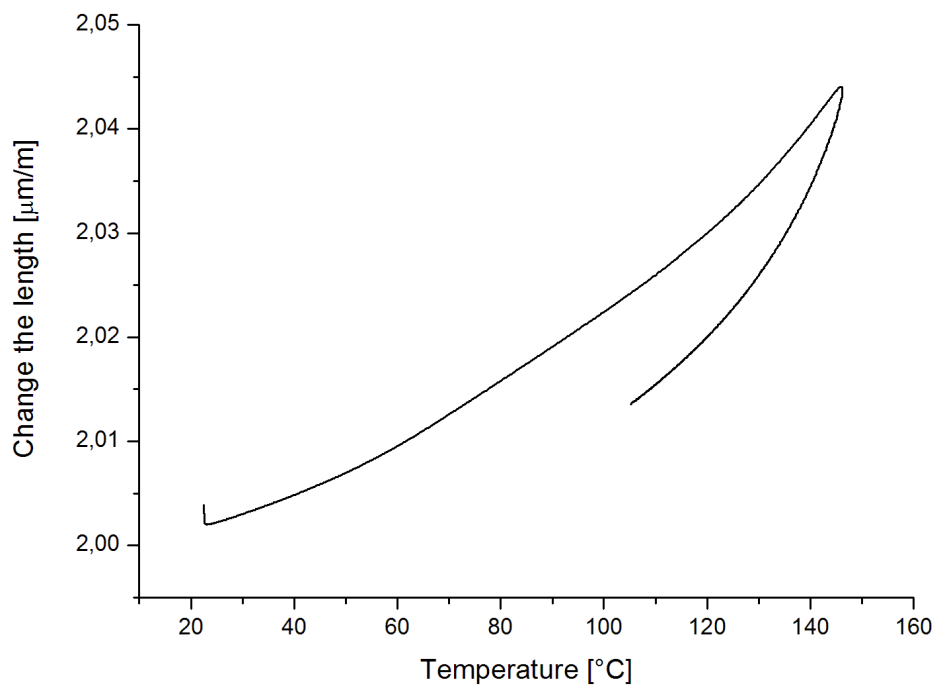


Figure A6. 5 - Curve for thermal expansion coefficient for PP30GF

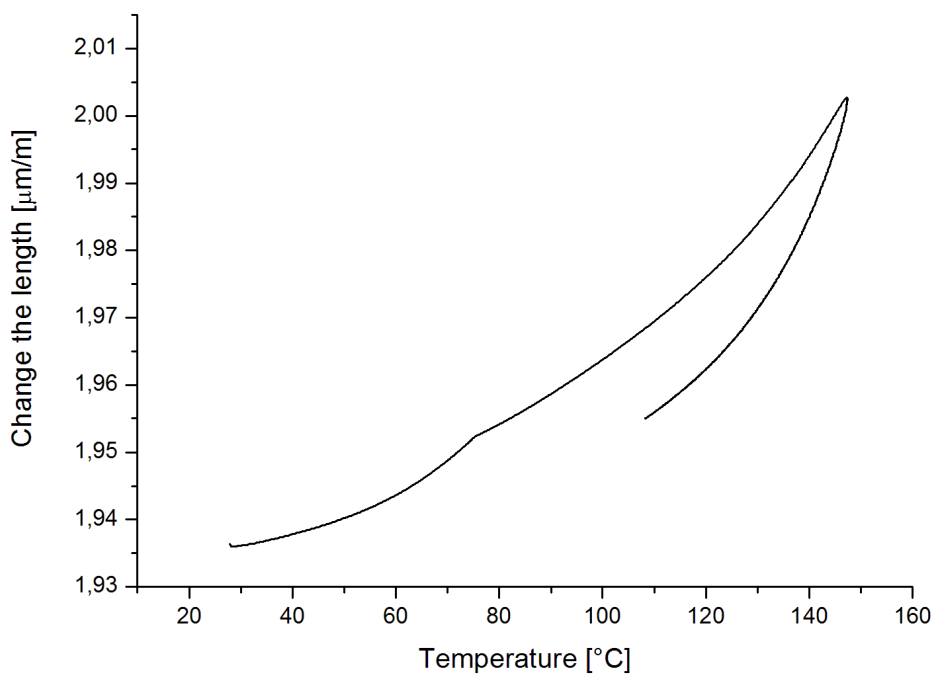


Figure A6. 6 - Curve for thermal expansion coefficient for PP10GF2N

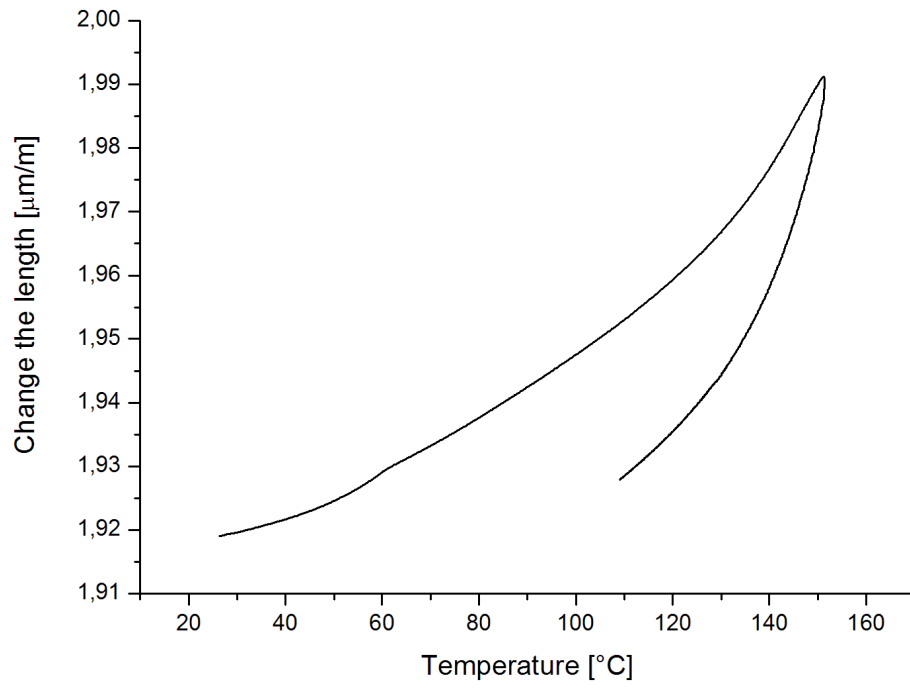


Figure A6. 7 - Curve for thermal expansion coefficient for PP30GF2N

A7 Parameters for model implementation for materials with glass fibres and nanoclays

Table A7. 1- Parameters used for polypropylene with 2% of nanoclay in the model

Polypropylene 2% nanoclay (PP2N)					
Parameter	Tm 30°C	Tm 50°C	Tm 75°C	Unit	source
Elastic modulus, E	0.7	0.65	0.6	GPa	*
Poisson coefficient, ν	0.38	0.38	0.38	-	
Thermal expansion coefficient, α	1.4×10^{-4}	1.4×10^{-4}	1.4×10^{-4}	K^{-1}	
linear compressibility, β	1.94×10^{-10}	1.94×10^{-10}	1.94×10^{-10}	MPa^{-1}	[3]
Friction coefficient, μ	0.13	0.17	0.20	-	*
Solidification temperature, T_s	122	122	122	°C	
Ejection average temperature,	42	61	79	°C	
Solidification pressure near ₁ , P_s	19.9	20.4	21.8	MPa	⊕
Solidification pressure far ₂ , P_s	12.6	13.2	14.4	MPa	

Table A7. 2 - Parameters used for polypropylene with 6% of nanoclay in the model

Polypropylene 6% nanoclay (PP6N)					
Parameter	Tm 30°C	Tm 50°C	Tm 75°C	Unit	source
Elastic modulus, E	0.7	0.65	0.6	GPa	*
Poisson coefficient, ν	0.38	0.38	0.38	-	
Thermal expansion coefficient, α	1.4×10^{-4}	1.4×10^{-4}	1.4×10^{-4}	K^{-1}	
linear compressibility, β	1.94×10^{-10}	1.94×10^{-10}	1.94×10^{-10}	MPa^{-1}	[3]
Friction coefficient, μ	0.13	0.17	0.20	-	*
Solidification temperature, T_s	122	122	122	°C	
Ejection average temperature,	42	61	79	°C	
Solidification pressure near ₁ , P_s	19.9	20.9	22.4	MPa	⊕
Solidification pressure far ₂ , P_s	12.2	14.0	15.0	MPa	

Table A7. 3 - Parameters used for polypropylene with 10% of nanoclay in the model

Polypropylene 10% nanoclay (PP10N)					
Parameter	Tm 30°C	Tm 50°C	Tm 75°C	Unit	source
Elastic modulus, E	0.7	0.65	0.6	GPa	*
Poisson coefficient, ν	0.38	0.38	0.38	-	
Thermal expansion coefficient, α	1.4×10^{-4}	1.4×10^{-4}	1.4×10^{-4}	K ⁻¹	
linear compressibility, β	1.94×10^{-10}	1.94×10^{-10}	1.94×10^{-10}	MPa ⁻¹	[3]
Friction coefficient, μ	0.13	0.17	0.20	-	*
Solidification temperature, T _s	122	122	122	°C	
Ejection average temperature,	42	61	79	°C	
Solidification pressure near ₁ , P _s	18.6	20.0	23.4	MPa	⊕
Solidification pressure far ₂ , P _s	11.1	13.1	15.1	MPa	

Table A7. 4 - Parameters used for polypropylene with 10% of glass fibre in the model

Polypropylene 10% glass fibre (PP10GF)					
Parameter	Tm 30°C	Tm 50°C	Tm 75°C	Unit	source
Elastic modulus, E	1.0	0.95	0.90	GPa	*
Poisson coefficient, ν	0.38	0.38	0.38	-	
Thermal expansion coefficient, α	2.5×10^{-4}	2.5×10^{-4}	2.5×10^{-4}	K ⁻¹	
linear compressibility, β	1.64×10^{-10}	1.64×10^{-10}	1.64×10^{-10}	MPa ⁻¹	[3]
Friction coefficient, μ	0.25	0.28	0.44	-	*
Solidification temperature, T _s	124	124	124	°C	
Ejection average temperature,	40	56	77	°C	
Solidification pressure near ₁ , P _s	21.7	22.5	23.4	MPa	⊕
Solidification pressure far ₂ , P _s	12.3	12.4	12.5	MPa	

Table A7. 5 - Parameters used for polypropylene with 30% of glass fibre in the model

Polypropylene 30% glass fibre (PP30GF)					
Parameter	Tm 30°C	Tm 50°C	Tm 75°C	Unit	source
Elastic modulus, E	0.92	0.91	0.90	GPa	*
Poisson coefficient, ν	0.38	0.38	0.38	-	
Thermal expansion coefficient, α	2.5×10^{-4}	2.5×10^{-4}	2.5×10^{-4}	K^{-1}	
linear compressibility, β	1.64×10^{-10}	1.64×10^{-10}	1.64×10^{-10}	MPa^{-1}	[3]
Friction coefficient, μ	0.25	0.32	0.45	-	*
Solidification temperature, T_s	123	123	123	°C	
Ejection average temperature,	44	59	77	°C	
Solidification pressure near ₁ , P_s	20.7	21.3	22.3	MPa	⊕
Solidification pressure far ₂ , P_s	12.4	13.0	13.7	MPa	

Table A7. 6 - Parameters used for polypropylene with 10% of glass fibre and 2 % of nanoclay in the model

Polypropylene 10% glass fibre 2% nanoclay (PP10GF2N)					
Parameter	Tm 30°C	Tm 50°C	Tm 75°C	Unit	source
Elastic modulus, E	1.05	1.04	1.03	GPa	*
Poisson coefficient, ν	0.38	0.38	0.38	-	
Thermal expansion coefficient, α	2.0×10^{-4}	2.0×10^{-4}	2.0×10^{-4}	K^{-1}	
linear compressibility, β	1.64×10^{-10}	1.64×10^{-10}	1.64×10^{-10}	MPa^{-1}	[3]
Friction coefficient, μ	0.29	0.35	0.49	-	*
Solidification temperature, T_s	127	127	127	°C	
Ejection average temperature,	39	56	75	°C	
Solidification pressure near ₁ , P_s	21.8	22.7	23.7	MPa	⊕
Solidification pressure far ₂ , P_s	15.8	16.4	16.4	MPa	

Table A7. 7 - Parameters used for polypropylene with 30% of glass fibre and 2 % of nanoclay in the model

Polypropylene 30% glass fibre 2% nanoclay (PP30GF2N)					
Parameter	Tm 30°C	Tm 50°C	Tm 75°C	Unit	source
Elastic modulus, E	0.92	0.91	0.90	GPa	*
Poisson coefficient, ν	0.38	0.38	0.38	-	
Thermal expansion coefficient, α	2.5×10^{-4}	2.5×10^{-4}	2.5×10^{-4}	K ⁻¹	
linear compressibility, β	1.64×10^{-10}	1.64×10^{-10}	1.64×10^{-10}	MPa ⁻¹	[3]
Friction coefficient, μ	0.25	0.31	0.45	-	*
Solidification temperature, T _s	122	122	122	°C	
Ejection average temperature,	38	57	75	°C	
Solidification pressure near ₁ , P _s	20.9	21.9	23.1	MPa	⊕
Solidification pressure far ₂ , P _s	14.6	15.1	15.4	MPa	

A8 DSC curves for materials used in this work

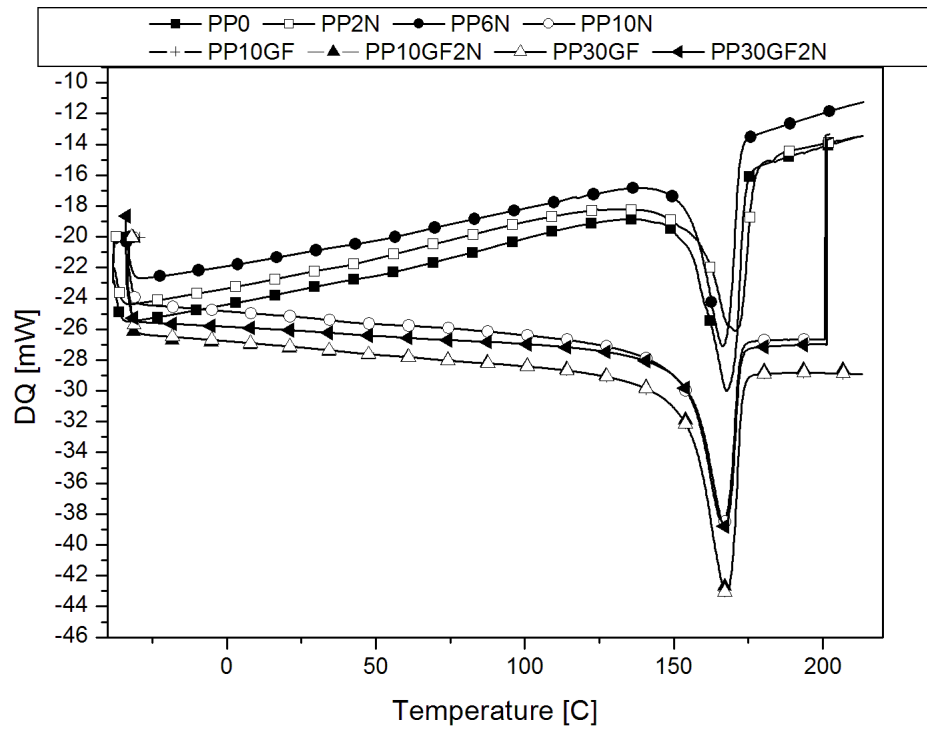


Figure A8. 1 - DSC curves for materials with different reinforcements

A9 Rheological curves

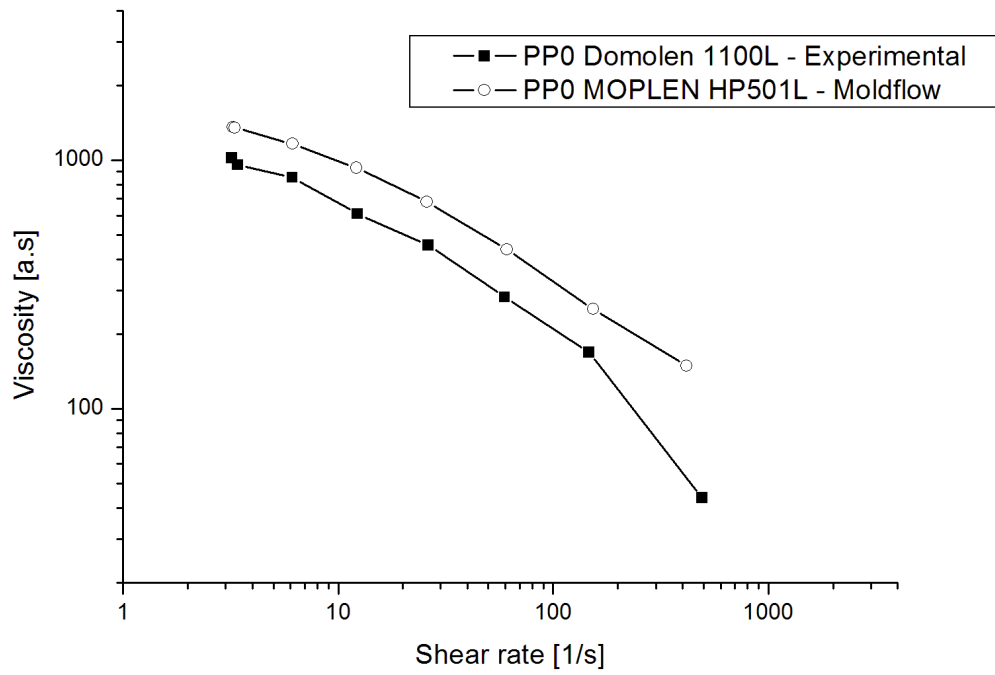


Figure A9. 1- Polypropylene without reinforcement in the temperature of 240°C

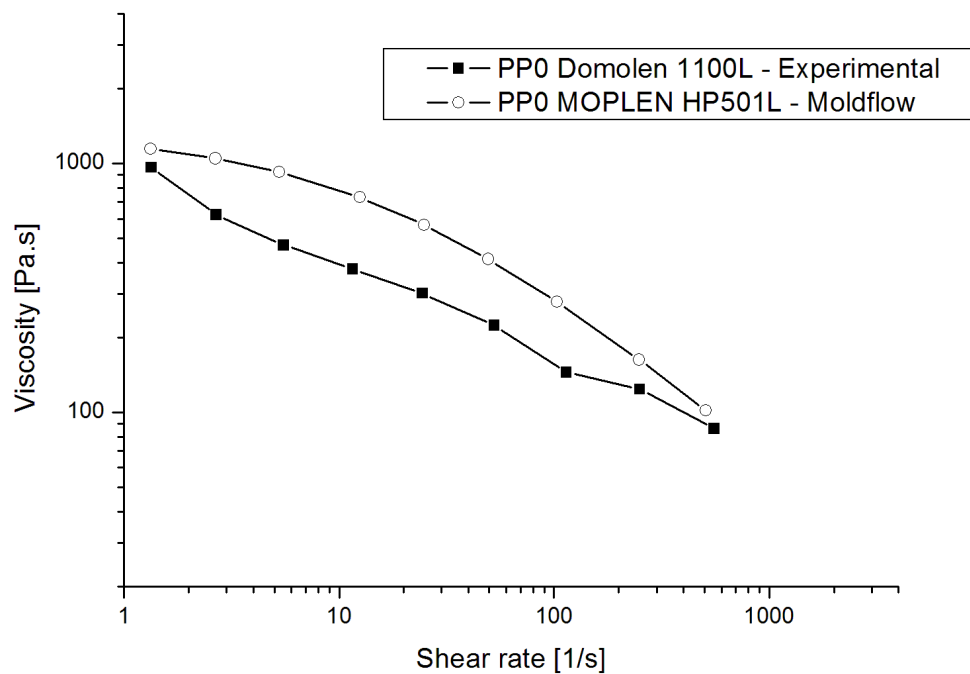


Figure A9. 2- Polypropylene without reinforcement in the temperature of 260°C

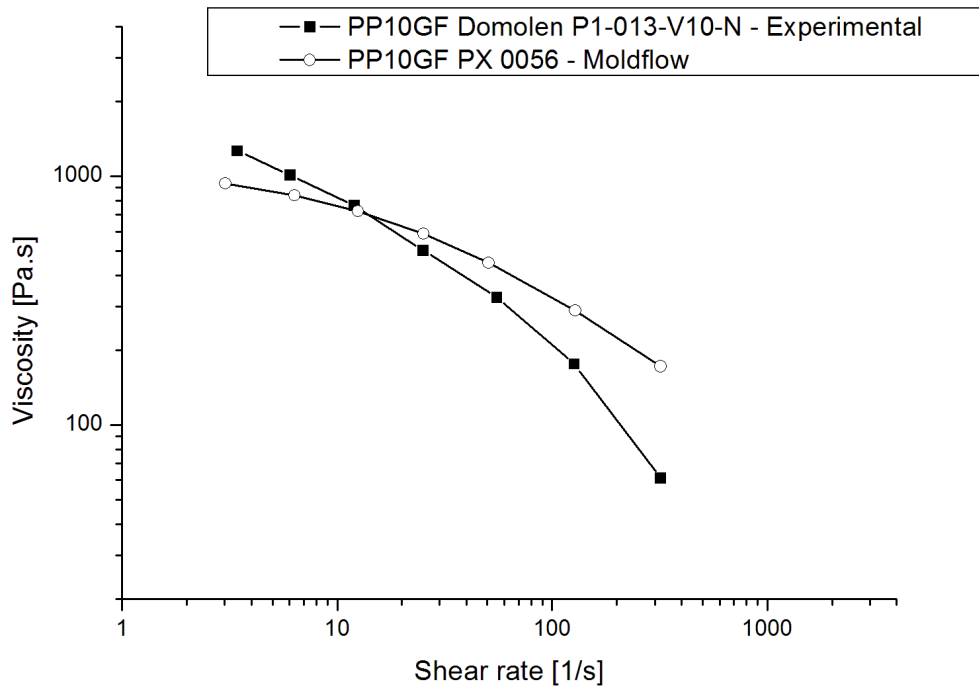


Figure A9. 3 - PP 10% glass fibre in the temperature of 200°C

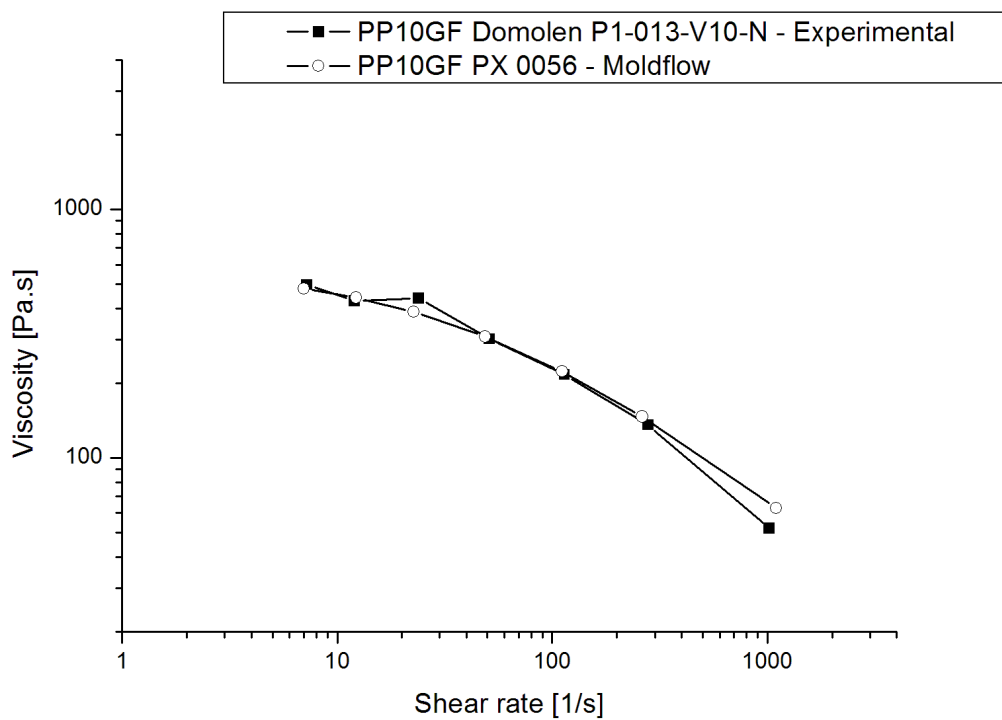


Figure A9. 4 - PP 10% glass fibre in the temperature of 240°C

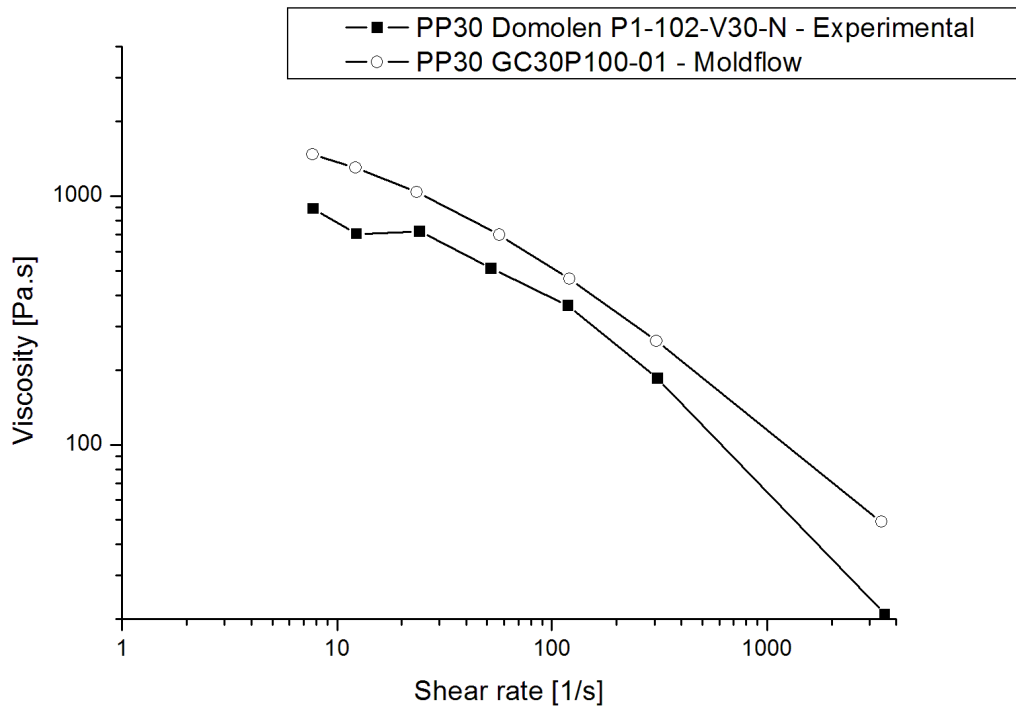


Figure A9. 5 - PP 30% glass fibre in the temperature of 200°C

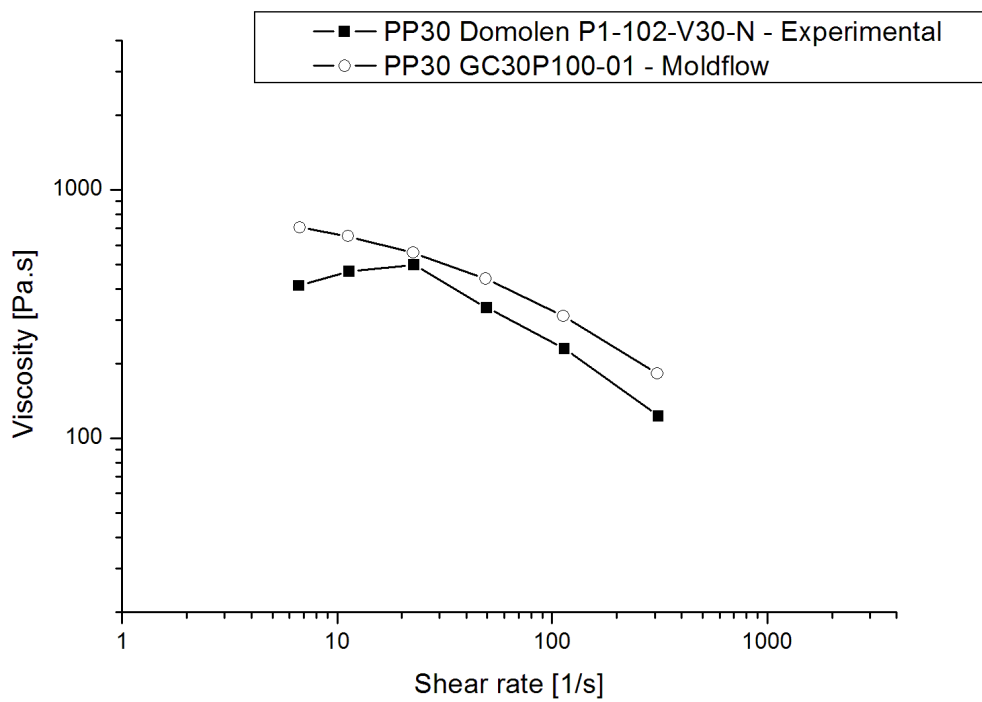


Figure A9. 6 - PP 30% glass fibre in the temperature of 253,3°